

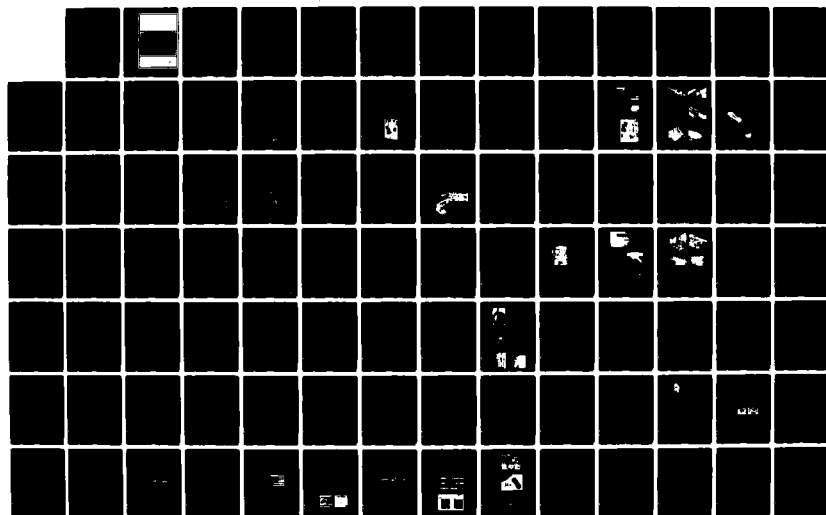
AD-A129 847

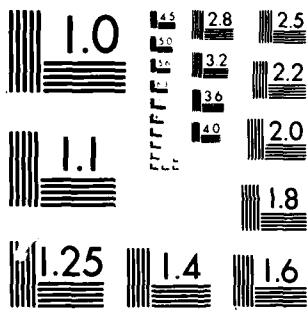
ENVIRONMENTAL EFFECTS ON MATERIALS FOR SPACE
APPLICATIONS(U) ADVISORY GROUP FOR AEROSPACE RESEARCH
AND DEVELOPMENT NEUILLY-SUR-SEINE (FRANCE) MAR 83
AGARD-CP-327 F/G 22/2

1/3

UNCLASSIFIED

NL





MICROCOPY RESOLUTION TEST CHART
NATIONAL BUREAU OF STANDARDS, 1963-A

AGARD-CP-327

ADA 1 298 47

DTIC FILE COPY

AGARD

ADVISORY GROUP FOR AEROSPACE RESEARCH & DEVELOPMENT

7 RUE ANCELLE 92200 NEUILLY SUR SEINE FRANCE

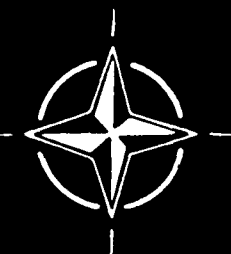
AGARD CONFERENCE PROCEEDINGS No. 327

Environmental Effects on Materials for Space Applications

This document has been approved
for public release and its
distribution is unlimited.

DTIC
JUN 29 1983
A

NORTH ATLANTIC TREATY ORGANIZATION



DISTRIBUTION AND AVAILABILITY
ON BACK COVER

83 06 28 167

AGARD-CP-327

NORTH ATLANTIC TREATY ORGANIZATION
ADVISORY GROUP FOR AEROSPACE RESEARCH AND DEVELOPMENT
(ORGANISATION DU TRAITE DE L'ATLANTIQUE NORD)

AGARD Conference Proceedings No.327
ENVIRONMENTAL EFFECTS ON MATERIALS FOR
SPACE APPLICATIONS



A

Papers presented at the 55th Meeting of the AGARD Structures and Materials Panel
in Toronto, Canada on 19-24 September 1982.

THE MISSION OF AGARD

The mission of AGARD is to bring together the leading personalities of the NATO nations in the fields of science and technology relating to aerospace for the following purposes:

Exchanging of scientific and technical information;

Continuously stimulating advances in the aerospace sciences relevant to strengthening the common defence posture;

Improving the co-operation among member nations in aerospace research and development;

Providing scientific and technical advice and assistance to the North Atlantic Military Committee in the field of aerospace research and development;

Rendering scientific and technical assistance, as requested, to other NATO bodies and to member nations in connection with research and development problems in the aerospace field;

Providing assistance to member nations for the purpose of increasing their scientific and technical potential;

Recommending effective ways for the member nations to use their research and development capabilities for the common benefit of the NATO community.

The highest authority within AGARD is the National Delegates Board consisting of officially appointed senior representatives from each member nation. The mission of AGARD is carried out through the Panels which are composed of experts appointed by the National Delegates, the Consultant and Exchange Programme and the Aerospace Applications Studies Programme. The results of AGARD work are reported to the member nations and the NATO Authorities through the AGARD series of publications of which this is one.

Participation in AGARD activities is by invitation only and is normally limited to citizens of the NATO nations.

The content of this publication has been reproduced directly from material supplied by AGARD or the authors.

Published March 1983

Copyright © AGARD 1983
All Rights Reserved

ISBN 92-835-0330-9



Printed by Specialised Printing Services Limited
40 Chigwell Lane, Loughton, Essex IG10 3TZ

PREFACE

The steadily increasing importance of space-related activities has focussed the attention of aerospace designers on the structural philosophies to be adopted in the construction of future spacecraft. In particular, the severe environment of space coupled with the need to retain geometrical constancy over very long exposure times imposes significant constraints on the designer. For example, he must have an adequate understanding of the effects of a space environment on the materials he intends to use; further, the very high dimensional accuracy demanded for the operation of some items, such as antennae can lead to special difficulties. In order to examine these constraints, the AGARD Structures and Materials Panel called a Specialists' Meeting in the Fall of 1982 with the aim of seeing how far characterization of materials had advanced, what data was available, and if existing methods of testing were satisfactory. In addition, the Panel wished to establish whether or not the introduction of advanced materials (both metallic and non-metallic) was likely to lead to particular problems which might call for special research effort.

The papers published here reflect interests in material properties (mechanical, surface, electrical and thermal) and environment (temperatures, vacuum, radiation including UV, charged particles, micro meteoroid, contamination and pre-launch environment), and in methods of testing. The Proceedings are concluded by a record of the round table discussion. The meeting has provided a sound basis from which the many problems brought out here may be considered further.

The Panel had a difficult task in making a selection from the papers offered by NATO nations; it acknowledges the wide response and expresses its sincere thanks to all those who read papers and also to all those who contributed to an interesting and useful discussion.

CONTENTS

	Page
PRFFACE	iii
	Reference
<u>SESSION I - GENERAL REQUIREMENTS AND RELATED DESIGN PHILOSOPHIES</u>	
FRACTURE MECHANICS AND FATIGUE CRITERIA IN MATERIAL SELECTION FOR SPACE APPLICATIONS by E.Vallerani, P.Marchese and G.Banino	1
STRUCTURAL DESIGN AND TEST OF THE SHUTTLE RMS by D.M.Gossain and P.J.Smith	2
SPACECRAFT THERMAL CONTROL SELECTION FOR SEVEN YEARS LIFETIME IN SYNCHRONOUS ORBIT by L.Preuss	3
REALISATION ET ESSAIS D'UNE STRUCTURE TREILLIS CARBONE-EPOXY POUR SATELLITES par J.F.Patin and J.L.Cecconi	4
RECORDER'S REPORT - Session I by D.G.Zimcick	RI
<u>SESSION II - ENVIRONMENT AND ENVIRONMENTAL EFFECTS</u>	
THE EFFECT OF SPACE ENVIRONMENT ON THE THERMAL DISTORTION OF POLYMER MATRIX COMPOSITES by R.C.Tennyson, G.E.Mabson and S.Ahmed	5
SPACE ENVIRONMENTAL EFFECTS ON MATERIALS by D.R.Tenney, G.F.Sykes and D.E.Bowles	6
SIMULATION DE L'ENVIRONNEMENT ACOUSTIQUE D'UN LANCEUR AU DECOLLAGE ET DE SES EFFETS VIBRATOIRES SUR LES STRUCTURES par A.Bourgine	7
SPACE ENVIRONMENTAL EFFECTS ON COMPOSITE MATERIALS* by V.F.Mazzio and W.B.Saylor	8
ELECTROSTATIC DISCHARGING BEHAVIOUR OF KAPTON AND OTHER DIELECTRIC MATERIALS IN A SIMULATED SPACE ENVIRONMENT by A.A.Dollery and D.Verdin	9
RECORDER'S REPORT - Session II by D.R.Tenney	RII
<u>SESSION III - PROPERTIES OF INTEREST</u>	
CANDIDATE MATERIALS FOR PRETENSIONED MEMBRANES OF FIBRE COMPOSITE MATERIALS FOR SPACE APPLICATION by W.Buchs	10
EFFECTS OF LONG DURATION EXPOSURE TO SIMULATED SPACE ENVIRONMENT ON NONMETALLIC MATERIAL PROPERTIES by C.L.Peacock, Jr. and A.F.Whitaker	11
STRUCTURAL DAMPING OF COMPOSITE MATERIALS FOR SPACE APPLICATIONS by L.Balis Crema, R.Barboni and A.Castellani	12

* Paper not available at time of publication.

SILICON SOLAR CELL CHARACTERIZATION AT LOW TEMPERATURES AND LOW ILLUMINATION AS A FUNCTION OF PARTICULATE IRRADIATION by A.F. Whitaker, S.A. Little and C.L. Peacock, Jr.	13
THE EFFECT OF SPACE ENVIRONMENT ON THE DAMPING OF POLYMER MATRIX COMPOSITES by R.C. Tennyson, W.D. Morison and G.E. Mabson	14
RECORDER'S REPORT - Session III by A.J. Russell	RIII
<u>SESSION IV - TESTS</u>	
TESTING OF FLEXIBLE DEPLOYED SOLAR ARRAY (L-SAT) by P.A. McIntyre, A.S. Jones, J. Renshall and G.W. Marks	15
THE MBB COMBINED EFFECTS CHAMBER FOR REAL TIME AND ACCELERATED TESTS UNDER SIMULATED SPACE ENVIRONMENT by O.K. Husmann	16
THE EFFECT OF COMBINED U.V. RADIATION AND HIGH ENERGY ELECTRONS ON THE BEHAVIOUR OF POLYMER MATRIX COMPOSITES IN HARD VACUUM by R.C. Tennyson, B.A.W. Smith and L.P. Hébert	17
THERMAL CYCLING TESTS ON MATERIALS AND COMPONENTS FOR SPACE APPLICATIONS by H. Hamacher, W. Ley and K.-V. Rehmann	18
LIFE PREDICTION CAPABILITY FOR SPACE LUBRICANTS* by H.E. Bandow, B.D. McConnell and W.E. Ward	19
RECORDER'S REPORT - Session IV by E.C. van Reuth	RIV

* Paper not available at time of publication

FRACTURE MECHANICS AND FATIGUE CRITERIA
IN MATERIAL SELECTION FOR SPACE APPLICATIONS

Prof. E.VALLERANI, Ing. P.MARCHESE, Ing. G.BANINO
AERITALIA, SPACE SECTOR
Corso Marche 41
10146 TORINO - ITALY

SUMMARY

The basic concepts employed in selecting fatigue and fracture resistance materials for the Spacelab design are reviewed, and specific examples of the application of these concepts are presented in detail.

The importance of the consideration of the strength and stress corrosion resistance in addition to toughness and fatigue strength is emphasized, specially for the selection of the aluminum alloys that cover most of the pressurized shell and internal structure. Weld material behaviour and welding processes were carefully evaluated prior to material selection, and after the selection largely tested to confirm the choice.

The possibility of automatic or manual repair without resulting in changes fracture-resistance and strength properties is considered.

Fracture mechanics and fatigue analysis is briefly summarized so the non destructive inspection methodologies and their practical application.

Finally a review of fatigue and fracture mechanics tests in full scale and component level on some Spacelab structural part is presented.

INTRODUCTION

The assumption that raw materials and finished products are defect-free and this quality is assured by appropriate non destructive inspections was the base, until recently, of the design approach to assure structural integrity either in space vehicles or in civil and fighter airplanes.

In the past, the structural integrity was assured from safety factor applied to the limit load and from the scatter factor imposed on the life load spectrum to protect against to fatigue failure.

However each of non destructive inspection methods has a "Detectability threshold" beyond which, any flaw with smaller size can not be detected.

This means that, in addition to the preceding design concepts, the structural design must assure that initial flaw present in the structure will not grow until catastrophic failure during predicted service life.

This aspect, of primary importance from safety standpoint, has been contractually imposed by the customer to the Spacelab structure, the first european space program able to provide an habitable environment for astronauts for a minimum of 50 whole different missions, and for which fracture mechanics criteria have been applied both in material selection and in analytical verification of the defect life.

FRACTURE MECHANICS APPLIED TO SPACE VEHICLES

The two main characteristics of manned space vehicles with respect to satellite projects are:

- Internal pressurization and environmental control to sustain life of astronauts in the best conditions even for a long stay in orbit (7-30 days for Shuttle, more for future applications).
- Reusability of the vehicle (50 missions for the Shuttle) from which derives the susceptibility to the fatigue and the crack propagation phenomena.

The basic requirements of the manned reusable space vehicles are to avoid, during the total operational cycle; loss of life, injury to personnel, loss of vehicle, and the loss of mission.

For all the structure of these vehicles, in order to cover the "safety aspects" imposed by the requirements, fracture mechanics analysis is of prime importance.

In fact all of the structural elements, whatever the product assurance practise, have to be considered with defects, and, under repetitive loadings, the defects tend to grow. The fracture mechanics analysis procedures ensure the means to predict such crack growth under the various loading conditions, while an appropriate plan of analysis and inspection provides the means to allow a structure with cracks, growing within specified limits during the operative life.

Spacelab, the european space laboratory, is the first european space program where the fracture mechanics concept has been imposed by the ESA and NASA criteria and requirements. Aeritalia as prime for the structure of the Spacelab Module, has been engaged in an extensive program of analysis, test verification and non destructive inspection to verify the adequacy of the design to the conditions imposed by the operative life requirements of 50 missions.

To reduce the possibility of catastrophic failures due to undetected flaws and to allow safe operations in the service period, a rigorous "failure control" was planned and performed.

A "fracture control plan" whose main subjects and disciplines include management, design, fracture analysis materials inspection and proof testing procedures, fabrication process and control, product assurance and test, is the management and engineering tool to ensure, relative to the life of the various structural elements, the adequacy of the specified safety levels.

Figure 1 shows the logic diagram summarizing the identification of the fracture critical items of the Spacelab structure based on the "fracture control plan".

SPACELAB STRUCTURE

The Spacelab Module Structure is designed according to a modular concept that allows the easy and rapid assembly of different basic configurations. The main components are the primary structure that consists of cylindrical elements with cone and closures, and the secondary structure consisting: floor, subfloor, racks for equipments and experiments, overhead racks. The cylindrical element has diameter of about 4 m, a length of 2.7 m, and is formed by six integrally numerically machined waffle pattern panels of aluminum alloy 2219-T851, welded together longitudinally, and welded circumferentially at the ends to forged rolled rings of same aluminum. The panel located on the top of each cylindrical elements incorporates a large hole, at the contour of which is permanently bolted a flange to support either the airlock or a simple closure. The cone shell is formed by seven panels of aluminum alloy 2219-T851, four of which are smooth and three of which have an opening of 0.4 m diameter and incorporate the flange that supports the "feed-through" or the windows. Cylinder and cone elements are terminated with rings supporting the inter-connecting flanges, and a single row of 128 bolts ensures the tightness of the cylinder-cylinder and the cylinder-cone joints. Each joint has incorporated the seal element moulded into an aluminum base ring. The module is supported in the orbit cargo bay at four points by titanium alloy integrally machined elements shaped to be bolted on the circum-

ferential flange ribs, providing a statically determinate attachment system, to preclude coupling between Spacelab and Orbiter. Inside the module shell is situated the secondary structure which supports the equipment and the experiments. The basic elements, floor and racks, that provide the highest utilization of the space within the module, are easily removable to permit a highly flexible experiment installation and checkout.

The figure 2 shows the main structure of the module while some details are represented in figure 3.

MATERIAL SELECTION BASED ON DESIGN CONCEPTS

In relation to the fundamental design criteria presented earlier, the materials used on the Spacelab structures have been chosen on the basis of the following concepts:

- Desirability to reduce the weight whenever feasible utilising aluminium and titanium alloys,
- Maximum welding characteristics to allow leak free modules,
- High residual static strength in presence of natural defects to assure control of crack growth,
- Low sensibility to stress corrosion, especially for the shell structure which can remain pressurized for 30 days, and the possibility to easily protect the surfaces from corrosion with films that can be strapped down whenever and wherever necessary,
- High fatigue resistance and low crack propagation velocity of eventual defects that may arise during the whole operational life, under flight, transportation, and handling loading,
- Possibility to apply normal non destructive inspections such as dye penetrants, X ray, ultrasonics, coupled to easy accessibility of internal structure to allow visual inspections during operational life.

The selection of materials based on the preceding concepts was complex as they must comply with different and sometimes conflicting requirements.

Of all the material properties to be accounted for considering the material state, (plate, sheet, forged, welded, extruded) and heat treatment, the more important considered were:

- Static strength and stiffness of basic material, defect free (σ , τ , ν , E, G, etc.)
- Fatigue strength characteristics of the material, defect free (σ versus N)
- Static strength of material in the presence of defined defects (fracture toughness K_{IC} , K_{IC})
- Crack propagation characteristics under repetitive loads (dl/dN) or under sustained loads (dl/dt)
- Stress corrosion cracking thresholds (K_{ISCC} , K_{SCC})

For module pressure shell the material 2219-T851 has been selected for its high strength properties associated with very good toughness properties. Also the properties of this material, welded with T.I.G. process using AL-2319 as filler wire are extremely good, a condition favouring selection.

Another relevant property of this material is its good behaviour under biaxial stress, as occurs under pressure when considering other aluminum alloys with higher uniaxial stress in unwelded sheet. This shows from the results of some tests performed from the ALCOA Research Laboratories using a hydraulic bulge test as a means to apply biaxial loads to sheet. In this test, circular or square samples of the material to be tested are clamped around the periphery by means of a hold-down ring, and hydraulic pressure is applied on one side. Figure 4 shows the results of bulge tests on a number of welded alloys using different fillers and varying welding states. For automatic weld and repairs, 2219 has higher strength than those in other high-strength, heat treatable alloys, and this indicates that this material is much less sensitive to all the possible welding conditions.

All other materials were chosen from those commonly used in the aeronautical industry considering always the following:

- Couple high strength with high fracture toughness
- Verify that the stress corrosion cracking threshold is adequate to the NASA-SE-R-0006 spec. requirements.

The list of basic materials selected in Spacelab structure are summarized in the following table where heat treatment, status of material before the machining, and the typical thicknesses of plates and of the final items are reported as well.

MATERIAL TYPE	MATERIAL DENOMIN.	HEAT TREATMENT	STATUS OF MATERIAL	PLATE THICKNESS t [mm]	ITEM THICKNESS t [mm]
ALUMINUM ALLOY	2219	T851	PLATE MACHINED	35 (PANELS) 105 & LONGER	1.6, 2.2, 8, 3.6, 4.5, 6.2, 6.8, 12.4,
	2219	T851	FORGING	—	4.5, 7.9, 14,
	2219	T851	WELDED	35	4.7,
	7075	T7351	PLATE MACHINED	30, 60	1.3, 4, 17, 23.5,
	2024	T76	SHEET	—	1.2, 1.0
TITANIUM	TI-6AL-4V	ANNEALED	PLATE MACHINED	30	8, 10, 25
	TI-6AL-4V	ANNEALED	FORGING	40 110 (KEEL) 240 (MAIN)	1.6, 7, 8, 9, 10, 11, 20, 30,
	IMI 550	—	PLATE MACHINED	—	10, 8,
NICKEL BASE ALLOY	INCONEL 718	SOLUBIL PRECIPIT. HEAT TREAT	BAR	φ 110	11, 8, 17, 21,
STAINLESS STEEL	CUSTOM 455	H1000	BAR	φ 70	φ 25, 18, 16,
	A 286	STANDARD	(BOLTS)	—	11.1, 7.9

TEST TO PROVIDE MINIMUM MATERIAL PROPERTIES

In order to collect from literature or standard material specifications, or measure by test, the material properties to be used in the structural design, it is necessary for each material to define the following parameters:

- Status of material at the purchase
- Heat treatment after working
- Surface treatments
- Final geometrical shape and dimension
- Final grain directions
- Environment (corrosion, humidity, etc.)
- Degradation of certain characteristics during the predicted life
- Temperature effects in service

All the material properties above defined as a basis of a correct design should also include:

- Stress/Strain curves and all other allowable parameters as σ , τ , ν , E, G, etc.
- Fatigue S-N curves at different stress concentration valve K_T
- Fracture toughness in plane strain (K_{IC}) and plane stress (K_C) conditions
- Crack propagation parameters and their threshold values
- Corrosion effects and threshold stress corrosion cracking (K_{ISCC} or K_{SCC})

and have to be evaluated considering the influence of all preceding parameters. For the selected materials many data were found in the specialized literature but to evaluate the influence of some relevant parameters (among the ones previously identified) and to guarantee the minimum value to be used in the analysis, Aeritalia has planned and performed many material tests, mostly at the beginning of the program as well as later, to cover certain doubts arising during the design phases.

Large number of tests (about 200) has been performed to determine the best static properties of aluminum alloy 2219-T851 in welded conditions.

Different welding parameters have been investigated at the beginning of the program and tests have been carried out coupled with tests to guarantee the minimum static properties of virgin material.

Another large number of tests was performed for defining the fracture mechanics properties (K_{IC}) of aluminum alloy 2219-T851 in different conditions and for the specific thickness chosen on the structure after the static analysis, including different samples with manual and automatic repairs of welding seam.

Figure 5 shows an example of the residual strength measured introducing surface flaws with different shape in the seam of 2219-T851 welded of 4.0 mm and 7.0 mm thickness with simple statistical evaluation of the best fit line to increase the confidence of the measured values.

Crack propagation tests (dl/dN) under sinusoidal load at constant amplitude were also performed especially for basic aluminum alloy under different conditions and for the materials where data were not collected in specialized literature.

Different type of defects (surface flaws with different shape and through cracks) were also tested to guarantee the leak before burst before the final catastrophic failure.

Results of through crack test propagation performed using test facility of figure 6 are shown in figure 7 for 2219-T851 plate, machined to 3.5 mm thickness and in figure 8 for 2219-T851 forging, 1.8 mm thickness.

Straight line assumed in fracture mechanics analysis and based on different test specimens is also included.

Crack propagation tests on stainless steel custom 455-H1000 using compact tension specimens were also performed under sinusoidal loads at constant amplitude but with different ratio, and the results are briefly summarized in figure 9.

The fatigue behaviour of the butt-welded joints in the presence of different mismatches to evaluate the actual geometry of welded aluminum alloy was also tested under sinusoidal load at constant amplitude with different R ratio to simulate the pressurization effects. One example of the results of these extensive tests included the final statistical evaluation is shown in figure 10.

Corrosion resistance to low humidity and laboratory air environment and sustained loads tests were made on basic aluminum alloy at Aeritalia, in addition a stress corrosion test program has been performed by ESA on parent material and welded joints to verify adequacy with NASA-SE-R-0006 spec. requirements as here reported.

MATERIAL FORM	TEST METHOD	TEST DURATION	RESULTS
2219-T851 PLATE	ASTM-G-38-73	48 DAYS	NO S.C.C. FAILURE
2219-T851 FORGING	ASTM-G-38-73	30 DAYS	NO S.C.C. FAILURE
2219-T851 WELDED	ASTM-G-44-75	30 DAYS	NO S.C.C. FAILURE
REPAIRED WELD	ASTM-G-44-75	30 DAYS	NO S.C.C. FAILURE

The following tables show a summary of type of test performed from Aeritalia on the chosen materials of Spacelab structure.

TYPE OF TEST	MATERIAL	TYPE OF DEFECT	THICKNESS t [mm]	NUMBER OF SPECIMENS
K _c (FEDDERSEN CONCEPT)	2219-T 851 MACHINED PLATE	SURFACE FLAW	1.6	7
			3.5	7
		THROUGH CRACK	1.6	3
			3.5	3
	2219-T 851 WELDING PLATES	SURFACE FLAW	4.0	7
			7.0	5
		THROUGH CRACK	4.0	3
			7.0	3
	2219-T 851 FORGING RINGS	SURFACE FLAW	1.8	4
			4.0	4
		THROUGH CRACK	9.0	4
			1.8	6
4.0	4	4		
	9.0	4		
2219-T 851 (AUTOMATIC OR MANUAL REPAIRS OF WELDING SEAM)	SURFACE FLAW	4.0	6	
		7.0	6	
K _{IC} (ACCORDING ASTM E 399-72)	CUSTOM 455 H1000 BARS	COMPACT TENSION SPECIMEN	13.0	4
	2219-T 851 MACHINED PLATE	SURFACE FLAW	1.6	4
3.5			4	
THROUGH CRACK		1.6	4	
		3.5	4	
2219-T 851 WELDING PLATE	SURFACE FLAW	-	-	
		THROUGH CRACK	4.0	4
7.0	4			

TYPE OF TEST	MATERIAL	TYPE OF DEFECT	SPECIMEN THICKNESS [mm]	NUMBER OF SPECIMENS
dL dN (L: TYPICAL DIMENSION OF DEFECT)	2219-T 851 MACHINED PLATE	SURFACE FLAW	1.6	8
			3.5	8
		THROUGH CRACK	1.6	6
			3.5	6
	2219-T 851 WELDED	SURFACE FLAW	4.0	9
			7.0	9
		THROUGH CRACK	4.0	4
			7.0	4
	2219-T 851 FORGED	SURFACE FLAW	1.8	3
			4.0	4
		THROUGH CRACK	9.0	4
			1.8	3
4.0	4	4		
	9.0	-		
2219-T 851 (AUTOMATIC OR MANUAL REPAIR OF WELDING SEAM)	SURFACE FLAW	4.0	4	
		7.0	4	
2219-T 851 WELDED	SURFACE FLAW (CURVED SPECIMENS)	3.4	12	
		CUSTOM 455 H1000 BARS	COMPACT TENSION SPECIMEN	13.0
FATIGUE BEHAVIOUR OF BUTT WELDED JOINTS WITH MISMATCH (STATICAL EVALUATION)	2219-T 851 WELDING PLATE	NO DEFECTS INTRODUCED MISMATCH d=0-1(mm) 2 DIFFERENT R RATIO R=0 AND R=0.5	4.0	ABOUT 8 SPECIMENS FOR EACH TYPE OF d AND R RATIO IN TOTAL 92

FRACTURE MECHANICS ANALYSIS AND RESULTS

To perform fatigue and fracture mechanics analysis more than 120 locations were chosen covering about 90% of primary structure and 50% of secondary structure typical areas.

Selection was made on the bases of the following criteria:

- Highly stressed zones
- Large stress amplitude areas
- All the elements for which "Leak before burst" is requested
- Regions where the inspection in service is difficult
- All preloaded connections (bolts) or element joining secondary to primary structure (lugs, bolts, pins, etc.)

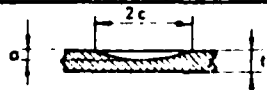
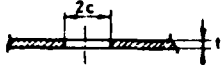
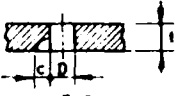
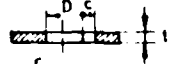
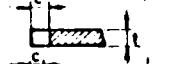
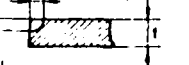
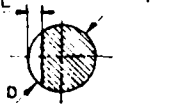
For each of these locations, a complete stress analysis has been performed then the final spectrum simulating one whole mission (flight, handling, transportation, etc.) constructed on the basis of the "unit loads or stresses" coupled with the accelerations.

For all the locations more than one type of defect has been considered on the basis of local stress field or geometrical dimensions including the presence of multiple holes, stringers, etc, to predict the growth and the critical crack length of the most critical defect that could arise in actual conditions.

The actual case was then modified to be coupled with analytical models found in literature or prepared for specific cases to permit the stress intensity factor formulation.

In addition, on the bases of the location geometry the stress concentration factor K_T was calculated on all the locations to permit fatigue analysis.

The last input to perform fracture mechanics analysis was to establish the minimum initial defect dimensions on the bases of the non destructive inspections (N.D.I.) that could be applied before and after the structure assembly. After extensive investigations it was decided to use the defect dimensions reported in next table which has the probability to be detected with standard N.D.I., on the Spacelab structure, of 90% and a confidence level of 95%.

DEFECT. TYPE	MINIMUM ASSUMED SIZES [mm]	APPLICABLE THICKNESS t [mm]	SKETCH OF DEFECTS
<ul style="list-style-type: none"> • SURFACE FLAWS <li style="padding-left: 20px;">$a/2c = 0,1$ <li style="padding-left: 20px;">$a/2c = 0,5$ 	<ul style="list-style-type: none"> $a = 1,5, 2c = 15.$ $a = 3,0, 2c = 6,0$ 	<ul style="list-style-type: none"> $t > 3,0$ $t > 3,0$ 	
<ul style="list-style-type: none"> • THROUGH CRACKS 	<ul style="list-style-type: none"> $2c = 6,0$ 	<ul style="list-style-type: none"> $t \leq 3,0$ 	
<ul style="list-style-type: none"> • SEMIELLIPTICAL FLAWS IN HOLES AND LUGS 	<ul style="list-style-type: none"> $a = c = 1,5$ 	<ul style="list-style-type: none"> $t > 1,5$ 	
<ul style="list-style-type: none"> • THROUGH CRACKS IN HOLES AND LUGS 	<ul style="list-style-type: none"> $c = 1,5$ 	<ul style="list-style-type: none"> $t \leq 1,5$ 	
<ul style="list-style-type: none"> • EDGE FLAWS 	<ul style="list-style-type: none"> $a = c = 1,5$ 	<ul style="list-style-type: none"> $t > 3,0$ 	
<ul style="list-style-type: none"> • EDGE CRACKS 	<ul style="list-style-type: none"> $c = 1,5$ 	<ul style="list-style-type: none"> $t \leq 3,0$ 	
<ul style="list-style-type: none"> • EDGE CRACKS IN PINS OR BOLTS 	<ul style="list-style-type: none"> $L = 1,5$ 	<ul style="list-style-type: none"> — 	

The fracture mechanics analysis was performed according to the flow chart logic diagram reported in figure 11 on the basis of the linear elastic fracture mechanics concepts. The defects propagation has been evaluated with "COLLIPRIEST" formulation which takes in to account the upper boundary of critical K valve, the stress intensity threshold valve ΔK_{TH} , and the influence of the stress ratio R .

Spectrum application simulating one mission for each of the considered locations is used and no retardation effects have been considered, increasing the conservative margin of the final results.

The fatigue analysis was performed using the PALMGREN-MINER formula based on cumulative damage calculated with interpolation of parametric S-N curves. Endurance limit was ignored during computer calculations.

The results of fatigue analysis were largely satisfactory and all the module structure met the requirement of 200 missions (50 x 4 L.F.) in spite of conservative K_T assumptions and stress levels.

The fracture mechanics analysis fulfills the requirements of leak before burst but revealed a limited number of problem areas out of the required life of 200 missions due to:

- Complex geometry (multiple holes, complicated lugs, etc)
- Unclear behaviour of material
- Difficulties of analytical schematization.

In these areas it was decided to perform a fracture mechanics tests at component level, simulating the actual geometry and stress distribution with proper set-up, and in parallel, to improve the analysis wherever it was possible.

NON DESTRUCTIVE INSPECTIONS APPLICATION AND METHODOLOGIES

The admission that the structure is not defect free leads to the necessity of having efficient non destructive methods to properly detect the size of cracks in structural elements and minimize the probability of propagation and final failure.

The NDI methods and requirements imposed to Spacelab module pressure shell and main structural items are:

- Ultrasonic inspection according to MIL-8750 class A
- Dye penetrant inspection after machining of final product
- X-Ray (only on weldments)

The minimum detection limit capability of these inspection methods are less than the minimum initial defect sizes assumed in fracture mechanics analysis and reported in preceding paragraph.

For weldments inspection with X Ray for example, the main defect acceptance criteria were

- Porosities and inclusions : 2(mm)
- Every type of crack : not acceptable
- Undercut, lack of fusion : not acceptable.

During manufacturing some weld defects (porosities and inclusions) outside specification limits have been accepted.

When an eventual repair could represent a potential risk of irreparably damage a F.M. analysis, was performed to guarantee the complete fulfillment of the "Structural Integrity" and the "Leakage Requirements".

To verify "Structural Integrity", through cracks flaws with a length equal to 1.2 times the "X Ray" 90° indication has been assumed in the analysis.

To verify "Leakage" it was necessary to develop a new X Ray inspection technique at two inclination, performed on two films, separated and exposed at the same time to establish the depth of defect and its position in the thickness.

The analysis based on "Embedded Flaw" schematization of the welding defect was then performed to verify that the defect will not grow through the thickness during the expected life.

The X Ray inspection at two inclination consists of two radiographic exposures on the same film using a known source displacement.

Two lead wires (or similar like copper), F1 and F2, are applied on each side of the object and the same distance from the defect and fitted in a way to be perpendicular to the direction of the source displacement as showed in figure 12.

The measurement of the displacements of each lead wire can be plotted in a diagram versus thickness in order to determine the defect position within the weld seam cross section, as showed in figure 13.

To minimize reading inaccuracy and to obtain reliable measurements, a second film has been adopted in Spacelab weld inspections, placed 20 mm from the original film, normally in contact with the lower weld side (figure 12), and the displacements versus thickness also plotted. The two couple of values (for example from one skin) have been compared and the extreme boundary assumed.

FATIGUE TEST

The Spacelab Module structure was submitted to a full scale fatigue test; the elements fully assembled as in flight condition in the vertical position were located on adapter cylinder (figure 14).

200 Spectra, simulating the whole flight mission (flight, handling, transportation), including the pressurization for each flight, were applied, and extensive non destructive inspections performed with disassembly of some part of internal structure after selected cycles.

The test was fully successful and no damage occurred in all the structure even after the application, at the end of the test, the limit loads of all the flight mission.

MAIN FITTING FRACTURE MECHANICS COMPONENT TEST

After the completion of the full scale fatigue test the whole main fitting , installed on the shell as in fatigue test configuration, was submitted to a fracture mechanics test to verify:

- Some areas where F.M. analysis did not met fully the requirements
- Not easily inspectable regions
- Area where linear elastic fracture mechanics concepts were not applicable

Briefly the test was foreseen to be performed according to the following steps:

- Mechanical introduction of 12 artificial defects in the areas chosen according to the preceeding criteria
- Sharpening of the artificial defect applying sinusoidal loads at constant amplitude which maximum level was 66% of max limit load, that occurs during whole mission
- Application of 100 spectra simulating flight missions measuring the propagation of artificial or natural defect that may arise during the test performance
- Verification of the maximum limit load capability of the main fitting when defects reach a length near the predicted critical value.

The figure 15,16,17, show some main fitting components (trunnion, pins, body) where artificial defects have been introduced mechanically with initial dimensions equal or larger than initial defects assumed in F.M. analysis.

For difficulties to sharp all the 12 locations in a same interval of time (or applied cycles) and for natural defects arized during the sharpening, some items have been sharpened at component levels with preparation of a specific set-up.

The measurement of the defect propagation under the application of the spectra simulating flight missions is still in progress and complete results are at the moment not available.

SUPPLEMENTARY F.M. COMPONENT TESTS

In other three limited locations, out of the fitting area where analitical results did not met the requirements , it was decided to perform F.M. tests at component level each with a proper set-up able to simulate actual geometry and stress distribution.

The three areas under test were (See figure 18):

- Top panel/Top ring connection
- Bolt 16 mm dia connecting floor support to the cylinder structure
- Spigot root of main inconel trunnion

In each test artificial defects were introduced then sharpened to simulate the fatigue crack and loaded with fatigue spectrum untill the defect dimension reached the predicted critical value. Finally it was demonstrated that the item was able to withstand the max limit load. One example of the pin cracked and its cross section showed clearly the fatigue propagation and the final failure as reported in figure 19.

The results of these tests were largely satisfactory showing that analitical predictions were based on too conservative assumptions.

REFERENCES

- LIU - Fracture control methods for space vehicles, NASA-CR-134596, Vol. 1, August 1974.
- EHRET - Fracture control methods for space vehicles, NASA-CR-134597, Vol. 2, August 1974.
- FIFTAL - Fracture mechanics data on 2219-T87 aluminum for space Shuttle external tank, report n. 826-2027, Martin Marietta, July 1975.
- MASUBUCHI, K - Welding of high-strength aluminum alloys, M.I.T., department of Ocean engineering, September 1973.
- LIEBOWITZ, H. - Fracture mechanics of aircraft structure, AGARD-AG-176, January 1974.
- VARIOUS - Alloy design for fatigue and fracture resistance, AGARD-CP-185, January 1976.
- VARIOUS - Fracture mechanics design methodology, AGARD-CP-221, September 1976.
- ERDOGAN - Crack propagation theories, NASA-CR-901, October 1967.
- SIH, G.C. - Handbook of stress intensity factors, Vol. I and II, Institute of fracture and solid material, Bethlehem, 1973.
- SIH, G.C. - Handbook of stress intensity factors, Lehigh University, Bethlehem, 1973.
- ROOKE, D.P., CARTWRIGHT, D.K. - Compendium of stress intensity factors, Her Majesty's Stationery Office, 1974.
- TADA, PARIS, IRWIN - Stress intensity factor handbook, June 1973.
- FEDDERSEN, C.E. - Plane strain crack toughness testing, ASTM, special technical publication n. 410, 1966.
- BROEK, P. - Elementary engineering fracture mechanics, Noordhoff International Publishing, Leyden, 1974.
- VARIOUS - Fracture toughness testing and its applications, ASTM-STP-381, 1964.
- VARIOUS - Fracture toughness and slow-stable cracking, ASTM-STP-559, 1973.
- VARIOUS - Fracture analysis, ASTM-STP-560, 1973.
- VARIOUS - Progress in flaw growth and fracture toughness testing, ASTM-STP-536, 1972.
- VARIOUS - Stress analysis and growth of cracks, ASTM-STP-513, 1971.

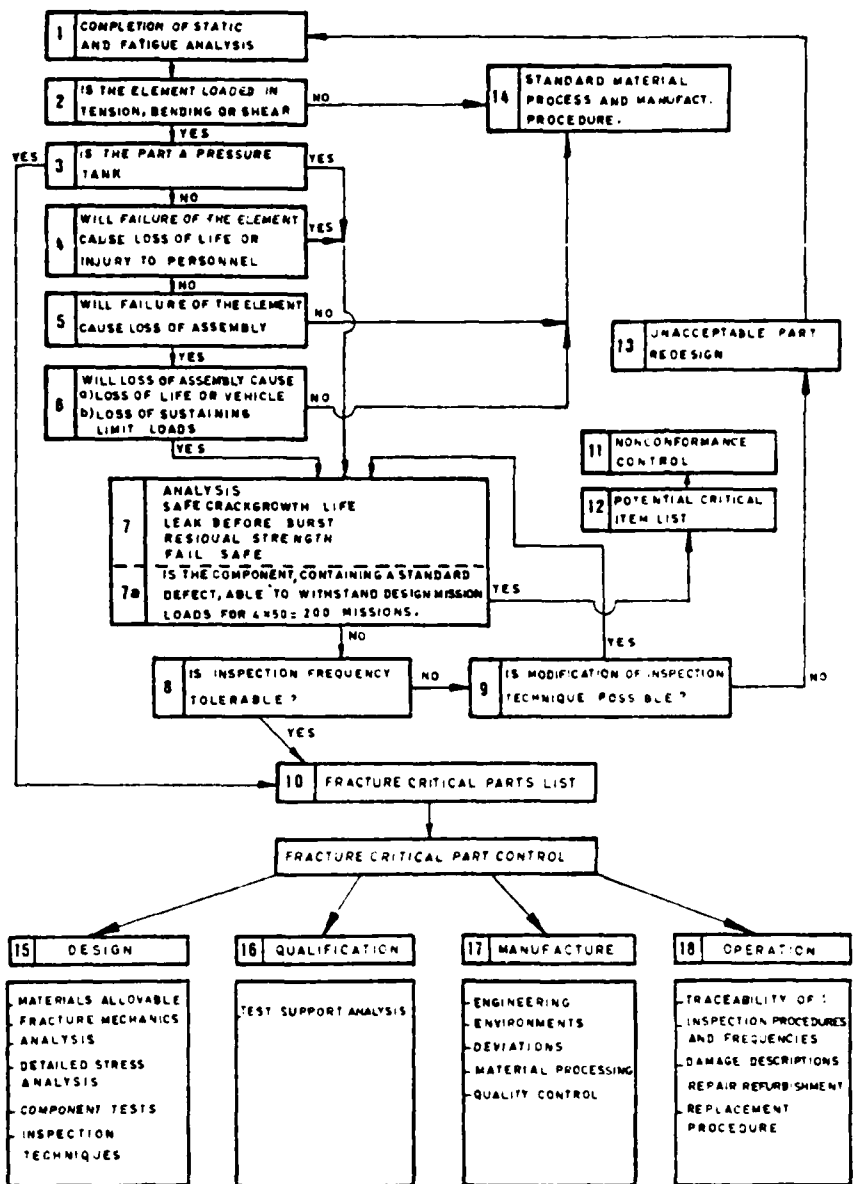


FIG. 1 - Fracture critical part identification logic

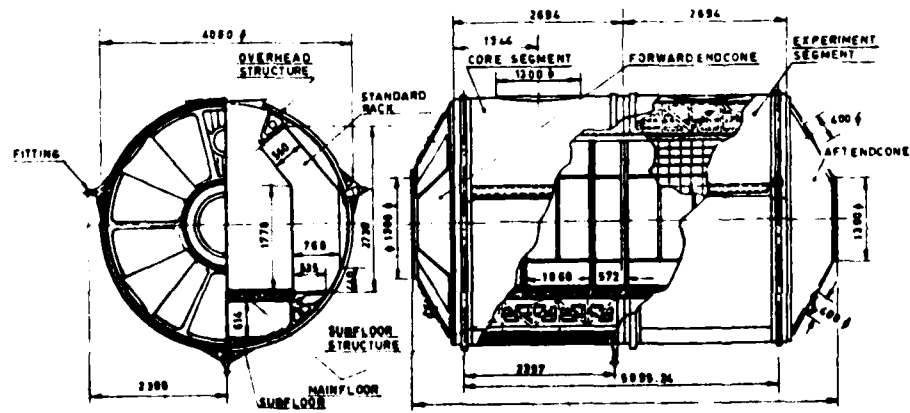
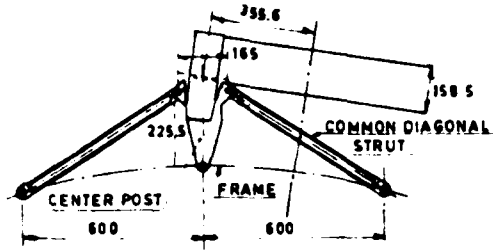
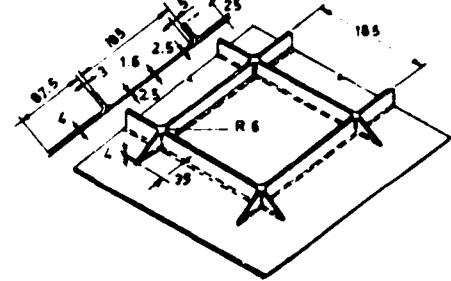


FIG. 2 - Spacelab module structure assembly

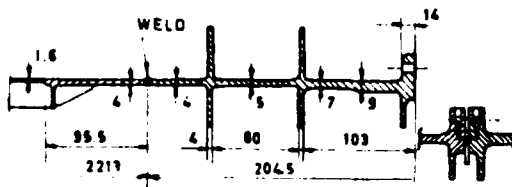
MAIN FITTING - DIAGONAL STRUTS



WAFFLE PANEL

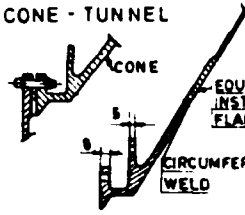


CYLINDER-CYLINDER



MAIN JOINTS

CONE - TUNNEL



CONE - CYLINDER

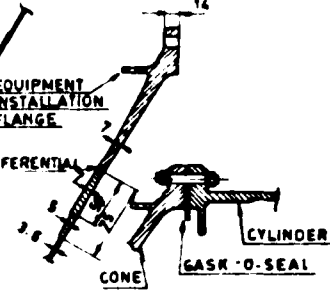


FIG. 3 - Spacelab module structure - some details

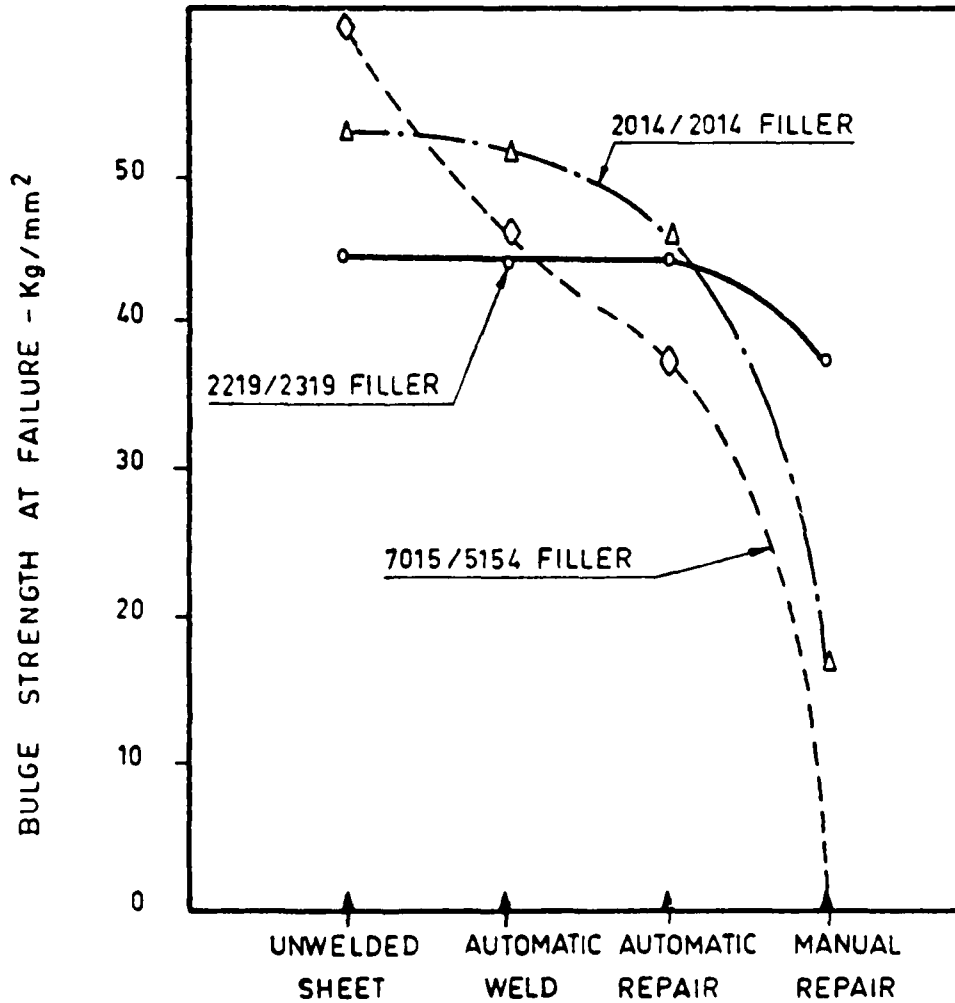


FIG. 4 - Effect of welding condition on bulge test

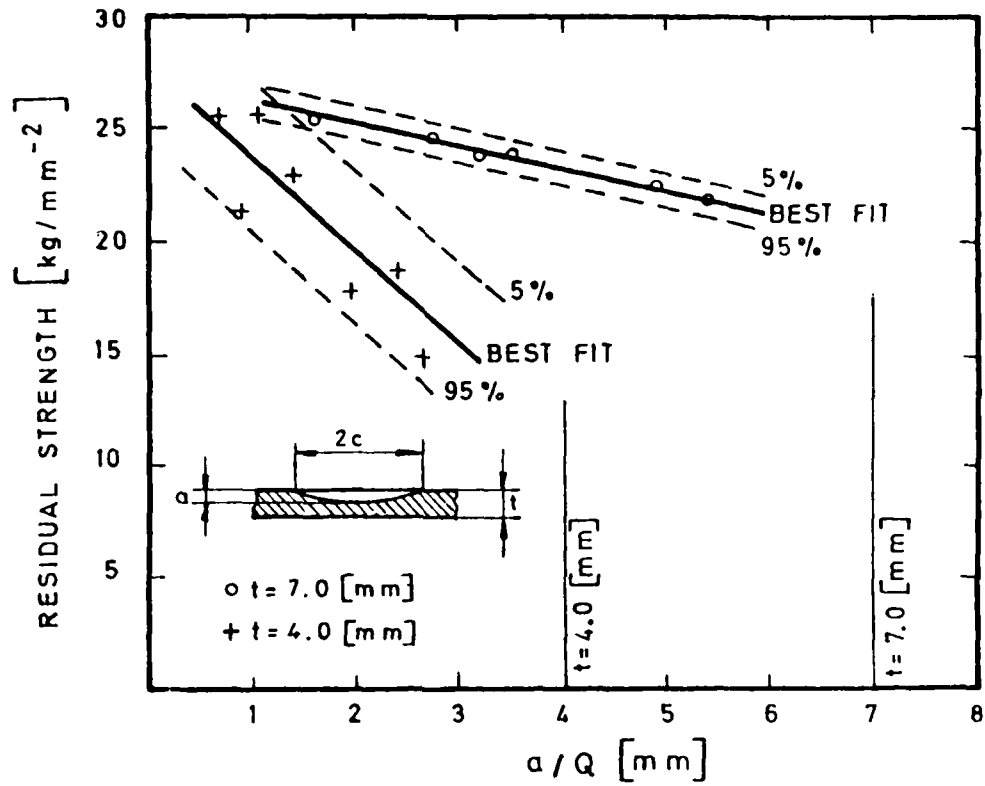


FIG. 5 - Residual strength versus flaw shape in 4.0 mm and 7.0 mm thickness of 2219-T851 welded



FIG. 6 - Test facility for crack propagation tests on aluminium alloy specimens

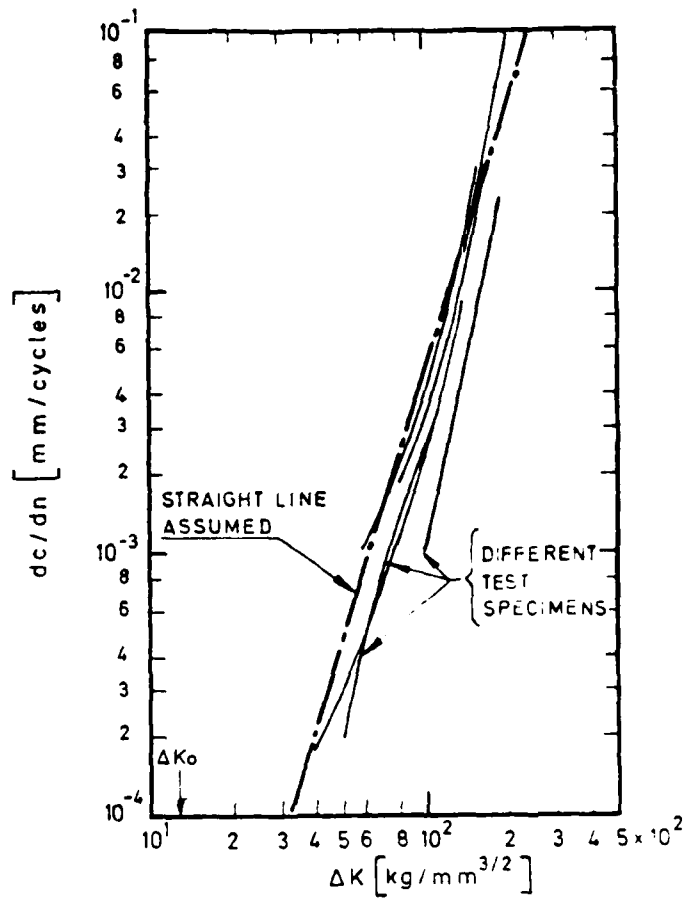


FIG. 7 - Through crack test propagation data of 2219-T851 plate, machined to 3.6 mm thickness

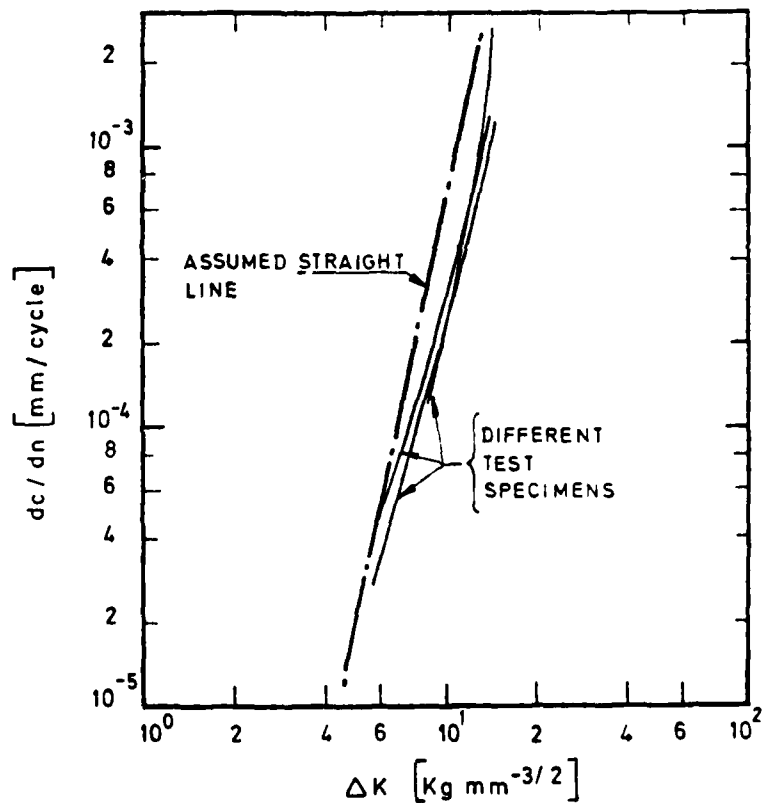


FIG. 8 - Through crack test propagation data of 2219-T851 forged to 1.8 mm thickness

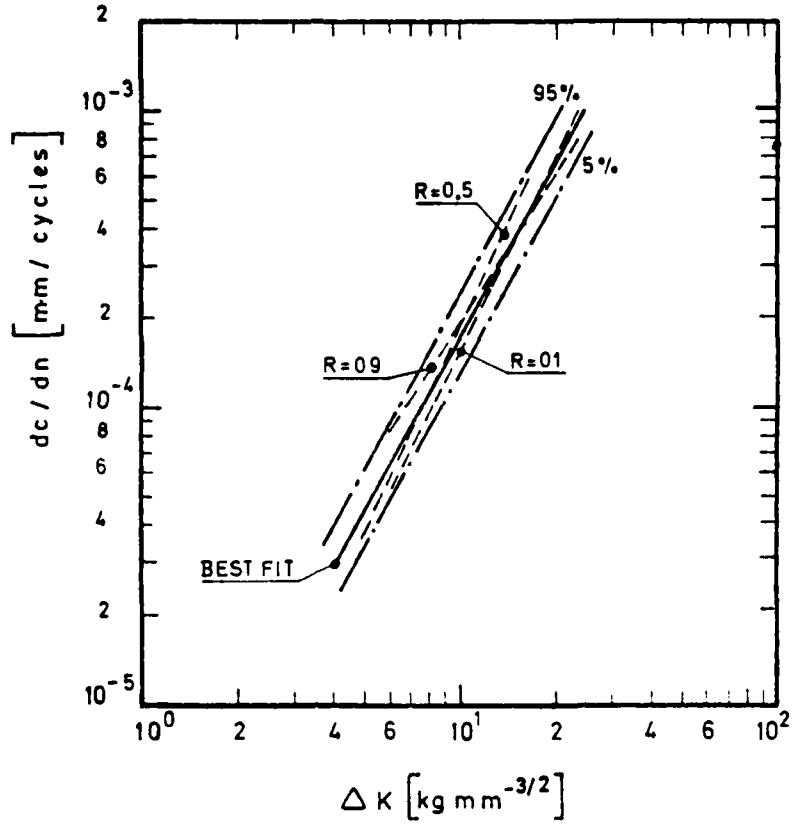


FIG. 9 - Test propagation data of custom 455-H1000 stainless steel, using compact tension specimens 13. mm thickness

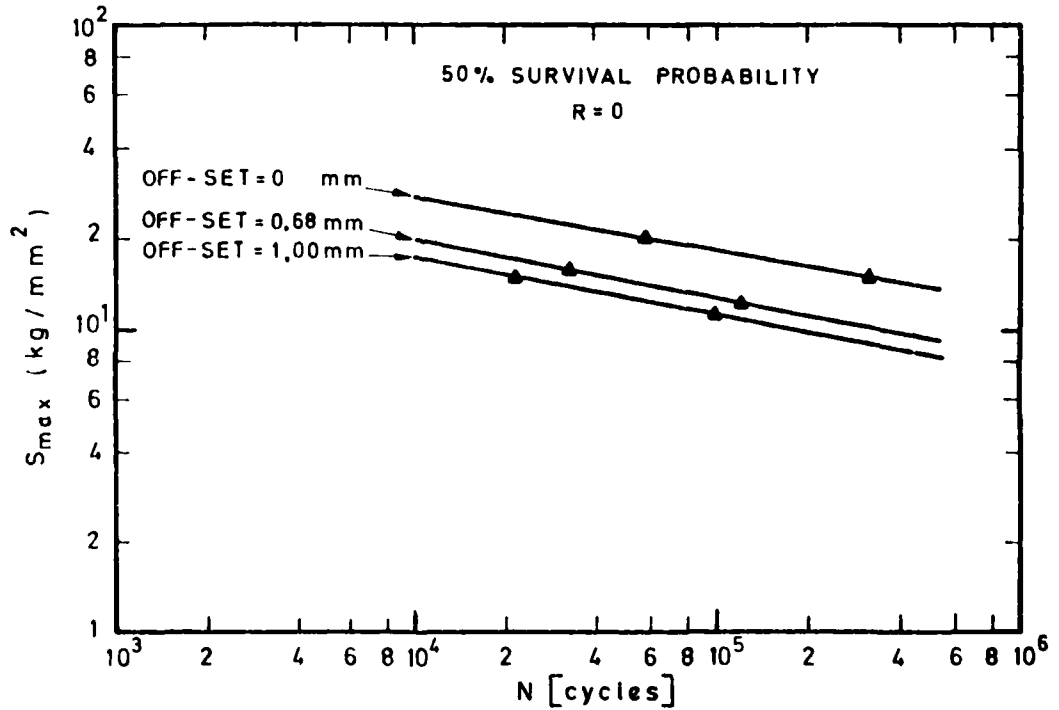


FIG. 10 - Fatigue behaviour of 2219-T851, butt-welded joints with different off-sets and r ratio

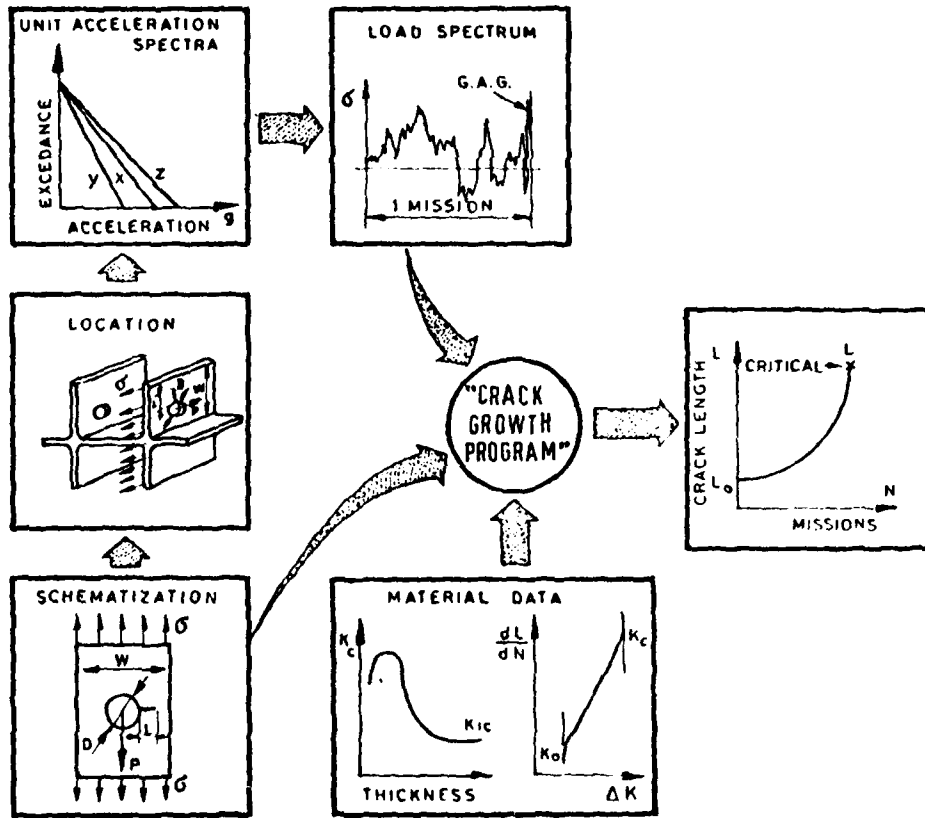


FIG. 11 - Logic diagram applied in fracture mechanics analysis of Spacelab structure

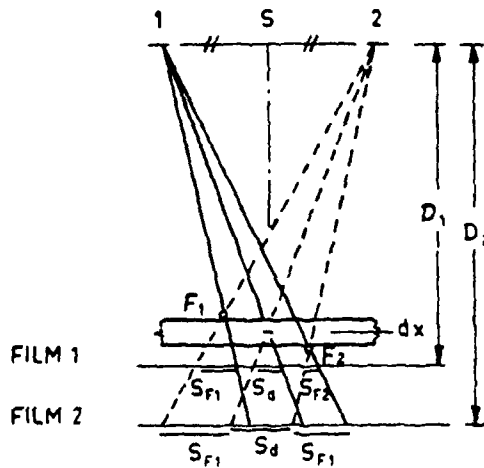
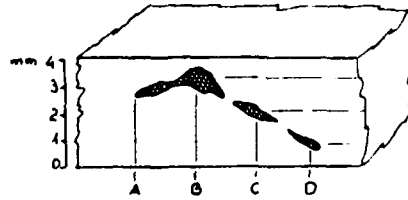
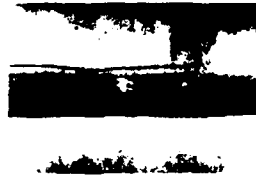


FIG. 12 - X-Ray at two inclinations (two films method)

SEZ. LONGITUDINALE



FILM A CONTATTO



FILM SEPARATO

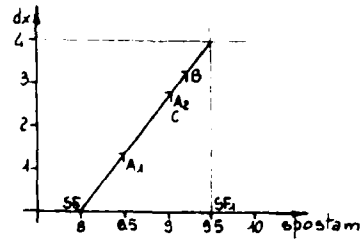
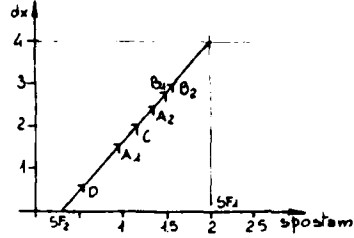


FIG. 13 - X-Ray films showing defect with lead wire and their analytical prediction in cross section of welded seam.



FIG. 14 - Fatigue full scale facilities.



FIG. 15 - Main Inconel 718 trunnion with defect mechanically introduced (see detail) for F.M. component test.

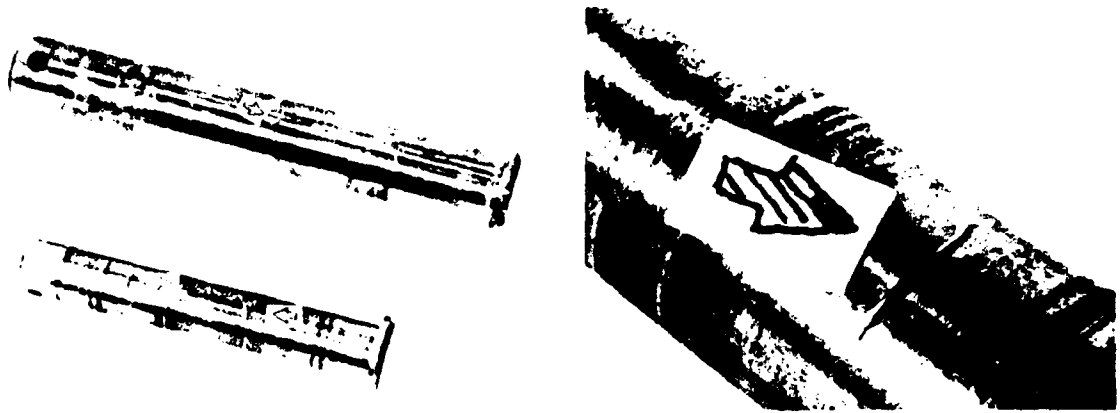


FIG. 16 - Custom 455-H1000 pins with defects mechanically introduced (see detail) for F.M. component test.



FIG. 17 - TI-6AL-4V main fitting body with defect mechanically introduced (see detail) for F.M. component test.

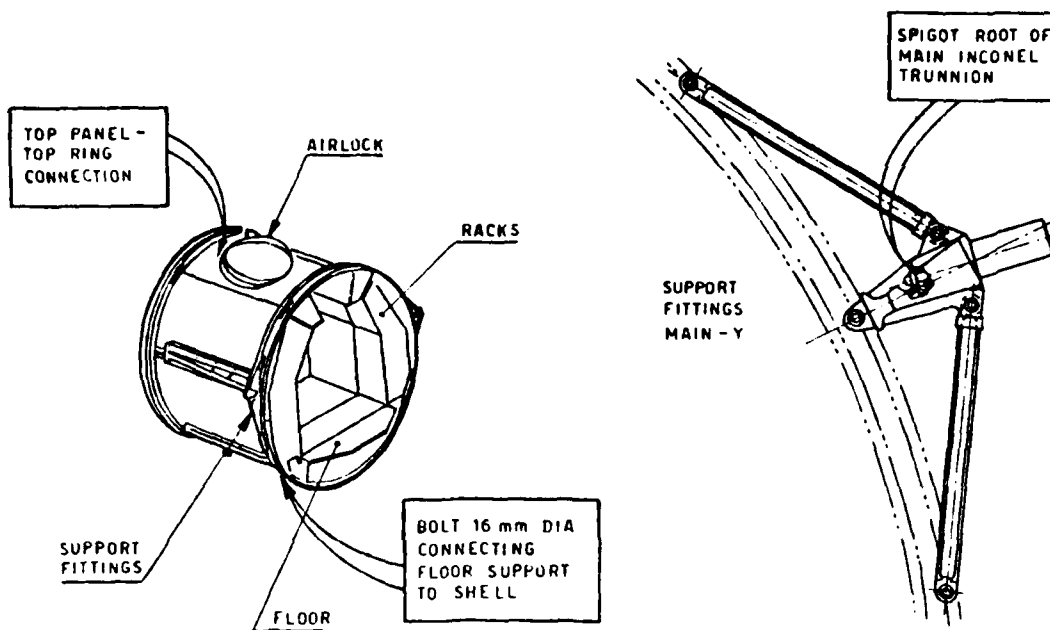


FIG. 18 - Spacelab areas where small component tests were performed



FIG. 19 - Cracked custom 455-H1000 pin and its cross section after failure



STRUCTURAL DESIGN AND TEST OF THE SHUTTLE RMS

by

D.M.Gossain and P.J.Smith
 SPAR Aerospace Ltd.,
 Space & Electronics Group
 1700 Ormont Drive
 Weston, Ontario M9L 2W7
 Canada

The 15.24 m (50 ft) long Mechanical Arm of the Remote Manipulator System (RMS) of the U.S. Space Shuttle Orbiter has been designed to meet stringent weight, stiffness and spatial envelope requirements. The arm is designed to deploy payloads up to 29,500 Kg (65,000 lbs) from the orbiter, has the ability to apply a minimum of 53 N (12 lbs) force at the tip and stop a 14,515 Kg (32,000 lb) payload moving at 0.061 m/sec (0.2 ft/sec) within 0.61 m (2 ft). Weight of the arm is limited to 363 Kg (800 lbs) and the maximum diameter of the arm is limited to 0.343 m (13.5 in).

This paper describes the design constraints on the arm structure and joints, evaluation of structural loads, selection of materials, and presents the design details of the structural elements and the joints. An extensive test program was undertaken to qualify and verify the design at component, joint, subsystem and system level. The paper discusses these tests with emphasis on dynamic and static structural tests of structural elements and joints.

Introduction

The Shuttle Remote Manipulator System (RMS) is a part of the payload handling system of the Space Transportation System (STS), and is designed primarily for the deployment and retrieval of payloads from the Space Shuttle Orbiter.

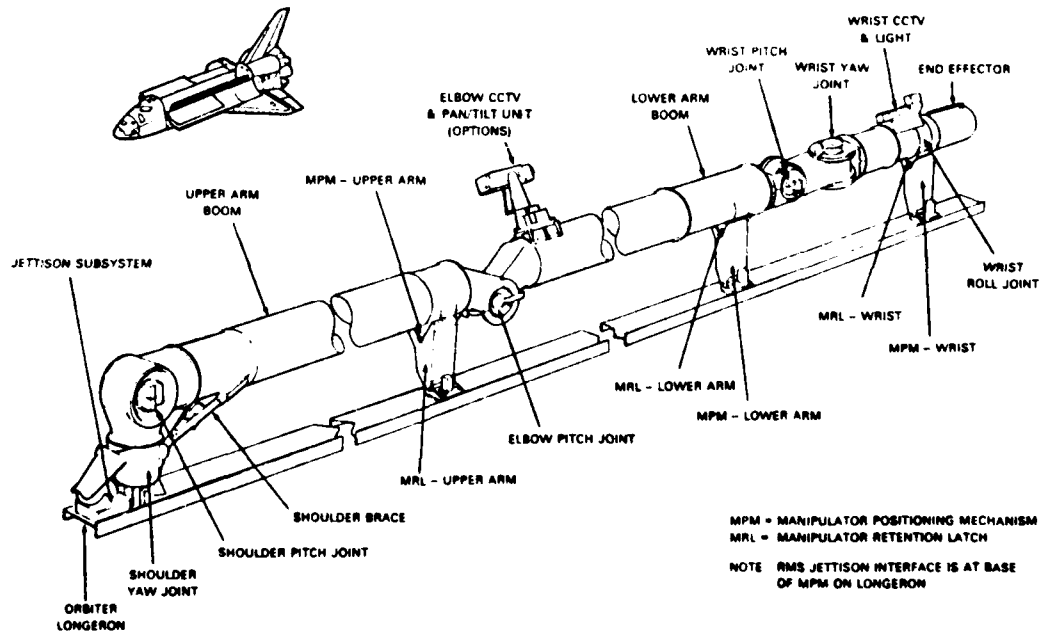


FIGURE 1 SHUTTLE RMS MECHANICAL ARM IN STOWED CONFIGURATION

The manipulator arm of the RMS (shown schematically in Figure 1) is a 15.24 m (50 ft.) long tubular structure consisting of six joints providing six rotational degrees of freedom. The joints correspond to the degrees-of-freedom (DOF's) of a human arm. The arm is attached at one end to the Manipulator Positioning Mechanism (MPM) of the Orbiter and the other end carries an end-effector which is designed to capture payloads. Three more supports are provided by Manipulator Retention Latches (MRL's) of the orbiter when the arm is stowed in the cargo bay. The joints near the MPM, called "shoulder joints", provide two DOF's and the joints near the end-effector, called "wrist joints", provide three DOF's. An "elbow joint" in the middle of the arm provides one DOF. The shoulder and elbow DOF's provide three dimensional translation of the end effector and the wrist joints provide three dimensional rotations of the end effector. The "joints" are electromechanical structures; the rotational DOF is provided by motor driven high ratio gearboxes. The joints are connected by 34.29 cm (13.5") diameter tubular members, called "booms".

Requirements and Constraints

The significant operational requirements for the manipulator arm, which resulted in structural/mechanical requirements, are:

- o Deploy/retrieve 14,515 Kg (32,000 lbs), 4.57 m (15 ft) diameter and 18.29 m (60 ft) long payloads.
- o Deploy and Berth 29,500 Kg (65,000 lbs) payload.
- o Stop a 14,515 Kg (32,000 lb) payload moving at 0.061 m/sec (0.2 ft/sec) within 0.61 m (2 ft).
- o Position tip of the arm within ± 5.08 cm (± 2 inches) and ± 1 degree.
- o Withstand orbiter VRCS loads while holding payload.
- o Apply a minimum force of 53N (12 lbf) at the tip.
- o Under manual control the rates of movements of the tip of the arm to be controlled within 9.14 mm/sec (0.03 ft/sec) and 0.09 deg/sec.
- o Operational life of 100 missions, as a design goal. Reference (1) gives details of the RMS system requirements.

The arm is stowed over the port (or starboard) longeron of the orbiter, on the MPM's. Spatial constraints of stowage allow a 0.381 m (15 inch) diametral envelope for the arm along its length. This is a dynamic envelope, i.e., no excursions beyond this envelope should occur under dynamic inputs to the arm structure. Total weight of the arm is limited to 363 Kg (800 lbs).

The operational requirements listed above resulted in a kinematic design using six joints, much like a human arm. The controllability of the arm, over the range of payload inertias, is greatly affected by the structural flexibility of the arm. In order to meet the operational controllability requirements, a design-goal stiffness of 17.5 N/cm (10 lbf/in) at the tip of the straight arm was established. The output torque and speed requirements established for the joints are shown in Table 1. The need for precise speed-control at the joints resulted in design requirements of high gear-ratios at the joints, as indicated in Table 1.

Table 1

Arm-Joint Requirements

Joint	Minimum	Minimum	Gear Ratio
	Output Torque N-m (ft-lbs)	Output Speed Rad/sec (deg/sec)	
Shoulder-Yaw	1047 (772)	0.04 (2.29)	1842:1
Shoulder-Pitch	1047 (772)	0.04 (2.29)	1843:1
Elbow-Pitch	716 (528)	0.056 (3.21)	1260:1
Wrist-Pitch	313 (231)	0.083 (4.76)	738:1
Wrist-Yaw	313 (231)	0.083 (4.76)	738:1
Wrist-Roll	313 (231)	0.083 (4.76)	738:1

One of the important requirements for the joints is their backdriveability. Backdriveability is defined as the ability of a joint to be driven from the output in opposition to the motor torque at the input. This feature is required to:

- (a) obtain dynamic braking of the arm,
- (b) limit the joint and structural loads to acceptable levels in situations such as removing a payload from, or inserting into, its retention fittings in the cargo bay,
- (c) allow the arm to assume the required geometry when grappling (and rigidizing the end-effector to) a fixed payload or a high inertia free-flying payload.

The operational life of 100 missions implies that the arm structure and components should be able to withstand the loads induced during launch, payload manoeuvring in orbit and landing, for 100 missions. The launch and landing environment (transient acceleration levels, random vibration, acoustic levels) seen by the stowed arm are specified by the orbiter/MPM designers. A typical payload handling scenario has been defined for arm operation in orbit.

Design Methodology

The first step in the structural/mechanical design process was to establish the "static" envelope into which the arm structure and joints had to be packaged. A dynamic analysis was performed on the preliminary arm and MPM designs (using finite-element models of the two structures) to estimate the displacements of the arm under dynamic inputs (transient accelerations and random vibrations) to the system at the longeron interface. Based on this analysis, a radial displacement of 1.9 cm (0.75 in) was allocated to arm dynamics and thermal hardware, resulting in a "static" diametral envelope of 0.343 m (13.5 in).

The stiffness and weight distribution along the length of the arm was then optimized with the constraints of maintaining commonality of parts (for example, in the gearboxes) and state-of-the-art manufacturing techniques, to minimize manufacturing costs. Stiffness constraint of 17.5 N/cm (10 lbf/in) at the tip of a straight arm was used. As a result, the wrist-region joint structures are within a smaller 0.241 m (9.5 in) diametral envelope and have lower stiffness than the shoulder and elbow joints. The stiffness and weight budgets established for the joints and arm booms are shown in Table 2.

Table 2
Stiffness and Weight Budget

<u>Item</u>	<u>Minimum Stiffness</u>	<u>Maximum Weight</u>	
		<u>Kg</u>	<u>(lbs)</u>
1. Shoulder Joint (Yaw & Pitch)	9.95×10^5 N-m/rad (7.34×10^5 ft-lb/rad)	117	(258)
2. Elbow Joint	10.24×10^5 N-m/rad (7.55×10^5 ft-lb/rad)	53	(117)
3. Wrist Joint (Pitch, Yaw, Roll)	2.37×10^5 N-m/rad (1.75×10^5 ft-lb/rad)	84.4	(186)
4. Upper Arm Boom (Shoulder to Elbow)	$EI = 4.0 \times 10^6$ N-m ² $(1.4 \times 10^9$ lb-in ²) $GJ = 2.0 \times 10^6$ N-m ² $(0.7 \times 10^9$ lb-in ²)	25	(55)
5. Lower Arm Boom (Elbow to Wrist)	$EI = 2.38 \times 10^6$ N-m ² $(0.83 \times 10^9$ lb-in ²) $GJ = 1.23 \times 10^6$ N-m ² $(0.43 \times 10^9$ lb-in ²)	24	(53)

The loads induced in the arm, which the structure and components are designed to withstand, are primarily developed under dynamic conditions during launch, ascent, reentry and landing and during payload handling in orbit. Since structural dynamics is a function of the design, an iterative approach for analysis and design is necessary till a suitable design is achieved. A finite-element model of the arm structure with models of high-gear-ratio joints, was used for prediction of loads in the stowed arm and the vibration environment for joints and subassemblies. The model is shown in Figure 2. A typical distribution of arm loads due to random vibration inputs is shown in Figure 3. Stress analysis, using detailed finite-element models where necessary, was then performed to verify positive strength margins in components. Assumptions made in the models (damping, gearbox characteristics at high frequencies, etc.) were separately evaluated by detailed sub-models and/or tests of subassemblies. The analysis details are discussed in References 2 and 3. Loads developed in payload handling were evaluated using digital computer simulations of the arm control system and the structure. In the preliminary phases of the project simulations using only the shoulder-joint were used;

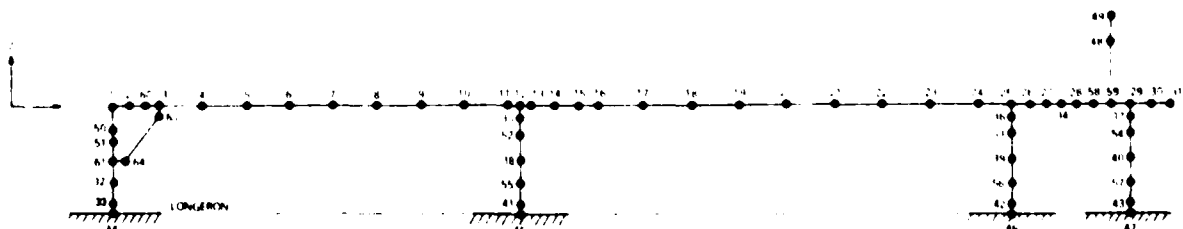


FIGURE 2 MATH MODEL STOWED ARM (RMS)
(CAMERA AT WRIST)

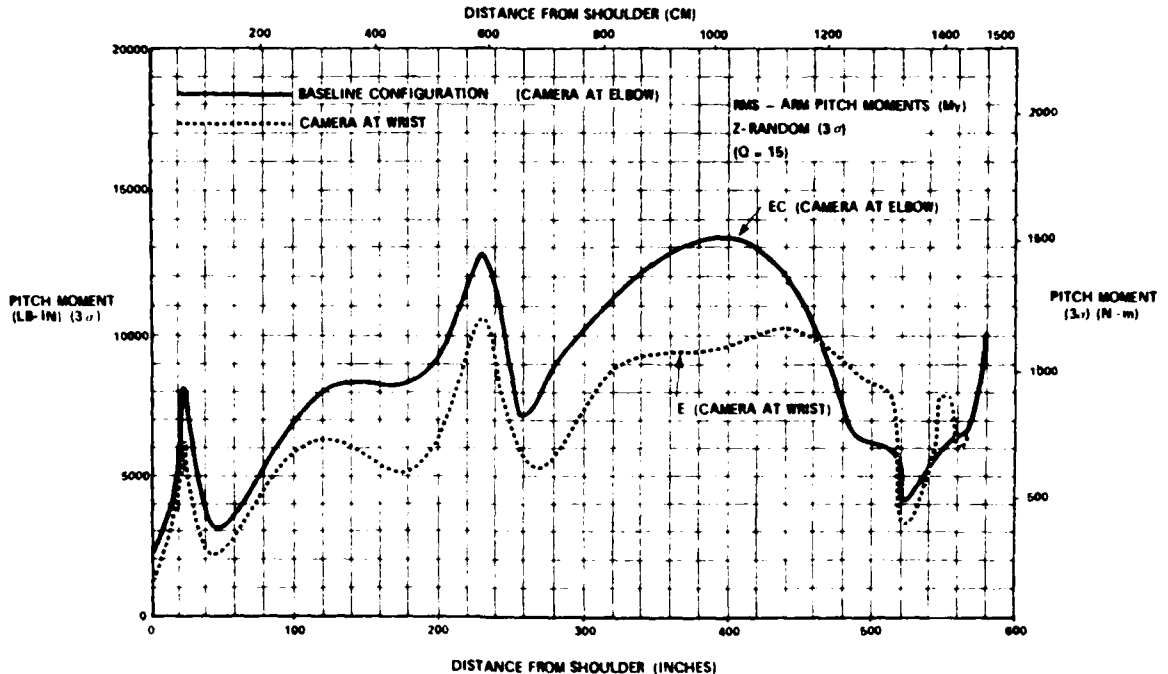


FIGURE 3 VARIATION OF PITCH BENDING MOMENT ALONG THE ARM FOR Z-DIRECTION RANDOM VIBRATION INPUT

preliminary phases of the project simulations using only the shoulder-joint were used; the loads were finally refined using a high-fidelity six-joint digital-computer simulation (called ASAD). These simulations incorporate the dynamic interaction of the arm structural flexibility and the control system, and are discussed in detail in References 4, 5 and 6.

Definition of loads was used to develop a load-spectrum for the arm and its components for a "design case" mission. The load-spectrum comprises the load levels (or vibration levels) for different parts of the arm and the number of cycles of their application (or the time duration of vibration levels) during different phases of the mission i.e., ground handling (transportation), lift-off, ascent, on-orbit operation, reentry and landing. The load spectrum was then used to perform a fracture-mechanics evaluation of the components. In this analysis, a pre-specified flaw in the component (based on the ability of inspection techniques to detect a flaw) was assumed and its growth analyzed with the application of the load spectrum. The component life was based on the number of "missions" applied till the flaw becomes unstable, leading to failure. A scatter factor of 4 has been used for life calculations; thus a numerical life of 400 "missions", as obtained by the fracture mechanics analysis, is considered to indicate an operational life of 100 missions for the component. The computer program FLAGRO developed by Rockwell International, has been used for the fracture-mechanics analysis. Some components such as gear-teeth, bolts and graphite-epoxy arm booms were designed by conventional fatigue-design criteria since reliable flaw-growth models for such items are not available.

Structural Design

Each joint of the arm has a motor-module, an encoder, a high-ratio gearbox and structural elements. The input and output sides of the drive motor-module are attached to structural elements which provide structural load paths and interfaces to other joints or components of the arm. The shoulder, elbow and wrist joints are shown in Figures 4, 5 and 6. Each motor module, shown in Figure 7, has a reversible brushless DC motor, primary and backup commutation scanner assemblies, a rotary inductosyn tachometer and a brake. The motor is powered by a servo power amplifier (SPA) which provides a pulse-width modulated current drive to the motor. The SPA and other electronics for the motor module are located in the electronics housing near the joint (reference Figures 4, 5 and 6). The encoder is an optical encoder with 16-bit resolution.

The gearbox comprises high-speed spur gear-trains and a low-speed bearingless-differential-planetary (epicyclic) drive. The differential planetary drive is at the output-end of the gearbox, and has a ratio of 40:1 for all joints. The gear-ratios for the spur gears are adjusted to get the required gear-ratios for different joints. The gear-train schematic for the shoulder is shown in Figure 8, as an example.

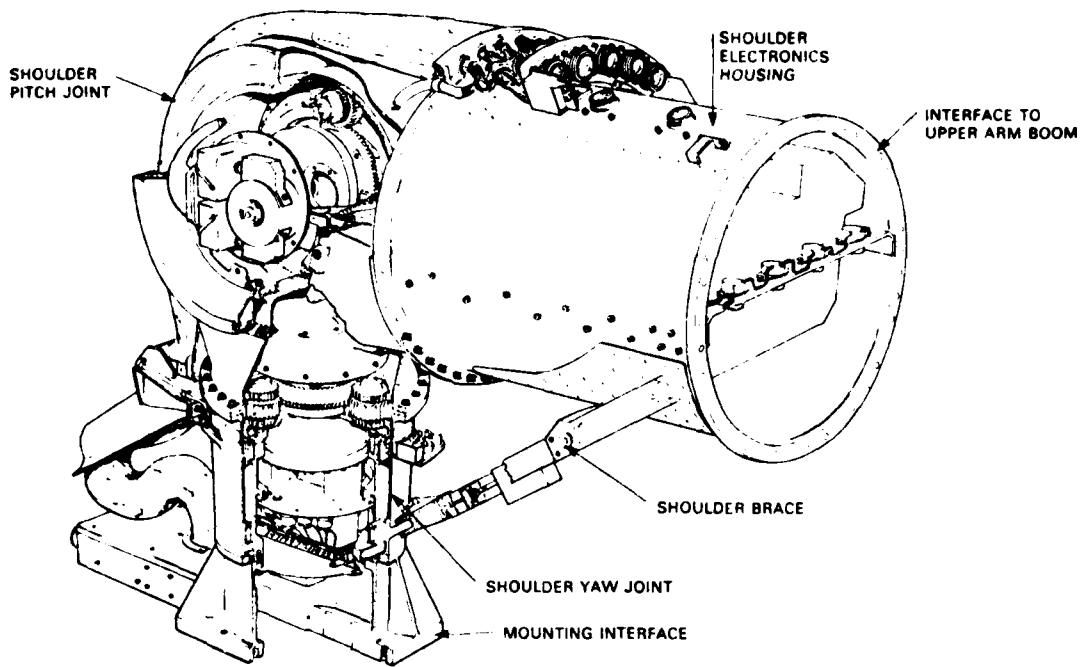


FIGURE 4 SHOULDER JOINT ASSEMBLY

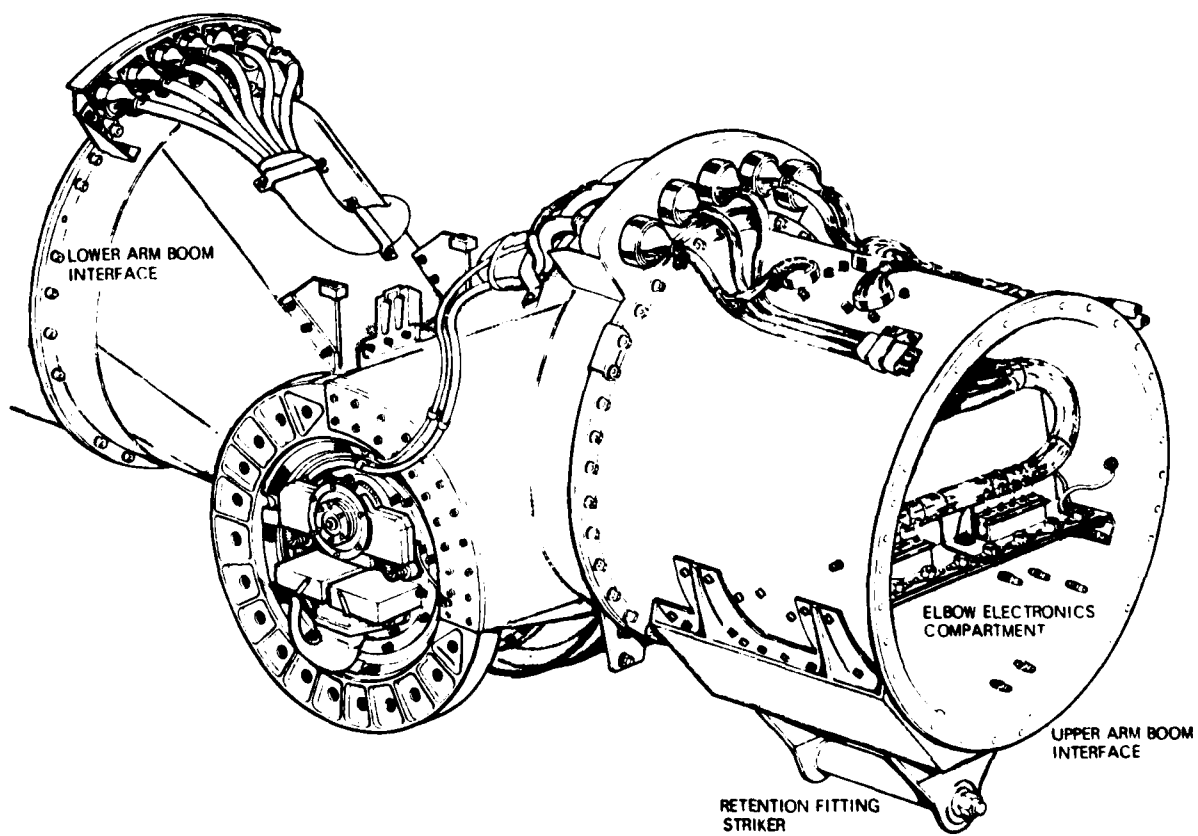


FIGURE 5 ELBOW JOINT ASSEMBLY

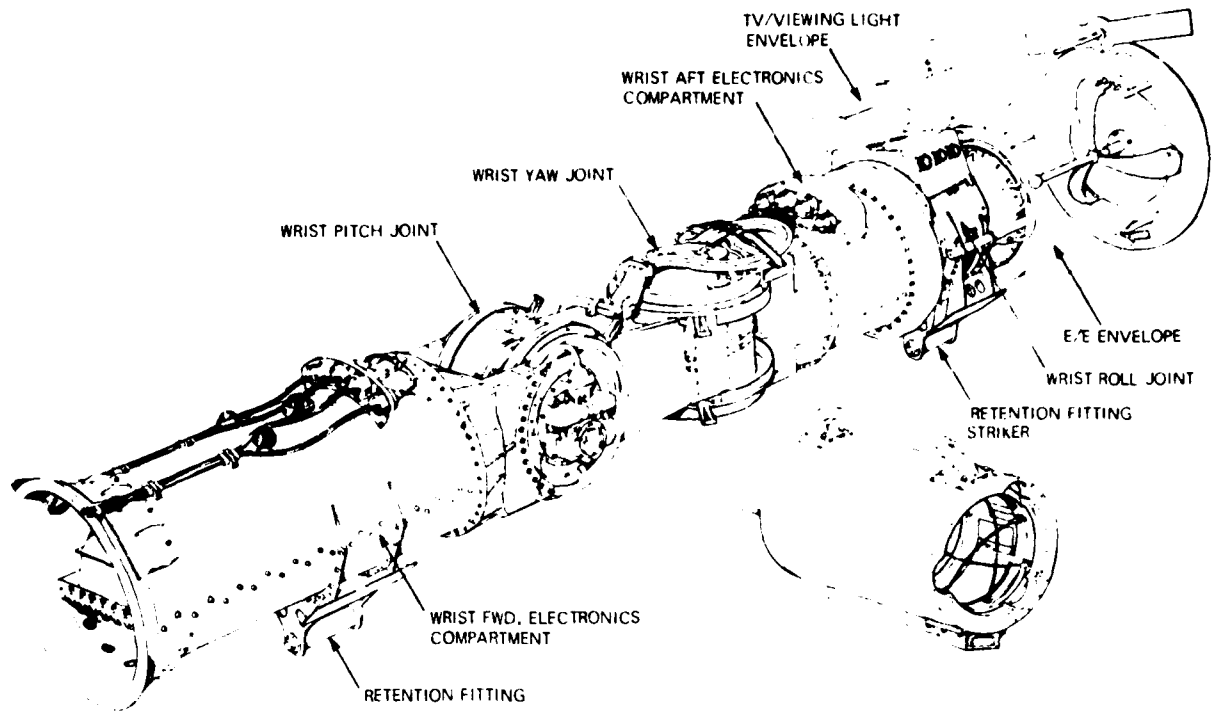


FIGURE 6 WRIST JOINT ASSEMBLY

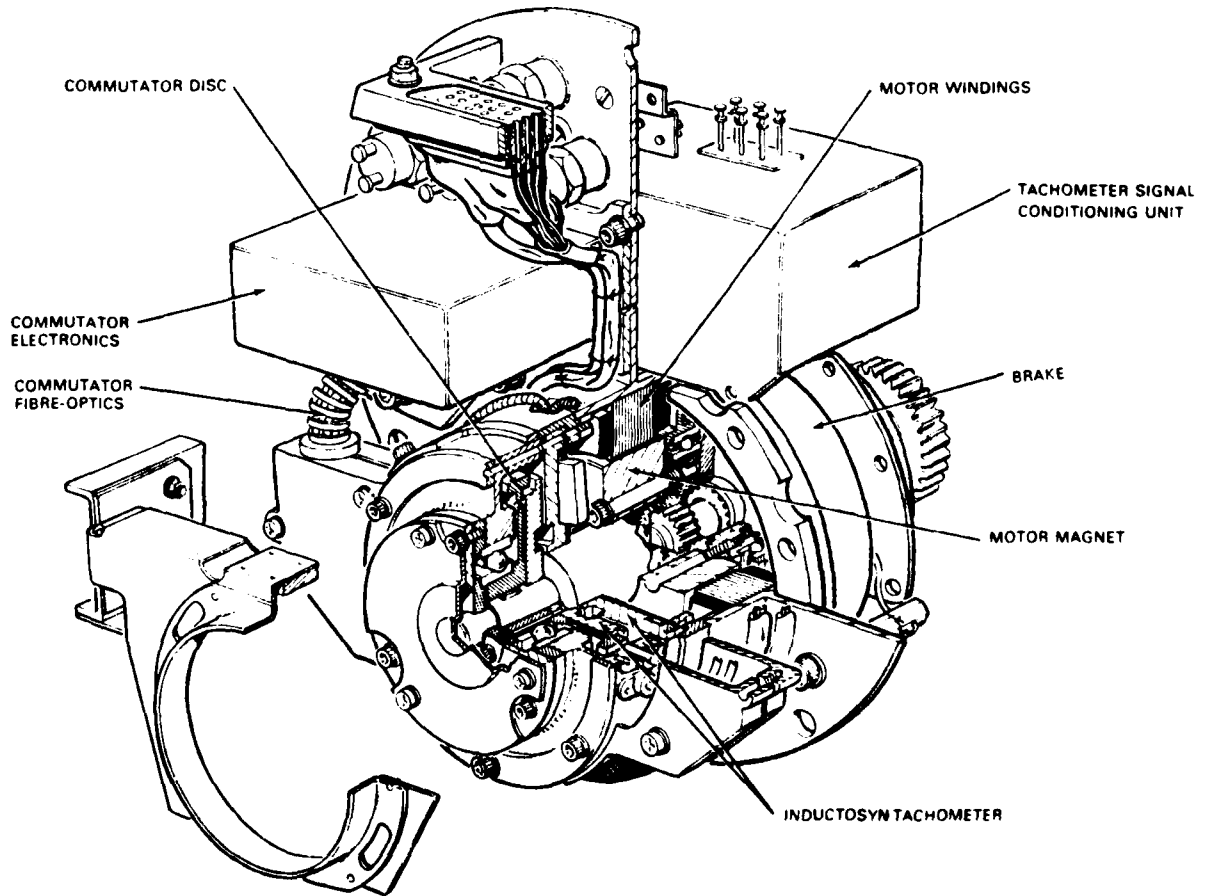


FIGURE 7 MOTOR MODULE

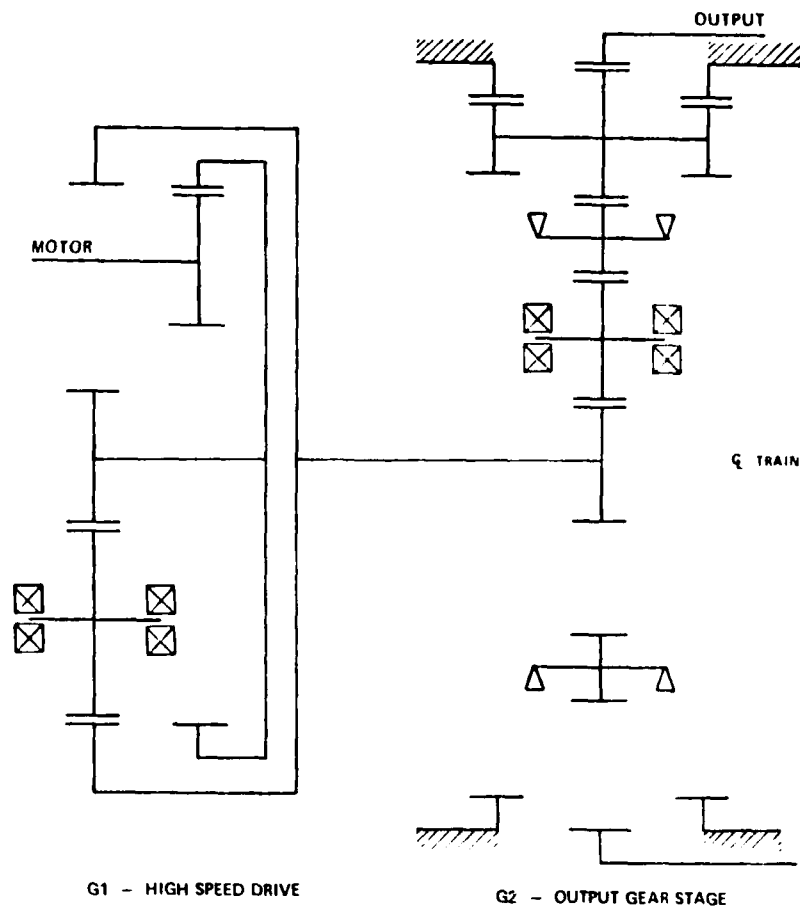


FIGURE 8 SHOULDER JOINT GEAR SCHEMATIC

Load transfer in the DOF direction across the joint is done through the gearbox. All other loading is carried across the joint via a roller bearing set and a duplex bearing pair. Roller bearings are used to accommodate thermal movements across the joint. The main bearing race and housing tolerances are selected such that under all thermal conditions the bearing is always under a pre-load. This eliminates slackness in the bearings. The loads are transferred from the joint to the electronics compartment/arm boom via transition pieces.

In the stowed condition the elbow and wrist joints are attached to the MRL through retention-fittings. The retention-fittings are attached to the electronics compartments, (except at the aft wrist) through a saddle structure. The saddle structure is riveted and bolted to the electronics compartment. The aft wrist retention-fitting is attached to the wrist-roll joint structure.

The joint structures and gearboxes are designed with conventional engineering materials such as stainless steels (17-4PH and Custom 455), aluminum alloys (A356, 7075-T7351, 7050-T6, 2219-T6) and titanium alloys (Ti-6Al-4V). Bolts are made from A286 steel and Inconel 718. The shoulder and elbow joint structural elements are designed primarily to meet the stiffness requirement, whereas the wrist-joint structure is designed primarily for strength. Structural elements are made from forgings, or castings where shapes are complex, and heat treated as appropriate. An important consideration in material selection has been good fracture properties especially at low temperatures (-40° to -50°C).

The structural design incorporates a brace at the shoulder between the shoulder-yaw joint and the electronics housing (Figure 4). The brace protects the shoulder pitch joint from the launch loads by providing an alternate load path. The brace is detached when the orbiter reaches the orbit. It is not re-attached before return to earth since re-entry and landing loads are relatively benign.

The arm booms, designed and manufactured by General Dynamics, San Diego, to requirements specified by Spar, are made of graphite/epoxy. Schematic details of a boom are shown in Figure 9. Ultra high modulus GY-70/934 graphite/epoxy by Fiberite was selected to meet the stiffness and strength requirements within the weight limits. The upper boom (shoulder to elbow) has 16 plies, 0.127 mm (0.005 in.) each, oriented at 0, +38 and -38 degrees. The lower boom (elbow to wrist) has 11 plies also oriented at 0, +38 and -38 degrees. To maintain stability of the thin-walled booms, intermediate stiffening rings

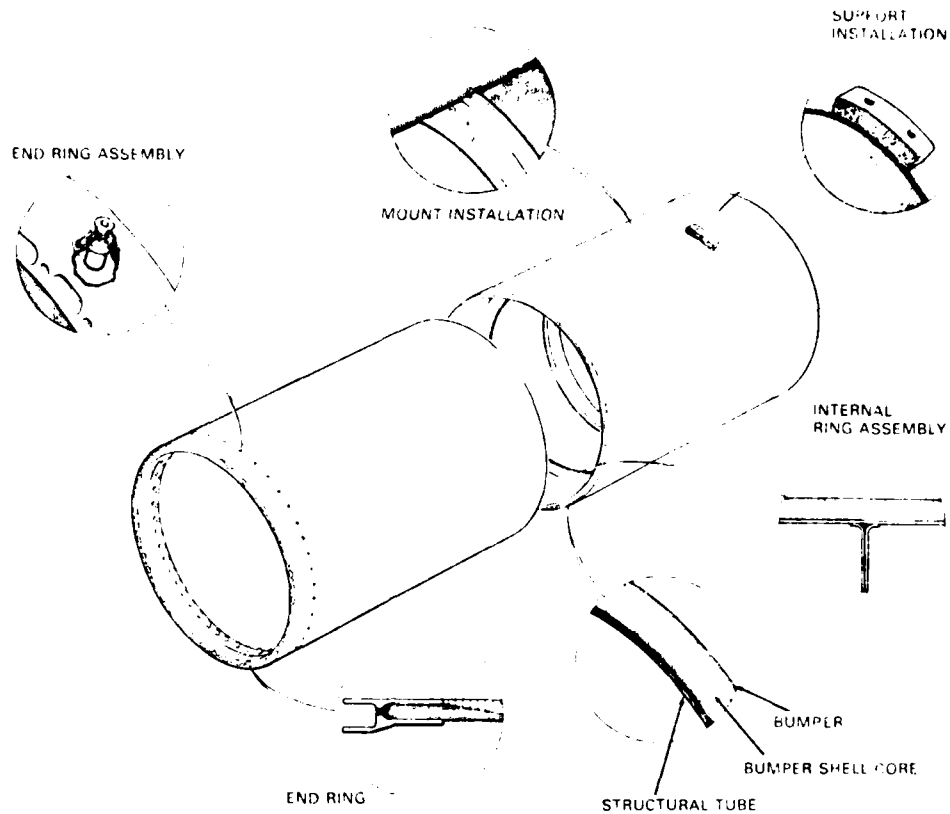


FIGURE 9 ARM BOOM

are placed internally at regular intervals along the length of each boom. The rings prevent Brazier-effect (which can flatten a tube under bending, leading to premature collapse of the tube wall and reduce bending stiffness) and increase the vibration frequency of the sidewall to well above the high energy acoustic range (ovalization frequencies above 180 Hz). Aluminum alloy (2124-T851) end rings are attached to the composite tubes through a specially designed bolted joint. High strength T300/934 graphite/epoxy is used to increase the tube wall thickness locally at the end rings for added strength.

The thin-walled booms are protected against accidental damage by a "bumper system". The bumper system comprises pre-crushed HR-10 Nomex honeycomb bonded to one-ply 102 Kevlar fabric skins, and the assembly bonded to the graphite/epoxy tubes. The bumper system absorbs energy of up to 6.8 N-m (5 ft-lb) without indenting the bumper material. An impact of higher energy leaves a visible indentation on the bumper as a signal of possible local delamination of the boom underneath. The design development and testing of the arm booms are discussed in detail in Reference 7.

Structural Tests

The analyses and simulations used to define loads and evaluate strength and stiffness characteristics of the structure were supplemented and verified by a series of development and qualification tests on flight-equivalent hardware. These principal structural tests included:

- (a) Stiffness and strength tests of joint structures in which joints were loaded statically to qualification-level loads (40% higher than design loads). Dummy booms were used to simulate the interface with arm booms and stress distribution in the structure was obtained from over 200 strain gauges. The stress distribution verified the finite-element analyses.
- (b) Stiffness and strength tests, as well as thermal cycling, fatigue and acoustic tests, on the arm booms. The bumper system was tested to verify its design performance by impacting it with a 1.8 Kg (4 lb), 5.08 cm (2 in) diameter steel ball dropped from 0.381 m (15 inches).
- (c) Load transfer characteristic tests of the gearboxes obtained by applying dynamic loads at varying frequencies (5Hz to 100 Hz) at the gearbox output and measuring response at the input (motor). These tests showed that the gearboxes were capable of transferring large loads (moments) at frequencies above 7 to 10 Hz.

- (d) Vibration and shock tests of the joints. Each joint was tested on a vibration table to the environment (random vibration and shock) obtained from the dynamic analysis of the total arm/MPM/MRL system. The effects of the rest of the arm structure were simulated by using hardware representing dynamic behavior of the system as reflected at the joint. The components in the joints (motor modules, encoders, electronics boxes) were also tested separately for vibration and shock.
- (e) System tests of the complete arm in the pitch-plane on an air-bearing test rig. The test rig supports the arm structure on low-friction air bearings through mechanisms (constant force/height linkages) which automatically compensate for changes in floor flatness (typically 3.157 mm (0.125) maximum variation over 0.9 m (3 ft)) and eliminates much of the loads on the joints due to gravity. Friction effects due to arm/test-rig manipulation across the floor can account for about 15% of the maximum joint output torque. An overview of the test rig is shown in Figure 10. Stiffness tests on the arm were performed on this test rig. The results showed that the arm stiffness is within the predicted range. Tests were conducted for arm operation, including payload grappling and handling, as well as berthing a payload in its retention fittings in the cargo bay. In certain geometric configurations, high forces can be generated at the arm/payload interface during berthing. The payload retention latching systems are designed to withstand these loads.
- (f) System flight tests on-orbit. Some of the system characteristics can only be checked in the zero-g environment orbit. The flight tests on STS-2, STS-3 and STS-4 missions were aimed at the final verification of the system performance and validating the math models used in simulations. These tests included operating the RMS in different modes as well as determining the effect of orbiter thruster firings on the arm dynamics with and without the RMS control system being active. Strain gauge measurements at the wrist and shoulder joints were used to determine arm loads on-orbit, as well as to derive data on structural damping. The strain-gauges measure moments about three orthogonal axes at wrist and shoulder joint locations and are mounted on the electronics compartments at the two joints. Arm tip oscillations were recorded on data acquisition cameras (DAC's) for photogrammetric analysis on ground to evaluate the frequencies and amplitudes of vibration of the arm.

The on-orbit tests have been very successful and have validated the math models used in simulations. They are discussed in greater detail in References 4 and 8.

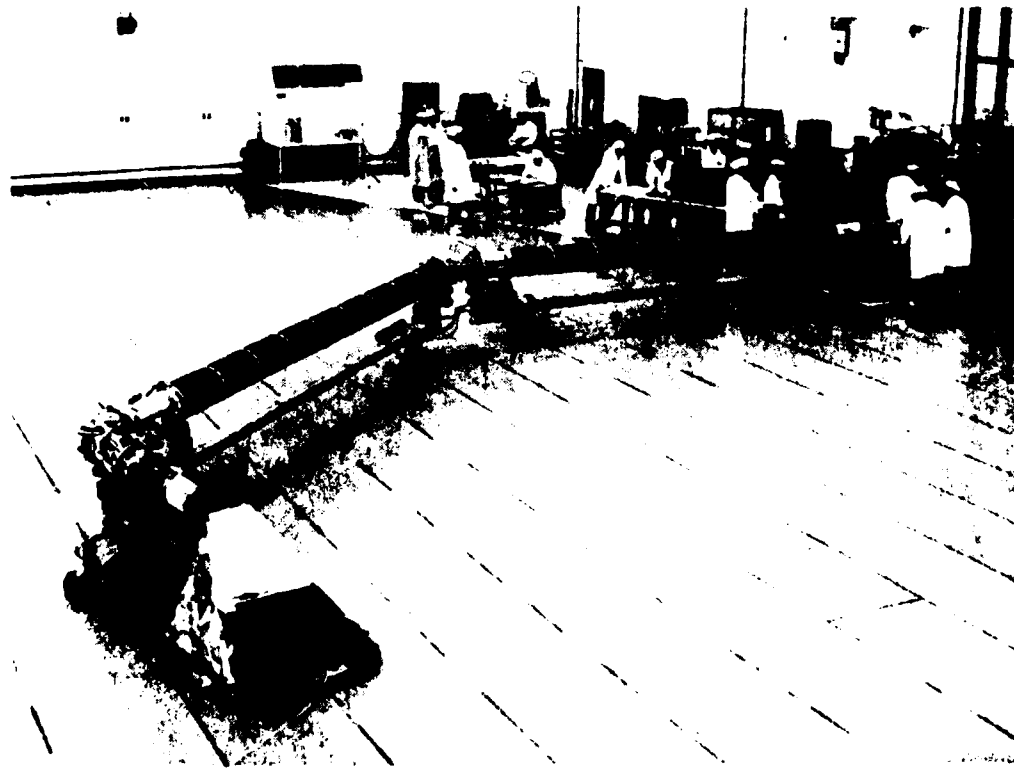


FIGURE 10 SYSTEM TEST — GENERAL VIEW

References

1. Kumar, P., Truss, P., Wagner-Bartak, C. "System Design Features of the Space Shuttle Remote Manipulator", Proceedings, Fifth World Congress on Machines and Mechanisms, July 1979, Montreal, Canada.
2. Gossain, D.M., Quittner, E., Sachdev, S.S., "Analysis and Design of the Shuttle Remote Manipulator System Mechanical Arm for Launch Dynamic Environment", Shock and Vibration Bulletin No.50, Naval Research Labs, Washington, D.C. September 1980.
3. Gossain, D.M. "Effect of a High Gear-Ratio Joint on Dynamics of an Articulated Structure", Canadian Aeronautics and Space Journal, Vol. 25, No.3, 1979.
4. Hunter, J.A., Ussher, T.H., Gossain, D. "Structural Dynamic and Design Considerations of the Shuttle Remote Manipulator System", 23rd AIAA/ASME/ASCE Structures, Structural Dynamics and Materials Conference, May 10-12, 1982, New Orleans, U.S.A.
5. Nguyen, P.K., Ravindran, R., Carr, R., Gossain, D., Doetsch, K.H., "Structural Flexibility of the Shuttle Remote Manipulator System Mechanical Arm", AIAA Guidance and Control Conference, 1982, San Diego, California, U.S.A.
6. Ravindran, R., Trudel, C.P.R., Nguyen, P.K. "Shuttle Remote Manipulator Control System", 18th IEEE Controls and Dynamics Conference, December 12, 1979, Fort Lauderdale, Florida, U.S.A.
7. Dunbar, D., Robertson, A., Kerrison, R. "Graphite/Epoxy Booms for the Space Shuttle Remote Manipulator", Aerospace Applications of Advanced Composite Materials, ICCM/2, April 16-20, 1978, Toronto, Canada.
8. Middleton, J., Ashworth, K., B. Aikenhead. "Flight Tests of the Shuttle Remote Manipulator System", to be presented at Second Canadian (CAS1) Astronautics Conference, Ottawa, Canada, November 30, 1982.

Acknowledgements

The Shuttle RMS has been designed and developed by Spar Aerospace under Contract (Number 15SR.31053-7-3839) to The National Research Council of Canada (NRCC) as a NASA/NRCC cooperative program. The authors would like to thank these organizations for permission to publish this paper.

SPACECRAFT THERMAL CONTROL SELECTION FOR
SEVEN YEARS LIFETIME IN SYNCHRONOUS ORBIT

L. Preuß

Messerschmitt-Bölkow-Blohm GmbH
D-8000 München 80

Improved nonconductive and conductive flexible SSMS with interference filters on top are presented. The SSM composition is analysed and defined. The optimization procedure for the SSMS is outlined. The qualification of the SSMS in laboratory scale for the synchronous orbit is demonstrated. The most essential characteristics of the improved SSMS are summarized. Handling-, application- and performance specifications for the SSMS have been established.

INTRODUCTION

For future application satellites lifetimes of more than 5 years will be required. One essential premise to meet this requirement is a reliable thermal layout of the satellites which amongst other points of view may rely on long-term stable thermal control coatings with a low α_s/ϵ_w ratio. Another important point of view is the spacecraft charging control to prevent electronic malfunctions. One essential contribution to solve this problem is to render the spacecraft surface coatings electrically conductive.

Up to now only the Optical Solar Reflector (OSR) based on metal backed fused silica substrate with or without an indium-two-oxide (ITO) overcoat is considered as the best solution in view of resistance against space induced degradation of thermal control and as far as applicable electrical characteristics. But it is known that this OSR is expensive in procurement and application.

An alternative solution with similar high resistance against degradation effects under space environment, but lower in cost and easier in handling and application, is an improved Second Surface Mirror (SSM) based on metal backed FEP-Teflon-foil with an interference filter (IF) on top. This improved SSM may be converted to an electrically conductive version by application of an intermediate layer and an ITO overcoat.

COMPOSITION

In principle the composition of the SSM respectively of the SSM/ITO is shown in the Figures 1 and 2. What mainly separates the SSM from the SSM/ITO is 1st the intermediate PMMA-layer between the FEP-Teflon-foil and the IF, introduced to reduce the sensitivity of the IF and consequently of the ITO-layer to crack-formation, which may cause serious increase in electrical resistance and 2nd the ITO-overcoat.

OPTIMIZATION OF CHARACTERISTICS

During an extensive analysis the most favorable material combinations for the SSMS have been identified.

Substrate

FEP-Teflon is known as the most suitable polymer foil for space application. Considering the color center formation and the charging-up to be volume effects and taking into account the request for a high value of the thermal emission coefficient (ϵ_w) the FEP-Teflon-foil type 500 A transparent, thickness 125 μm , was selected.













	ZnS	$\lambda/4$
	Al ₂ O ₃	$\lambda/4$
	ZnS	$\lambda/4$
	Al ₂ O ₃	$\lambda/4$
	ZnS	$\lambda/4$
	Al ₂ O ₃	$\lambda/4$
	ZnS	$\lambda/4$
	Al	20 - 30 Å
	Teflon	127 μm
	Al	20 - 30 Å
	Ag	1700 - 2000 Å
	Inconel	200 - 300 Å

Figure 1: Composition of SSM


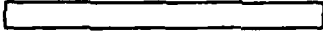





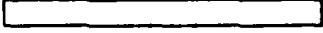

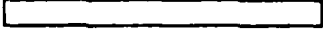


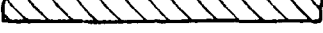

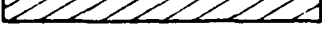
	ITO	90-100 Å
	ZnS	$\lambda/4$
	Al ₂ O ₃	$\lambda/4$
	ZnS	$\lambda/4$
	Al ₂ O ₃	$\lambda/4$
	ZnS	$\lambda/4$
	Al ₂ O ₃	$\lambda/4$
	ZnS	$\lambda/4$
	Al ₂ O ₃	50 - 70 Å
	PMMA	1-2 μm
	Al	20 - 30 Å
	Teflon	127 μm
	Al	20 - 30 Å
	Ag	1700 - 2000 Å
	Inconel	200 - 300 Å

Figure 2: Composition of SSM / ITO

Reflector

Silver (Ag) is known as a very high reflecting material. Below 350 nm Ag and the selected IF have similar absorption characteristics. Thus the influence of the IF on the reflectance of Ag is quite low. As reflector an Ag-layer 1700 to 2000 Å thick was used.

Protection Layer

The protection layer to prevent corrosion of the Ag-reflector should be an electrically conductive material to allow an electrical bonding of the SSMs to the spacecraft structure. As suitable material Inconel with layer thickness 200 - 300 Å was selected.

Interference Filter

As a result of an extensive test program, during which a lot of material combinations have been investigated, the combination zinc sulfide (ZnS) as high refractive material and aluminium oxide (Al_2O_3) as low refractive material turned out to be the best.

The IF shall have a high reflectance in the solar maximum in order to reduce the effect of colour centers, formed in the FEP-Teflon-foil, on the solar absorption coefficient (α_s). The higher the number of alternating ZnS/ Al_2O_3 layers, the higher the reflectance (see Table 1) but also the higher the danger of crack formation in the IF. As a compromise an IF with 4 ZnS and 3 Al_2O_3 layers was selected.

Table 1: Theoretical reflecting power of the IF dependent on the number of alternating ZnS/ Al_2O_3 layers

IF-Layers	Reflecting Power
3	59 %
5	76 %
7	87 %
9	93 %

The reflectance maximum has been adapted to 475 μm for the SSM and 460 μm for the SSM/ITO because the ITO overcoat causes a shift of the IF maximum to larger wavelengths. Measurements indicated a weak response of the α_s -value to the position of the reflectance maximum within $\pm 50 \mu m$ wavelength range (see Figure 3).

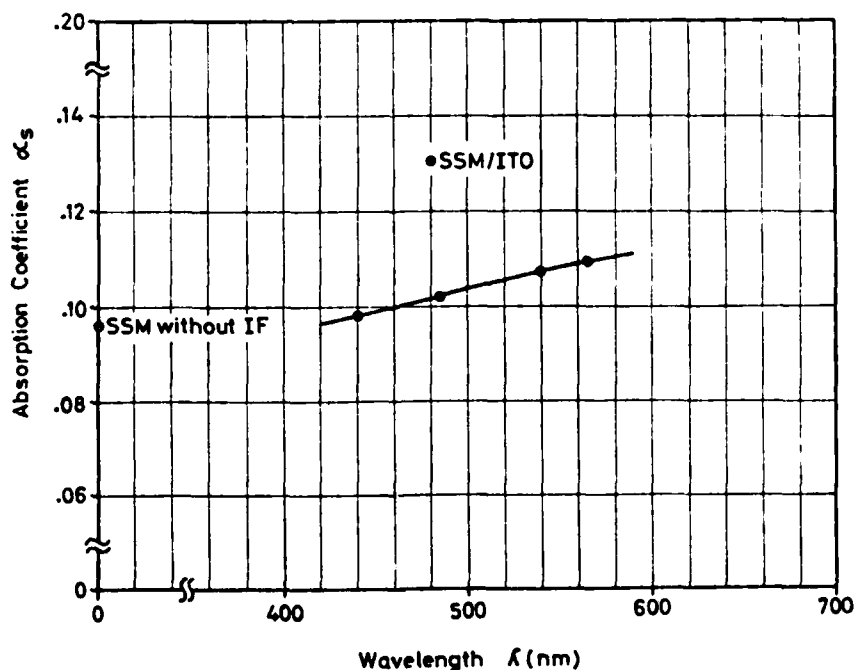


Figure 3: Variation of absorption coefficient of the SSM vs position of IF reflectance maximum

Intermediate Layer

The IF deposited on the FEP-Teflon foil formed cracks during handling and testing. The cracks do not have any influence on the α_g -value but would seriously increase the electrical resistance of the ITO layer. Intensive investigations indicated that an intermediate layer with a high Young's modulus between the FEP-Teflon-foil and the IF will reduce considerably crack formation. As PMMA is known to be relatively stable against UV- and particle radiation and in addition is soluble in common solvents this material has been selected as intermediate layer. Layer thickness is 1 - 2 μm .

Adhesive Layers

To attain sufficient adhesion of the Ag-, IF- and intermediate layers on the FEP-Teflon-foil a transparent Al-layer, 20 - 30 \AA thick, had to be deposited on the foil. The Al together with the fluorine of the foil form an intermediate layer with high adhesive strength.

Also between the IF and the PMMA-intermediate layer a 50 - 70 \AA thick A_2O_3 -layer is necessary to attain a strong adhesion.

Conductive Coating

A conductive overcoat on the SSM should influence the thermooptical characteristics α_g and ϵ_n unessentially and in addition should be transparent in the wavelength range 200 - 2500 nm. A favorable solution proved to be tin-oxide (SnO_2) doped indium-two-oxide (ITO) because this material meets the physical requirements and its vacuum deposition technology is fully developed. The ITO-thickness was selected to be 100 - 10/ + 50 \AA .

LAB QUALIFICATION

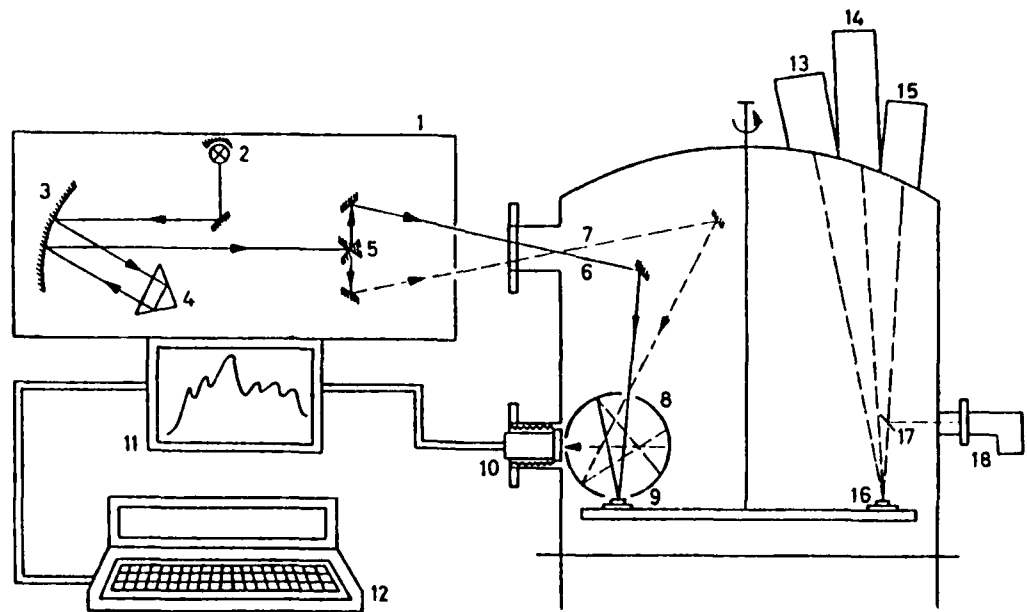
The SSM and SSM/ITO were qualified under simulated ground and space environment.

Test and Measurement

The following tests have been conducted:

- Tesa-tape-test
- Climatic test
 - o temperature cycle - 30/ + 50 $^{\circ}$ C
 - o rel. humidity max. 80 %
- Thermal vacuum test
 - o temperature cycle - 135/ + 55 $^{\circ}$ C
 - o pressure 10^{-7} mb-range
- Vibration test
 - o sinusoidal vibration
 - o random vibration
- Irradiation test
 - o 11000 ESH in the UV
 - o 10^{16} p^-/cm^2
 - o 10^{16} p^+/cm^2

The irradiation test was conducted in the MBB-combined effect chamber. The α_g -values and the electrical resistance were measured in-situ during the test. The measurement concept for α_g is shown in Figure 4.



- | | | |
|----------------------|--------------------------|---|
| 1 Spectrophotometer | 7 Reference Beam | 13 e ⁻ Gun |
| 2 Light Source | 8 Integration Sphere | 14 p ⁺ Generator |
| 3 Parabolic Mirror | 9 Sample | 15 UV Source |
| 4 Prisma | 10 Detector | 16 Sample Exposure Area |
| 5 Oscillating Mirror | 11 Recorder | 17 Deflection Mirror |
| 6 Sample Beam | 12 Programmed Calculator | 18 SCHOEFFEL-GM-100-3
Double Monochromator |

Figure 4: Measurement concept for α_s in-situ

RESULTS

The SSM and SSM/ITO passed the mechanical (tesa-tape, vibration) and thermal (climate, thermal vacuum) tests without any damage. No changes in α_s were detected. After some tests (tesa-tape, vibration) the electrical resistance of the SSM/ITO increased by one order of magnitude but remains far below a critical value (10^8 - $10^{10} \Omega$). The α_s -degradation behavior of the SSM and SSM/ITO is shown in Figure 5. For comparison the degradation behavior of common SSMs without IF-protection is plotted in the figure. The degradation behavior of the electrical resistance of the SSM/ITO is presented in Figure 6.

SPECIFICATIONS

For the SSM and SSM/ITO the most essential specifications have been established.

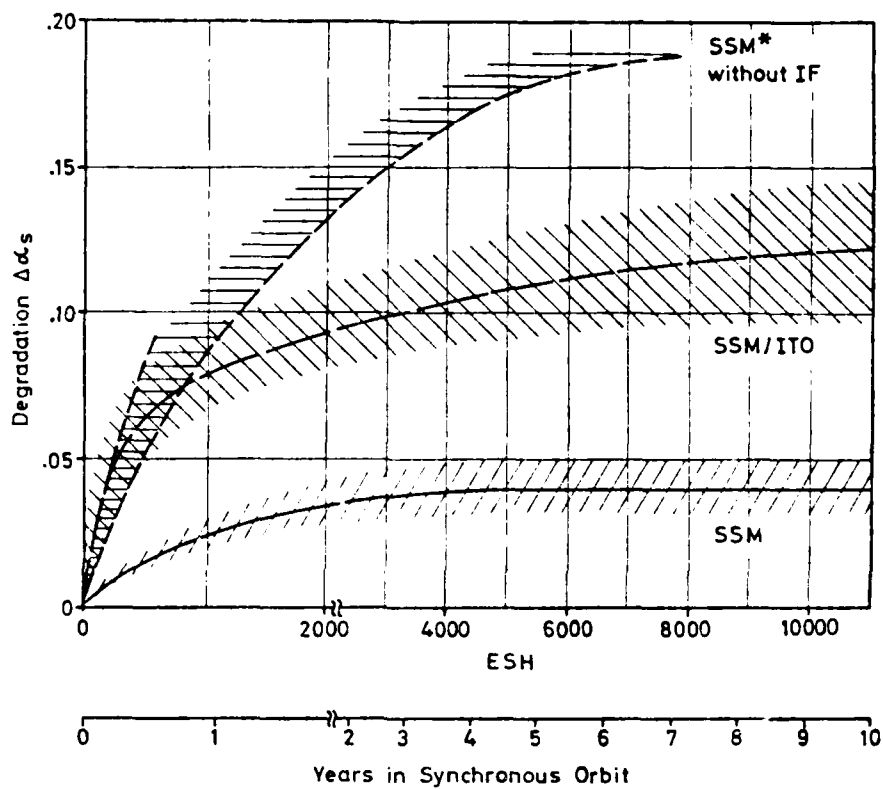
Application and Performance Specification

- Application on the ground
 - Temperature range - 30/ + 50° C
 - Maximum rel. humidity 90 %
 - No condensed water vapor deposition admissible
- Application during launch
 - No restriction for vibration modes and levels
- Application in space
 - Temperature range -120/ + 60° C
 - Thermo-optical characteristics

	SSM	SSM/ITO
α_s	.1 - .11	.13 - .14
ϵ_n	.73 - .74	.73 - .74

α_s - and R-behavior in synchronous orbit on the north or south panel of a 3-axis stabilized spacecraft after a mission lifetime of 10 years.

	SSM	SSM/ITO
$\Delta \alpha_s$	$\approx .04$	$\approx .12$
R	-	$10^3 \rightarrow 10^9 \Omega$



* Results of BOEING and DERTS

Figure 5: Degradation $\Delta \alpha_s$ vs lifetime in synchronous orbit for various SSM types

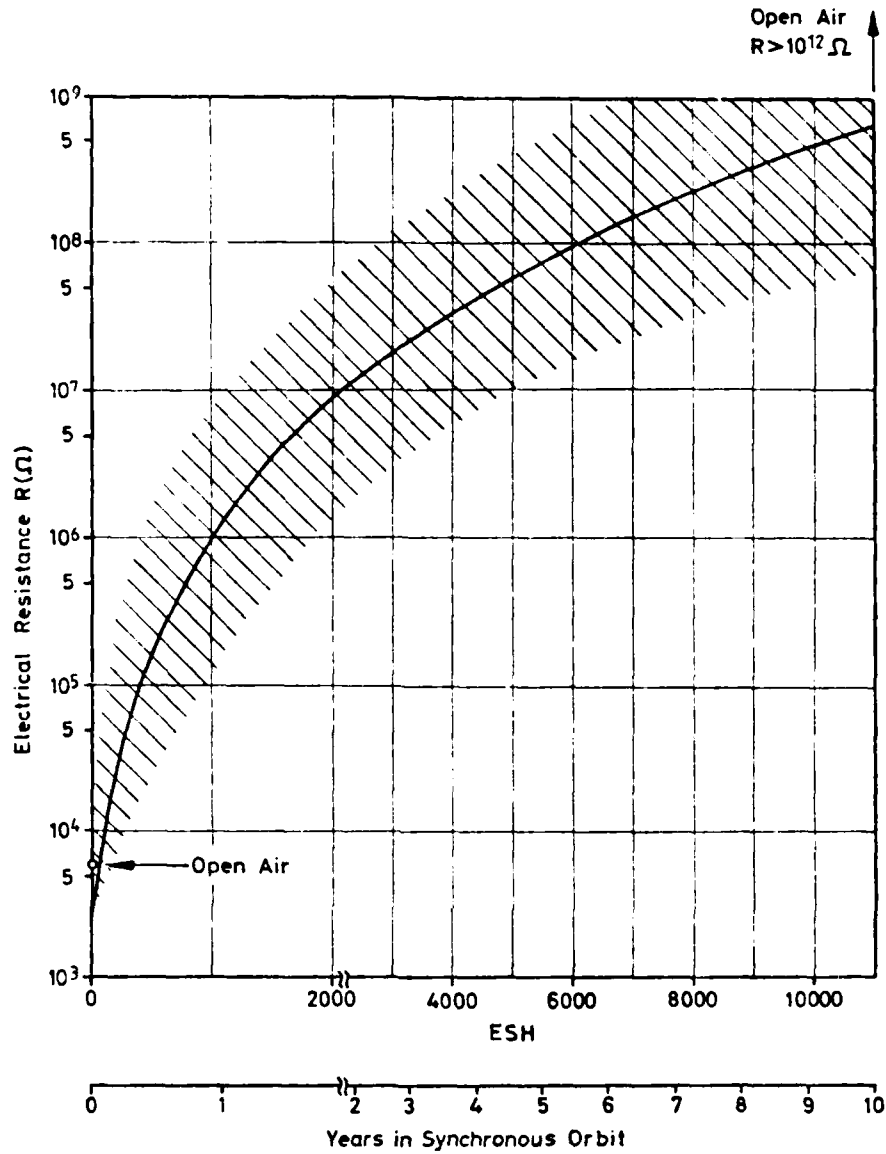


Figure 6: Electrical resistance vs lifetime in synchronous orbit for SSM/ITO

Degradation effects coming from contamination and electrostatic charging are not considered.

Handling Specification

- Remark:

The SSM and SSM/ITO shall not be buckled at all. At bending radii < 10 mm cracks may be formed in the IF and ITO. Therefore cutting and punching shall be performed on a plane and rigid support. If possible, the SSM and SSM/ITO shall be pasted on a support structure under vacuum conditions to avoid formation of bubbles and as a consequence of cracks in the IF and ITO.

- Cleaning

Apply cautiously a pad of cotton wool soaked with ethanol or MEK.

- Cutting

Cutting shall be performed preferably with hammer shears. Cutting with scalpel or sharp knife shall be conducted only on a plane and rigid support covered with a thin intermediate paper layer to protect the cutting devices. The cutting angle shall be as small as possible to avoid crack formation (see Figure 7).

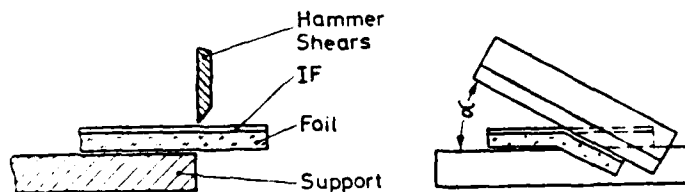


Figure 7: Cutting of SSM and SSM/ITO

- Punching

Punching shall be performed with an auger as shown in Figure 8.

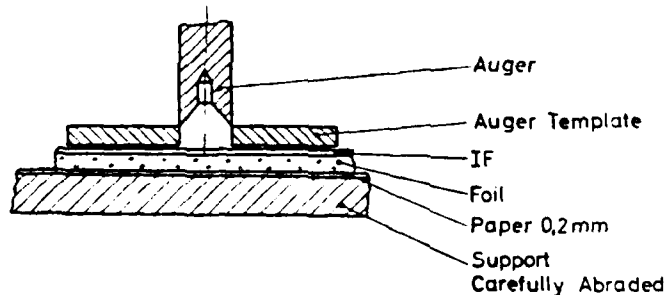


Figure 8: Punching of SSM and SSM/ITO

- Pasting

Pasting preferably under vacuum conditions. In case of pasting in the air apply a roller for close pressing. Diameter of roller and radii of roller edges > 20 mm.

- Size

Maximum size of SSM- and SSM/ITO-sheets at the moment is $250 \times 250 \text{ mm}^2$.

CONCLUSIONS

The deposition of an interference filter (IF) on a common FEP-Teflon SSM improves the stability against space radiation considerably due to two effects. Below 350 nm the IF absorbs UV-radiation very strongly before it penetrates the FEP-Teflon-foil, thus protecting the foil from color center formation.

On the other hand the IF reflects particularly in the solar maximum with the effect that solar radiation will not be absorbed by color centers already formed in the foil.

By application of an indium-two-oxide (ITO) cover-coat the SSM with IF may be rendered electrically conductive (SSM/ITO). To diminish danger of crack formation in the IF and consequently in the ITO, which may increase considerably the electrical resistance, an intermediate PMMA-layer has to be applied between the FEP-Teflon foil and the IF. The PMMA-layer as well as the ITO overcoat seem to have a negative influence on the stability against space radiation. Therefore the conductive SSM/ITO is less stable than the nonconductive SSM.

All the other characteristics of the improved SSMs are similar to those known from the common FEP-Teflon SSM.

The improved SSM and SSM/ITO are lab-qualified. Space qualification is being performed with a combined space and lab program.

ACKNOWLEDGEMENTS

The author gratefully acknowledges the comprehensive contributions of K. Kerner, BOSCH, J. Naegle, BALZERS, and O.K. Husmann to MBB in developing and qualifying these improved SSMs.

REALISATION ET ESSAIS D'UNE STRUCTURE TREILLIS

CARBONE-EPOXY POUR SATELLITES

J.F. PATIN et J.L. CECCONI

AEROSPATIALE
100 bd du Midi - BP 99
06322 CANNES LA BOCCA CEDEX
France

Une structure treillis à haute stabilité dimensionnelle a été étudiée et réalisée par l'Etablissement de CANNES de l'AEROSPATIALE. Le CENTRE NATIONAL D'ETUDES SPATIALES a participé au financement de ce programme.

Les barres du treillis à base de fibres très haut module GY 70 et haute résistance T 300 ont une rigidité spécifique élevée et un coefficient de dilatation voisin de zéro. Les éléments de liaison entre barres sont à base de fibres haut module M40. Les coefficients de dilatation de chaque élément ont été ajustés de façon à avoir un coefficient de dilatation équivalent entre les points de convergence des barres, voisin de zéro. La stabilité dimensionnelle des différentes liaisons en fonction de la température a été vérifiée.

Un cyclage thermique de type espace n'affecte pas le comportement mécanique de la structure.

L'essai statique du treillis a montré que la rigidité élevée de la structure est conforme aux hypothèses de dimensionnement. La tenue mécanique a été confirmée par des essais, suite à une première étape ayant nécessité un renforcement des liaisons.

1 - INTRODUCTION

L'AEROSPATIALE (Etablissement de CANNES) a étudié et réalisé une structure treillis carbone/époxy de type porte-source destinée aux satellites de télécommunication et de télévision directe.

Les caractéristiques essentielles de ce treillis sont une bonne stabilité dimensionnelle et une rigidité spécifique élevée.

Cette structure probatoire représentée en figure 1 a servi de modèle de faisabilité pour la tour porte-antenne des satellites de télévision directe en développement aujourd'hui. Le satellite géostationnaire TDF (vue artistique figure 2) assurera la transmission des programmes de télévision français à la fin des années 80. De même TV-SAT pour l'Allemagne Fédérale.

Le programme structure treillis probatoire a été cofinancé par le CNES (CENTRE NATIONAL D'ETUDES SPATIALES) et l'AEROSPATIALE.

2 - SPECIFICATIONS

Ces spécifications se rapportent au treillis défini figure 3.

- Rigidité

Fréquence du premier mode latéral supérieure à 20 Hz dans les conditions suivantes :

- . masse de 135 kg répartie sur chaque noeud (à l'exception des 4 noeuds de base), soit 8,5 kg par noeud
- . centre de gravité à 1,8 m au dessus de la base
- . inertie massique de 500 m² kg par rapport à la base.

- Résistance

- . accélération longitudinale : 6 g
- . accélérations latérales définies en figure 4.

PREVIOUS PAGE
IS BLANK



- Coefficients de dilatation

- . coefficient de dilatation entre points de convergence des barres Ø 32
 $-0,5 \cdot 10^{-6} \text{ C}^{-1} < \alpha < 0,5 \cdot 10^{-6} \text{ C}^{-1}$
- . coefficient de dilatation des montants Ø 50 entre points de convergence
 $-1 \cdot 10^{-6} \text{ C}^{-1} < \alpha < 1 \cdot 10^{-6} \text{ C}^{-1}$
- . stabilité dimensionnelle sous cyclages thermiques de type espace (entre 30 et -60°C)
 Dans le cas d'un gradient thermique de type équinoxe (-20°C/-50°C entre deux faces de la structure) translation maximale au niveau d'un noeud inférieure à 0,2 mm
- . dégazage TML < 1 % CVCM < 0,1 %.

3 - CONCEPTION DU TREILLIS PROBATOIRE

Il est représentatif des deux premières mailles du treillis représenté en figure 3.

Le treillis est constitué de quatre montants verticaux et de barres de liaison. Les montants verticaux et les barres de liaison sont réalisés à partir de tubes en composite carbone - résine époxy de diamètres extérieurs respectifs 50 et 32 mm.

Les noeuds de jonction entre barres sont entièrement réalisés en matériaux composites carbone/résine époxy.

Pour l'ensemble des pièces, la résine utilisée est la Vx 108, résine époxy polymérisant à 180°C et satisfaisant aux normes de dégazage pour usage spatial.

3.1 - Barres

Les barres sont constituées de nappes carbone unidirectionnelles. Le composite réalisé est un hybride très haut module (GY 70) haute résistance (T 300). Le drapage symétrique comprend huit couches de nappes très haut module à 0° comprises entre des nappes haute résistance à $\pm 20^\circ$.

3.2 - Noeuds

Le noeud présenté et utilisé résulte de la sélection d'une solution à la suite d'une analyse et d'essais comparatifs.

Pour chacune des solutions envisagées, l'étude a été faite sur un noeud dans le plan (c'est-à-dire deux barres de liaison et un montant vertical) ; puis, la possibilité d'extension de la conception à un noeud tridimensionnel (quatre barres de liaison et un montant vertical) a été évaluée.

Ont été successivement étudiées les trois solutions suivantes :

- Solution demi-coquilles non raidies (figure 5)
- Solution demi-coquilles raidies (figure 6), la solution précédente n'étant pas suffisamment rigide
- Solution avec plaque traversante.

Cette troisième solution a été celle retenue pour les raisons suivantes :

- rigidité plus élevée
- meilleur compromis entre caractéristiques mécaniques, masse et coûts. L'utilisation de matériaux, drapages et épaisseurs différents pour chacune des pièces élémentaires permet d'optimiser les caractéristiques mécaniques et le poids de la liaison
- possibilité de réaliser des angles différents sans modifier les outillages de fabrication.

Enfin, cette solution peut être étendue à un noeud tridimensionnel par l'utilisation d'un gousset en croix ce qui est plus simple que les modifications qu'entraînerait l'autre solution.

La solution finale retenue est représentée par les schémas des figures 7 et 8.

La jonction entre deux barres Ø 50 est assurée par un gousset en croix et quatre quarts de renforts.

La liaison barre Ø 32 - gousset en croix est réalisée par deux demi-coquilles.

Le collage est réalisé avec l'HYSOL EA 934 particulièrement adapté aux programmes spatiaux par ses bonnes caractéristiques mécaniques et ses valeurs de dégazage acceptables.

La photographie de la figure 9 représente un noeud dans l'espace assemblé.

Les matériaux utilisés sont respectivement pour les goussets en croix et les quarts de renforts un tissu carré haut module et pour les demi-coquilles un tissu unidirectionnel haut module.

4 - ESSAIS ELEMENTAIRES

Dans le but de vérifier les concepts retenus, des essais élémentaires ont été réalisés sur des sous-ensembles de la structure représentatifs de parties critiques.

4.1 - Essais mécaniques

4.1.1 - Essais de compression sur barres

Les modules et contraintes mesurés en compression sont les suivants :

- pour les barres \emptyset 32

195 000 MPa < E < 215 000 MPa

500 MPa < σ < 600 MPa

- pour les barres \emptyset 50

205 000 MPa < E < 240 000 MPa

475 MPa < σ < 675 MPa.

4.1.2 - Noeud dans le plan

L'objectif de cet essai est de déterminer les propriétés d'un noeud de liaison entre un montant vertical et deux barres transversales coplanaires. La rigidité du noeud permet de déterminer les fréquences de la structure treillis complète en utilisant un modèle dynamique aux éléments finis.

Ces fréquences sont les suivantes : 1er mode : 23,6 Hz
2ème mode : 29,5 Hz.

Elles sont supérieures à la spécification (20 Hz).

La charge de rupture garantit une marge de 40 % par rapport à la charge réelle.

charge réelle : 13 770 N

spécification : 16 000 N

valeur mesurée : 19 000 N.

L'éprouvette noeud dans le plan est représentée figure 10.

4.1.3 - Noeud tridimensionnel

Le but de cet essai est de déterminer l'influence du gousset en croix sur les caractéristiques mécaniques d'un noeud de dimension 3 comparées à celles des noeuds dans le plan.

Chacun des deux plans a été essayé successivement. Ces essais ont donné des déformations d'ensemble équivalentes à celles observées pour le noeud dans le plan. De même pour les charges de rupture.

4.2 - Essais de dilatation

4.2.1 - Barres

Mesuré entre -30°C et 90°C, le coefficient de dilatation est constant et égal à $-1,30 \cdot 10^{-6} \text{ } ^\circ\text{C}^{-1}$.

La dispersion des mesures est très faible en fonction du lot de préimprégné et du lot de fabrication des barres.

4.2.2 - Montant vertical Ø 50

L'éprouvette utilisée est représentée figure 11.

Mesuré entre -30°C et 90°C, le coefficient de dilatation est égal à $-1,05 \cdot 10^{-6} \text{ } ^\circ\text{C}^{-1}$.

La présence d'un noeud sur une barre Ø 50 rapproche de zéro le coefficient de dilatation global.

4.2.3 - Liaison barre gousset

L'éprouvette utilisée est représentée figure 12.

Le coefficient de dilatation mesuré entre -30°C et 90°C est de $0 \pm 10^{-7} \text{ } ^\circ\text{C}^{-1}$.

4.3 - Essais de cyclage thermique

L'influence d'un cyclage thermique représentatif de cas réels de fonctionnement sur le comportement mécanique de la structure a été étudiée au moyen d'une éprouvette de type "noeud dans le plan" définie au paragraphe 4.1.2.

Le cyclage réalisé était le suivant :

- nombre de cycles : 2 000
- températures minimales : $-75^\circ\text{C} \leq t \leq -66^\circ\text{C}$
- températures maximales : $38^\circ\text{C} \leq t \leq 42^\circ\text{C}$
- durée moyenne des cycles : $23 \text{ mn} \leq t \leq 30 \text{ mn}$.

Le cyclage thermique ne modifie ni la rigidité ni la charge de rupture de l'éprouvette. Son influence sur le comportement mécanique d'une structure carbone/époxy du type étudié est donc nulle.

4.4 - Conclusion des essais élémentaires

A partir des essais précédents, il est possible de déterminer les modules et coefficients de dilatation des barres du treillis entre points de convergence.

Ce recadrage des modèles mathématiques utilisés par le dimensionnement permet de déterminer avec précision les réponses du treillis sous sollicitations thermiques (stabilité dimensionnelle) et/ou mécaniques

	E équivalent (MPa)	α équivalent °C ⁻¹
Barre Ø 32 horizontale	128 000	-0,15
Barre Ø 32 diagonale	140 000	-0,38
Barre Ø 50	200 000	-1,04

Dans le cas d'un gradient thermique -20°C/-50°C entre deux faces de la structure (gradient type équinoxe), la translation maximale au niveau d'un noeud est de 0,15 mm.

Le modèle dynamique aux éléments finis de la structure treillis complète donne les résultats suivants :

- premier mode : F = 22,2 Hz (latéral)
- deuxième mode : F = 28 Hz (latéral)

(la spécification est de 20 Hz).

Les essais élémentaires confirment donc la conception et le dimensionnement de la structure.

5 - FABRICATION

La structure est assemblée en quatre étapes qui correspondent chacune à la fabrication d'une face sur un même outillage. La gamme d'assemblage était la suivante :

- fabrication d'une première face
- fabrication d'une seconde face
- positionnement vertical des deux faces précédentes et fabrication de la troisième face
- rotation de l'ensemble et réalisation de la dernière face.

L'adhésif EA 934 a été polymérisé à la température ambiante.

Après collage de la structure, un traitement de stabilisation a été réalisé, soit 25 cycles de -70 à +80°C sous 10⁻³ Torr.

La masse totale pesée de la structure sans ses embouts d'essais est de 7,15 kg.

6 - ESSAIS

6.1 - Essais statiques

Les charges appliquées sont telles que le torseur des efforts à la base du spécimen d'essai est identique à celui à la base de la tour treillis complète définie figure 3.

Une étude théorique ayant montré que les conditions d'appui interviennent peu sur la rigidité, la structure probatoire a été encastrée sur l'outillage d'essais.

La figure 13 montre la configuration de l'essai statique.

La structure probatoire présente un comportement élastique pendant l'essai statique. Les déplacements mesurés sont pratiquement identiques à ceux prévus d'après les essais élémentaires (noeud dans le plan et noeud tridimensionnel).

De plus, il a été vérifié que la structure ne s'est déformée en aucun de ses points de plus de 0,1 mm entre la sortie d'outillage et la relaxation des efforts après essai statique.

6.2 - Essais dynamiques

Il avait été prévu un balayage en fréquence de 5 à 2 000 Hz. Une rupture du spécimen d'essai a été observée en vibration latérale à 12 Hz à l'extrémité des quarts de renfort. L'expertise effectuée dans les zones de rupture a mis en évidence des problèmes de délaminage au fond des fentes usinées dans les barres Ø 50. Ce sont ces délaminages qui ont entraîné la rupture.

Les modifications suivantes ont été apportées au procédé de fabrication et à la conception du treillis :

- amélioration des procédés d'usinage des fentes. Il a été vérifié par micrographies que le nouveau procédé d'usinage utilisé n'entraîne plus de délaminages
- modification du concept (décalage du niveau des fonds de fentes et quarts de renforts prolongés au delà des fonds des fentes (figure 14).

Des essais dynamiques ont été réalisés sur des éprouvettes élémentaires représentatives des deux concepts, mais sans délaminages.

Au nouveau concept correspond une rupture dans la section courante du tube Ø 50 et non plus à l'extrémité des quarts de renfort.

Les charges de rupture dynamique observées sont les suivantes :

	Charge de rupture (10 ⁴ N) dans montants verticaux
- concept initial délaminages de fabrication (structure complète)	2
- concept initial pas de délaminages (éprouvette élémentaire)	5
- concept amélioré (éprouvette élémentaire)	5,5

Les résultats obtenus sur éprouvettes élémentaires sont satisfaisants, la contrainte maximale étant de 4 10⁴ N environ.

7 - CONCLUSIONS

Le concept de treillis développé est conforme aux spécifications et répond aux besoins de rigidité spécifique et de stabilité dimensionnelle des tours de satellites de télécommunication ou télévision directe.

Pour chaque application particulière, il sera possible de développer une structure dérivée de ce concept qui satisfasse exactement les spécifications propres au programme.

8 - REMERCIEMENTS

M. GERBER du CNES nous a apporté son concours et ses conseils tout au long de ce programme.



Figure 1 - Structure treillis probatoire

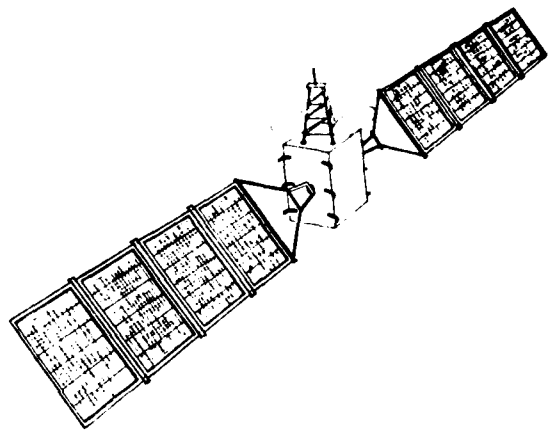


Figure 2 - T.D.F

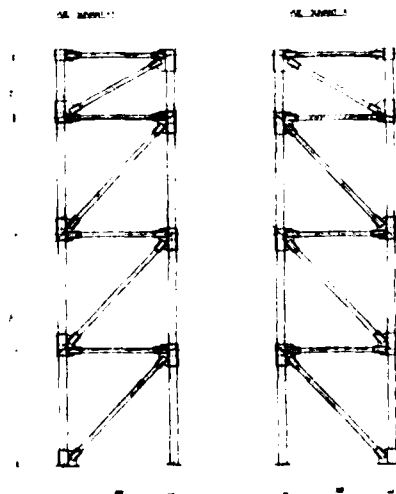


Figure 3 - Treillis de base
(la structure réalisée est représentative des 2 premières mailles de ce treillis)

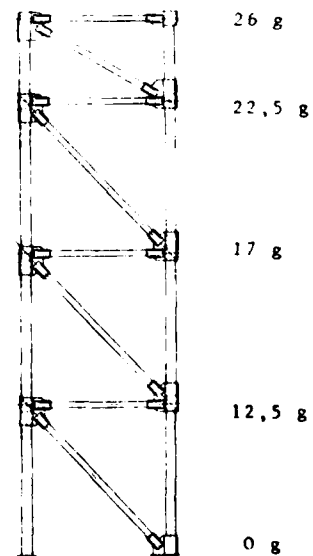


Figure 4 - Accélérations latérales

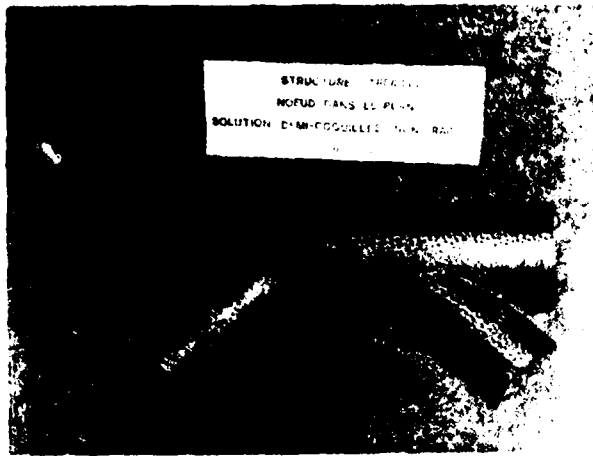
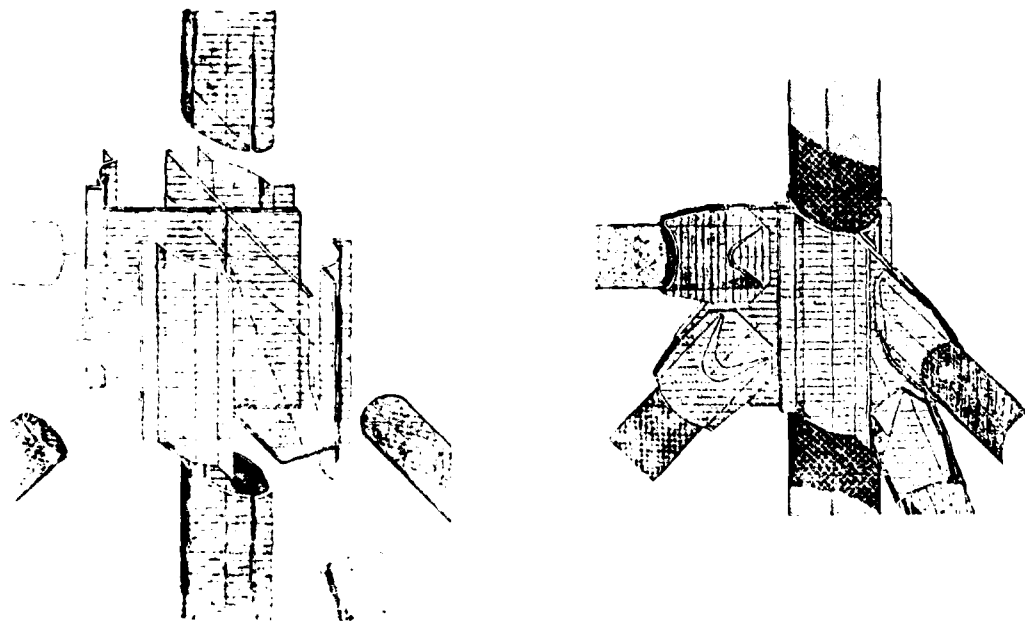


Figure 5 - Noeud dans le plan
Solution demi-coquilles non raidies



Figure 6 - Noeud dans le plan
Solution demi-coquilles raidies



Figures 7 et 8 - Noeud dans l'espace
Solution retenue



Figure 9 - Noeud dans l'espace

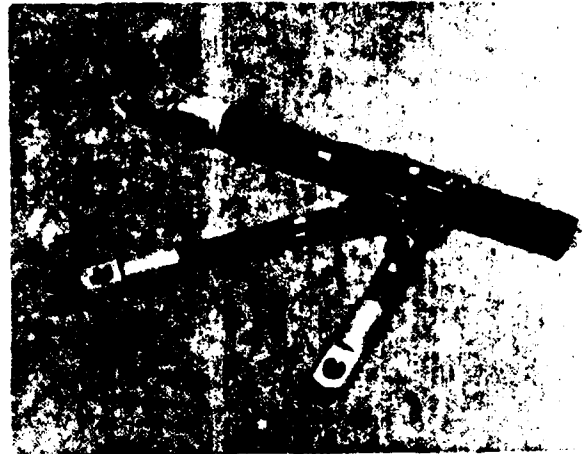


Figure 10 - Epreuve noeud dans le plan



Figure 11 - Epreuve de dilatation (montant vertical)



Figure 12 - Epreuve de dilatation (liaison barre gousset)

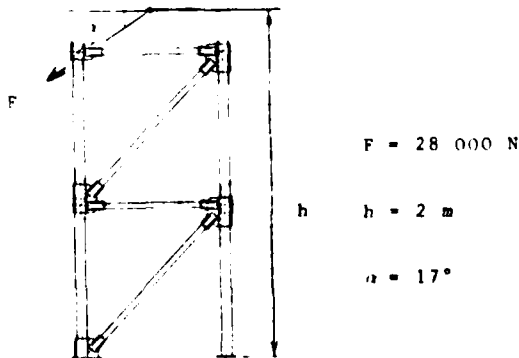


Figure 13 - Essai statique

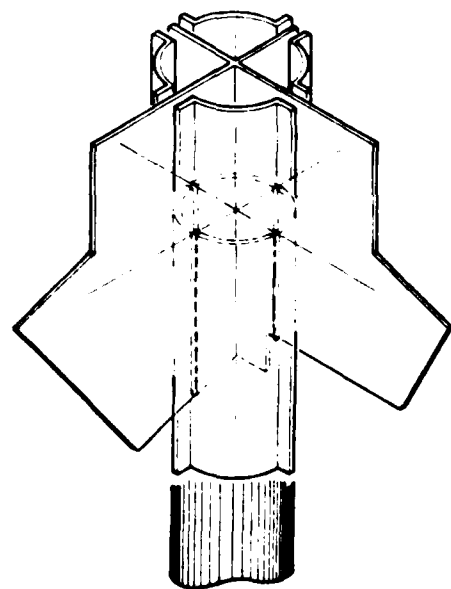


Figure 14 - Modification du concept initial

RECORDER'S REPORT

SESSION I - GENERAL REQUIREMENTS AND RELATED DESIGN PHILOSOPHIES

by

D.G. Zimcick
Communications Research Centre
P.O. Box 11490, Station H
Ottawa, Ontario K2H 8SZ
Canada

Paper 1: Fracture Mechanics and Fatigue Criteria in Material Selection for Space Applications.

Discussion centered on the fabrication technique of machining from a solid cylinder and the possibility and effect of welding. Results quoted for TIG welding with Al filler (AA2319) as a fabrication and repair procedure generated considerable debate with reports of conflicting experience.

Paper 2: Structural Design and Test of the Shuttle RMS.

Discussion concerned the particular choice of materials such as bearing lubricants (molybdenum disulfide dry lubrication) and the epoxy resin for the arm booms (chosen by General Dynamics, subcontractor). Details of environmental tests for thermal cycling and electromagnetic compatibility were reviewed.

Paper 3: Spacecraft Thermal Control Selection for Seven Years Life in Synchronous Orbit.

Questions were posed to identify the effects of environment not specifically stated in the paper including: condensed film contamination (not investigated), molecular oxygen as observed on STS (will be tested on Long Duration Exposure Facility (LDEF), low temperature below -135° (not yet tested), vibration spectrum (represented a rocket launch but information not available), machining technique in conjunction with thermal cycling (small cracks that might grow would affect electrical conductance but not solar absorptance), and electrical connection to prevent charge-up (tests have shown some problems - more work to be done).

Paper 4: Realisation et Essais d'une Structure Treillis.

The joint optimization goals between stiffness, elongation and weight were expanded in discussion. The joint between the spacecraft and feed structure was not considered in the design optimization but was specified in overall requirements.

GENERAL DISCUSSION

General discussion was initiated with a short description of the information on special requirements imposed on structures and materials used for high frequency communication antennas. These requirements formed part of a scheduled paper on requirements for large parabolic satellite antennas which was unavailable for presentation. Together with the material selection requirements of the presented papers, it was noted that the subject of materials selection for space applications had many common and unique constraints depending on the mission.

Of particular concern to participants was the recently observed effects of atomic oxygen on polymeric materials in low earth orbit (LEO). It was noted that recent flights of the NASA Space Transportation System (STS) had shown erosion of polymeric materials (e.g. Kapton, thermal coatings) predominantly in locations exposed to solar radiation on surfaces normal to the direction of flight of the shuttle. The exact mechanism is not entirely understood but the effect was not completely surprising since there is a body of knowledge on atomic oxygen at LEO. The effect appears to be a surface phenomenon with no noted change to the base material. Also the effect does not appear to cause enough damage for a short STS flight and no remedial action is planned although longer duration flights might encounter problems. In the interim, it was noted that NASA plans several experiments on upcoming STS flights to investigate the mechanism.

Further discussion addressed the issue of extended missions at various orbit attitudes and the problems associated with extrapolating data from accelerated tests to longer times with confidence without flight experience.

THE EFFECT OF SPACE ENVIRONMENT
ON THE THERMAL DISTORTION
OF POLYMER MATRIX COMPOSITES

R. C. Tennyson and G. E. Mabson
University of Toronto
Institute for Aerospace Studies
Toronto, Ontario, Canada

S. Ahmed
Communication Research Centre
Department of Communications
Ottawa, Ontario, Canada

SUMMARY

A study has been undertaken to evaluate the combined effects of vacuum, thermal cycling and U.V. radiation on the thermal distortion of selected polymer matrix composites. Data have been obtained for exposure periods exceeding 400 days in hard vacuum and over 180 equivalent sun days of U.V. radiation. During this time, insitu measurements of the thermal distortion and coefficients of thermal expansion (CTE) have been made using strain gauges and laser interferometry. Results have also been compared to an analytical model to demonstrate the usefulness of the data in predicting the thermal response of arbitrary laminates.

NOMENCLATURE

$\bar{A}_{ij}, \bar{B}_{ij}, \bar{D}_{ij}$	$\int_{-\frac{h}{2}}^{\frac{h}{2}} (\bar{Q}_{ij})_k (1, z, z^2) dz$, respectively
E_{11}, E_{22}	orthotropic moduli of elasticity measured in the 1 and 2 directions, respectively
G_{12}	shear modulus of elasticity measured in 1-2 plane
h	total laminate thickness
m, n	$\cos\theta, \sin\theta$, respectively
\bar{n}	total number of laminae in laminate
\bar{Q}_{11}	$Q_{11}m^4 + 2(Q_{12} + 2Q_{66})n^2m^2 + Q_{22}n^4$
\bar{Q}_{22}	$Q_{11}n^4 + 2(Q_{12} + 2Q_{66})n^2m^2 + Q_{22}m^4$
\bar{Q}_{12}	$(Q_{11} + Q_{22} - 4Q_{66})n^2m^2 + Q_{66}(m^4 + n^4)$
\bar{Q}_{66}	$(Q_{11} + Q_{22} - 2Q_{12} - 2Q_{66})n^2m^2 + Q_{66}(m^4 + n^4)$
\bar{Q}_{16}	$(Q_{11} + Q_{12} - 2Q_{66})nm^3 + (Q_{12} - Q_{22} + 2Q_{66})n^3m$
\bar{Q}_{26}	$(Q_{11} - Q_{12} - 2Q_{66})n^3m + (Q_{12} - Q_{22} + 2Q_{66})nm^3$
\bar{a}_{11}	$E_{11}/(1 - \nu_{12}\nu_{21})$
\bar{a}_{22}	$E_{22}/(1 - \nu_{12}\nu_{21})$
\bar{a}_{12}	$\nu_{21}E_{11}/(1 - \nu_{12}\nu_{21}) = \nu_{12}E_{22}/(1 - \nu_{12}\nu_{21})$
\bar{Q}_{66}	G_{12}
T	temperature
x, y	orthogonal in - plane structural axes
<u>Greek Symbols</u>	
α	coefficient of thermal expansion
γ, ϵ	shear and normal strain, respectively
κ	curvature
θ	fiber angle relative to X axis
ν	Poisson's ratio
σ, τ	normal and shear stress, respectively

PREVIOUS PAGE
IS BLANK

1. INTRODUCTION

The success of the U.S. Space Transportation System (Space Shuttle) and the published plans of the European Space Agency (ESA) to progressively augment the launch capability of its Ariane booster offer new opportunities for future space related activities. These events will particularly affect satellite missions requiring heavier and larger spacecraft in orbit.

Launch capabilities for payloads of 29,500 kgm to low earth orbit by the U.S. Space Shuttle or 4000 kgm to geostationary transfer orbit with ESA's expendable rocket (Ariane IV) are planned to be routinely available within the next five years. Beyond that time, the U.S. is actively planning to further augment the present shuttle geostationary orbit capability from the present 2250 kgm to 5000 kgm through the development of a Centaur stage based liquid propulsion booster [1]. These developments indicate that launch volume and mass distribution will be more important design considerations than overall mass, requiring efficient packaging through deployable and extendable concepts. Furthermore, higher reliability components, larger development and fabrication investment, and the possibility of refurbishment combine to yield an ever increasing mission life for future spacecraft.

The main effort in design is directed towards earth orbital platforms which fall into two generic categories, viz: geosynchronous (GEO) (of which most are more specifically geostationary) and low earth orbit (LEO). Space structures destined for interplanetary travel and exploration are often unique unto themselves due to individual mission profiles. However, certain requirements are common to structures in either of the former classifications. In particular, the flight profile for low earth orbit missions may be varied in both altitude, ranging from a minimum of approximately 100 km to highly elliptical orbits with apogees of many thousands of kilometers, and inclination angles including both equatorial and polar orbits. Furthermore, due to earth rotation, these space craft do not always traverse the same path through the earth's expanded atmosphere. Consequently, although it is difficult to define a specific generic mission environment, it can be generally stated that thermal excursions are more frequent due to short orbital periods and often these orbits do not traverse the trapped radiation belts surrounding earth with the exception of the South Atlantic Anomaly [2]. In addition most LEO platforms support earth resources payloads, an example of which is the Canadian proposed RADARSAT, thus imposing rigid requirements on stiffness and thermal stability of large instruments in order to achieve the positional and pointing accuracy necessary for high resolution. Of course, these requirements must be met with a minimum mass structure which can be deployed from a high packing efficiency launch configuration. Such systems necessitate joints, mechanisms, etc. with the accompanying interfaces generally of metal to composite, thus requiring thermal compatibility, localized strength, and creep resistance. Generally, for the large structures envisioned, strength is not a design driver provided the stowed structure can withstand launch [3].

Satellites in geosynchronous orbit experience fewer thermal excursion cycles due to the longer rotational period, but, these craft do traverse the trapped radiation belts surrounding earth [2]. In addition, the popularity of satellite communications, particularly over the Western Hemisphere, and the demand for high power transmission, impose payload positioning and pointing constraints to minimize interference due to beam spillover. For example, a joint Canadian-U.S. operational mobile communications satellite which has been proposed, utilizes a large (up to 100 m dia) reflector connected to the main bus containing the feed network by a rigid, dimensionally stable structural member (up to 100 m in length) to maintain accurate separation and position to produce the multiple spot beam ground pattern [4]. Again, this configuration will be deployed on station, necessitating interfaces and joints with the attendant thermal compatibility, localized strength and creep resistance for a design life of 10 years. The size, fabrication, and control of these very large structures impose severe requirements on the materials and structural design for high stiffness, light-weight members. Advanced composite materials seem ideally suited to meet this challenge because of their high specific stiffness and thermal dimensional stability. However, of primary concern at this time is the effect of space environment on the degradation of polymer based composites. Although numerous composite material components have been successfully flown on spacecraft, these have often been protected inside the relatively benign environment of the bus. In the future, larger more complex structures may involve numerous payload elements held away from a central bus structure with high structural dynamic stiffness requirements for spacecraft control and again often demanding positional accuracy. Of particular importance, these members will be exposed to the full effects of space environment protected only by super-insulation, or equivalent, if thermal control is required. Moreover, increased design life translates directly into increased number of thermal cycles, radiation doses, etc. which must be sustained without degradation of structural performance below specification requirements. Unfortunately, the long term effect of space environmental exposure on polymer matrix advanced composites are not completely defined. In this regard, an extensive study was undertaken with the following objectives in mind:

- (a) evaluate the effects of a simulated space environment on the thermal distortion and coefficients of thermal expansion of different polymer matrix composites;
- (b) develop analytical models for predicting the CTE and creep response for any laminate configuration.

2. EXPERIMENTAL PROGRAM

2.1 Objectives

To separate out the various environmental factors which might influence the thermal distortion characteristics, the following effects were investigated;

- (a) long term storage,
- (b) thermal cycling,
- (c) vacuum,

(d) U.V. radiation.

Several different material systems were used in this program, a summary of which is given in Table 1. Samples were fabricated in both tubular and flat plate forms. In addition, a hybrid laminate having a 'zero' CTE configuration often utilized as waveguides in Canadian communication satellites was also included. The following sections briefly describe the test facilities.

2.2 Thermal-Vacuum Facility

All thermal cycling tests of tubular samples in hard vacuum were conducted in the space simulator shown in Fig. 1. Combined action of roughing and oil diffusion pumps with a liquid nitrogen cryogenic trap above the diffusion pump permitted 10^{-6} torr to be achieved in about one hour. Automatic temperature control and LN_2 monitors allowed the facility to run continuously for periods up to two weeks. In addition, recording of strains and temperatures was also automated, thus enabling thermal-vacuum test data to be obtained over any selected time interval. Figure 2 shows the support apparatus used to thermally cycle the tubes while in a vacuum environment. The fixture consisted of nine vertical heating coils (nichrome wire), shielded from one another and mounted on an aluminum base plate. The coils were oriented vertically which allowed easy access to the specimens and posed no problem with respect to thermal gradients since convection is not present in a vacuum.

Each coil was capable of thermally loading a specimen 5cm to 18cm in length, and 5cm to 8cm in diameter. The coils were individually wired to an external power source and individually shielded; thus, the apparatus provided nine different thermal spectra, or cycled nine samples of varying absorptivity and emissivity through the same spectrum. The system was capable of heating specimens from room temperature to 350°F with thermal gradients less than 2°F on any specimen.

2.3 Thermal-Vacuum Radiation Facility

Another thermal-vacuum facility (Fig. 3) was developed containing a U.V. source. Using a 1000 watt Xenon H.C. arc lamp (Conrad-Hanovia, USA: 1000 hr lifetime) in conjunction with a variable current regulated power supply provided a capability of simulating a wavelength range of 200 nm - 400 nm. Measurements of the actual U.V. intensity were made with both short (220 nm - 280 nm) and long wave (300 nm - 400 nm) sensor cells ("Blak-Ray" Meters UVP Int. Inc., USA). This system was mounted vertically in an air-cooled quartz tube centered in the chamber, thus providing 360° of exposure. Thus, using a carousel arrangement (Fig. 4) a total of 30 flat samples (- 2.54 cm. in width) could be tested. Since it was desired to separate out radiation and thermal vacuum effects, it was important that control samples be used. Ideally, all samples would be exposed to the same temperature and vacuum histories, the only difference being exposure to the radiation. To attain this goal, a strip of sheet aluminum was attached to the framework on the carousel. This was positioned so as to shield the lower half of each sample from direct UV radiation. Since little if any UV radiation was reflected, the lower half of each sample acted as a control for the upper half of that same sample. The main drawback of this scheme was that temperatures on the upper and lower parts of each sample would not be exactly the same. This aspect was taken into account by mounting a thermogauge on each section. In addition, the strains in the exposed and shielded portions of each sample were monitored using two longitudinal strain gauges. To prevent possible degradation of the strain gauges due to UV radiation, all gauges were placed on the outside of the samples away from the UV source. Finally, it should be noted that before and after each irradiation period, the UV output of the bulb was recorded. These data were then used to obtain integrated irradiance values for both the short (250 nm) and long (350 nm) wavelength UV bands. It was found that the UV spectral irradiance was, on average, about 4.2 times that due to the sun at one astronomical unit (1 a.u.).

2.4 CTE Measurements

In-situ measurements of thermal strains were made using bonded surface strain gauges. However, for the tubular samples, laser interferometry was employed to calibrate the strain gauges. This was particularly important for the low CTE configurations. The test apparatus consisted of a helium-neon laser beam which produced interference fringes corresponding to 3164 Å axial end displacement. Thermal-vacuum cycling effects on the strain gauge behaviour were obtained from an aluminum sample which itself had been calibrated in the laser interferometer. Further details of the test procedure can be found in Ref. 5.

3. ANALYTICAL MODELS

Two analytical models were employed to predict the thermal response of the composite materials. The first model (see Appendix A) was based on laminate theory and was found suitable for calculating the CTE for various ply configurations using lamina material properties. However, to account for viscoelastic effects, a creep model was developed, details of which are also given in Appendix A. Such a model was deemed necessary to account for the long term dimensional drift often observed in low CTE configurations.

4. EXPERIMENTAL RESULTS

4.1 Effect of Storage on CTE

Circular tubes of hybrid construction containing HMS and T300 fibers in the form of $0^\circ_{T300} [+52^\circ/-52^\circ/-52^\circ/+52^\circ]_{HMS}$ with a 5208 Rigidite matrix were subjected to 6 months storage in ambient laboratory conditions and in a 'dry' desiccator environment. The purpose here was to determine the extent to which 'zero' CTE configurations could be expected to change. From Table 2 it is evident that for two cases (lowest CTE values), significant increases were found whereas the other two samples did not show any noticeable effect.

4.2 Effect of Thermal Cycling at Ambient Conditions

Using specimens taken from the same material batch as in Section 4.1, a series of thermal cycling tests over a moderate temperature range ($75^{\circ}\text{F} \leq T \leq 200^{\circ}\text{F}$) were conducted to examine the change in CTE. From Table 3, it can be seen that, on the average, a small increase in CTE was obtained.

4.3 Effect of Thermal Cycling in Vacuum

Thermal cycling tests were also run in hard vacuum ($10^{-6} \sim 10^{-7}$ torr) over varying periods of time for several material systems, including the hybrid laminate described previously. The additional materials included SM's graphite/epoxy (SP288T300), Kevlar[®]/epoxy (SP306) and Boron/epoxy (SP290).

For the hybrid structures, it is clear from Table 3 that significant increases in CTE were found due to the vacuum exposure, probably resulting from moisture outgassing.

Similar tests were then conducted on the graphite/epoxy system SP288T300 in the form of ± 0 laminates. Of particular interest were the ($\pm 22^{\circ}$) and ($\pm 43^{\circ}$) samples which corresponded to large negative and near 'zero' CTE configurations, respectively. In these experiments, duplicate specimens were taken from the same material batch and thermally cycled at the same time under ambient conditions. Figures 5 and 6 present the data and it is evident that the 'vacuum effect' again changes the CTE values.

Subsequent tests were then made on SP288T300, SP306 and SP290 materials for other ($\pm \theta$) laminates. These results indicate (Fig's 7,8,9) that in some cases, a drift in CTE occurs.

4.4 Thermal Cycling in Vacuum with U.V. Radiation

Extensive thermal/strain data were obtained for different U.V. exposure periods. A complete set of results can be found in Ref. 6. However, two summary plots are presented in Fig's 10 and 11 for graphite/epoxy and Kevlar[®]/epoxy, respectively. In general, when one compares the unshielded and shielded specimen results, there appears to be no significant U.V. effect for the exposure times investigated.

4.5 Viscoelastic Creep Parameters

To investigate long term dimensional changes it was necessary to obtain 0° and 90° creep compliance data in the thermal-vacuum environment. Such tests were performed in the radiation facility since the carousel could rotate samples into load grips. Each specimen was subjected to a given load for a prescribed length of time. Once the load was removed and the sample left unconstrained, the strain was recorded as a function of time. Using the analysis described in Appendix A, it was possible to obtain the creep compliance data from the strain/time curves. Further details on the experimental procedures and analysis can be found in Ref. 6.

It was observed that the 0° laminates did not exhibit any significant creep behaviour. Results for the 90° SP288-T300 material are presented in Fig. 12. Note that the change in compliance (ΔS) was set to zero at 2 seconds because of the comparatively large variations associated with the initial compliance values which tend to mask the time dependent variations. In examining the data in Fig. 12, it is evident that the rate of change of the creep compliance becomes smaller with greater exposure to the thermal vacuum environment in the simulation chamber. There is generally no consistent difference between the exposed and shielded sample results. By comparing compliance values recorded for the same stress level at the same time, it may be noted that a higher temperature results in a larger compliance value and a greater time dependence.

5. DESIGNING FOR THERMAL DISTORTION

5.1 Laminate CTE

To demonstrate that application of principal CTE data to design, it is possible to calculate the theoretical variation in CTE with fiber angle for symmetric laminates knowing α_1 and α_2 . Using Eq (A.11), the predicted variation in CTE with fiber angle for a ($\pm \theta$)_S laminate is shown in Fig 13, based on 220 days of exposure $\sim 10^{-6}$ torr and subject to 48 thermal cycles. Comparing test results with analysis shows excellent agreement.

5.2 Creep Response

To illustrate the application of viscoelastic analysis (see Appendix A) to composite design, including the effects of space environment exposure, consider a ($\pm 43^{\circ}$)_S graphite/epoxy laminate which represents a 'zero' CTE configuration at ambient pressure. If this laminate is then subjected to a step change in temperature (say from $+275^{\circ}\text{F}$ down to 75°F), the corresponding change in axial strain as a function of time is shown in Fig. 14. Although the ambient CTE for this laminate (neglecting creep effects) was not 'zero' but slightly negative, these results demonstrate that one cannot obtain a constant CTE for all time. For both the ambient and exposed materials, the CTE's are negative and become more so with time. It is also evident that the effects of the thermal-vacuum-radiation environment must be taken into account when initially designing a dimensionally 'stable' structure.

5.3 Sensitivity of CTE to Material Property Changes

Using the laminate analysis of Appendix A, it is possible to investigate the sensitivity of the CTE to changes in the orthotropic elastic constants and principal coefficients of thermal expansion (α_1 , α_2). Consider a symmetric balanced laminate of (0 , $\pm \theta$)_S construction fabricated from Narmco HMS/5208 material. Based on ambient test data (Table 1), variations in α_x and α_y were calculated for varying ply angle θ as a function of α_1 (Fig. 15), α_2 (Fig. 16), E_{22} (Fig. 17) and G_{12} (Fig. 18). It is clear that small changes in wrapping angle can produce deviations in the CTE comparable to the variations observed in the test data near the zero CTE configuration. Furthermore, these effects are compounded by differences in the material properties, although the effect of shear modulus is small.

6. CONCLUSIONS

- (a) Viscoelastic creep is regarded as the cause for any long term dimensional changes for low CTE configurations. The presence of high residual lamina stresses may well prevent one from obtaining a 'distortion free' structure for all time.
- (b) Due to polymer outgassing (initially comprised of mostly moisture), there is a significant change in CTE, depending on the laminate configuration.
- (c) There is no significant effect of U.V. radiation on the CTE for the materials investigated, up to 180 ESD @ 10^{-7} torr.
- (d) The successful design of a 'dimensionally stable' (ie; within a prescribed range of thermal distortion) composite structure for long term space applications should be based on a viscoelastic analysis using vacuum - corrected material properties. Other radiation induced effects must also be considered (possibly including atomic oxygen) once they are known.

ACKNOWLEDGEMENTS

The authors wish to gratefully acknowledge the financial support for this program received from the Communication Research Centre of Canada under Contract No. OSU81-00082 and from the United States Air Force Office of Scientific Research (AFOSR-78-3694-A).

REFERENCES

1. Rector, W. F., "Centaur Capabilities for Communications Satellite Launches", Proc. AIAA 9th Communications Satellite Conf., San Diego, March 1982.
2. Haffner, J. W., "Radiation and Shielding in Space", Academic Press, N.Y.
3. Hedgepeth, J. M., Mikulas, M. M. Jr., MacNeal, R. H., "Practical Design of Low-Cost Large Space Structures", Aeronautics and Astronautics, Vol. 16, No. 10, Oct. 1978.
4. "Large Space Systems Technology, 1981", NASA Conference Publication 2215, Nov. 16-19, 1981.
5. Tennyson, R. C., "Composite Materials in a Simulated Space Environment", Proc. 21st AIAA/ASME/ASCE/AHS Structures, Structural Dynamics and Materials Conf., May 1980, Seattle, Washington.
6. Smith, B. A. W., "Polymer Matrix Composite Materials in a Simulated Space Environment: UV and Vacuum Effects", M.A.Sc. Thesis, University of Toronto Institute Aerospace Studies, 1981.
7. Schapery, R. A., "Stress Analysis of Viscoelastic Composite Materials", J. Composite Materials, 1, 1967.

TABLE 1 SUMMARY OF AMBIENT MATERIAL PROPERTIES

Material	E_{11} (10^6 PSI)	E_{22} (10^6 PSI)	G_{12} (10^6 PSI)	ν_{12}	α_{11} (10^{-6} IN/IN/ $^{\circ}$ F)	α_{22} (10^{-6} IN/IN/ $^{\circ}$ F)
Narmco HMS/5208	24.97	1.17	0.624	0.21	-0.443	20.4
Narmco T300/5208	16.92	1.41	0.687	0.32	-0.266	24.0
3M SP288T300	20.5	1.40	0.590	0.26	- .20	21.0
3M SP306 (Kevlar [®] /Epoxy)	12.6	0.80	0.30	0.34	-1.7	39.5
3M SP290 (Boron/Epoxy)	30.0	3.5	1.8	0.20		

TABLE 2 EFFECT OF STORAGE ON CTE

Specimen	Initial CTE (10^{-6} IN/IN/°F)	Ambient Storage (6 mo) CTE (10^{-6} IN/IN/°F)	Desiccator Storage (6 mo) CTE (10^{-6} IN/IN/°F)
U1B0	2.1	2.0	-
U3A1	0.9	1.7	-
U1A0	2.5	-	2.4
U2A1	0.8	-	2.1

TABLE 3 EFFECT OF THERMAL CYCLING ON CTE

Specimen	Initial CTE (10^{-6} IN/IN/°F)	Ambient Thermal Cycling CTE (10^{-6} IN/IN/°F)	Vacuum Thermal Cycling CTE (10^{-6} IN/IN/°F)
U1C0	1.8	1.8	} 1060 Cycles
U2A2	0.9	1.4	
U3A2	0.7	1.1	
U5A1	0.9		(Cycles) 1.46 117
U2B1	0.9		2.19 77
U3B1	0.8		1.92 77
U3B2	0.8		2.33 77
U2B2	0.9		2.14 77

APPENDIX A

ANALYTICAL MODELS FOR PREDICTING
THERMAL STRAIN DISTORTION

A.1 Laminate CTE Model

In general, if one considers a temperature change ΔT acting on a thin laminate composed of an assembly of 'homogeneous' orthotropic laminae, the thermal stresses (referenced to some arbitrary set of structural axes X, Y) in the k-th lamina are given by

$$\begin{bmatrix} \sigma_x \\ \sigma_y \\ \tau_{xy} \end{bmatrix}_k = [Q]_k \left\{ \begin{bmatrix} \epsilon_{x_0} \\ \epsilon_{y_0} \\ \nu_{xy_0} \end{bmatrix}_T + z \begin{bmatrix} \kappa_x \\ \kappa_y \\ \kappa_{xy} \end{bmatrix}_T \right\} - [T]_k^{-1} [Q]_k \begin{bmatrix} \alpha_1 \\ \alpha_2 \\ 0 \end{bmatrix}_k \Delta T(z) \quad (A.1)$$

assuming linear elastic behaviour. For an arbitrary assembly of laminae, we can integrate this equation over \bar{n} laminae to obtain the following stress resultants acting on the laminate:

$$\begin{bmatrix} N \\ - \\ M \end{bmatrix} = \begin{bmatrix} A & B \\ B & D \end{bmatrix} \begin{bmatrix} \epsilon_0 \\ \nu \end{bmatrix} - \begin{bmatrix} F \\ - \\ G \end{bmatrix} \quad (\text{A.2})$$

where

$$[F] = \sum_{k=1}^{\bar{n}} [T]_k^{-1} [Q]_k \begin{bmatrix} \alpha_1 \\ \alpha_2 \\ 0 \end{bmatrix}_k \int_{h_{k-1}}^{h_k} \Delta T(z) dz$$

$$[G] = \sum_{k=1}^{\bar{n}} [T]_k^{-1} [Q]_k \begin{bmatrix} \alpha_1 \\ \alpha_2 \\ 0 \end{bmatrix}_k \int_{h_{k-1}}^{h_k} \Delta T(z) z dz$$

for constant thermal resistivity in the z direction:

$$[F] = \sum_{k=1}^{\bar{n}} [T]_k^{-1} [Q]_k \begin{bmatrix} \alpha_1 \\ \alpha_2 \\ 0 \end{bmatrix}_k \left[\left(\frac{T_u - T_L}{2h} \right) (h_k^2 - h_{k-1}^2) \right. \\ \left. + \left[\frac{T_L + T_u}{2} - T_{\text{ref}} \right] (h_k - h_{k-1}) \right] \quad (\text{A.3})$$

and

$$[G] = \sum_{k=1}^{\bar{n}} [T]_k^{-1} [Q]_k \begin{bmatrix} \alpha_1 \\ \alpha_2 \\ 0 \end{bmatrix}_k \left[\left(\frac{T_u - T_L}{3h} \right) (h_k^3 - h_{k-1}^3) \right. \\ \left. + \frac{1}{2} \left[\frac{T_L + T_u}{2} - T_{\text{ref}} \right] (h_k^2 - h_{k-1}^2) \right] \quad (\text{A.4})$$

where h = total laminate thickness,

T_{ref} = temperature where there is no strain or curvature in the laminate,

T_L = temperature of lower surface of laminate,

T_u = temperature of upper surface of laminate,

$\Delta T(z)$ = temperature at position z in laminate minus T_{ref} .

If one considers a stress free state (i.e., free expansion) and no temperature gradient through the laminate thickness, then

$$\begin{bmatrix} N \\ - \\ M \end{bmatrix} = \begin{bmatrix} 0 \\ - \\ 0 \end{bmatrix}$$

and Eq. (A.2) reduces to

$$[A_{ij}] \begin{bmatrix} \epsilon_{x_0} \\ \epsilon_{y_0} \\ \gamma_{xy_0} \end{bmatrix}_T + [B_{ij}] \begin{bmatrix} \kappa_x \\ \kappa_y \\ \kappa_{xy} \end{bmatrix}_T = \Delta T \sum_{k=1}^{\bar{n}} [T]_k^{-1} [Q]_k \begin{bmatrix} \alpha_1 \\ \alpha_2 \\ 0 \end{bmatrix}_k (h_k - h_{k-1}) \quad (\text{A.5})$$

$$[B_{ij}] \begin{bmatrix} \epsilon_{x_0} \\ \epsilon_{y_0} \\ \gamma_{xy_0} \end{bmatrix}_T + [D_{ij}] \begin{bmatrix} \kappa_x \\ \kappa_y \\ \kappa_{xy} \end{bmatrix}_T = \frac{\Delta T}{2} \sum_{k=1}^{\bar{n}} [T]_k^{-1} [Q]_k \begin{bmatrix} \alpha_1 \\ \alpha_2 \\ 0 \end{bmatrix}_k (h_k^2 - h_{k-1}^2) \quad (\text{A.6})$$

solving these equations for the mid-plane thermal strains and curvatures yields:

$$\begin{aligned}
 \{\epsilon\}_T &= \Delta T \left\{ [D_{ij}] - [B_{ij}] [A_{ij}]^{-1} [B_{ij}] \right\}^{-1} \\
 &\cdot \left\{ \frac{1}{2} \sum_{k=1}^{\bar{n}} [T]_k^{-1} [Q]_k \begin{bmatrix} \alpha_1 \\ \alpha_2 \\ 0 \end{bmatrix}_k (h_k^2 - h_{k-1}^2) - \right. \\
 &\left. [B_{ij}] [A_{ij}]^{-1} \sum_{k=1}^{\bar{n}} [T]_k^{-1} [Q]_k \begin{bmatrix} \alpha_1 \\ \alpha_2 \\ 0 \end{bmatrix}_k (h_k - h_{k-1}) \right\}
 \end{aligned} \tag{A.7}$$

and

$$\{\epsilon_o\}_T = \Delta T [A_{kj}]^{-1} \sum_{k=1}^{\bar{n}} [T]_k^{-1} [Q]_k \begin{bmatrix} \alpha_1 \\ \alpha_2 \\ 0 \end{bmatrix}_k (h_k - h_{k-1}) - [A_{ij}]^{-1} [B_{ij}] \{\epsilon\}_T \tag{A.8}$$

Note that for the special case of a symmetric laminate, $[B_{ij}] = 0$ and the above equations reduce to:

$$\{\epsilon\}_T = \frac{\Delta T}{2} [D_{ij}]^{-1} \sum_{k=1}^{\bar{n}} [T]_k^{-1} [Q]_k \begin{bmatrix} \alpha_1 \\ \alpha_2 \\ 0 \end{bmatrix}_k (h_k^2 - h_{k-1}^2) = 0 \tag{A.9}$$

$$\{\epsilon_o\}_T = \Delta T [A_{ij}]^{-1} \sum_{k=1}^{\bar{n}} [T]_k^{-1} [Q]_k \begin{bmatrix} \alpha_1 \\ \alpha_2 \\ 0 \end{bmatrix}_k (h_k - h_{k-1}) \tag{A.10}$$

Defining a matrix of coefficients of thermal expansion by

$$\begin{bmatrix} \alpha_x \\ \alpha_y \\ \alpha_{xy} \end{bmatrix} = \begin{bmatrix} \epsilon_{x_o} / \Delta T \\ \epsilon_{y_o} / \Delta T \\ \gamma_{xy_o} / \Delta T \end{bmatrix}$$

one obtains

$$\begin{bmatrix} \alpha_x \\ \alpha_y \\ \alpha_{xy} \end{bmatrix} = [A_{ij}]^{-1} \sum_{k=1}^{\bar{n}} [T]_k^{-1} [Q]_k \begin{bmatrix} \alpha_1 \\ \alpha_2 \\ 0 \end{bmatrix}_k (h_k - h_{k-1}) \tag{A.11}$$

for a symmetric laminate. Equation (11) then provides the necessary analytical means for calculating the structural CTE values for the GRE tubes, knowing the principal material coefficients.

A.2 Viscoelastic Creep Model

In general, polymer matrix composite materials must be regarded as viscoelastic in nature. Such materials exhibit a time dependent stress/strain response which may be linear or nonlinear. Moreover, because of the viscoelastic characteristics, creep relaxation (i.e., time dependent material deformation that can arise either under constant load or due to internal stresses for example) may play an important role in explaining the dimensional changes that can occur in a laminate even at constant temperature. Because of the mismatch in CTE's of the various plies used to construct a laminate, large internal (or residual) stresses can arise after cool-down to ambient conditions.

The constitutive relationships for an isothermal, linear viscoelastic material may be written in the following form:

$$\sigma_{ij} = \int_0^t C_{ijkl}(t-t') \frac{\partial \epsilon_{kl}}{\partial t'} dt' \tag{A.12}$$

A standard method of solving such equations is to apply a Laplace (or Fourier) transform and then to use elastic analysis to obtain the transformed solution. After transformation (A.12) becomes:

$$\hat{\sigma}_{ij} = s \hat{C}_{ijkl} \hat{\epsilon}_{kl} \tag{A.13}$$

where

$$\hat{f}(s) = \int_0^{\infty} f(t) e^{-st} dt \quad (\text{A.14})$$

If the temperature is not constant, (A.12) takes the following form:

$$\sigma_{ij} = \int_0^t C_{ijkl}(T, t-t') \frac{\partial \epsilon_{kl}}{\partial t'} dt' - \int_0^t \beta_{ij}(T, t-t') \frac{\partial \Delta T}{\partial t'} dt' \quad (\text{A.15})$$

where ΔT represents a temperature change relative to some reference value. For thermorheologically simple materials, (A.15) may be written as

$$\sigma_{ij} = \int_0^{\xi} C_{ijkl}(\xi - \xi') \frac{\partial \epsilon_{kl}}{\partial \xi'} d\xi' - \int_0^{\xi} \beta_{ij}(\xi - \xi') \frac{\partial \Delta T}{\partial \xi'} d\xi' \quad (\text{A.16})$$

where ξ is a transformed time variable used to take into account the effect of temperature (or moisture) on the time dependent material properties. It is defined as:

$$\xi = \int_0^t \frac{dt}{a_T(T)}; \quad \xi' = \int_0^{t'} \frac{dt'}{a_T(T)} \quad (\text{A.17})$$

where a_T is the temperature scaling factor. Note:

$$a_T(T) = 1 \quad \text{for } T = T_{\text{ref}} \quad (\text{A.18})$$

Perhaps the simplest class of thermorheologically 'complex' materials can be described by:

$$\frac{\sigma_{ij}}{a_g(T)} = \int_0^{\xi} C_{ijkl}(\xi - \xi') \frac{\partial \epsilon_{kl}}{\partial \xi'} d\xi' - \int_0^{\xi} \beta_{ij}(\xi - \xi') \frac{\partial \Delta T}{\partial \xi'} d\xi' \quad (\text{A.19})$$

where $a_g(T)$ is a "vertical" scaling factor, equal to 1 when $T = T_{\text{ref}}$. This is the type of material which this analysis considers. Applying a Laplace transform to Eq. (A.15) gives,

$$\frac{\hat{\sigma}_{ij}}{a_g(T)} = s \hat{C}_{ijkl} \hat{\epsilon}_{kl} - s \hat{\beta}_{ij} \hat{\Delta T} \quad (\text{A.20})$$

where in this case

$$\hat{f}(s) = \int_0^{\infty} f(\xi) e^{-s\xi} d\xi \quad (\text{A.21})$$

Using (A.20) the usual laminate thermal analysis may be performed to obtain solutions in the transform domain.

The problem of transforming the 'Laplace transformed' solutions back into the time domain still must be faced. One method used by Schapery (Ref. 7) is a collocation inversion. He assumes the time response to some step input (at $t = 0$) will be a series of decaying exponentials (Dirichlet Series), i.e.,

$$f(t) = S_{\infty} + \sum_{i=1}^N S_i e^{-t\lambda_i} \quad (\text{A.22})$$

where S_i 's are constants. The values of λ_i are chosen arbitrarily. Schapery recommends choosing them one decade apart over the region of interest.

Once a solution for a step input has been obtained, it is reasonably straightforward to obtain a solution for a general input. Letting $f(t)$ represent the response to a step input, then the response to a general input $I(t)$ is $O(t)$ where:

$$O(t) = \int_0^t f(t-t') \frac{dI}{dt'} dt' \quad (\text{A.23})$$

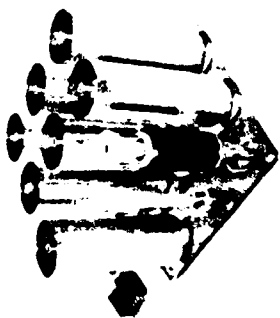
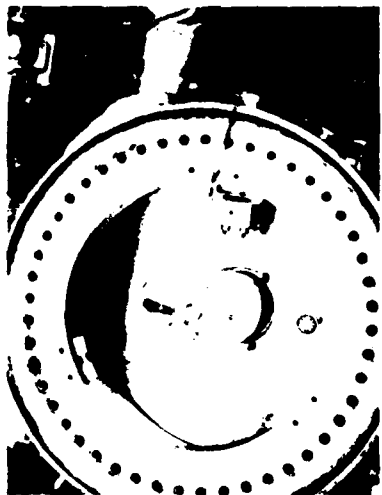


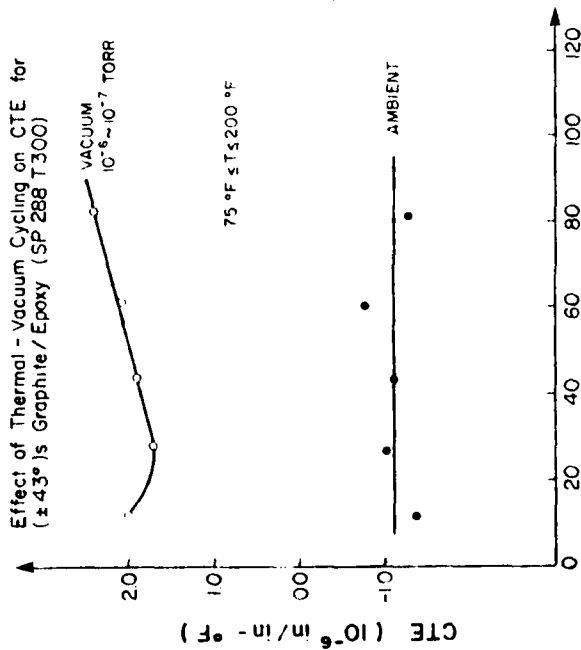
FIG. 1

FIG. 2

FIG. 3

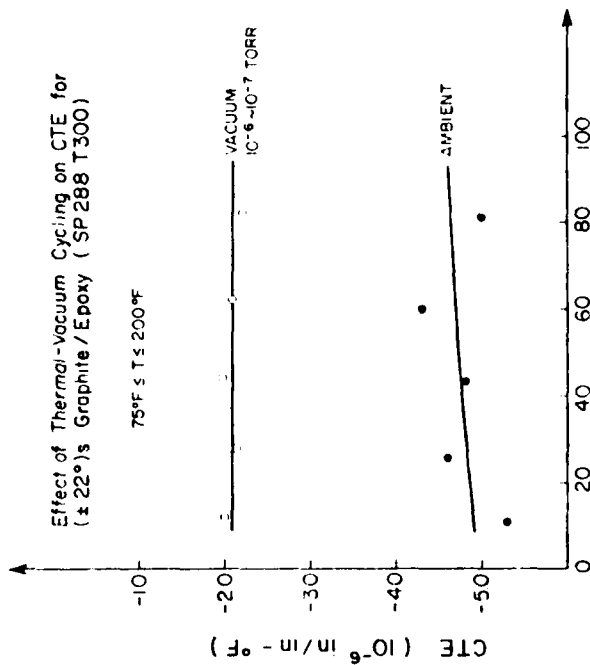


FIG. 4



No. OF THERMAL CYCLES

FIG. 5



No. OF THERMAL CYCLES

FIG. 6

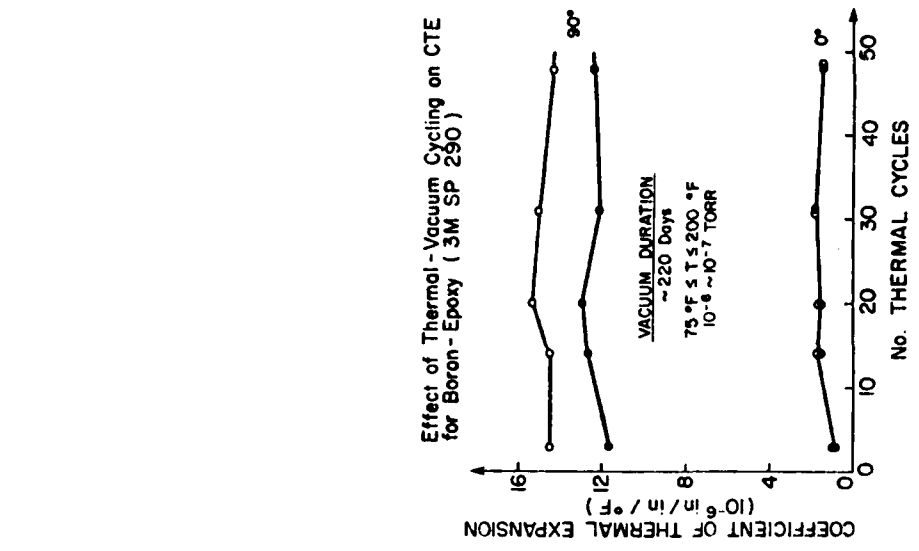


FIG. 9

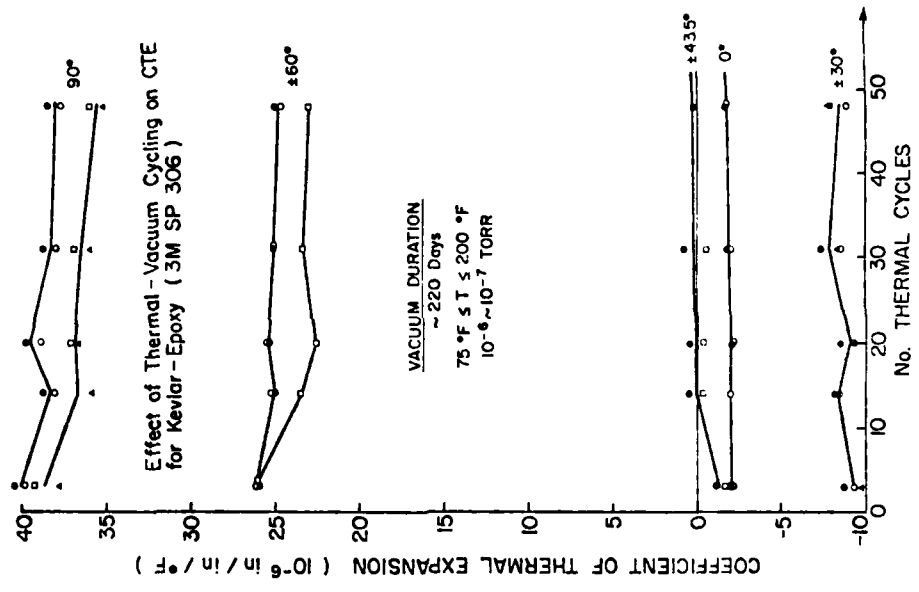


FIG. 8

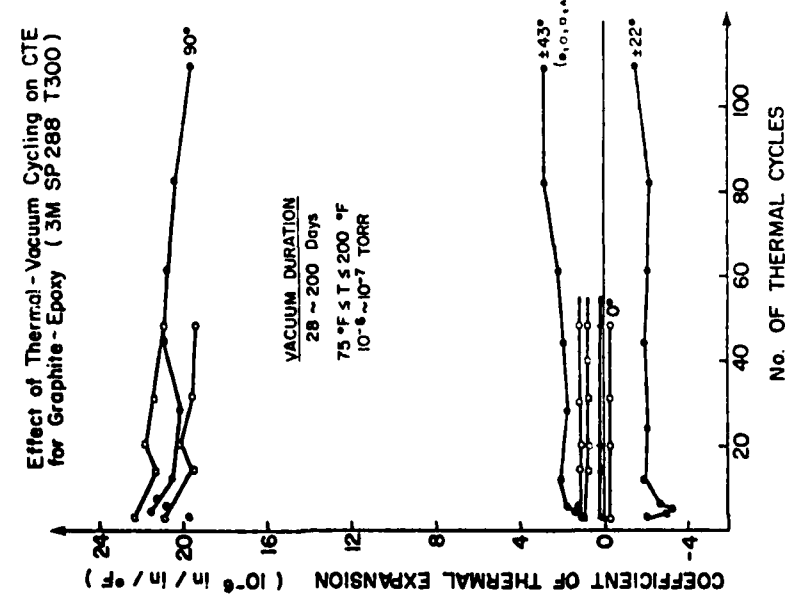


FIG. 7

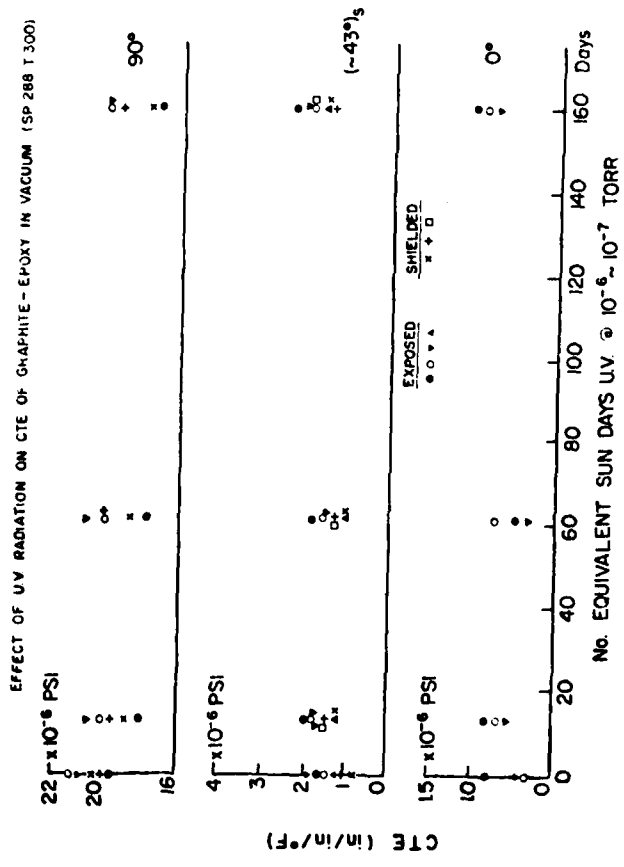


FIG. 10

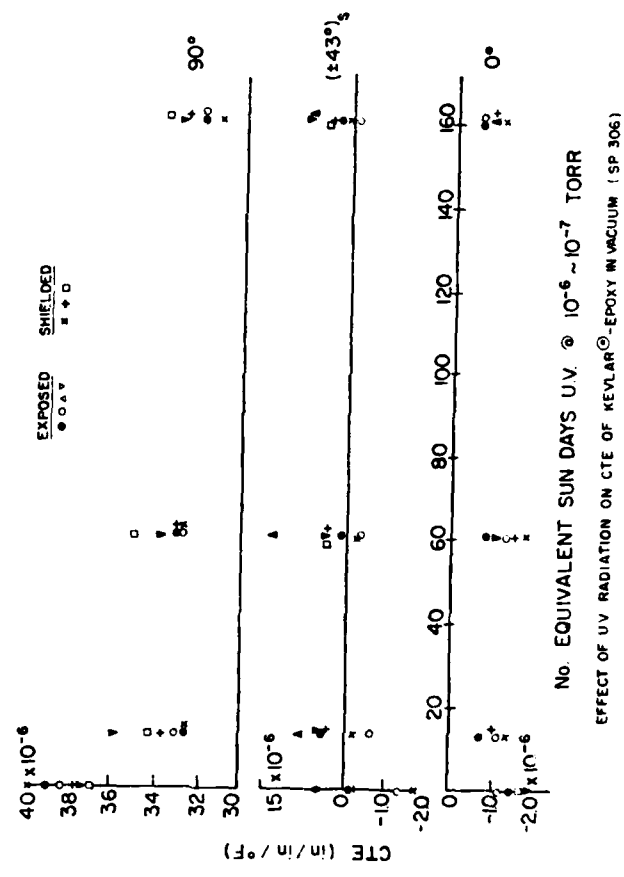


FIG. 11

CREEP TESTS ON GRAPHITE / EPOXY 90° SAMPLES (SP 288 T 300)

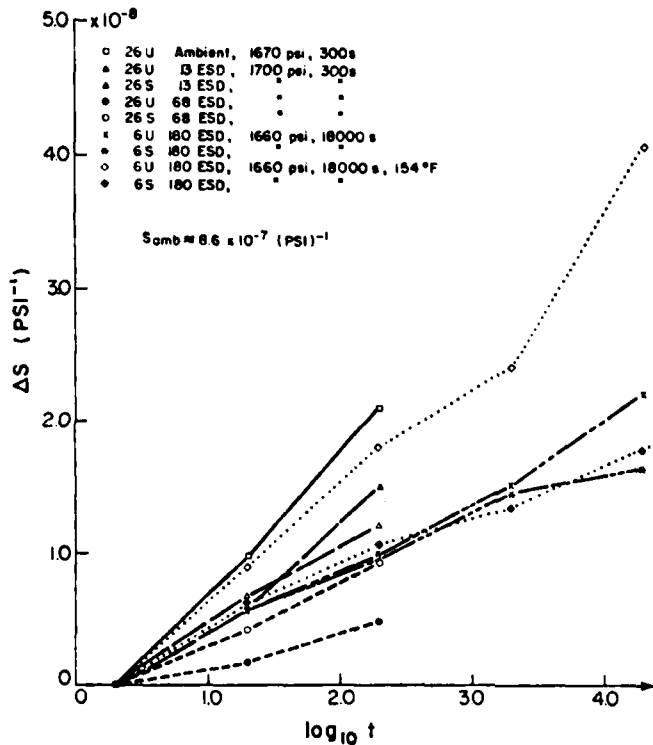


FIG. 12

CTE for Kevlar/Epoxy ($\pm \theta$)_s Construction (SP 306)

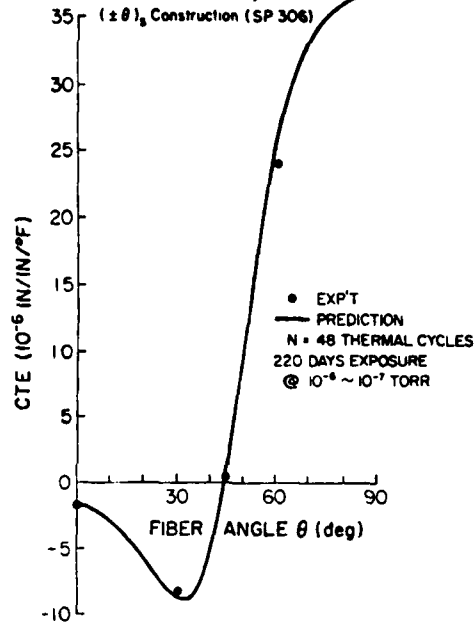


FIG. 13

RESPONSE OF ($\pm 4.3^\circ$) GRAPHITE/EPOXY LAMINATE TO TEMPERATURE CHANGE FROM 275 TO 75°F

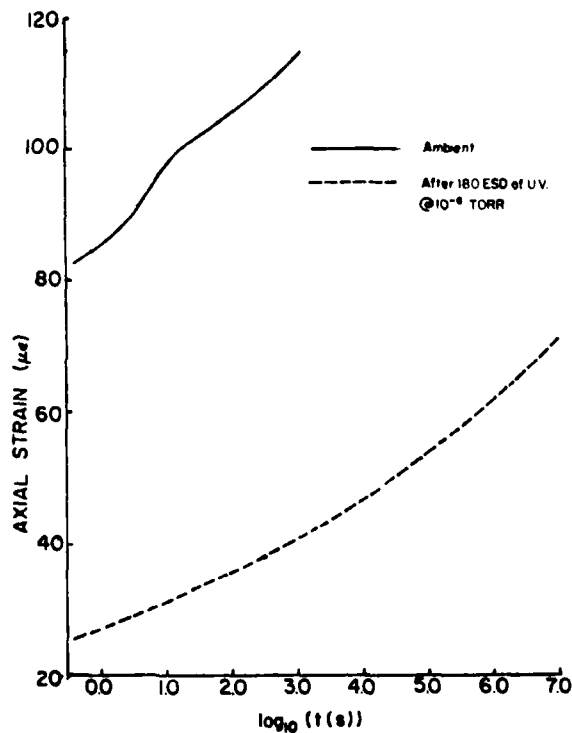


FIG. 14

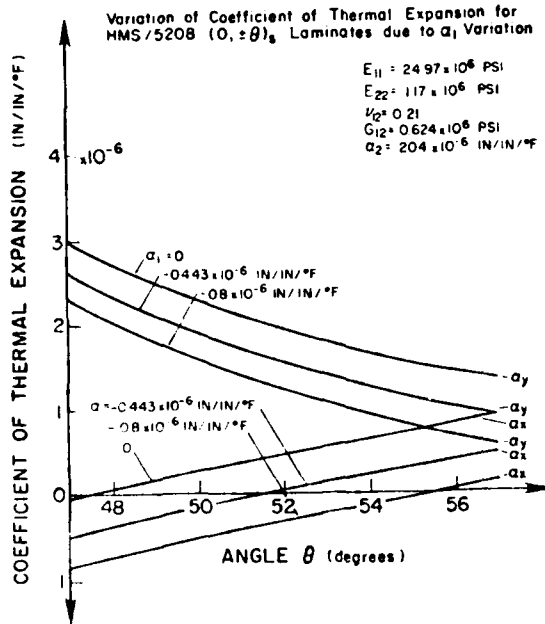


FIG. 15

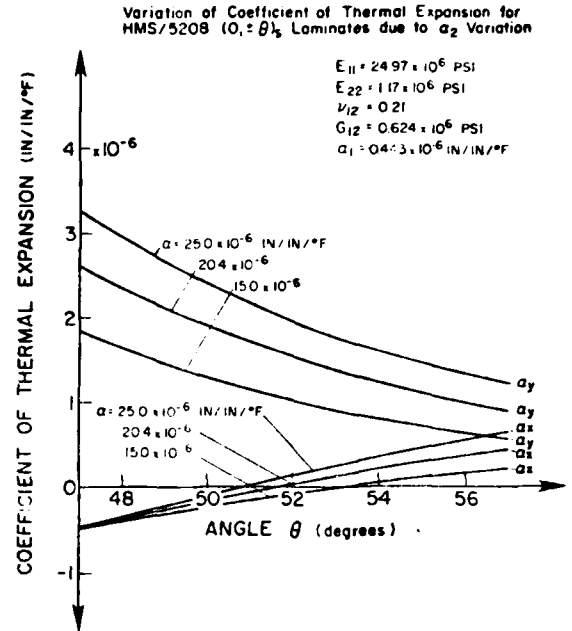


FIG. 16

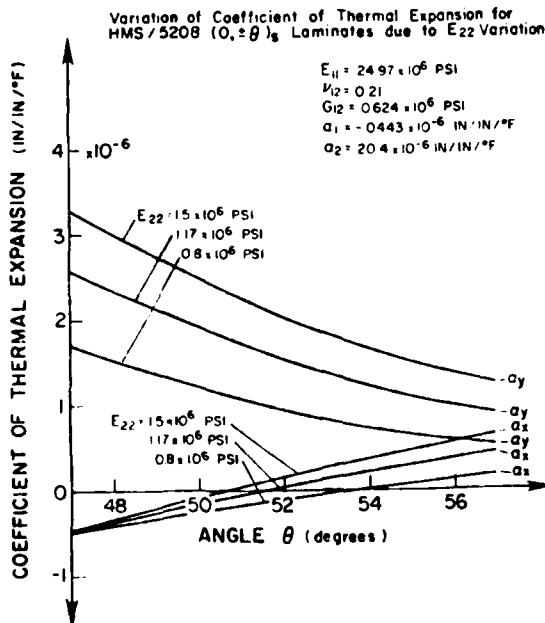


FIG. 17

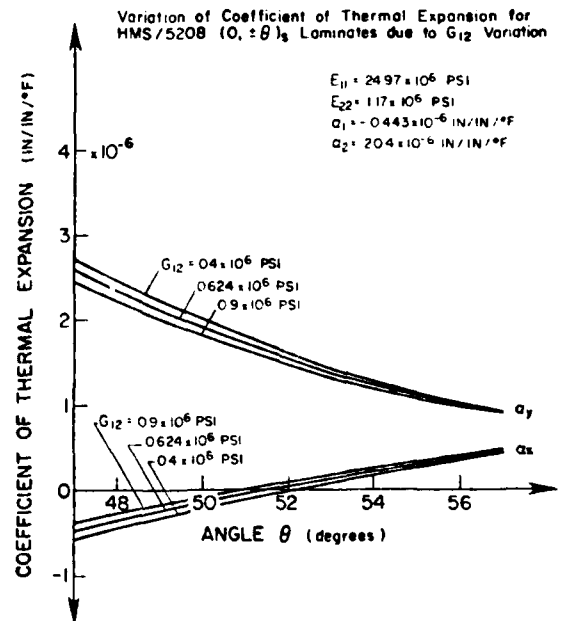


FIG. 18

Space Environmental Effects on Materials

Dr. Darrel R. Tenney, George F. Sykes, and David E. Bowles
NASA-Langley Research Center
Hampton, VA 23665

SUMMARY

Composite materials will be used for future space missions such as communication antennae, solar reflectors, satellite power systems, and a space operations center because of their unique combination of high specific stiffness and low coefficient of thermal expansion. For long-life space missions (10-20 years) the durability of these materials in the hostile space environment has been identified as a key materials technology need.

This paper reviews NASA-Langley's research efforts on the space durability of materials including: radiation effects on polymer matrix composites, and films; dimensional stability of polymer matrix composites, and tension stabilized cables; and thermal control coatings. Research to date has concentrated on establishing a fundamental understanding of space environmental effects on current graphite reinforced composites and polymer systems, and development of analytical models to explain observed changes in mechanical, physical, and optical properties. As a result of these research efforts, new experimental facilities have been developed to simulate the space environment and measure the observed property changes. Chemical and microstructural analyses have also been performed to establish damage mechanisms and the limits for accelerated testing. The implication of these results on material selection and system performance are discussed and additional research needs and opportunities in the area of tougher resin/matrix and metal/matrix composites are identified.

INTRODUCTION

Large space structure systems technology is a continuing research activity within National Aeronautics and Space Administration (NASA) [1-5]. This research relates to several spacecraft concepts for future space missions such as communication antennae and a space operations center as illustrated in figure 1. The key materials technology needs identified for these large space structures include both structural efficiency and environmental stability. Research related to several identified needs has been initiated.

Structural requirements generally focus on light weight, high stiffness and dimensional stability. Conventional aerospace materials such as aluminum and titanium do not provide these characteristics whereas advanced graphite reinforced composites do. The coefficient of thermal expansion (CTE) values and specific stiffnesses of graphite composites and selected other low expansion materials are compared in figure 2. Quartz and ULE (titanium silicate glass) fall within the preferred range of CTE but do not provide the needed stiffness. A range of values are shown for both the graphite/resin and graphite/metal composites indicating the flexibility that these composites offer for tailoring properties by varying the fiber type and ply orientation. Graphite/resin and graphite/metal composites both provide the needed CTE values and can be selected for a particular application depending on the stiffness requirements. Graphite/glass has a very low CTE and high stiffness but its low thermal conductivity may make it undesirable in applications where large thermal gradients could cause warping of the structure.

The environmental stability or materials durability in the space environment becomes a dominant issue for long-life space missions (10-20 years), figure 3. In low earth orbit (LEO), materials will be subjected to repeated thermal cycles of approximately $\pm 125^{\circ}\text{C}$, ultra-violet (UV) radiation, and ultra-high vacuum. Micrometeoroids and space debris are also considered hazards in LEO. For higher orbits, such as geo-synchronous earth orbit (GEO), the materials will also be subjected to large doses of high energy electrons and protons. The primary concerns for resin/matrix composites are radiation induced changes in mechanical and physical properties and dimensional instability caused by microcracking due to residual stresses produced during thermal cycling. Similarly, the residual strains produced by the thermal expansion mismatch between the fibers and the matrix in metal/matrix composites are likely to affect the dimensional stability of these materials. Long-life coatings which are required to keep the spacecraft system within design temperature limits, are also affected by the space environment. Degradation of the optical properties of these coatings by UV and particulate radiation and by contamination appears to be a significant problem that must be solved to achieve long-life (10 to 20 years) systems.

The ability to predict the long-term performance of all classes of materials in space must be a central part of any space environmental effects program and may require flight experiments, such as the Long Duration Exposure Facility (LDEF), for verification of ground exposure data and analytical predictions. The remainder of this paper will discuss NASA-Langley's research efforts to address the key materials technology needs in the areas of radiation effects, dimensional stability, and thermal control coatings. Examples of current materials research directed toward large space structures are described and additional research needs and opportunities are noted. A reference

list is included of selected references that describe large space structural concepts and related technology needs in detail.

Reference to specific commercial materials in this paper in no way implies recommendation or endorsement of the material by NASA.

LONG-TERM RADIATION STABILITY OF POLYMERS AND COMPOSITES

The space radiation effects program at NASA-Langley is divided into 3 areas of research. The first area is aimed at developing improved facilities and methodology for exposing polymers, films, and composites to a simulated space environment. The objective is to develop the capability for long-term low dose-rate exposure with single parameter radiation and to develop a facility for combined environmental exposure. This combined exposure will include electrons, protons and UV, simultaneously focused over an area large enough to irradiate mechanical test specimens. The second area of research is aimed at establishing the bounds of material property changes expected in the space environment. The objective of this area of research is to collect experimental data on the physical chemical and mechanical properties of materials, both before and after radiation exposure, and to correlate the observed changes with corresponding chemical characterization. The third area of the program is to develop a fundamental understanding of the radiation interaction with polymers. This effort involves establishment of kinetic models of the radiation interaction and identification of energy absorption processes and subsequent chemical degradation mechanisms. This is an essential part of establishing the "correct test" to evaluate materials and for developing an accelerated test methodology. A fundamental understanding of the interaction mechanism is also vital to any new materials development program. Results obtained in these three areas of research are discussed in the following sections.

The Space Environment

A major factor affecting the selection and application of materials is understanding the service environment and its interaction with the materials of interest. For the space environment, the significant exposure parameters and the magnitude of each are summarized in table 1. Also given in this table is a brief statement of the possible interaction of each component with spacecraft materials. Space debris and micrometeoroids also exist in the environment but are not considered in this paper.

The actual exposure environment for a space structure will depend upon its particular orbit. As already discussed, both LEO and GEO missions are being considered and the principal environmental concerns in each were mentioned. In general, the charged particle environment, consisting of large fluxes of electrons and protons [6-8], is a concern for all orbits passing through the Van Allen radiation belts. For a GEO environment, the absorbed dose for a typical organic polymer (polystyrene in this example) as a function of material depth is shown in figure 4. The absorbed dose, in rads, is shown for both 1 and 30 year missions and the thickness for a 4-ply composite is shown to provide a reference for thin gauge structural members. Low energy electrons and most protons are absorbed near the surface producing a very high surface dose. The absorbed dose through the thickness of the laminate is approximately 5×10^4 rads for 30 years exposure. Literature data [9] indicate that this level exceeds the damage threshold for most polymer systems and therefore property changes, which would limit the useful life of the structure, might be expected. Radiation induced crosslinking to produce a brittle matrix resin might be expected based upon these literature data. Because only limited experimental data exist [10] for the radiation durability of current high performance materials such as epoxies, polyimides, and advanced thermoplastics, these materials are the subject of our current radiation effects program.

Experimental Facilities

Several unique experimental facilities are being developed by NASA to verify material performance and provide the characterization needed for development of models and ultimately an accelerated test methodology. Simulation of the space environment will be performed in a single chamber as illustrated figure 5. This facility will incorporate a 1 MeV electron accelerator, a 2.5 MeV proton accelerator and a solar UV simulator all targeted at a 300 mm diameter specimen mounting plate. This equipment is schematically shown in the upper left of this figure. A comparison of the operational energy range of the facility with the electron and proton space environment is shown in the upper right. This comparison shows that the facility will duplicate a significant portion of the energy/flux range of the actual environment. The exposure chamber and beam expansion for the electron accelerator are shown in the lower portion of the figure. Ultra high vacuum low contamination pumps enabling 10^{-19} Pa pressures are used to evacuate the chamber and beam tube.

Characterization of the fundamental radiation interaction mechanisms is obtained by using smaller single parameter exposure chambers. In these chambers, polymer films are subjected to low energy (100 KeV) electrons. Chemical and physical properties such as weight loss, outgassing and condensable products, infrared (IR) absorption and dynamic moduli are followed during the irradiation. Mechanical properties of the films are obtained after irradiation. These characterization data serve as a sensitive measure of the radiation interaction and provide data for development of mechanistic models of the interaction process.

Development of Test Procedures

Because real-time exposures to evaluate space materials are not practical, a test acceleration methodology must be established that can be used to accurately predict long-term performance from short-time data. Test variables such as temperature, particle energy, dose rate and type of energy must be evaluated to develop this methodology. Figures 6 and 7 demonstrate some initial results of this effort. Figure 6 shows the effect of dose rate (test acceleration rate) on sample temperature for both polysulfone films and a graphite/polysulfone composite (4-ply, unidirectional). Because of the low-thermal conductivity of polymers and difficulties in maintaining good contact with the specimen cooling plate, the temperature of the composite specimen was found to increase substantially with dose rate. For polysulfone films, contact with the cooled base plate was easier to achieve and the maximum temperature at 10^8 rads/hr. was about 50°C which is significantly below its glass transition temperature, (190°C) and no major effect due to temperature is anticipated. High specimen temperatures, particularly those near the glass transition temperature, may change the radiation interaction mechanism and therefore produce material changes not representative of changes expected in actual service. For composites, long and thus expensive tests are required.

Figure 7 shows the effects of dose rate and total dose on the glass transition temperature of electron irradiated polysulfone films. From these results, it appears that dose rate, within the range studied, does not affect the radiation interaction mechanism. However, comparison of these data with similar information obtained at much lower dose rates must be made before any definite conclusions concerning dose-rate effects on the interaction mechanism can be made. Very low dose-rate studies are underway.

Effect of Ionizing Radiation on Mechanical Properties of Composites

The effect of radiation on composite mechanical properties has not been fully explored. Limited data [11-13] have shown, as indicated in figures 8 and 9, that radiation does not significantly affect physical properties. Figure 8 shows the flexural properties of small (1.2 x 2.5 cm) unidirectional specimens of T300/5208 graphite/epoxy composite after exposure to electron radiation. These miniature specimens were used because the exposure area was small. Exposures in vacuum for doses up to and including 8×10^9 rads are shown. The fiber direction was in the direction of specimen length (longitudinal), so the flexural properties were fiber dominated. The flexural strength, figure 9, appears to slightly increase with dose, approximately four percent at 8×10^9 rads. However, the size of the confidence band is large and could mask small changes in flexural properties. This scatter is typical of composite specimens and is a major problem in conducting environmental effects studies on composites.

Figure 10 shows the effect of electron irradiation on tensile properties of C6000/P1700 graphite/polysulfone composite specimens exposed to electron doses to 1×10^{10} rads. Again, miniature 4-ply composite specimens with a $\pm 45^\circ$ orientation were tested. Slight increases in the indicated properties were found when the materials were tested at room temperature following exposure. The modulus data for this composite increases in a similar manner as that found for film samples of this material (figure 11). However, the magnitude of the change is less.

Effect of Ionizing Radiation on Chemical Properties of Matrix Polymers

Thermoplastics with improved properties are being actively considered for structural applications. One class that has received considerable attention for space and aircraft application is polysulfone. For space use, these materials are attractive because of their thermoformability. To assess long-term durability of these materials in space, a study [14] of their radiation stability was performed. A series of 4 materials, each with a different chemical structure, was exposed to either an electron or a proton environment using several different dose rates and particle energy sufficient to give a uniform dose through the polymer film. The absorbed dose was varied between 10^8 and 10^{10} rads. Film samples of all materials were used because chemical characterization of films is much easier than composites and provides a more sensitive measure of radiation damage.

The effect of total electron dose on the observed modulus of the four polysulfone films is shown in figure 11. The modulus of the unirradiated film is given on the ordinate. Modulus values were obtained using an automated Rheovibron Dynamic Viscoelastometer [15], with all data obtained at a frequency of 3.5 Hz. When determining modulus, the film sample was inserted, removed and reinserted several times to eliminate sample mounting effects. All reported values are the average of at least three measurements.

For all materials, modulus increased as dose increased, and the threshold value for a major change in modulus appears to be near 10^9 rad. The percent increase ranges from about 24% for P-1700, to 58% for Radel 5000. This increase with dose suggests that crosslinking is occurring in all materials, particularly after 10^9 rad.

The glass transition temperatures (T_g) for these polysulfones after exposure is shown in figure 12. T_g was measured by a Dupont Model 943 Thermal Mechanical Analysis System in the film stretch mode. T_g followed very closely the trends observed in modulus. That is, a significant increase in T_g , compared to the unirradiated materials was found to begin at 10^9 rads total

dose. The observed brittleness, and increase in T_g and modulus at this dose level indicate that crosslinking has occurred. The T_g values for exposures between 10^8 and 10^9 rads were lower than the initial value indicating that in this range chain-scission reactions predominate. These data suggest that the ratio of chain scission to crosslinking changes with total dose and therefore must be included in any attempt to model the radiation interaction processes that occur in these materials.

In figure 13, two infrared spectra, each made from a separate film of polyethersulfone, are shown. This polysulfone is representative of the four materials studied. The lower curve represents the portion from 1600 to 600 cm^{-1} frequency, of the IR spectrum of unirradiated polyethersulfone. The upper curve represents that same portion of the spectrum of polyethersulfone irradiated with electrons to 10^{10} rads. The SO_2 absorption band occurs at approximately 1400 cm^{-1} which can be clearly seen as an absorption peak (an inverted peak) on the unirradiated curve. However, after irradiation this peak is greatly diminished. Near 1300 and 1150 cm^{-1} are the asymmetric and symmetric $\phi\text{-SO}_2\text{-}\phi$ absorption bands, respectively. These bands are present in the lower curve, but have almost disappeared in the upper curve of the irradiated material. At approximately 1070 cm^{-1} the C-O-C absorption band, that appears on the spectrum for the unirradiated specimen is absent in the spectrum for the irradiated polyethersulfone. The spectra shown here are the two extremes of the data actually obtained. The spectra of those specimens irradiated at lower doses resemble the spectra of the unirradiated material, and, as the dose was increased, the spectra approached that of the curve at 10^{10} rads. All four polysulfones exhibited this same basic trend, with the SO_2 , $\phi\text{-SO}_2\text{-}\phi$ and C-O-C bands being the most significantly affected by the radiation. The proton data, not shown here, also followed this trend, but the magnitude of change is less.

Following irradiation of each polysulfone film, a chemical analysis was performed to determine changes in elemental composition. Figure 14 shows this elemental composition data for one material (P1700), normalized relative to the chemical analysis of the starting material, as a function of total dose. Similar chemical analysis data were obtained on all polysulfones studied and showed trends as presented in this figure. The analysis showed considerable loss of oxygen and losses of sulfur and hydrogen. The threshold for a major decrease in oxygen occurs near 2×10^8 rads. About 24% of the initial oxygen content is lost for P-1700 at 10^{10} rads and that loss could establish sites for crosslinks. This apparent loss is supported by the diminished absorption bands associated with oxygen in the IR data. The breaking of an oxygen bond by irradiation and subsequent combination of oxygen atoms to form oxygen molecules, which could then be lost to the surroundings, would explain the decrease in oxygen content and the diminished absorption bands. These data provide an indication of the type of outgassing products expected during irradiation and the associated changes in chemical structure.

Figure 15 compares the normalized oxygen composition of P1700 polysulfone irradiated by electrons and protons. As noted above, the electron irradiated sample showed a loss of oxygen through the dose range studied. The proton exposed materials, however, showed a loss of oxygen only after 5×10^9 rads indicating that a different mechanism of interaction may be involved with protons.

Development of Radiation Interaction Models

Development of durable materials for future space missions requires development of mechanistic models that can predict chemical and mechanical stability over long periods (10-30 years). A fundamental requirement of these models is the understanding of the primary processes of energy absorption in the material and the resultant energy dissipation which may involve bond cleavage and chemical change. These changes ultimately result in chemical composition, T_g and modulus changes in the material as demonstrated in polysulfone data shown above. Figures 16 - 18 show some results of an effort to first, characterize and predict the site of the primary energy absorption processes and second, to identify the products of the initial bond cleavage resulting from this energy absorption.

Electron impact mass spectral data of molecules with similar composition to structural parts of the matrix polymer have been used to predict the likely interaction site of space electrons with an epoxy as shown in figure 16. In the right side of this figure (results of mass spectrometer data), the probabilities of breaking major bonds are compared. The H-N bond exists in both the cured epoxy and in the simple molecule in a similar configuration (adjacent to the benzene ring). The data demonstrate that this bond is more susceptible to breakage than the C-C bond, also adjacent to the ring. Applying this procedure to the epoxy structure using mass spectral data of many simple molecules, the possible electron interaction sites have been identified and are shown with arrows on the epoxy structure. In addition, taking the prediction procedure one step further, the reactive radicals expected from the material when bonds break, can be identified.

Experimentally, the radical concentration in irradiated polymeric materials is being measured with electron spin resonance (ESR) techniques. This technique measures the presence of unpaired electrons in the material. The specimen is simultaneously subjected to a fixed frequency and a sweeping magnetic field. At a particular combination of frequency and magnetic field, characteristic of the electron's environment, the unpaired electron's spin is flipped and a net absorption of energy is detected. Figure 17 shows typical ESR spectra of an epoxy that has been irradiated to various levels and compares these to the unirradiated material spectrum. The epoxy's

signal shown in the figure is due to radiation-generated radicals, the number of which varies with dose. The signal magnitude, position, and structure vary with radiation dose as shown.

The variation of radical concentration, in a 177°C cure epoxy, with electron dose is shown in figure 14. For 1.3×10^8 rads, the radical concentration was approximately 1.9×10^{18} spins/g, or one radical for every 55 molecules. As shown in figure 19, this radical concentration decays with time once the exposed material is removed from the radiation source. For these data, the samples remained at room temperature while being transported from the radiation source to the ESR apparatus therefore, some decay occurred before the radical concentration could be measured. The data show, however, that many radicals are long lived. Literature data suggest that each radical would, if given sufficient time, generate a cross-link or chain scission.

Summary and Future Directions

Research on the long-term radiation stability of polymers and composites is underway. The major accomplishments to date include: (1) construction of a unique space simulation facility incorporating sources for electrons, protons and UV exposure of a large temperature controlled exposure area; (2) development of initial test procedures to insure that an "accurate" simulation is being performed; and (3) assessment of mechanical and chemical property changes in polyimide, epoxy, and polysulfone films and graphite reinforced composites. Initial characterization shows that significant chemistry changes occur during irradiation of the polymer. Major changes in mechanical property of the composite, however, have not been found. Future efforts will focus on this inconsistency and the need to run long-time low-dose rate exposure tests to more closely simulate the natural space environment.

DIMENSIONAL STABILITY OF COMPOSITES

As discussed earlier, the performance characteristics of many large space structures are dependent upon their dimensional stability. Materials to be used in these structures include graphite and quartz cables, resin/matrix composites, and metal/matrix composites. The primary factors controlling the dimensional stability of these materials include both thermal and mechanical load cycling, moisture desorption, radiation exposure, and microcracking. These factors may cause permanent changes in the thermoelastic properties, as well as permanent residual strains in the composite materials.

The dimensional stability program at NASA-Langley is divided into three major areas of research. The first of these is aimed at developing a thorough understanding of the stability aspects of current graphite/resin composite systems. This includes studying the effects of thermal cycling, radiation, and processing variability on the dimensional stability of these composites, both experimentally and analytically. Research to date has focused on the development of precise laser-based measurement systems for measuring small dimensional changes in composites, and the effect of microcracking on the dimensional stability. The second major research area is the dimensional stability of advanced composite systems, including hybrids, tougher resin/matrix composites, and advanced metal/matrix composites. Research in this area is just beginning. The third area is the dimensional stability aspects of candidate tension-stabilized cable materials. Results from all of these areas will be discussed in the forthcoming sections.

Techniques for Measuring Small Thermal Strains

The composite laminates used in structures where dimensional stability is critical will have CTE's approaching zero. Therefore, any measurement system used to characterize the dimensional stability of these composites must be capable of detecting strains on the order of 1×10^{-6} . Two laser interferometer systems have been developed to accomplish this goal, a moire interferometer and a Priest interferometer, each having its own advantages and disadvantages depending upon the particular measurements requirements.

Schematic diagrams of the moire [16] and Priest [17] interferometers are shown in figures 20 and 21. The interferometers are enclosed in chambers in which the temperature of circulating air is controlled by a resistance heater and liquid nitrogen, and a helium neon laser is used for illumination. Both techniques utilize a change in interference fringe density to determine the thermal strain of the specimen. A major advantage of the moire interferometer as opposed to the Priest interferometer is that it does not use the ends of the specimen for measurement, thus eliminating end effects and allowing for a combination of mechanical and thermal loading. The moire technique also provides full-field displacement information permitting the determination of non-homogeneous strain fields. The major disadvantage of the moire technique currently used is that measurements cannot be made below -75°C due to embrittlement of the silicone rubber used for the specimen grating. Alternate grating materials are being investigated to extend the measurement capability to -150°C. Measurements can be made over the full temperature range of interest, -150°C to 150°C, with the Priest and it also provides a better theoretical resolution, approximately 4×10^{-6} /fringe compared to 25×10^{-6} /fringe for the moire. For these reasons the Priest interferometer is preferred for normal thermal expansion measurements.

Typical thermal expansion data collected for unidirectional and quasi-isotropic T300/5208 graphite/epoxy over a temperature range from -150°C to 100°C, are shown in figure 22. These data show the large range of CTE values that can be obtained in composites depending on the laminate configuration. As can be seen unidirectional T300/5208 provides a very small CTE, -0.13 to

$0.17 \times 10^{-6}/^{\circ}\text{C}$, over the entire temperature range. The expansion behavior of these laminates is expected to bound the behavior of the laminates chosen for space structures. This type of data for different graphite fibers and resins is essential for verification of analyses used for tailoring laminates to achieve required stiffness and low CTE.

The Effects of Microcracks

Microcracks are small cracks in the matrix material which extend parallel to the fiber direction. They occur when the internal stresses exceed the transverse strength of an individual lamina. The two primary causes of microcracking are thermal stresses due to repeated thermal cycling and mechanical loading. A limited amount of research has been conducted concerning the causes and effects of microcracking in composites. Repeated thermal cycling has been shown to cause microcracking in graphite/epoxy laminates thereby causing the CTE to approach that of the CTE for the unidirectional material [18]. Research has also shown that residual strains, due to microcracking, of up to 20×10^{-6} may develop in graphite/epoxy during the first cooling cycle to -140°C [19].

An experimental and analytical investigation is being conducted to quantitatively correlate the change in CTE with microcrack density. Microcracks were induced in the laminates by mechanical load because the amount of damage could be easily controlled and characterized. Specimens from two quasi-isotropic T300/5208 laminate configurations were loaded to produce varying amounts of microcracking in plies perpendicular to the load direction. The amount of microcracking was characterized by computing an average crack density in the damaged plies. The average CTE, over the temperature range 25 to 150°C , for the various specimens was measured using the moiré interferometry technique. A photomicrograph of a microcracking pattern along the edge of a quasi-isotropic specimen is shown in figure 23. The effect of this type of damage on the thermal expansion is shown in figure 24. Microcracking reduces the thermal strain for a given change in temperature thus lowering the CTE.

The effect of microcracks on the CTE was modelled with a finite-element analysis. A generalized plane strain formulation was used with four noded, linear general quadrilateral isoparametric elements, capable of handling orthotropic material properties. The finite-element computer code [20] was modified for the current study. Numerical results were generated for both the $[0_m/90_n]_s$ ($m, n = 1, 2, 3$) class of laminates and two quasi-isotropic configurations, $[0/+45/90]_s$ and $[0/90/+45]_s$, using typical material properties for T300/5208. Results are presented in the form of CTE as a function of linear crack density in the 90° plies which was varied from 0 to 3 cracks/mm. The value of 3 cracks/mm was found to be an upper limit on the crack density formed in these materials during the experimental phase of this research. The results presented are preliminary in nature and represent the efforts of an ongoing research project.

The analytical results for the $[0_m/90_n]_s$ family of laminates are shown in figure 25. As would be expected the laminate configuration with the largest percentage of 90° plies experiences the largest reduction in CTE. The CTE at 3 cracks/mm for the three laminates, $[0/90_3]_s$, $[0_2/90_2]_s$, and $[0_3/90]_s$, are reduced by approximately 90, 65, and 40 percent, respectively. For all of these laminates, the CTE was reduced in a direction towards the value of the CTE for the unidirectional material, $-0.1 \times 10^{-6}/^{\circ}\text{C}$, and approached a stabilized value after approximately 2 cracks/mm.

Analytical results for the quasi-isotropic laminates were compared with experimental data as shown in figure 26. Experimental results are normalized with respect to the average CTE values of the uncracked $[0/+45/90]_s$ and $[0/90/+45]_s$ laminates. The experimental and predicted values both show the same trends, however, the analysis consistently underpredicts the effect, especially for the $[0/90/+45]_s$ laminate. A possible explanation for this discrepancy is that not all of the damage present in the specimens was accounted for in the analysis. At very low crack densities, some of the microcracks could have been missed in the visual inspection. Also, some specimens contained visible microcracks in the adjacent 45° plies. This occurred in specimens that were loaded to a large percentage of their ultimate strength. Both of these factors would contribute to the underprediction when not included in the analysis.

In general, these two laminates show the same trends as the $[0_m/90_n]_s$ family of laminates. The $[0/+45/90]_s$ laminate exhibited a larger reduction in CTE than the $[0/90/+45]_s$ for the same crack density. The reason for this is that the 90° ply in the $[0/+45/90]_s$ laminate is constrained by an uncracked ply on one side, and another cracked 90° ply on the other side. The 90° plies in the $[0/90/+45]_s$ laminates are separated and therefore each 90° ply is constrained by two uncracked plies. This added constraint reduces the magnitude of the overall effect on the CTE. This demonstrates that the effect on CTE is not only a function of the amount of 90° plies, as demonstrated for the $[0_m/90_n]_s$ family of laminates, but is also a function of the constraint on the 90° plies (i.e. stacking sequence).

Classical laminated plate theory can also be used to predict the effect of microcracks on the CTE by appropriate reduction of the transverse stiffness of the cracked ply [21]. This method is being applied to predict the effect on the CTE of cracks in more than one direction, as in the case

Tests to determine the thermal cycling response of graphite/epoxy are currently in progress. However, earlier tests on graphite/polyimide (C6000/PMR15) have also been conducted to determine the effect of thermal cycling on residual mechanical properties [22]. Specimens were cycled 150 and 500 times between -156°C and 316°C . Residual mechanical properties were then measured at both room temperature and 316°C . Thermal cycling did induce microcracks in the specimens. The amount of microcracking was about the same after 150 and 500 cycles, although the size of the microcracks was larger after 500 cycles and extended into adjacent plies, as shown in figure 27. Figure 28 shows the results of the interlaminar shear and flexure residual strength tests. In general, thermal cycling had a larger effect on the interlaminar shear strength than the flexure strength, with a reduction of as much as 40% for the quasi-isotropic laminate. This was as expected because the interlaminar shear strength is matrix dominated, and microcracks tend to reduce the matrix strength.

Improved Polymer Matrix Composites

Research opportunities to enhance the potential of polymeric materials for large space structures include the development of tougher matrix resins. Current graphite/epoxy composites appear to meet stiffness, CTE, and weight requirements, but the brittle nature of epoxies makes them suspect for long life missions. Resistance to microcracking from thermal cycling and radiation induced embrittlement is of primary concern. Other resin systems such as thermoplastics and modified thermosets would appear to have excellent potential to improve composite toughness. One approach in new resin development is shown in figure 29, where a flexible linkage and thermoplastic properties have been incorporated into a normally brittle polyimide system. Research concerning the dimensional stability aspects of these new resins is just beginning. This type of research should provide guidance in the synthesis of new polymer resins having the potential of long-time structural stability in the space environment.

Improved Tension Stabilized Cable Materials

Lightweight deployable cables are currently being used in certain antenna designs to shape the mesh reflector surfaces, and are being considered for the same purpose on the Hoop-Column Antenna Concept [23] under study by NASA. Current cables are made of quartz fibers because quartz has a low thermal expansion, is inherently stable in the space environment, and can be made in small diameter fibers. A typical cable, approximately 450 μm in diameter, is composed of approximately 2000 individual quartz fibers, 9 μm in diameter, held together by a Teflon cross wrap. One of the problems with this type of construction is that it is very difficult to get all of the fibers aligned and keep them aligned during handling and storage of the cables with the result that a small (60×10^{-6}) but significant residual strain is produced in the cable when subjected to repeated load or thermal cycles. Also, considerable variability is observed in this residual strain making it difficult to accurately bias this out during fabrication when the precise length of each cable is determined.

The results of a recent program conducted by Harris Corporation [23], under NASA contract, to develop an improved cable are summarized in figure 30. Two major improvements were made which significantly advanced space cable technology. Unidirectional composites were made by impregnating the bare fibers with Teflon while holding the fibers straight under tension to achieve a better alignment of fibers and minimize the amount of twist in the fiber along the cable. This resulted in a substantial increase in the relative stiffness of the cable and reduction in residual strain after repeated thermal/mechanical cycling. Further improvements were achieved by using graphite fibers in place of the quartz fibers.

Summary and Future Directions

Research to date has concentrated on an understanding of the factors which influence the dimensional stability of currently available graphite/resin composite systems. Research remaining to be done includes further work on the effect of thermal cycling and radiation on the dimensional stability of graphite/resin composites, both experimentally and analytically. These factors must also be assessed for tougher resin/matrix composites that are less susceptible to microcracking, and hybrids designed to have near zero CTE's. The potential of metal/matrix composites for dimensional stability applications appears promising and future plans should include assessing their performance in the space environment. Successful application of composites for dimensionally stable structural members requires manufacturing techniques capable of producing precision members with very little material variability. Therefore, the effect of processing variables such as voids, resin content, cure cycle, etc. have an important role in dimensional stability and are also included in future research plans.

THERMAL CONTROL COATINGS

The basic requirement for thermal control coatings is to keep spacecraft components within allowable temperature limits. Thermal designers have two major problems: one where the temperature limit is dictated only by the solar heat input, for example, large area structures, and the second where both solar and internal heat are thermal inputs, for example, a manned habitat. In each case a coating with a different ratio of solar absorptance to thermal emittance is required. In table 2 the coating requirements for a composite structure in GEO are compared to the requirements for a manned habitat in LEO. The major differences are: (1) low emittance coatings

are required for the composite structure to reduce the extent of cool-down during a solar occult, (2) coating to be used in GEO must be able to withstand high energy electrons and protons in addition to UV, and (3) a higher electrical conductivity is required in GEO to eliminate spacecraft charging. Contamination would be a major source of coating performance degradation for the manned habitat because of the shuttle. However, repair or refurbishment of coatings can be considered for this application but not for GEO missions.

Table 3 summarizes some of the existing and previously used radiator thermal control coating materials and identifies the major problem with each of these materials. The table also points out that no low emittance paint-type coatings are available for use on large space structural components. Because of the weight penalty associated with use of this type coating on small thin gauge tubular structural elements, organic matrix white paint coatings would not likely be considered. New coating concepts which are easily adapted to any structural configuration and have good long-term durability in the radiation (ionized particle and UV) environment must be developed.

Some of the best available long-time data on coating performance in space flight are shown in figure 31. These data are from an Air Force flight experiment [24] conducted in a polar orbit. The interesting part of this figure is that the 3 white paints exhibit a substantial increase (130%) in solar absorptance in 5 years and all three have about the same degradation rate. The second-surface mirror type coatings, which do not have pigments, also are grouped together in degradation but exhibit a much lower degradation of only 40% and remained stable over long periods. Because most of this degradation occurred in the first 2 or 3 months of flight, contamination is suspected as a primary source of degradation for these nonpigmented coatings.

High Performance Polymer Films

Recent developments of high performance polymer films are particularly noteworthy for thermal control coating applications. From a study of structure/property relationships, a colorless polyimide, figure 32, has been developed [25] which may be used as a replacement for FEP Teflon on second-surface mirror type thermal control coatings. Polyimides are inherently more radiation stable, because of their highly aromatic structure, than FEP Teflon and therefore should give longer service in GEO type orbits where high doses of electrons and protons will be encountered. A clear polyimide could also be considered as a replacement for Kapton in such applications as thermal control blankets. A low solar absorptance cannot be achieved with Kapton because of its coloration. By replacing Kapton with the clear polyimide, a lower solar absorptance could be obtained and thus less heat input into these blankets.

Another development in high performance polymer films [26], with potential applications for coatings, is shown in figure 33. By incorporating metals into polymers, the mechanical and electrical properties of films are significantly improved. Figure 33 illustrates the magnitude of improvements which were observed in the adhesive strength and electrical conductivity of films. Improvements in the thermal conductivity have also been noted. The improved electrical conductivity however may be their most important property particularly when used as thermal control coatings because of their ability to dissipate static electrical charges. Many other applications for these materials may exist depending on their color and radiation stability.

LDEF Flight Experiment

In addition to development of new coating concepts, Langley has also maintained a continuing role in both ground testing and development of flight tests of coatings. Specialized equipment developed and used for the laboratory evaluation of coatings is shown in figure 34. This equipment provides for UV and proton exposure of thermal control coatings and allows for optical property evaluation of these materials without removal from the vacuum system. To verify the ground based test of coating performance, the Long Duration Exposure Facility (LDEF) is being used. This flight is outlined in figures 35, 36, and table 4. The objectives of LDEF are to determine the effects of both the shuttle induced environments and the space radiation environment on selected sets of spacecraft thermal control coatings. The experimental approach is to passively expose samples of thermal control coatings to shuttle induced and space radiation environments, return the samples for post-flight evaluation and compare with pre-flight measurements to determine the effects of environmental exposure. Two additional sets of samples will remain in the laboratory and will be analyzed for comparison with the flight data. Optical measurements of the samples will include total normal emittance and spectral reflectance. The experiment will use a 15.2 cm deep tray and an Experiment Exposure Control Canister (EECC) to provide protection for some of the samples against the launch and reentry environment. The EECC will be programmed to open about 2 weeks after LDEF deployment and close prior to LDEF shuttle retrieval.

Some samples will not be housed in the EECC and will be exposed to the shuttle-induced environment during launch and reentry. Comparison of data from these samples with that of samples in the EECC will yield information about possible contamination induced degradation effects. The thermal control coatings that are being considered for this experiment are listed table 4.

CONCLUDING REMARKS

Polymer matrix composite materials will be used for future space structures because of their excellent properties. This paper has presented results from an investigation of the effects of

these space structures. Data were obtained in this investigation on graphite reinforced composites, cables and thermal control coatings. Test results suggest that currently available composites will not undergo significant mechanical property changes for 20-30 years of service in space. No significant degradation has been observed in residual strength of composites upon laboratory exposure to electron radiation doses to 5×10^9 rads (equivalent to 30 years exposure in GEO). However, results to date are preliminary and were obtained using high dose rates (30-60 hours of test to simulate for 30 yrs. exposure). Longer-term, low-dose rate tests which are more representative of the conditions expected in space need to be conducted to determine if dose rate effects are significant. These tests are underway.

Extensive chemical characterization of polymer films exposed to radiation doses expected in space have shown that radiation does produce significant chemical changes. Degradation mechanisms have been established for a polysulfone and similar studies are ongoing on a number of other polymers. The point at which mechanical property changes appear has yet to be established. Radiation degradation models currently under development are expected to aid in understanding how radiation damage occurs in polymers and how chemical and mechanical properties are changed.

Thermal expansion measurements of composites are difficult because of the orthotropic nature of composites and because of their low coefficient of thermal expansion. To make precision strain measurements of composites, two laser interferometer techniques were developed. The effect of mechanically induced microcracks on the CTE was determined experimentally and an analysis was formulated to predict the observed changes. Results showed that microcracks reduce the CTE towards the value for the unidirectional material, and the reduction is a function of both the crack density and laminate configuration. Tests on graphite/polyimide have shown that thermal cycling induces microcracks and reduces matrix sensitive mechanical properties. Research in the area of improved cable materials has resulted in the development of a Teflon impregnated graphite cable with a higher stiffness, lower CTE, and greatly reduced residual strain than the conventional quartz cable.

An assessment of current thermal control coatings indicates that they will not meet the thermal control requirements for large space structures. Existing white paint coatings are heavy and undergo significant degradation in optical properties in 5 years of space exposure. Langley is working new advanced-coatings concepts including unique particulate and UV radiation stable polymer films which may be suitable for thermal control coatings and blankets. The development of a clear polyimide and high conductivity polymer films offer good potential for developing improved coatings. The planned coating experiment on IDEF will provide useful data for evaluating shuttle contamination of coatings and for verification of ground based simulation tests.

Confidence in advanced composites technology is being developed to the extent that designers of current spacecraft are making extensive use of composites for selected space hardware components. Composites will be used to an even larger extent in future large space systems as additional confidence is gained in their long-term durability in space.

REFERENCES

1. Large Space Systems Technology - 1980, Vols. I and II, NASA CP-2168.
2. Large Space Systems Technology - 1981, Vols. I and II, NASA CP-2215, 1981.
3. Bush, H. G. and Heard, W. L.: Recent Advances in Structural Technology for Large Deployable and Erectable Spacecraft. NASA TM-81905, Oct. 1980.
4. Wright, R. L. (Editor): The Microwave Radiometer Spacecraft - A Design Study. NASA RP 1079, Dec. 1981.
5. Russell, R. A.; Campbell, I. G.; and Freeland, R. E.: A Technology Development Program for Large Space Antennas. NASA TM-81902, 1980.
6. Moritz, J.: Measurement of Radiation Belt Protons in the Energy Range 0.25 to 1.65 MeV on Board the Satellite "AZUR." J. Geophys., 37, 1971.
7. Vette, J. I.; Locero, A. B.; and Wright, J. A.: Models of the Trapped Radiation Environment, V. II: Inner and Outer Zone Electrons. NASA SP-3024, 1967.
8. Teague, M. J.; Chan, K. W.; and Vette, J. I.: AE6: A Model Environment of Trapped Electrons for Solar Maximum. NASA TM X-72597, 1976.
9. Kircher, J. F.; and Bowman, R. E.: Effects of Radiation on Materials and Components. Reinhold Publ. Co., New York, 1964.
10. McGrath, J. E.: An Independent Assessment of the Need for NASA Research on the Durability of Materials in the Space Environment and for a New NASA Facility to Accomplish the Research. Virginia Polytechnic Institute and State University, Blacksburg, VA, 1979.

11. Kurland, R. M.; and Thomasson, J. F.: Radiation Testing of Composite Materials, In Situ vs. Ex Situ Effects. NASA CR 3475, 1981.
12. Composite Data for Spacecraft. General Electric Company, 1982, 80SDS4214, Air Force Contract F33615-79C-5114.
13. Fornes, R. E.; Memory, J. D.; and Naranong, N.: "Effect of 1.33 Mev γ Radiation and 0.5 Mev Electrons on the Mechanical Properties of Graphite Fiber Reinforced Composites," J. Applied Polym Sci. 26: 2061-2067 (1981).
14. Santos, B.; and Sykes, G. F.; Radiation Effects on Polysulfone Films. 13th National SAMPE Tech. Conf., Mt. Pocono, PA, Oct. 1981.
15. Marayama, T.: Dynamic Mechanical Analysis of Polymeric Material. Materials Science Monographs 1, Elsevier Scientific Publishing Co., NY, 1968.
16. Bowles, D. E.; Post, D.; Herakovich, C. T.; and Tenney, D. R.: Moire Interferometry for Thermal Expansion of Composites. Experimental Mechanics, Vol. 21, No. 12, Dec. 1981.
17. Short, J. S.: Thermal Expansion of Graphite/Epoxy Composite Laminates Between 116 and 366 K. M. S. Thesis Virginia Polytechnic Institute and State University, Blacksburg, VA, July 1982.
18. Camahort, J. L.; Rennhack, E. H.; and Coons, W. C.: Effects of Thermal Cycling Environment on Graphite/Epoxy Composites. ASTM STP 602, 1976.
19. Eselun, S. A.; Neubert, H. D.; and Wolff, E. G.: Microcracking Effects on Dimensional Stability. 24th National SAMPE Conf., San Francisco, CA, May 8-10, 1979.
20. Buczek, M. B.: Finite Element Analysis of Crack Growth in Composites. M. S. Thesis, Virginia Polytechnic Institute and State University, Blacksburg, VA, August 1982.
21. Bowles, D. E.: The Effect of Microcracking on the Thermal Expansion of Gr/Ep. Large Space Systems Technology - 1981, NASA CP-2215, Nov. 1981.
22. Tompkins, S. S.; and Williams, S. L.: Effects of Thermal Cycling on Residual Mechanical Properties of C6000/PMR-15 Graphite Polyimide. AIAA 23rd SDM Conference, New Orleans, LA, May 1982.
23. Sullivan, M. R.: Maypole (Hoop/Column) Concept Development Program. Large Space Systems Technology - 1981, NASA CP-2215, Nov. 1981.
24. Winn, Robert A.: Thermal Control Coatings: ML-101 Five-Year Space Exposure. AFML-TR-78-99, July 1978.
25. Harris, F. W.; and Seymour, R. B.: Structure-Solubility Relationships in Polymers, Academic Press, NY, 1977.
26. St. Clair, A. K. and Taylor, L. T.: Incorporation of Metal Related Materials into Electrically Neutral Polymers. J. Macromol. Sci-Chem. A16(11), 1981.

Acknowledgement

Several NASA researchers participated in developing the data in this paper. The authors gratefully acknowledge the contributions of the following: Mr. W. S. Slomp; Dr. S. S. Tompkins; Dr. E. R. Long and Ms. B. Santos.

Table 1. Summary of important space environmental parameters and materials uncertainty associated with each parameter.

ENVIRONMENTAL PARAMETER	NOMINAL RANGE OF PARAMETER	REASON FOR INTEREST IN PARAMETER
VACUUM	PRESSURE $10^{-11} - 10^{-19}$ Pa	VACUUM OUTGASSING RESULTS IN LOSS OF MOISTURE AND SOLVENTS RESULTING IN DIMENSIONAL AND MECHANICAL PROPERTY CHANGES
ULTRAVIOLET	WAVELENGTH 0.1 - 0.4 μ m INTENSITY 1.4 Kw/m ²	DEGRADATION OF COATINGS
PROTONS	ENERGY 0.1 - 4.0 MeV FLUX 10^8 p ⁺ /cm ² - sec	DEGRADATION OF COATINGS AND SURFACE PLIES OF COMPOSITES
ELECTRONS	ENERGY 0.1 - 4.0 MeV FLUX 10^8 e ⁻ /cm ² - sec	SURFACE AND BULK DAMAGE; SPACECRAFT CHARGING
TEMPERATURE CYCLING	MATERIAL TEMPERATURE 80 K TO 420 K	MICROCRACKING, THERMAL WARPING, DETERIORATION OF CRITICAL SURFACES

Table 2. Thermal control coating requirements.

	<u>COMPOSITE STRUCTURE</u> GEO	<u>MANNED HABITAT</u> LEO
OPTICAL PROPERTIES	α/ϵ - SELECTIBLE WITH $\epsilon \leq 0.3$	α/ϵ - SELECTIBLE WITH $\epsilon \geq 0.8$
TEMPERATURE	-100 ^o TO +80 ^o C	-100 ^o TO +40 ^o C
ENVIRONMENT	UV, e ⁻ , p ⁺ , VAC, ΔT	UV, VAC, ΔT
ELECT. CONDUCTIVITY	$\leq 10^{-8}$ (OHM ⁻¹ - CM ⁻¹)	$10^{-8} - 10^{-17}$ (OHM ⁻¹ - CM ⁻¹)
LIFETIME	10 TO 20 YEARS	10 YEARS

Table 3. Current thermal control coatings.

RADIATOR COATINGS (LOW ABSORPTANCE, HIGH EMITTANCE)

<u>COATING</u>	<u>PERFORMANCE</u>
S-13 GLO (ZnO/RTV-602)	RTV 602 DISCONTINUED, NEW SILICONE BINDER FOR QUALIFICATION
ZOT (Zn ₂ TiO ₄ /SILICATE)	ABSORBS MOISTURE, HARD TO CLEAN
Z-93 (ZnO/SILICATE)	ABSORBS MOISTURE, EASILY CONTAMINATED
Al OR Ag/TEFLON	LARGE AREA APPLICATION DIFFICULT

STRUCTURAL COATINGS (LOW ABSORPTANCE, LOW EMITTANCE)

NO QUALIFIED PAINT-TYPE COATINGS AVAILABLE

Table 4. Coatings in LDEF flight experiment.

TYPE	COMPOSITION	SUBSTRATE	USE
PAINTS	ZnO/SILICONE (S-13GLO)	Al, Gr/Ep	CONTAMINATION (C) ADHERENCE (A)
	Zn ₂ TiO ₄ /SILICONE (ZOT)	Al, Gr/Ep	C, A
	TiO ₂ /POLYURETHANE (A-276)	Al, Gr/Ep	C, A
	Cr ₂ O ₃ /SILICONE (EXP.)	Al, Gr/Ep	LAB-CALIB-ILC), C, A
	CHEM-GLAZE BLACK	Al, Gr/Ep	LC, C, A
ANODIZE	CHROMIC ACID - a/e ~ 1.5	Al	LC, C, A
	CHROMIC ACID - a/e ~ 0.5	Al	LC, C, A
SECOND-SURFACE MIRRORS	QUARTZ/SILVER (Ag) (GSR)	Al	LC, C, A
	TEFLON/Ag	Al, Gr/Ep	LC, C, A
	DIFFUSE TEFLON/Ag	Al, Gr/Ep	LC, C, A
VACUUM DEPOSITED	Al/Al		C
	Al/QUARTZ		C
	Al/QUARTZ		C
	Ni/QUARTZ		C
POLISHED	NICKEL		C
	PLATINUM		C

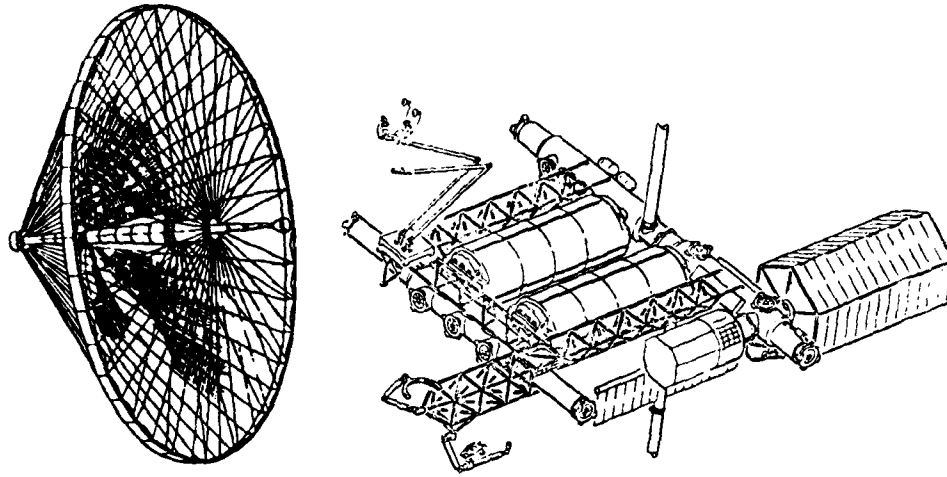


Figure 1. Focal missions for advanced technology developments.

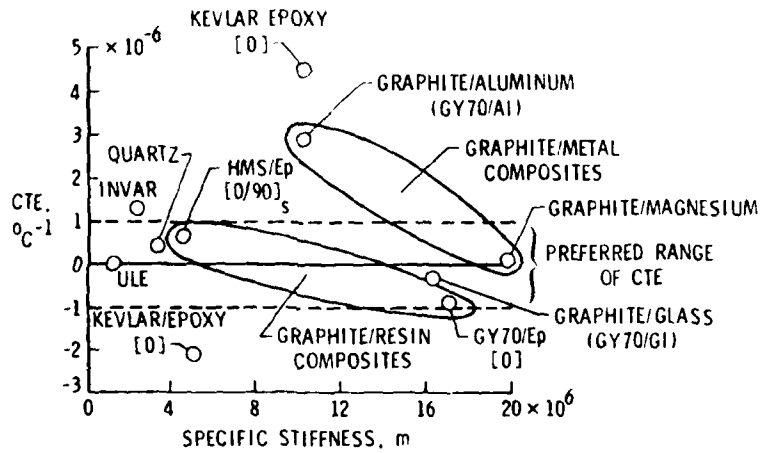


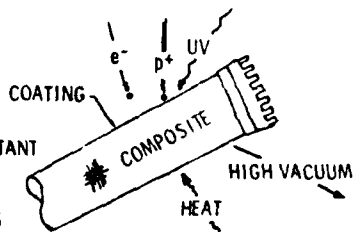
Figure 2. High stiffness low thermal expansion space materials.

DESIRED PROPERTIES OF THERMAL CONTROL COATINGS

- TAILORED OPTICAL PROPERTIES
- AMENABLE TO LARGE AREA COVERAGE
- UV AND PARTICULATE RADIATION RESISTANT
- NONDEGRADING OR RENEWABLE OPTICAL PROPERTIES
- MINIMUM SENSIVITY TO CONTAMINANTS

DESIRED COMPOSITE PROPERTIES

- HIGH STIFFNESS
- HIGH SPECIFIC STRENGTH
- THERMAL FATIGUE RESISTANCE
- GOOD DIMENSIONAL STABILITY
- HIGH IMPACT RESISTANCE
- LOW MINIMUM GAGE
- RADIATION/UV RESISTANCE
- LOW RATE OF OUTGASSING



ENVIRONMENTAL CONCERNS

- COMPOSITE PROPERTY CHANGES
- OPTICAL CHANGES IN COATINGS
- SPALLING OF COATINGS
- SPACECRAFT CHARGING
- IS OF LOW MOL. WT. SPECIES
- LOSS OF SHEAR STRENGTH IN ADHESIVE BOND JOINTS
- THERMAL FATIGUE DAMAGE

Figure 3. Durability concerns for structural composites in space.

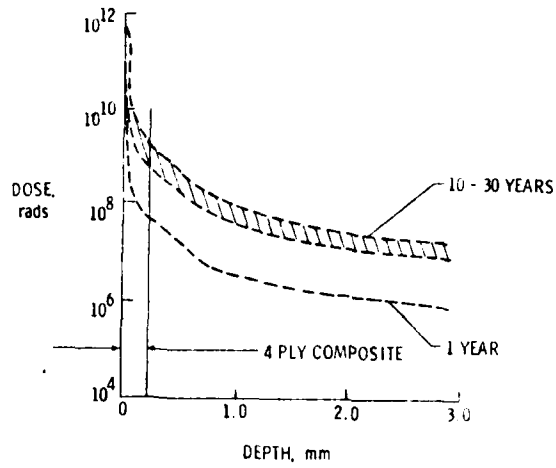


Figure 4. Combined electron-proton dose-depth profile for a polymer in GEO.

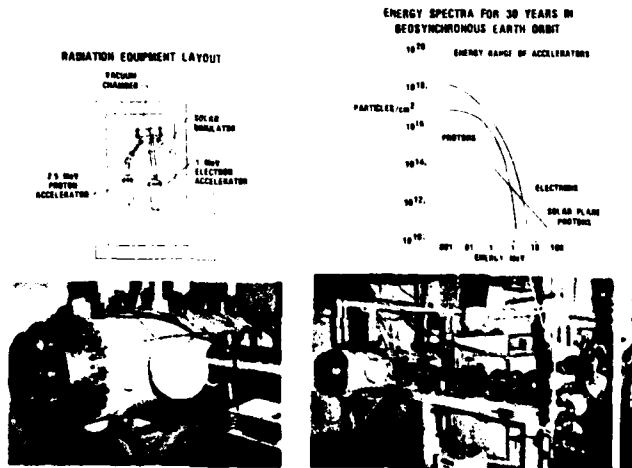


Figure 5. Space materials durability laboratory.

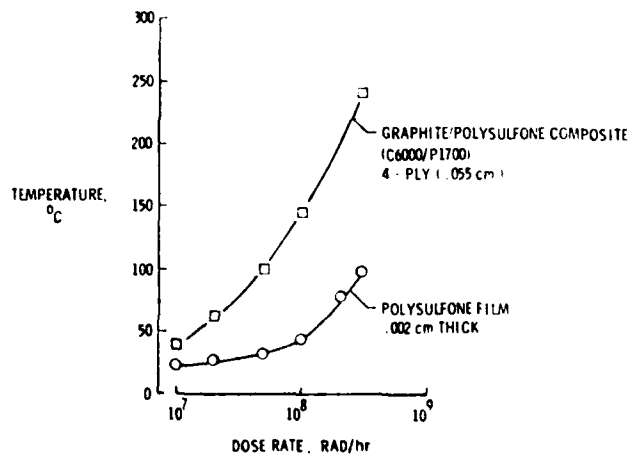


Figure 6. Effect of electron dose rate on the temperature of polysulfone film and composites.

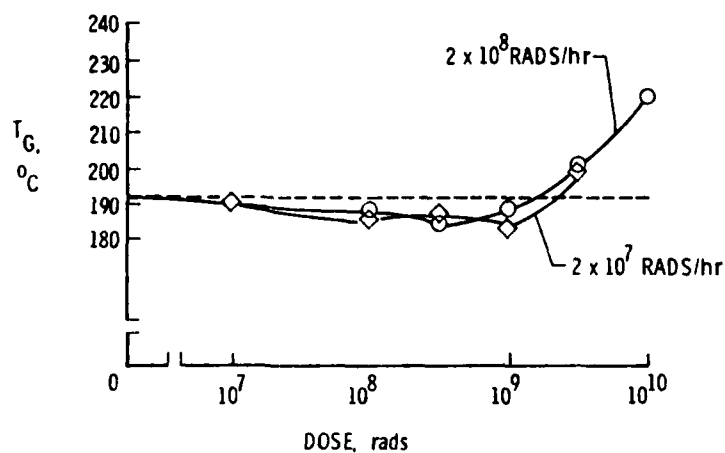


Figure 7. Dose rate effects on the glass transition temperature of electron irradiated polysulfone film.

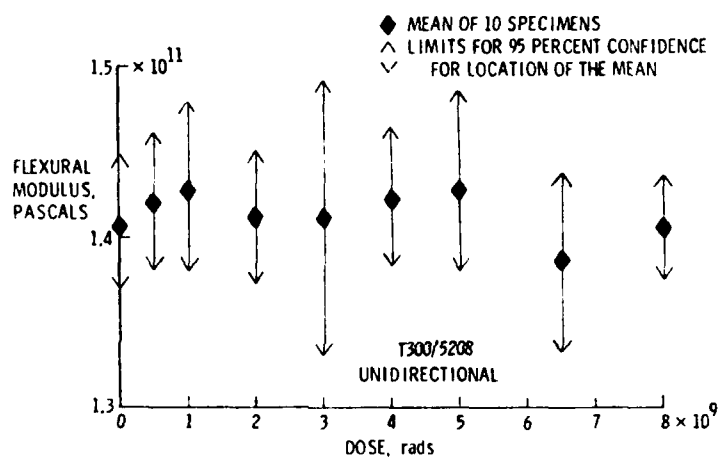


Figure 8. Flexural modulus of irradiated unidirectional T300/5208 graphite/epoxy composites.

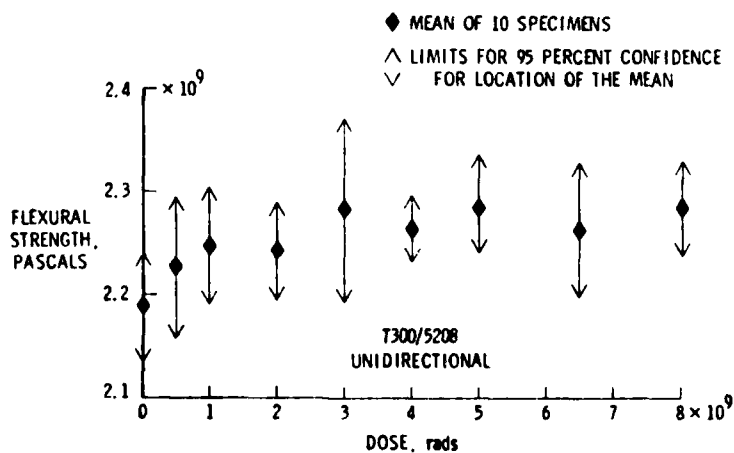


Figure 9. Flexural strength of irradiated unidirectional T300/5208 graphite/epoxy composites.

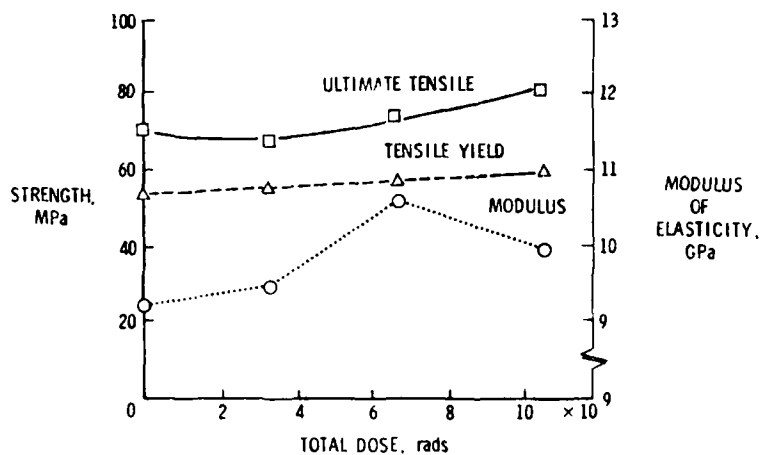


Figure 10. Tensile properties of irradiated C6000/P1700 graphite/polysulfone composites.

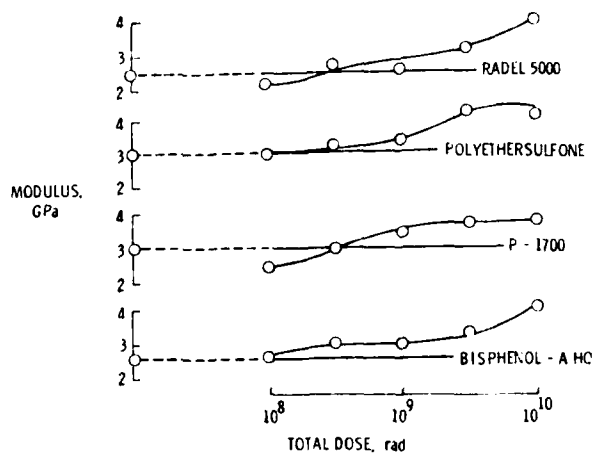


Figure 11. Modulus of irradiated polysulfone films.

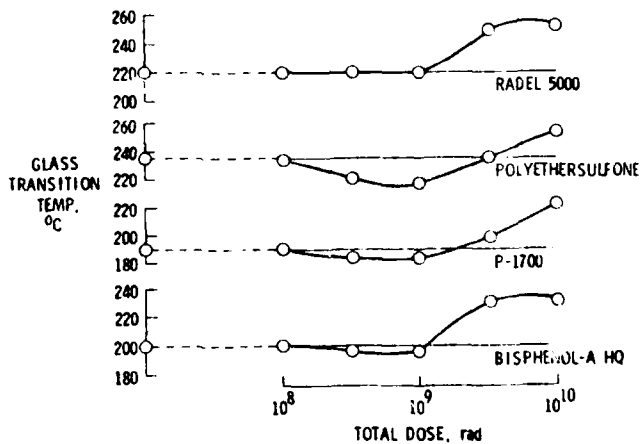


Figure 12. Glass transition temperature of irradiated polysulfone films.

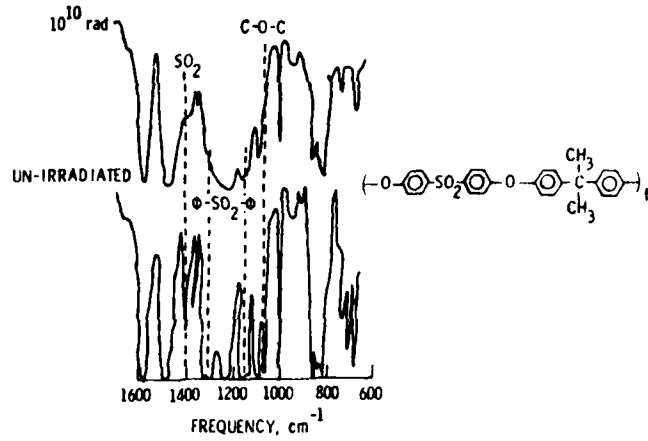


Figure 13. Effect of electron radiation on the infrared spectra of polyethersulfone.

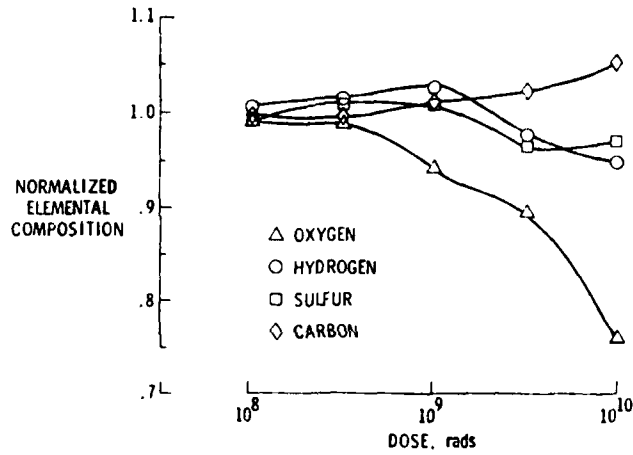


Figure 14. Normalized elemental composition of irradiated P-1700.

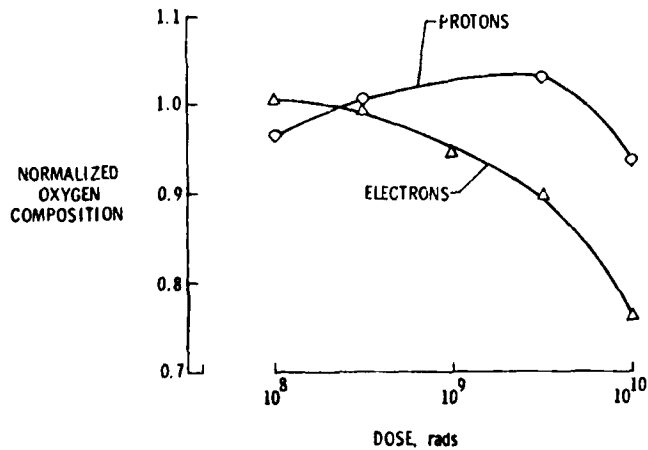


Figure 15. Effect of type of radiation on the normalized oxygen content of P-1700.

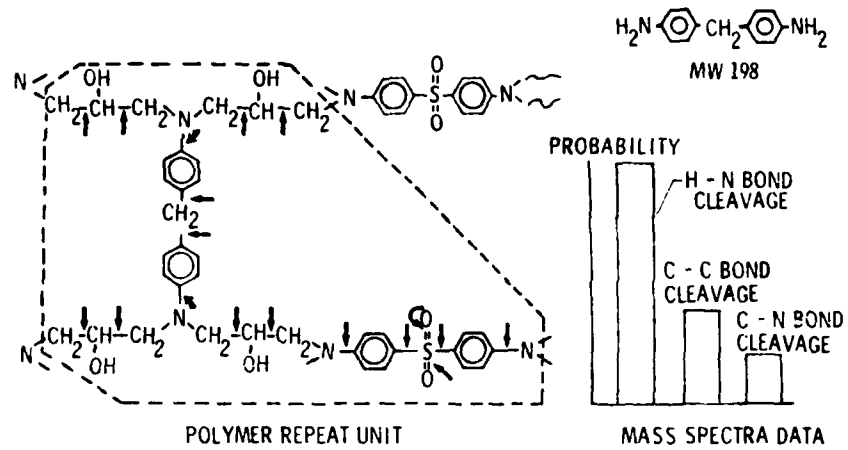


Figure 16. Prediction of most probable locations of chain scission due to electron radiation.

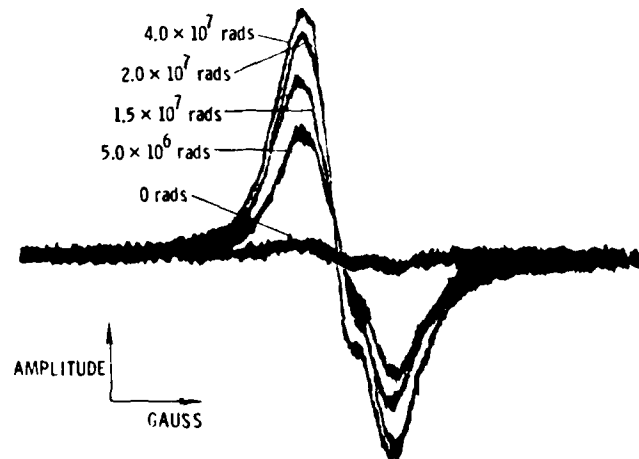


Figure 17. Typical electron spin resonance spectra of electron irradiated epoxy.

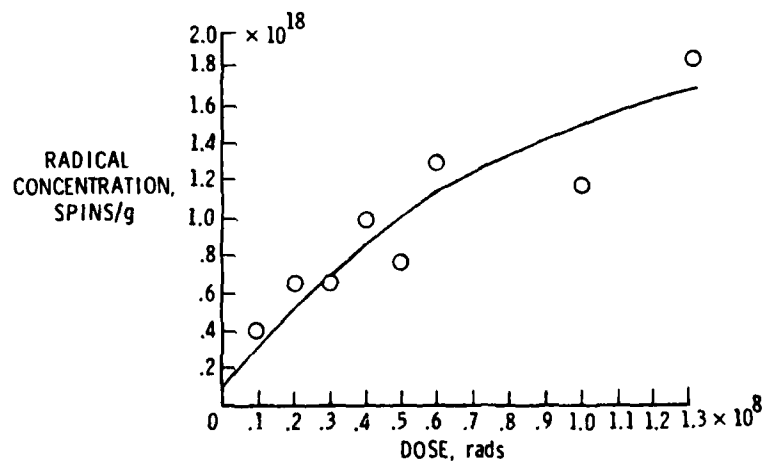


Figure 18. Initial radical concentrations in epoxy resin after electron irradiation.

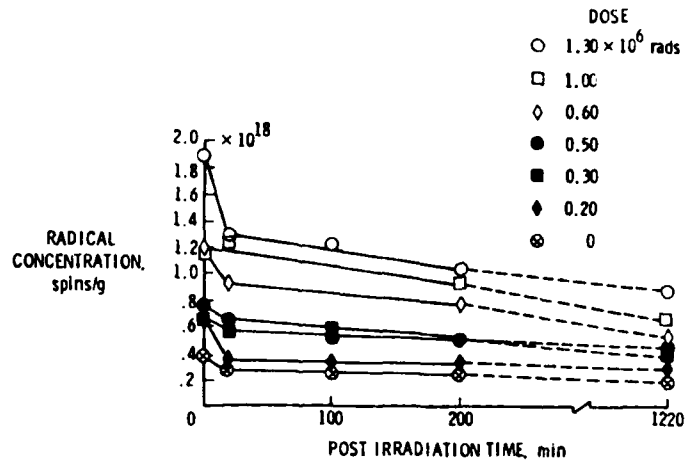


Figure 19. Room-temperature decay of electron radiation generated radicals in epoxy resin.

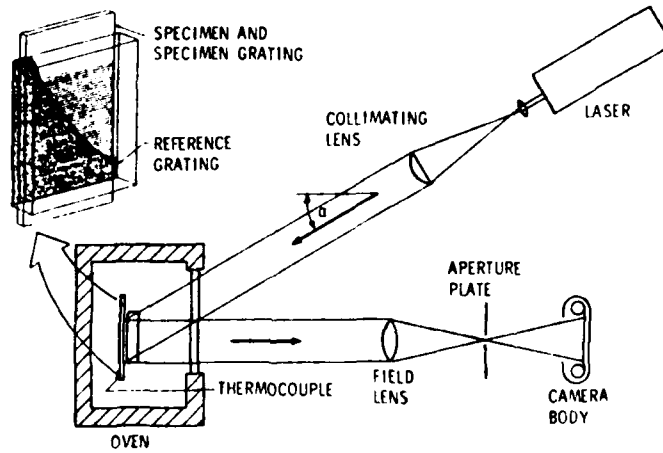


Figure 20. Schematic diagram of moiré interferometer.

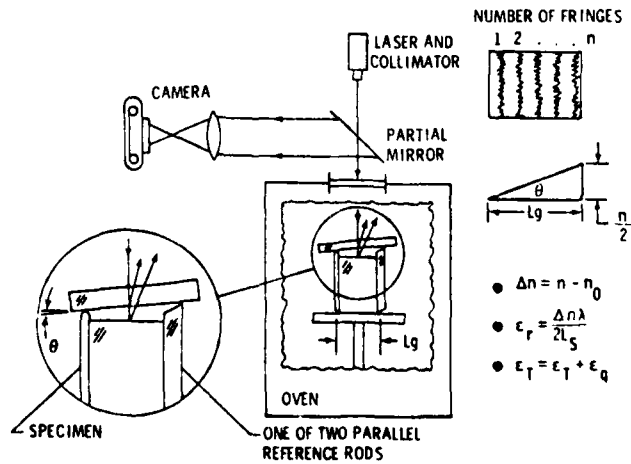


Figure 21. Schematic diagram of Priest interferometer.

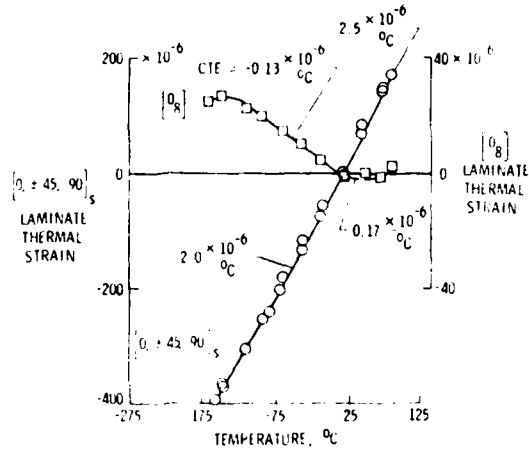


Figure 22. Thermal expansion of unidirectional and quasi-isotropic T300/5208 graphite/epoxy.

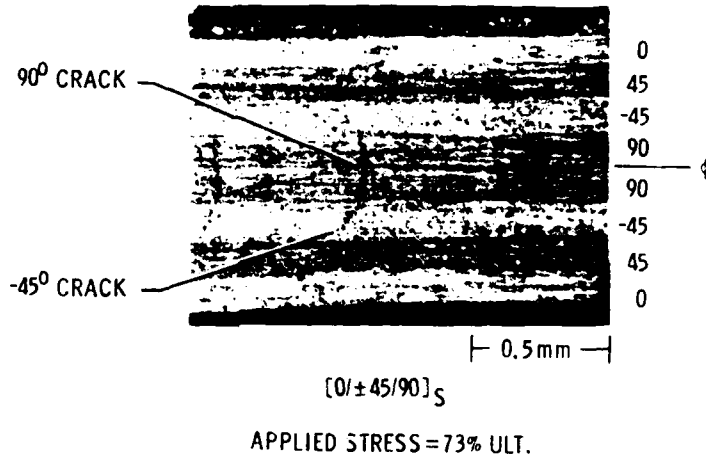


Figure 23. Microcrack pattern viewed along the edge of a mechanically loaded specimen.

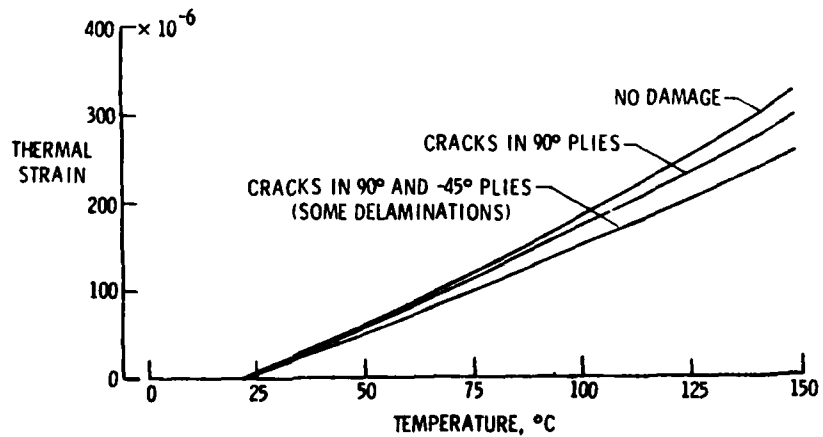


Figure 24. Effect of microcracks on the thermal expansion of quasi-isotropic T300/5208 graphite/epoxy.

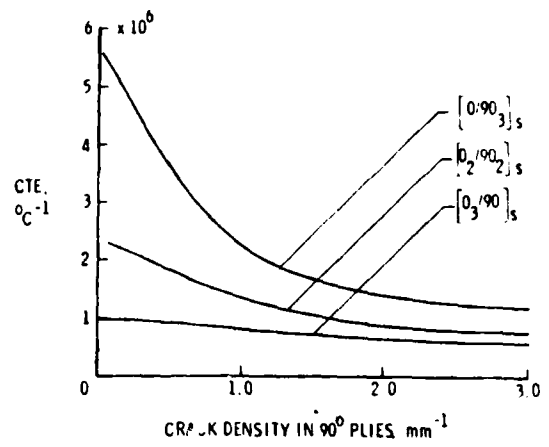


Figure 25. Effect of microcracks on the CTE of $[0_m/90_n]_s$ laminates.

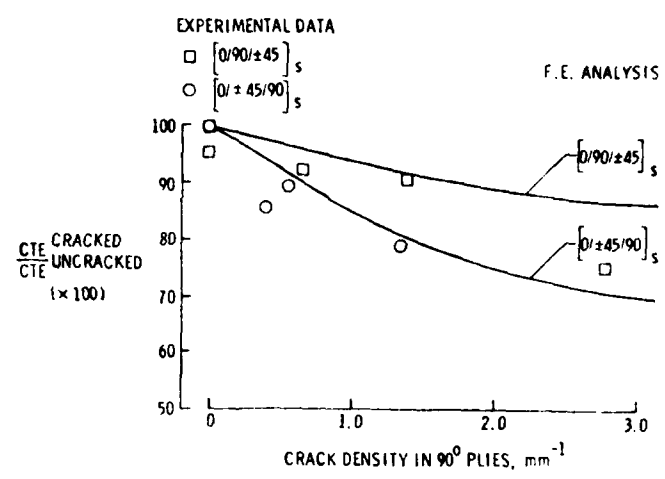


Figure 26. Comparison of predicted and measured changes in CTE with crack density.

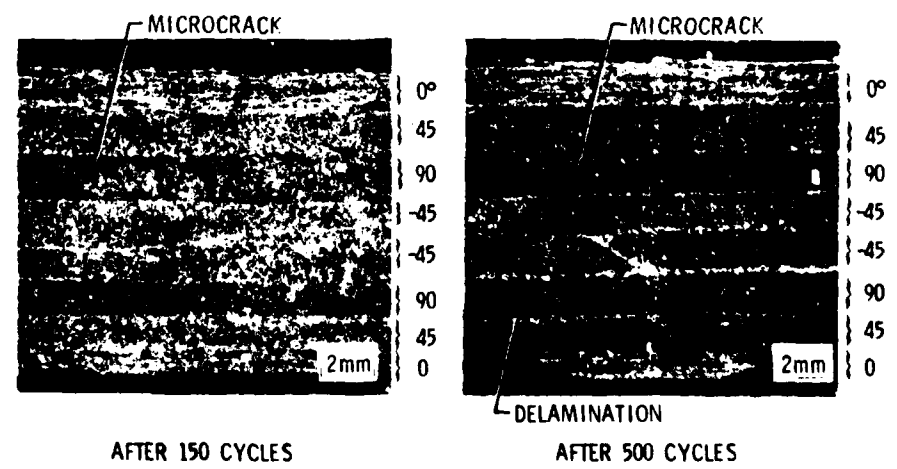


Figure 27. Typical microcracking pattern induced in graphite/polyimide by thermal cycling between -156°C and 316°C .

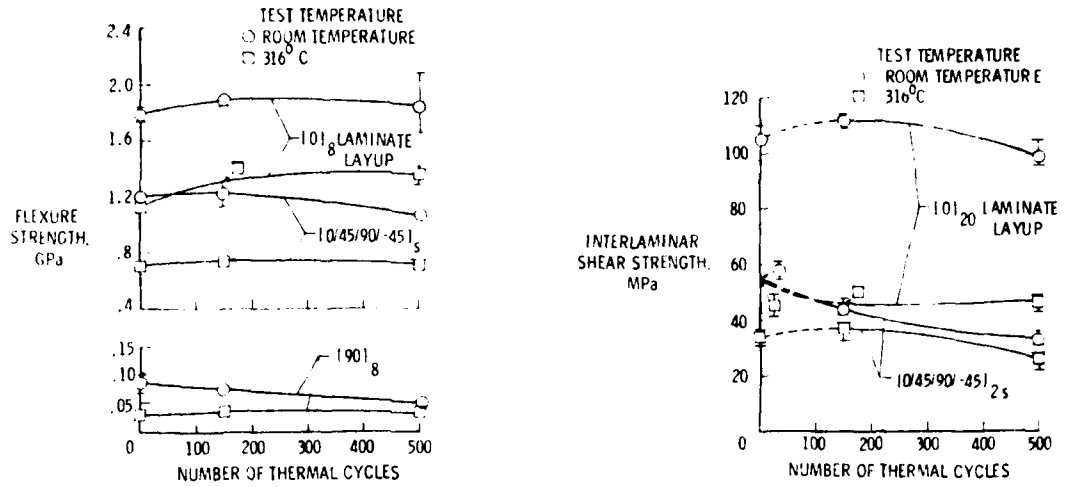


Figure 28. Effect of thermal cycling on residual mechanical properties of graphite/polyimide.

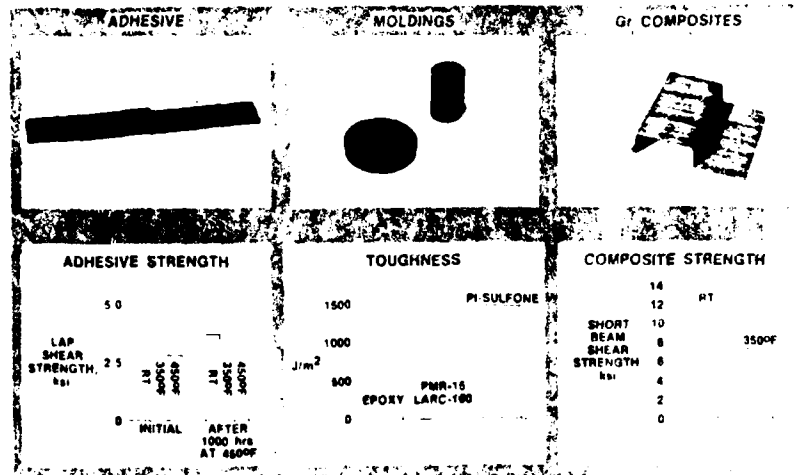


Figure 29. Development of a high toughness matrix resin.

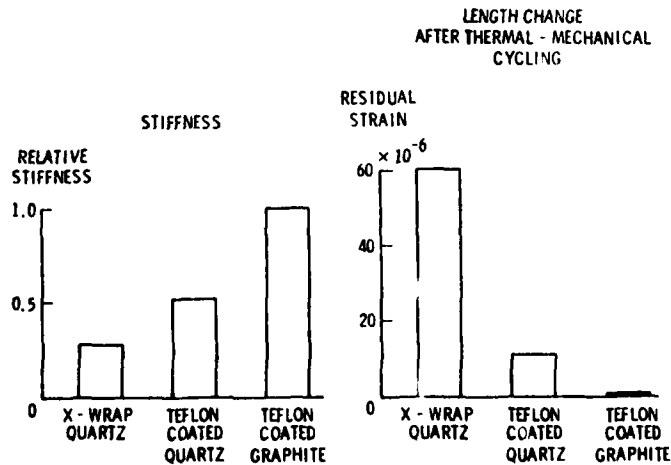


Figure 30. Improved antenna tension cable materials.

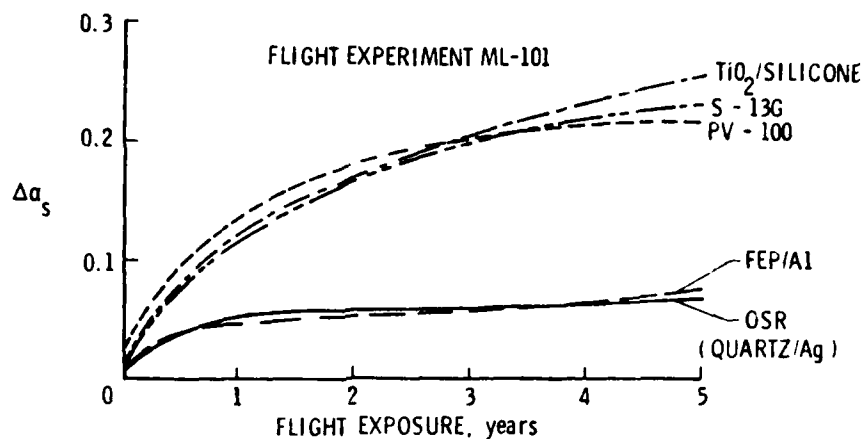


Figure 31. Degradation of thermal control coatings.

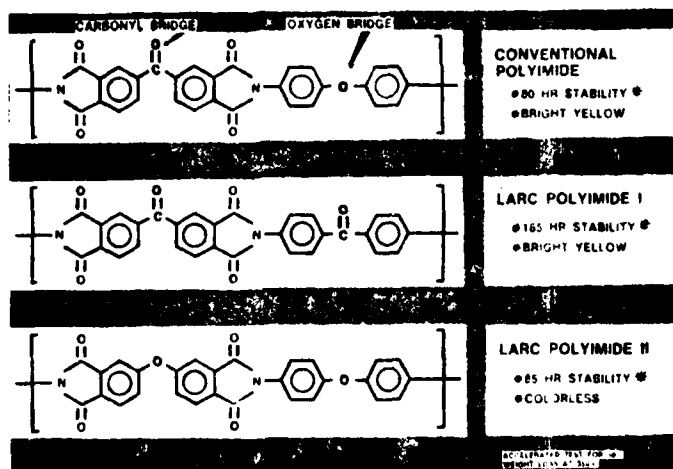


Figure 32. Development of a clear polyimide for space applications.

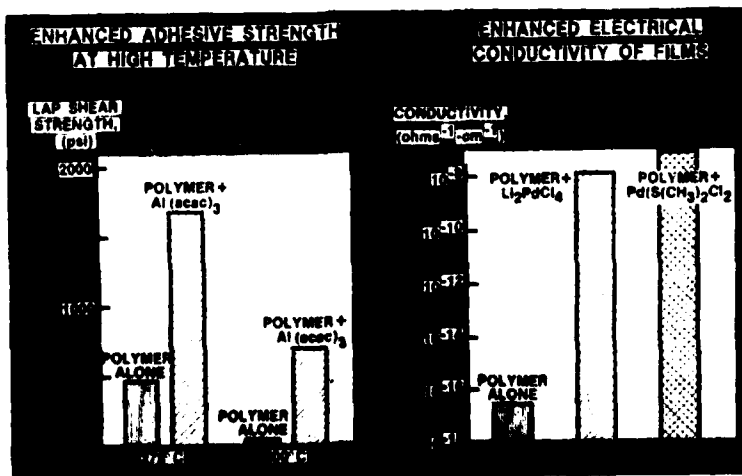


Figure 33. Development of high conductivity polymer films.

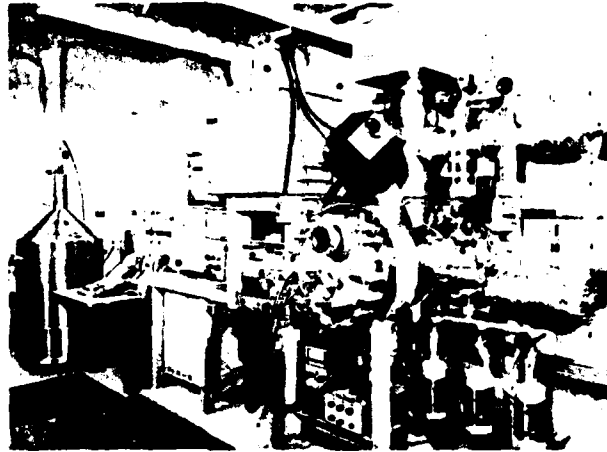


Figure 34. Equipment for evaluation of thermal control coatings.

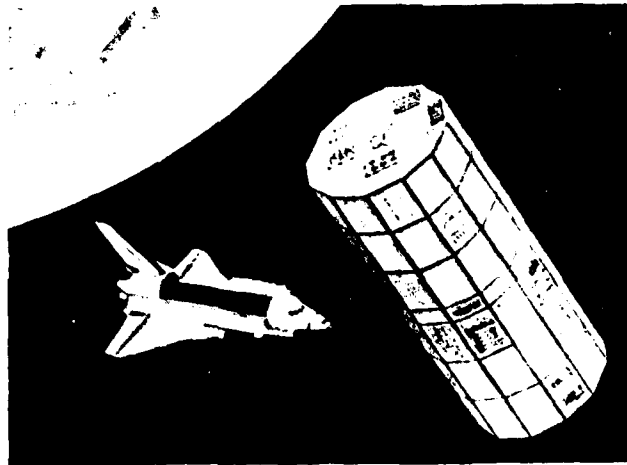


Figure 35. LDEF flight experiment.

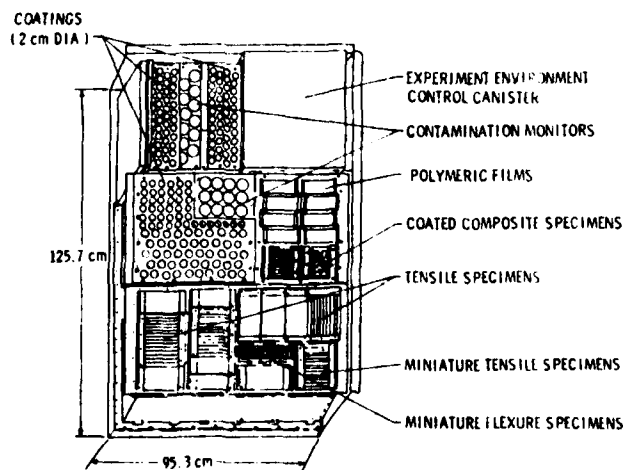


Figure 36. Layout of NASA-Langley's thermal control coatings experiment on LDEF.

SIMULATION DE L'ENVIRONNEMENT ACOUSTIQUE D'UN LANCEUR AU
DECOLLAGES ET DE SES EFFETS VIBRATOIRES SUR LES STRUCTURES

par Dr. Alain BOURGINE

Office National d'Etudes et de Recherches Aéropatiales (ONERA)
92320 Châtillon (France)

RESUME

Au cours du lancement et du vol transsonique des fusées, des vibrations intenses, dans une bande de fréquences large, sont transmises à la charge utile et aux équipements sensibles du lanceur. Les essais de simulation en laboratoire ont pour but de reproduire fidèlement ces phénomènes dangereux. Mais les moyens d'essais classiques (chambres acoustiques réverbérantes) ne permettent pas en général de reproduire correctement les excitations du vol réel.

La méthode proposée ici consiste à imposer la réponse vibratoire de la paroi du lanceur, par exemple sur la coiffe abritant le satellite. (Les caractéristiques de cette réponse sont obtenues par un calcul prévisionnel préalable). On utilise pour cela un petit nombre d'excitateurs électrodynamiques agissant à la paroi ; les N forces aléatoires appliquées sont obtenues par synthèse numérique sur ordinateur. La simulation correcte est réalisée lorsque les réponses vibratoires mesurées en N points ont des caractéristiques statistiques voisines de celles du vol. Le champ acoustique dans la cavité et les vibrations transmises à la charge utile sont alors également très proches des conditions de vol. Des exemples d'application à des structures réelles, en particulier sur la coiffe de la fusée Ariane, sont présentés.

SIMULATION OF THE ACOUSTIC ENVIRONMENT OF A LAUNCHER
AND OF THE NOISE-INDUCED VIBRATIONS ON ITS STRUCTURES

SUMMARY

During the launching and transonic flight of a launcher, high level and wide-band frequency vibrations are transmitted to the payload and equipments. Preliminary simulation tests are planned to reproduce these dangerous phenomena. But, generally speaking, classical test facilities (reverberant acoustic chambers) do not provide simultaneously the true space and time distribution of the flight pressure fluctuations.

The method described in the paper consists in forcing the vibratory response of the launcher wall, for instance at the shroud which shelters the satellite. (Statistical characteristics of this response are known by a previous analytical prediction). Forced vibrations are produced by using a few number of electrodynamic shakers acting on the wall ; the N random forces are simultaneously synthesized on a digital computer. The proper simulation is realized when measured responses at N points exhibit spectral distributions and overall RMS levels very close to the predicted flight values. Then, the noise level inside the shroud and the vibrations transmitted to the payload are also very close to the flight conditions. Some examples of applications to realistic structures, as the shroud of the Ariane vehicle, are presented.

I - ORIGINE DU PROBLEME

Le bruit émis par les jets des moteurs d'une fusée au décollage est considéré en général comme la principale source de vibrations des structures et des matériels embarqués. En raison du niveau élevé et de la large bande de fréquences de cette émission acoustique, les vibrations aléatoires induites peuvent atteindre une intensité considérable susceptible d'entraîner des ruptures locales sur certaines parties exposées de la structure, ou des défaillances graves dans le fonctionnement de certains équipements. On est donc amené, classiquement, à entreprendre des essais partiels en environnement acoustique ou sur pots vibrants, en vue de contrôler, en laboratoire, à un stade suffisamment précoce du développement du projet, que les vibrations du vol ne risquent pas de faire échouer la mission.

Mais la définition des moyens d'essais de simulation vraiment représentatifs, ainsi que celle des spécifications précises de l'expérimentation, soulèvent des difficultés importantes, pour plusieurs raisons principales :

I.1 - Connaissance de l'environnement de vol. L'exemple du lanceur ARIANE

L'environnement de vol réel est lui-même en général mal connu : l'expérience acquise dans des lancements antérieurs et les études de base sur le bruit des jets permettent souvent d'obtenir des estimations "raisonnables" du niveau global et du spectre des fréquences émises, mais la géométrie du champ acoustique dans lequel est plongé le lanceur est en général ignorée. En outre, l'ensemble de ces caractéristiques du bruit évolue de bas en haut du lanceur, ainsi qu'en fonction de l'altitude de celui-ci par rapport au pas de tir. Enfin, dans la phase initiale du lancement, les interactions des jets des moteurs avec le sol et les structures du pas de tir peuvent influencer fortement ces caractéristiques, surtout à l'arrière de la fusée.

Une étude assez détaillée de ces différents facteurs a été faite par l'ONERA, dans le cadre du développement du lanceur ARIANE [1], à l'aide de deux maquettes à échelle réduite (1/20 et 1/10) de la fusée et de son pas de tir. Ces maquettes étaient munies de moteurs utilisant les mêmes propergols (N_2O_4 - UDMH) et présentant les mêmes caractéristiques de fonctionnement (rapport de mélange, pression de combustion et rapport de détente) que les moteurs réels. La bonne concordance des résultats obtenus aux échelles 1/20 et 1/10 (fig.1) a permis d'extrapoler à l'échelle grandeur les niveaux et spectres obtenus, avant de pouvoir contrôler cette prévision lors des premiers lancements du véhicule réel. La figure 2 fournit des indications globales sur les niveaux de bruit, en fonction de l'altitude, à l'arrière, au milieu et à l'avant du lanceur. Le spectre du bruit maximum, au cours du décollage, à la paroi de la coiffe protégeant la charge utile est présenté figure 3. Enfin, une étude plus fine des caractéristiques spatiales du champ acoustique mesurée à la paroi du lanceur a permis de localiser les principales sources acoustiques dans certaines régions des carneaux, ces régions se déplaçant légèrement en fonction de l'altitude (fig.4). Il résulte de ces caractéristiques qu'il est possible de construire un modèle simplifié de l'environnement acoustique du lanceur : en particulier, au voisinage de la coiffe abritant le satellite, donc à une distance assez grande des sources principales, le bruit se propage par ondes planes de direction et d'intensité connues avec une précision suffisante pour effectuer des calculs prévisionnels de la réponse vibratoire de la coiffe.

Si l'on revient maintenant à la définition d'un essai de simulation en laboratoire, sur cette partie de la structure, la reproduction du phénomène réel exigerait manifestement un tunnel à ondes propres de grandes dimensions, avec un niveau d'excitation considérable (145dB). A défaut d'une telle installation, des tests effectués dans une chambre acoustique réverbérante demeurent possibles, mais ne simulent pas le phénomène réel du vol. Dans tous les cas, le niveau de bruit à créer au voisinage de spécimens très volumineux est voisin des limites des possibilités des installations existantes. La construction de nouveaux moyens d'essai de ce type, de très grandes dimensions et de performances plus élevées - donc d'un coût également très élevé - ne peut donc dans ce cas être justifiée par une meilleure garantie de représentativité des essais de simulation.

Pour terminer avec les problèmes liés à la connaissance de l'environnement de vol, il convient encore d'attirer l'attention sur les dangers de certains raisonnements simples, non appuyés sur l'expérience, pour l'estimation des niveaux de bruit intéressant les structures du lanceur.

Une illustration de ce point est fournie ici à nouveau par l'expérimentation au 1/20 de la fusée Ariane dans la version où le premier étage du lanceur est muni de deux propulseurs à poudre latéraux destinés à fournir un complément de poussée au décollage (fig.5). Les résultats obtenus montrent, comme il fallait s'y attendre, une augmentation sensible du bruit, variable en fonction de l'altitude, sur la partie arrière du premier étage (+3 à +10dB). Par contre, la croissance observée au niveau de la coiffe est extrêmement modérée (environ +1dB) au maximum au cours du lancement ; dans les premières secondes suivant le décollage, le niveau baisse même dans cette région d'une manière très notable (-11 à -12dB), ce qui est encore plus surprenant au premier abord. Mais, l'analyse de la localisation des sources acoustiques indique alors clairement que la mise à feu des propulseurs d'appoint à basse altitude modifie la position moyenne de ces sources dans les carneaux (elles s'éloignent de l'axe du lanceur) et les étale dans l'espace, ce qui en diminue donc l'influence à grande distance. Les interactions des jets entre eux et avec les infrastructures du pas de tir, qui sont probablement à l'origine de cet effet global, jouent donc ici un rôle très favorable qui permet de ne pas pénaliser les tests de qualification des structures et équipements au voisinage de la charge utile.

Ces quelques indications sommaires permettent de caractériser une première difficulté dans l'exécution de simulations vibratoires réalistes : l'environnement de vol réel doit être connu avec une marge d'incertitude aussi faible que possible. De ce point de vue, des essais acoustiques préalables, à échelle réduite, fournissent un cadrage tout à fait indispensable du problème réel.

I.2 - Réponse vibratoire de l'enveloppe du lanceur

On admet en général que l'énergie vibratoire transmise à la charge utile au cours du lancement provient principalement de l'environnement acoustique de la coiffe. La réponse vibratoire de la paroi de celle-ci est donc à l'origine du bruit qui règne dans la cavité interne et qui, à son tour, est une source d'excitations des sous-structures qu'elle contient. Or, le comportement vibratoire de l'enveloppe de la coiffe, sous l'influence du bruit au décollage, n'est pas seulement déterminé par la distribution spectrale de l'énergie de l'excitation (ou son intensité en chaque point, dans une bande de fréquences donnée) mais également par la distribution de la phase de cette excitation en tous les points de la paroi. Dans le cas du lanceur Ariane, nous avons montré ci-dessus que l'excitation de la coiffe pouvait être schématisée en première approximation par une propagation d'énergie acoustique par ondes planes : sur une génératrice de la coiffe, on a alors une évolution linéaire de la phase avec la distance, pour une fréquence d'excitation donnée. Comme cette propriété joue un rôle important dans la réponse vibratoire de l'enveloppe, il est alors certain qu'un essai en simulation qui ne respecterait pas la condition supplémentaire sur la phase de l'excitation ne serait pas représentatif : un test réalisé en champ diffus, par exemple, ne conviendrait pas. D'un point de vue pratique, toutefois, un essai de ce type pourrait être acceptable si l'on était en mesure de prouver qu'il présente une "sévérité au moins équivalente" pour le spécimen. En général, rien ne permet de garantir ce résultat, et la difficulté du problème reste entière.

Il ressort de cette rapide analyse des conditions à satisfaire pour exécuter une simulation réaliste des phénomènes acoustiques et vibratoires rencontrés au cours du lancement d'une fusée, que le seul dispositif expérimental convenable semble être... le lancement réel lui-même. C'est pour essayer de sortir de cette impasse que l'ONERA a proposé une approche nouvelle des essais de simulation conduisant à une méthode expérimentale originale dont le développement est en cours.

II - UNE APPROCHE NOUVELLE DU PROBLEME : PREVISION ET SIMULATION

Dans les essais de simulation "classiques", on s'efforce de reproduire en laboratoire un environnement acoustique, supposé bien connu, autour du spécimen destiné à subir des vibrations. Dans le cas d'une coiffe, par exemple, la mise en vibration des parois s'accompagne d'une transmission d'énergie à l'intérieur, vers la charge utile, par voie solide et par voie acoustique. Si l'on regarde maintenant le problème uniquement sous l'aspect de cette transmission d'énergie, on peut considérer que "l'entrée" du système est un champ de vibrations de l'enveloppe, en ignorant provisoirement la manière dont ce champ vibratoire a pu être créé par des sollicitations externes. En particulier, si l'on se donne les caractéristiques de ces vibrations de la paroi en un nombre N fini, de points, on pourra toujours imaginer une configuration d'excitation externe, également concentrée en N points, reproduisant exactement ces mêmes caractéristiques vibratoires à la paroi aux points d'observation choisis. Selon ce raisonnement, on est donc conduit à substituer au champ acoustique externe, agissant en tout point de la structure, une répartition discrète de N forces aléatoires dont les effets vibratoires, également observés en N points, doivent être identiques à ce qu'ils seraient sous l'action au champ acoustique. Ceci nous conduit à une approche différente du problème de la simulation, qui est maintenant fondée sur la reproduction d'un champ de vibrations à la paroi de la structure, et non plus sur la reproduction difficile d'un environnement acoustique complexe.

Cette conception soulève toutefois deux questions préalables :

- a) le champ vibratoire pariétal de la structure n'étant pas connu a priori, comment le considérer comme une "donnée" de l'essai de simulation ?
- b) en supposant qu'il soit possible de reproduire fidèlement les vibrations de la paroi en N points discrets, n'est-il pas nécessaire d'augmenter N indéfiniment pour obtenir une simulation réaliste ?

II.1 - Prévision et simulation

La réponse à la première question fait appel à un calcul de prévision des caractéristiques statistiques des vibrations de la paroi de la structure, selon la méthode dynamique statistique [2], employée avec succès à l'ONERA depuis quelques années. Ce calcul repose sur la formule fondamentale :

$$(1) \quad S_{YY}(M_0, f) = \iint_{\Sigma} \varphi_{M_0}(M_i, M_j, f) S_{PP}(M_i, M_j, f) dM_i dM_j$$

dans laquelle $S_{YY}(M_0, f)$ est la densité spectrale de puissance de la réponse-accelération au point M_0 , à la fréquence f ; $S_{PP}(M_i, M_j, f)$ est la densité spectrale croisée de la pression acoustique à la paroi Σ , aux points M_i et M_j : ce terme complexe est connu à partir d'expérimentations sur maquettes à échelle réduite telles qu'elles ont été présentées au paragraphe I. $\varphi_{M_0}(M_i, M_j, f)$ est un terme de transfert structural, désigné par "fonction de Green généralisée", qui peut être obtenu expérimentalement de façon simple sur le spécimen réel ; dM_i et dM_j sont les éléments d'aire associés aux points courants M_i et M_j .

Pour l'application de cette formule, on substitue en fait aux quantités figurant dans les deux membres, leurs moyennes fréquentielles sur une bande étroite, ce qui permet d'intégrer les effets des nombreux modes de vibration qui interviennent dans le comportement "haute fréquence" de la structure. A titre d'illustration, on présente figure 6 les résultats comparés d'une prévision et d'un essai en chambre acoustique réverbérante en deux points d'un spécimen de coiffe en matériau composite. Ces résultats sont relatifs aux densités spectrales de puissance des réponses, présentées avec des échelles linéaires. Ils peuvent être considérés comme satisfaisants compte tenu de la connaissance approchée de l'environnement acoustique du spécimen.

La méthode de prévision ayant été validée par de nombreux tests dans des configurations variées de structures et d'environnements acoustiques, il devient donc possible d'envisager de prendre les valeurs prévisionnelles comme des données en vue d'un essai de simulation par excitations discrètes. Les phases de prévision et de simulation deviennent donc étroitement liées, et se trouvent d'ailleurs pratiquement

imbriquées lors de l'essai global sur le spécimen réel.

II.2 - Simulation par excitations discrètes en quelques points

Pour aboutir à un système de simulation de dimension raisonnable, mais néanmoins réaliste quant au phénomène à simuler, on doit espérer que la répartition des niveaux RMS et des spectres vibratoires sur la structure est relativement "homogène" ou encore, à défaut, au moins "localement homogène" c'est-à-dire que l'on pourra découper la structure en quelques zones, chacune d'elles étant de construction assez homogène elle-même pour pouvoir estimer que les réponses vibratoires en deux points appartenant à la même zone présenteront des caractéristiques de réponse voisines. L'expérience montre que ceci est assez bien vérifié sur des structures réelles, le choix des différentes zones à considérer étant d'abord du domaine de "l'art de l'ingénieur". A titre d'illustration, on présente figure 7 la répartition spatiale des niveaux de vibrations efficaces à la paroi de la coiffe en matériau composite, de construction hétérogène - c'est-à-dire d'épaisseur variable suivant une génératrice - lors d'un essai témoin exécuté dans une chambre acoustique réverbérante. Les niveaux efficaces sont reportés linéairement, suivant une unité arbitraire, sur une génératrice et sur un parallèle de la structure, pour une bande spectrale d'excitation d'environ 3000Hz. On peut observer que ces niveaux globaux varient très peu d'un point à un autre. La distribution spectrale de ces réponses vibratoires, visible sur la figure 8 pour 4 accéléromètres répartis sur une génératrice de la coiffe, présente également la même allure générale, sauf en quelques points de fréquence particuliers. Dans une telle configuration structurale, on peut donc escompter obtenir des résultats convenables avec un nombre très restreint de points d'excitation et de mesure. Nous montrerons au paragraphe 4 que ceci est en effet bien vérifié avec $N = 2$. Pour des cas plus complexes rencontrés en pratique, il semble très raisonnable de réaliser des simulations avec 4 ou 6 points d'excitation seulement, au maximum.

III - PRINCIPE DE LA SIMULATION PAR EXCITATIONS DISCRETES

III.1 - Relation entrée-sortie en régime aléatoire

On considère maintenant la structure mécanique réelle comme un système vibratoire linéaire discret (figure 9) possédant N entrées (point d'application de N forces aléatoires) et N sorties ou points d'observation de la réponse vibratoire. En désignant par H la matrice de transfert ($N \times N$) de ce système, la matrice spectrale des paramètres de réponse $\phi_{ss}(f)$ est liée à la matrice spectrale des forces d'excitation $\phi_{ee}(f)$ par la relation classique :

$$(2) \quad \phi_{ss} = H^* \phi_{ee} H^T$$

où $(*)$ désigne la quantité conjuguée et (T) la transposition. Les matrices spectrales ϕ_{ss} et ϕ_{ee} étant de la forme (pour $N = 2$) :

$$(3) \quad \phi_{ss} = \begin{vmatrix} \phi_{s_{11}} & \phi_{s_{12}} \\ \phi_{s_{21}} & \phi_{s_{22}} \end{vmatrix} ; \quad \phi_{ee} = \begin{vmatrix} \phi_{e_{11}} & \phi_{e_{12}} \\ \phi_{e_{21}} & \phi_{e_{22}} \end{vmatrix}$$

les termes diagonaux représentent les densités spectrales de puissance de chaque paramètre de sortie (ou d'entrée), et les termes diagonaux les densités spectrales croisées entre ces paramètres, avec les propriétés :

$$(4) \quad \phi_{ii} \geq 0 \quad \forall i \quad | \phi_{ij} |^2 \leq \phi_{ii} \phi_{jj} \quad (i \neq j)$$

Dans le problème posé ici, la matrice spectrale de sortie ϕ_{ss} est supposée connue (elle résulte d'un calcul prévisionnel comme indiqué ci-dessus en II). Il s'agit donc, à partir de la connaissance de la matrice de transfert H (identification de la structure), d'obtenir la matrice spectrale des forces d'excitation ϕ_{ee} (par inversion de la relation (2)), puis d'élaborer des signaux aléatoires (e_1, e_2, \dots, e_N) dont ϕ_{ee} est la matrice spectrale (synthèse aléatoire). Ces différentes opérations d'analyse spectrale, d'identification et de synthèse aléatoire sont confiées à un ordinateur rapide selon le schéma général présenté figure 10.

Dans tout ce qui suit, on conviendra de désigner par H la matrice de transfert globale de l'ensemble "amplificateurs de puissance - excitateurs électrodynamiques - structure - capteurs et amplificateurs de sortie".

III.2 - Fonctions principales du dispositif de pilotage

Les opérations principales du dispositif de pilotage sont les suivantes :

- Au cours de l'opération d'analyse, les signaux de sortie S_1, S_2, \dots, S_N sont dirigés sur des convertisseurs analogiques numériques, puis dans l'ordinateur qui exécute l'analyse spectrale rapide en des points de fréquence discrets $f_k = k \Delta f$. On obtient donc une suite de matrices spectrales discrètes ϕ_{ss}^k . Des précautions particulières au niveau du traitement des signaux numérisés permettent d'assurer que chaque terme des matrices ϕ_{ss}^k représente la moyenne, sur la bande élémentaire Δf , du spectre réel continu.
- Au cours de l'opération de synthèse, on part d'une suite de matrices spectrales ϕ_{ee}^k , également connues pour des valeurs discrètes de la fréquence, et on élabore des signaux analogiques d'excitation de spectre de fréquence continu. Cette opération est complexe : elle utilise une triangularisation de ϕ_{ee}^k , suivie d'un calcul de transformées de Fourier inverses des termes de la matrice triangulaire, puis d'une combinaison de ces échantillons temporels après pondération par une fenêtre temporelle convenable.

Le détail des caractéristiques de ce traitement est fourni dans [3].

c) L'opération d'identification utilise la relation (2) sous une forme particulière, qui s'écrit :

$$(2bis) \quad \Psi_s(f) = \mathcal{H}(f) \cdot \Psi_e(f)$$

où Ψ_s et Ψ_e représentent maintenant les vecteurs à N^2 composantes constitués à partir des matrices spectrales ϕ_{ss} et ϕ_{ee} . Pour $N = 2$, on a :

$$(5) \quad \Psi_s(f) = \begin{pmatrix} \phi_{s_{11}} \\ \phi_{s_{12}} \\ \phi_{s_{21}} \\ \phi_{s_{22}} \end{pmatrix}$$

et une forme analogue pour $\Psi_e(f)$. La matrice \mathcal{H} est alors du type ($N = 2$) :

$$(6) \quad \mathcal{H} = \begin{pmatrix} |H_{11}|^2 & H_{11} H_{12}^* & H_{11}^* H_{12} & |H_{12}|^2 \\ H_{11} H_{21}^* & H_{11} H_{22}^* & H_{12} H_{21}^* & H_{12} H_{22}^* \\ H_{21}^* H_{11} & H_{21}^* H_{12} & H_{22}^* H_{11} & H_{22}^* H_{12} \\ |H_{21}|^2 & H_{21} H_{22}^* & H_{22} H_{21}^* & |H_{22}|^2 \end{pmatrix}$$

Dans l'opération d'identification, c'est cette matrice globale, constituée de produits de fonctions de transfert élémentaires, qui est déterminée par voie expérimentale. Pour cela, le système de pilotage synthétise successivement quatre configurations de quatre signaux d'excitation indépendants (soit 4 vecteurs Ψ_e indépendants) qui sont envoyés sur la structure. L'analyse spectrale des réponses conduit ensuite aux 4 vecteurs réponse Ψ_s à partir desquels on peut déduire les termes de $\mathcal{H}(f)$ (ou, plus exactement, les moyennes de ces termes sur chaque bande de fréquence élémentaire). Des précautions particulières doivent être observées au cours de cette opération d'identification de \mathcal{H} : en effet, si on se donne $\Psi_s(f)$ (ou la matrice spectrale ϕ_{ss} qui est équivalente), on peut inverser l'expression (2bis) pour déterminer $\Psi_e(f)$, puis la matrice spectrale d'entrée $\phi_{ee}(f)$, qui doit vérifier la propriété (4) pour être physiquement admissible (c'est-à-dire permettre de synthétiser effectivement des signaux de commande). Le conditionnement correct de la matrice "expérimentale" \mathcal{H} constitue une des difficultés principales du problème de la simulation par excitations discrètes.

III.3 - Configuration du système de pilotage

La configuration actuelle du système informatique est présentée figure 11. Elle repose sur l'association d'un mini-ordinateur HP 21 MXE et d'un calculateur parallèle FPS - AP 120B. A l'entrée, 4 voies de filtres anti-repliement, d'échantillonneurs-blocurs et de convertisseurs analogiques numériques permettent l'acquisition des données à cadence élevée. Le traitement complet des signaux est effectué en temps réel dans une bande spectrale de 5000Hz sur chaque voie. En sortie, 4 voies de conditionnement et de conversion numérique-analogique sont disponibles pour délivrer les signaux d'excitation désirés.

Actuellement, le système est opérationnel dans une version probatoire à deux voies. L'extension en cours portera sa capacité à quatre voies.

IV - APPLICATION A DES PROBLEMES DE SIMULATION SUR STRUCTURES REELLES - TRANSPARENCE ACOUSTIQUE

Dans une version prototype monovoie, le système de pilotage a pu être testé en 1979 sur la coiffe de la fusée Ariane [4]. Malgré les insuffisances de cette première réalisation, des résultats très encourageants avaient pu être obtenus dans la tentative de reproduction des spectres et des niveaux vibratoires à la paroi de la coiffe, pour la phase de décollage du lanceur. Une estimation raisonnable du bruit dans la cavité avait alors été obtenue par mesure directe à l'intérieur de la coiffe au cours de l'essai de simulation.

Depuis lors, un certain nombre de progrès ont pu être accomplis dans le traitement et la synthèse des signaux, aboutissant à un nouveau système à deux voies dont les performances ont pu être testées sur une structure-coiffe en matériau composite.

Pour cela, la structure a d'abord été placée dans une chambre acoustique réverbérante et soumise au bruit ambiant. Des mesures nombreuses d'accélération pariétales et de bruit interne ont été exécutées. Comme il a été indiqué précédemment, les résultats de l'analyse spectrale des vibrations de la paroi ont pu être confrontés d'une manière satisfaisante aux prévisions effectuées par ailleurs.

Les essais de pilotage destinés à simuler cet essai acoustique de référence ont ensuite été entrepris. Deux points de mesure utilisés lors de l'essai acoustique ont été à nouveau choisis pour y reproduire les mêmes spectres vibratoires. On a pu observer expérimentalement que les résultats les meilleurs étaient obtenus, en simulation, lorsque les points d'application de chaque force étaient relativement proches des points de mesure choisis. Bien entendu, ces points étaient assez distants entre eux pour assurer une répartition plus homogène des vibrations engendrées par le système.

AD-A129 847

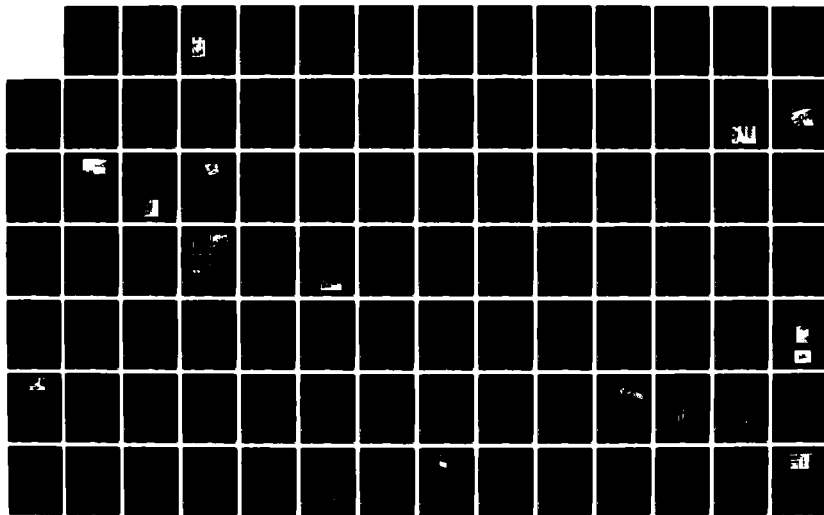
ENVIRONMENTAL EFFECTS ON MATERIALS FOR SPACE
APPLICATIONS(U) ADVISORY GROUP FOR AEROSPACE RESEARCH
AND DEVELOPMENT NEUILLY-SUR-SEINE (FRANCE) MAR 83
AGARD-CP-327

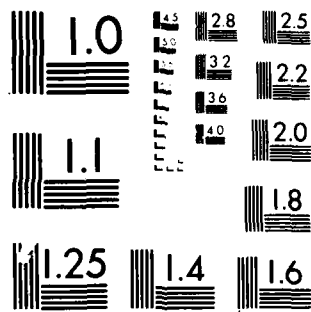
2/3

NL

UNCLASSIFIED

F/G 22/2





MICROCOPY RESOLUTION TEST CHART
NATIONAL BUREAU OF STANDARDS 1963-A

On présente ici les résultats obtenus dans deux configurations d'implantation des excitateurs et des points de mesure. Dans chaque cas, on désigne par "consignes" les spectres vibratoires à reproduire. Les figures 12 et 15 montrent que le système de simulation impose les forces convenables pour reproduire les spectres de sortie désirés. En d'autres points du spécimen, comme il est normal, la simulation à deux voies ne reproduit pas exactement la même distribution spectrale de réponse que l'essai acoustique de référence (figures 13 et 16). Seule l'allure générale du spectre est conservée.

On présente enfin, figures 14 et 17 l'analyse spectrale du bruit dans la cavité, c'est-à-dire le niveau d'excitation affectant la charge utile ou les équipements. On peut observer que la simulation reproduit encore assez correctement le phénomène réel. Ces résultats seraient toutefois certainement améliorés avec le dispositif de pilotage à 4 voies dont le développement est en cours. Considérée globalement, la méthode proposée semble donc adaptée à la résolution pratique du problème de la simulation et de l'étude de la transparence acoustique des structures spatiales.

V - CONCLUSION

Les difficultés rencontrées pour reproduire, en laboratoire, en vue de sa simulation, l'environnement acoustique complexe d'un lanceur spatial au décollage, a conduit à rechercher une approche originale du problème. A l'aide d'un petit nombre de forces ponctuelles agissant à la paroi, et dont les signaux sont obtenus par synthèse numérique sur ordinateur, on s'efforce de reproduire assez fidèlement la distribution spectrale de la réponse au champ acoustique externe réel. Un calcul prévisionnel préalable est nécessaire pour obtenir, en quelques points, une estimation correcte de ce spectre vibratoire. L'expérience montre qu'avec un nombre limité de points d'excitation et de mesure, une simulation réaliste des vibrations et du bruit transmis peut être obtenue.

REFERENCES

- [1] - A. Bourguine et J.J. Dordain
"Review of acoustic studies carried out at ONERA in the field of space vehicles"
16ème Symposium Spatial Européen - Stresa (Italia) 3-5 Juillet 1979
JBIS, Volume 34 n° 2, February 1981
- [2] - A. Bourguine
"A statistical approach to the vibratory dynamics of structures"
Publication ONERA n° 149 (1973)
English translation ESRO TT 98 (1974)
- [3] - G. Le Deunff, Ph. Fréchon et A. Bourguine
"Un système de pilotage multivoies en régime aléatoire" (à paraître)
- [4] - A. Bourguine et P. Monteil
"Simulation, using computer piloted point excitations, of vibrations induced on a structure by an acoustic environment"
12th Congress of ICAS, Munich 12-17 October 1980

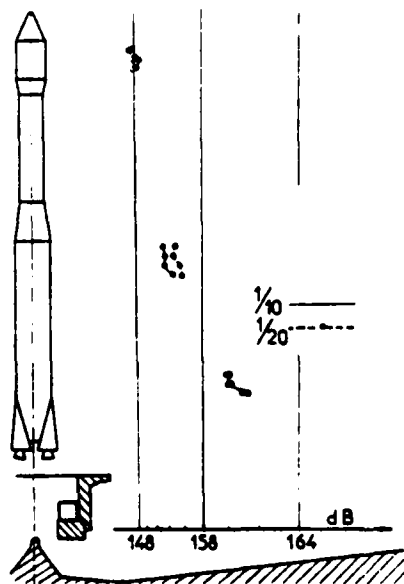


Fig. 1 - Ambiance acoustique Ariane au décollage. Comparaison d'essais sur maquettes au 1/20 et au 1/10 (Altitude 8,40 m).

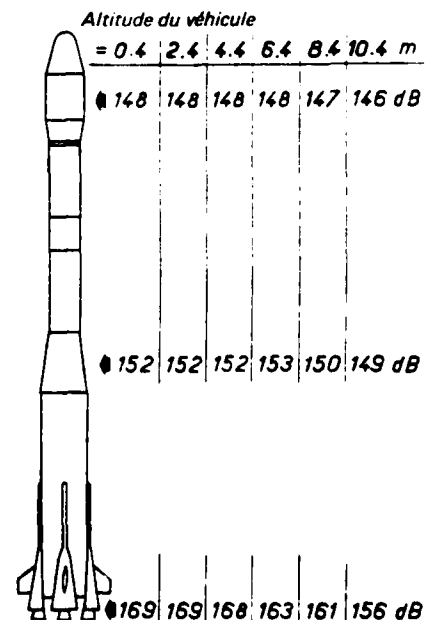


Fig. 2 - Niveau global du bruit sur le lanceur Ariane en cours de décollage.

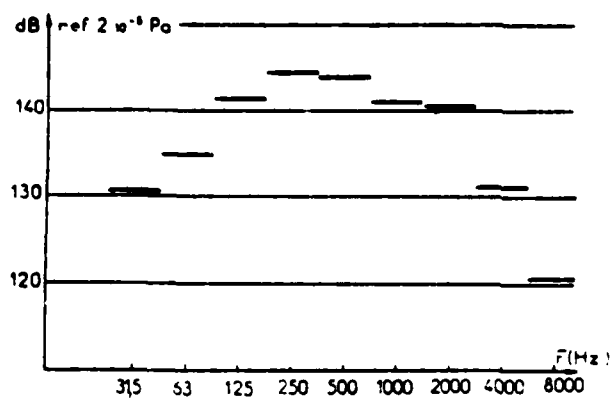


Fig. 3 - Répartition spectrale du bruit (par octaves) au niveau de la coiffe Ariane au décollage (échelle 1).

Fig. 4 - Localisation apparente des sources acoustiques principales au cours du décollage.

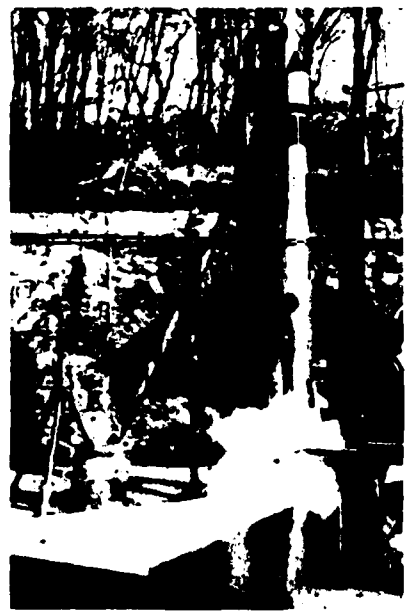
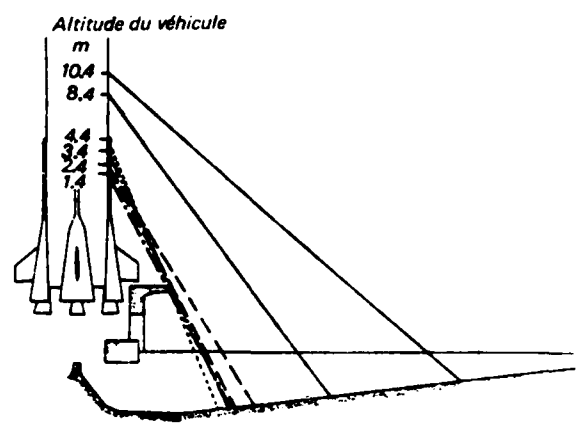
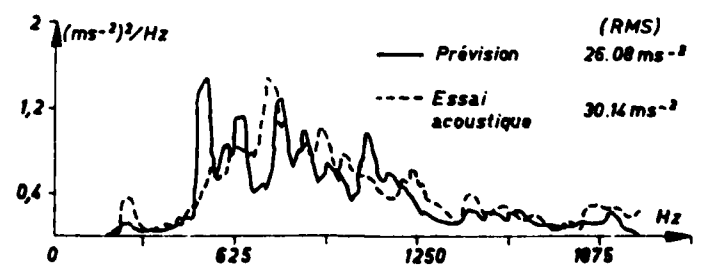
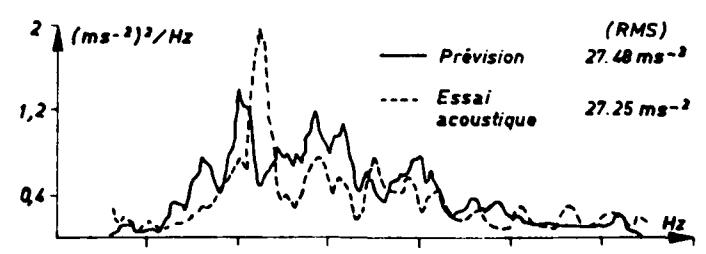


Fig. 6 - Densité spectrale de puissance de la réponse d'une coiffe en matériau composite soumise à un champ acoustique réverbérant. Comparaison prévision-expérience en deux points.

Fig. 5 - Essai sur maquette au 1/20 du lanceur Ariane 3 au décollage.



Récapitulation
mesures accélérométri-
ques

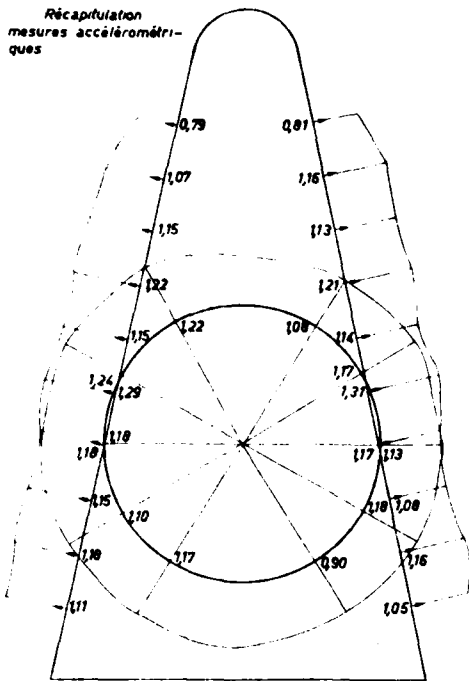
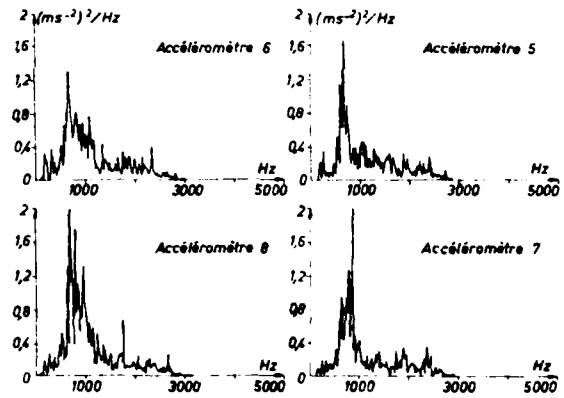


Fig. 7 - Niveau efficace de réponse de la coiffe en chambre acoustique réverbérante.

Fig. 8 - Distribution spectrale des réponses en différents points, sous excitation acoustique réverbérante.



Mesure du bruit à l'intérieur de la coiffe

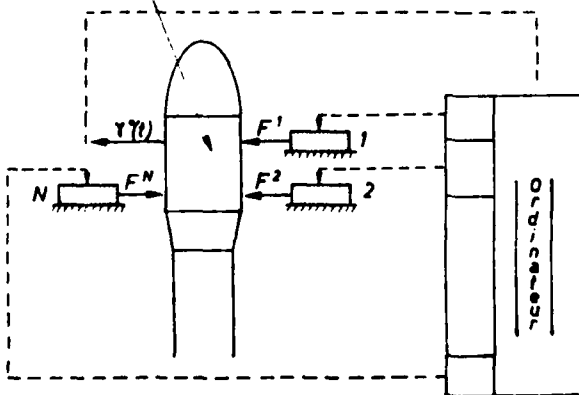


Fig. 9 - Principe de la simulation par excitations discrètes pilotées par ordinateur.

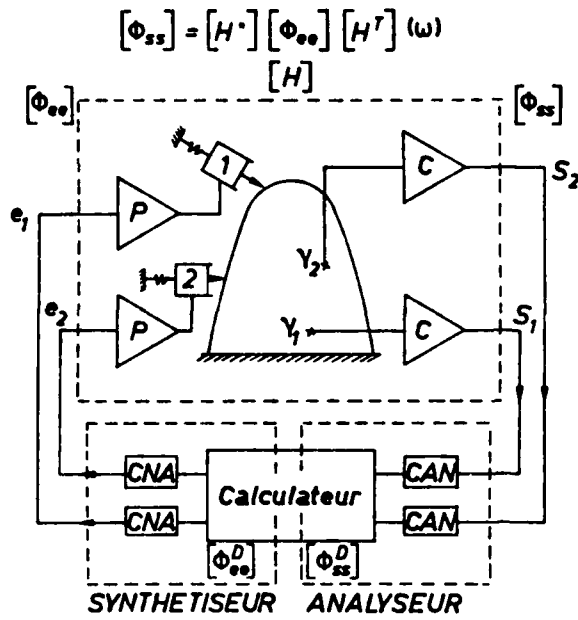


Fig. 10 - Principales fonctions du système de pilotage.

Fig. 11 - Configuration du système informatique.

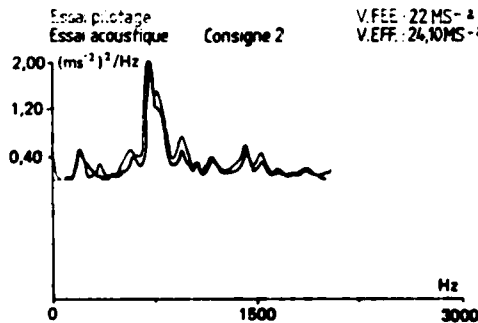
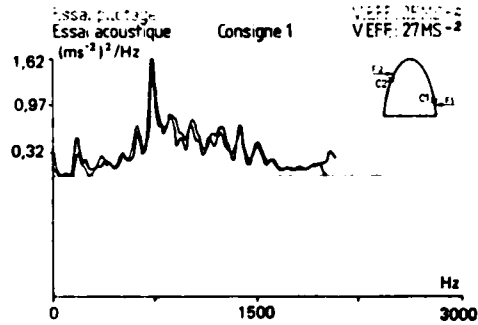
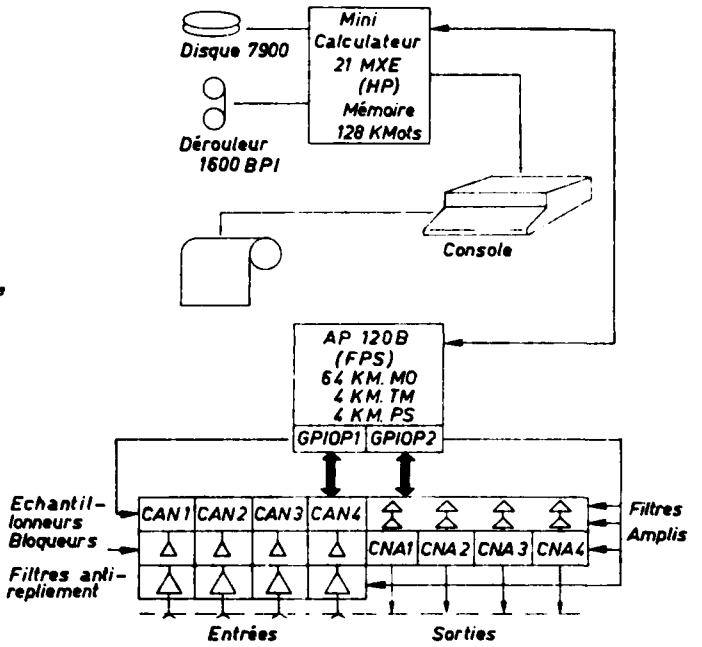


Fig. 12 - Essai sur coiffe - Accélérations pariétales.

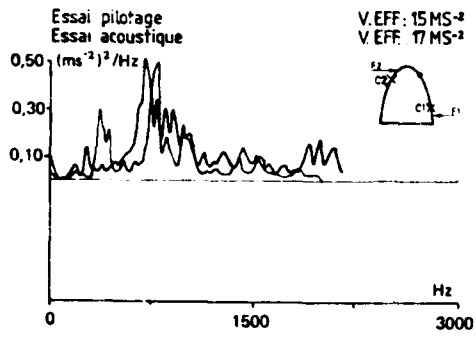


Fig. 13 - Essai sur coiffe - Accélérations pariétales.

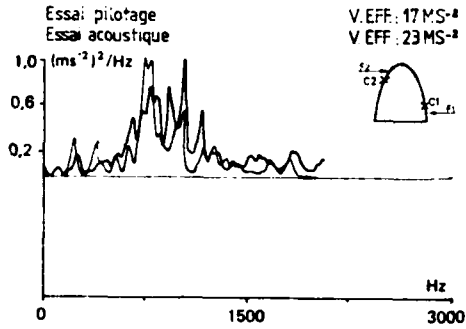


Fig. 14 - Essai sur coiffe - Bruit interne.

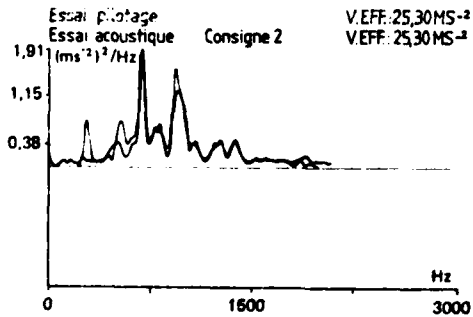
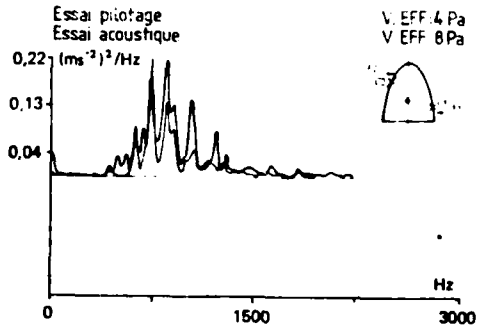
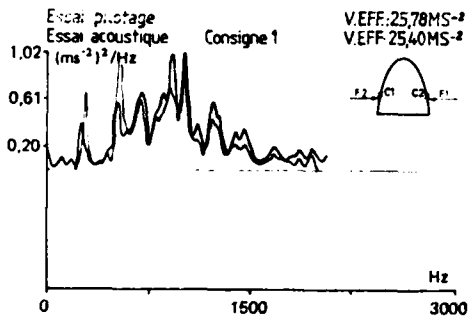
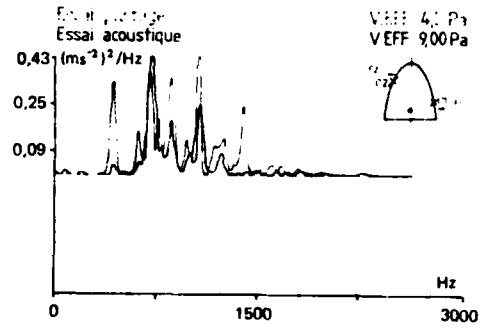


Fig. 15 - Essai sur coiffe - Accélérations pariétales.

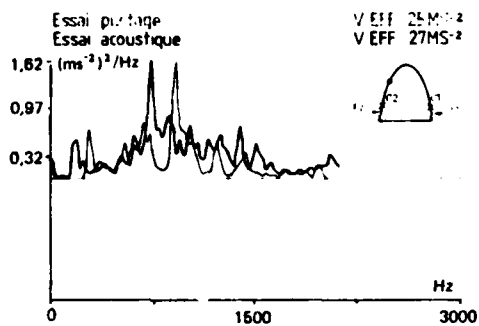


Fig. 16 - Essai sur coiffe - Accélération pariétales.

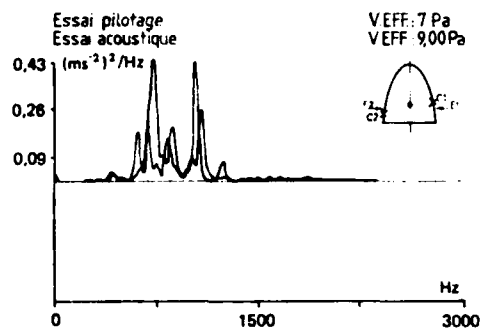
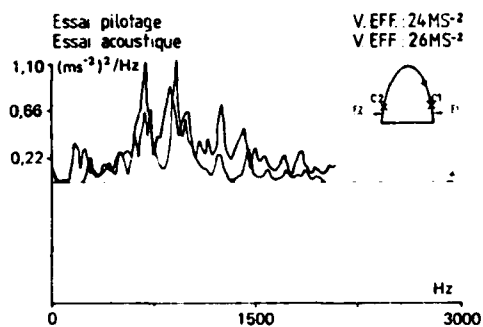
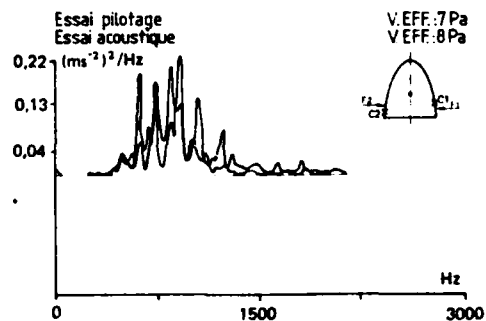


Fig. 17 - Essai sur coiffe - Bruit interne.



ELECTROSTATIC DISCHARGING BEHAVIOUR OF KAPTON AND OTHER
DIELECTRIC MATERIALS IN A SIMULATED SPACE ENVIRONMENT

by
A.A. Dollery
Royal Aircraft Establishment,
Farnborough,
Hants. GU14 6TD,
U.K.

D. Verdin
Atomic Energy Research Establishment,
Harwell
Oxon. OX11 0RA,
U.K.

SUMMARY

The electrostatic charging and discharging of different thicknesses of Kapton when irradiated in vacuum with mono-energetic electrons of 5 to 30 keV energy has been studied at different temperatures. The leakage currents and rates of discharging always increased with the incident electron energy and flux, whereas the surface voltage showed a more complex behaviour, exhibiting a maximum and then falling at higher energies for the thinner films. The surface voltage, the rate of discharging, the peak current, and the total charge flow during a discharge were enhanced as the temperature was decreased from +70°C to -180°C. The results are discussed in terms of the resistivity of the polymer and the secondary emission of electrons, and they demonstrate that very thin Kapton films are markedly less susceptible to electrostatic charging and discharging.

The electrostatic behaviour of Kapton when it is incorporated into a laminated material, or when used as an insulator for an electric heater pad, or in the form of a substrate for a flexible solar array is also described. In addition, data are presented which demonstrate the performance of thermal control paints (Chemglaze A276 and L300), aluminised PTFE, and solar cell cover glasses under similar conditions.

1. INTRODUCTION

Kapton film is widely used on geostationary satellites as the outer layer of passive thermal control systems, and as a substrate for flexible solar arrays. Since the exposed dielectric can be of large area, is relatively thin, and usually has a conductive backing, large capacitances exist, which under the conditions prevailing in geosynchronous orbit and in the absence of sunlight, can become electrostatically charged during geomagnetic substorms and result in arc discharges. These may physically damage the polymer and its substrate, and the associated electromagnetic radiation can cause serious communication and telemetry problems.

Many aspects of the charging and discharging of various dielectrics have been reported⁽¹⁾, but there is a sparsity of data obtained by varying a wide range of irradiation parameters under identical experimental conditions. Such data has been obtained for Kapton as part of a materials characterisation programme, and since very few observations exist of the effect of temperature on the surface voltage and discharging activity of Kapton, this parameter has been studied in some detail.

In spacecraft Kapton is employed in several different configurations which may modify its electrostatic behaviour. Thus, it can be laminated with aluminium, or it may be used with a conductive coating applied to its exposed surface. Electric heaters used on wave guides and batteries are embedded between two layers of Kapton, and under some circumstances these units may be exposed to the ambient electron flux. When employed as a substrate for a flexible solar array⁽²⁾ the Kapton exposed on the reverse side of the array is shielded from sunlight, and will be susceptible to charging in the absence of photoemission. The electrostatic behaviour of Kapton used in each of the above ways has been examined, and comparable tests have been performed on other dielectric materials. These include two thermal control paints, aluminised PTFE, and solar cell modules.

2. EXPERIMENTAL TECHNIQUES

The equipment used for this work (Fig. 1) was based on a 0.5m diameter vacuum chamber, operating at a pressure of $\approx 2 \times 10^{-7}$ torr, in which samples could be irradiated with mono-energetic electrons at temperatures from 25°C to 75°C, or at about -180°C. The electron energies were in the range 3 to 30 keV, and the beam flux was from 0.02 to 35 nA.cm⁻². The Kapton samples consisted of 140 mm diameter circles having projections for electrical connections (Fig. 2). A central current collector (101 mm diameter in "standard" samples) and a concentric guard ring of aluminium were vapour deposited on the lower surface, and subsequently sprayed with an insulating coating. To facilitate heat transfer the samples were secured on the sample holder with a silicone encapsulant (Dow Corning 93-500) used as a low bond strength adhesive. The area of the sample irradiated was defined by a 110 mm aperture in an earthed collimating plate just above, and insulated from, the sample. The beam uniformity over the irradiated zone was + 30%.

During irradiation the leakage current from the central collector to earth was measured with an electrometer (Keithley, model 610C), the output of which was displayed on a chart recorder to show the frequency of discharges. The pulse characteristics were monitored with a fast current probe (Tektronix, type P6303) inductively coupled to the lead from the sample to the electrometer. The output of the probe



amplifier was displayed on a 100 MHz storage oscilloscope (Tektronix, type 466) so that pulses could be photographed for measurement of peak current, pulse duration, and the area beneath the trace, which gives the total charge flowing during a discharge. For automatic measurement of the charge flow associated with large numbers of pulses the output of the current probe amplifier was fed into a transient recorder (DataLab, model DC922) and the areas of the displayed peaks were converted into Coulombs.

The surface voltage profile of the top surface of the samples was measured during irradiation by a non-contacting electrostatic voltmeter (Trek, model 340HV) equipped with a probe (type 4031S) having a voltage sensing aperture of 0.5 mm diameter. This was swept, about 3 mm above the sample surface across a diameter of the sample in 12 seconds, and operated at the potential it was measuring, thus avoiding distortion of the surface voltage, and the risk of discharges between the probe and the sample. The output of the probe was not affected by the electron beam, and it was established that the light emitted by the electron gun had no significant effect on the surface voltage of Kapton.

The electromagnetic radiation associated with the current discharges was monitored with a circular loop antenna mounted in the vacuum chamber. The voltage induced in this loop by discharges was displayed on a second identical oscilloscope. For the particular components employed, this system gave relative measurements of the electromagnetic signal at 20 MHz.

Visual and photographic observation of samples during irradiation was made through a port in the vacuum chamber.

3. IRRADIATION OF KAPTON - RESULTS AND DISCUSSION

(a) Surface Voltage and Leakage Current

Measurement of voltage profiles across the surface of Kapton during irradiation showed that it required several minutes to attain an equilibrium level at a flux of 5 nA.cm^{-2} . Figure 3 shows how the profile changed for 5 keV electrons incident on a sample having a small diameter collector. The equilibrium level was $\sim 1 \text{ kV}$ below the energy of the incident electrons, and this was also true of the maximum levels attained over the unaluminised areas of the sample with higher energy electrons (Fig. 3). The surface voltage profiles also show that earthed aluminium on the rear surface of the Kapton lowered the potential of the irradiated surface. The maximum surface voltages attained on unaluminised Kapton, and those measured at the centre of standard samples are presented in Figure 4 as a function of the incident electron energy and the thickness of the Kapton, for irradiations performed at -180°C with a beam flux of 5 nA.cm^{-2} . The plots all extrapolate to an intercept which indicates that under certain conditions the surface tends to attain a voltage which is 1.3 kV below the energy of the incident electrons.

The leakage current through Kapton to the aluminium collector during irradiation was proportional to the area of the collector from 8 to 80 cm^2 , and to the incident electron flux, up to the maximum attainable current of 35 nA.cm^{-2} . It was also a function of the energy of the electrons, and the data in Figure 5 for $51 \mu\text{m}$ thick Kapton irradiated at two temperatures show that at 25°C it accounts for essentially all of the incident flux at the highest energy.

The above observations are consistent with a charging mechanism for dielectrics in which the surface voltage attained represents a balance between the incident flux and the loss of electrons by conduction and by secondary emission and backscattering. When there is no aluminium on the lower surface, or for very thick films, where conduction is low, secondary emission plays a decisive role⁽³⁾ in the absence of light. For a surface to attain equilibrium under these conditions with electrons of incident energy E , the secondary emission coefficient δ must be unity i.e. one electron leaves for each one arriving at the surface. If δ were always >1 or always <1 the surface would charge positively or negatively respectively, and could never attain equilibrium. δ is a function of the incident electron energy⁽⁴⁾ such that it is greater than unity in the range $\sim 1 \text{ eV} < E < \sim 1 \text{ keV}$, so that when irradiation commences with electrons of energy $E > 1 \text{ keV}$ very little secondary emission occurs. However, as the incident electrons are trapped (assuming the dielectric is thick enough) the resulting potential of the surface retards the electrons subsequently arriving, and the surface will charge up negatively until its potential reaches a level at which it retards the incoming electrons to an energy for which their secondary emission coefficient is unity. Davies⁽³⁾ showed this energy was 0.9 keV for Kapton at 25°C , and the present results indicate that there is very little effect of temperature on the upper threshold for secondary emission, since at -180°C the Kapton surface acquires a voltage which is 1.3 kV lower than the energy of the incident electrons.

The lower resistance between the front and rear surfaces of the thinner samples permits higher leakage currents to flow through the polymer, thus providing a second route for electron loss when the lower surface is earthed. Equilibrium is therefore maintained by a decrease in secondary emission, δ falls below unity, and equilibrium is established with incident electrons of higher energy. There is therefore less retardation of the incident electrons so that the surface is at a lower potential. However, the variation of resistance with thickness alone cannot account for the differences between the plots in Figure 4. The greater penetration of the more energetic electrons during the charging process will presumably result in a radiation-induced contribution to the conductivity⁽⁵⁾ which extends to a greater fraction of the thickness of the film at the higher electron energies, thus raising the leakage current (Fig. 5). The range of 30 keV electrons in Kapton is estimated from electron range data⁽⁶⁾ to be $12.3 \mu\text{m}$, which represents a penetration of half of the thickness of the $25 \mu\text{m}$ film, but only 1/10 of that of the thickest film. When the penetration is a significant fraction of the thickness the enhanced conductivity results in even lower secondary emission to maintain equilibrium, and so the surface voltage falls at the highest energies.

In the case of the thinnest film ($6.9 \mu\text{m}$) studied, the range of 22 keV electrons is equal to the thickness of the film, and therefore above this energy the surface voltage would be expected to be very low, as was indeed found (Fig. 4). These low voltages were accompanied by high leakage currents. With a flux of 5 nA.cm^{-2} of 5 keV electrons incident on the film the leakage current at -180°C was $0.3 \mu\text{A}$, and it

reached a level of 0.49 μ A for electrons having energies of 20 keV or higher. The leakage current therefore rises much more rapidly than in the case of 51 μ m thick Kapton (Fig. 5), presumably as a consequence of the greater radiation-induced conductivity associated with the higher penetration of the electrons in the thin film.

For low energy (<5 keV) electrons impinging on the thinner films the above conduction effects are negligible since the penetration is low, and secondary emission is still the decisive factor; all of the plots in Figure 4 therefore approach that for unaluminised Kapton.

The above considerations indicate that the use of the thinnest Kapton films available as the outer component of thermal blankets would facilitate the removal of even the lower energy incident electrons, and result in very low surface voltages, with a consequent reduction in susceptibility to dielectric breakdown by arc discharge. This conclusion has recently been reached independently on theoretical grounds by Fellas⁽⁷⁾.

(b) Discharging Behaviour

Electrical discharges were observed when Kapton was irradiated with electrons having an energy exceeding a threshold value, which was about 15 keV for 51 μ m thick Kapton at 25°C. The discharges were not of constant size, nor did they occur at regular intervals, so that there were short term variations in the rate of discharging, which fell progressively as irradiation continued, and eventually ceased, as a result of the production of permanent low-resistance routes to earth due to repeated dielectric breakdown. The rate of discharging varied in a non-linear manner with the beam flux (Fig. 6), presumably because apart from the rate of arrival of electrons at the sample surface other factors control the initiation of discharges and the amount of charge removed in a single event, e.g. variation of the radiation-induced component of the surface conductivity with the incident flux.

For the majority of discharges observed the current rose within about 0.5 μ sec to a peak, which was as high as 20A, and then decayed to the level of the leakage current in a period of several μ sec. The charge associated with the pulse is given by the area under the current trace. For a particular example this was 7.6 x 10⁻⁶ Coulomb, and since the corresponding voltage profiles indicated a fall in potential of about 11 kV, then the energy associated with this discharge was about 40 mJ, which was a typical value for 51 μ m thick Kapton irradiated with 25 keV electrons at -180°C. Many of the current pulses were more complex and exhibited smaller secondary pulses superimposed on the decay of the initial pulse, presumably due to secondary dielectric failure within the area from which the first discharge was collecting electrons. The signal induced in the antenna by the electromagnetic radiation associated with the current pulses exhibited initial peak amplitudes of up to about 9V and decayed in about 1 μ sec.

The surface voltage profiles provided an indication of the extent in terms of area and voltage level to which a surface was discharged in a single event. The scans reproduced in Figure 7 were recorded during the irradiation at -180°C of a standard 51 μ m thick Kapton sample with 30 keV electrons at a beam flux of 5 nA.cm⁻². The first scan shows that when the surface was at only about 11.5 kV a discharge occurred which reduced the voltage to zero. Immediate reversal of the probe traverse revealed in the second scan that the whole width of the sample had discharged, and if account is taken of the partial recharging of the surface by the electron beam during the sweep, which was estimated by comparison of these two scans to be at a rate of about 170 V/sec, then the whole sample must have fallen very close to zero volts. The third scan, commenced immediately after a discharge, illustrates the fact that in other cases the full width of the sample discharged, but the surface did not fall below 5 kV. The fourth scan shows the result of another common type of discharge which was very localised and reduced the voltage over only a fraction of the Kapton surface. This was towards the edge of the sample, which is the region of maximum voltage gradient and where initiation of discharges would be expected. These wide variations in the changes in surface voltage caused by discharges are consistent with the differences which exist between the amounts of charge associated with the individual discharges occurring in a sample under steady irradiation conditions.

The behaviour of 25 μ m thick Kapton differed from that of the thicker films in that the discharges which occurred had almost no influence on the surface voltage, in spite of involving significant amounts of charge. Furthermore, the charge associated with the largest pulse observed for each incident electron energy decreased with increase in this parameter, being 29.8, 17.1 and 3.8 x 10⁻⁷ C for 20, 25 and 30 keV electrons respectively. It is suggested that these effects result from the greater penetration of higher energy electrons in the thin film due to its lower surface voltage (Fig. 4), with the consequence that a higher proportion of the electrons become trapped at distances approaching the range of electrons possessing the incident energy. Thus, 30 keV electrons penetrate nearly to the centre of the 25 μ m film, and dielectric breakdown in this case will involve only half of the thickness of the Kapton. This will presumably remove fewer electrons as the incident energy is increased, since they will be trapped more diffusely in the upper part of the film at the higher energies, and probably only those electrons from the zone near the maximum range will be involved in a discharge. Removal of electrons primarily from the deeper trapping zones would also account for the small changes in surface voltage caused by discharges from the 25 μ m film. Moreover, since the breakdown voltage involved would be that of about half of the thickness of the Kapton, then the occurrence of discharges at the surface voltages observed (Fig. 4) does not contradict the reported dielectric strength of 19 kV for 25 μ m thick Kapton -180°C⁽⁸⁾.

With the 6.9 μ m thick film the normal type of discharges were observed only with 10 and 15 keV electrons, and they were very small, the charge associated with the largest pulses being 6.9 and 2.5 x 10⁻⁸ C respectively. The discharges had no effect on the surface voltage, and presumably occurred at the edge of the central collector, in the unaluminised annulus, where the voltage was up to 2 kV higher than in the centre of the sample. At higher energies the electrometer recorded no discharges of this type but did show small negative displacements, indicating a change in behaviour when the incident electrons had sufficient energy to penetrate the film completely.

The discharge arcs produced pinholes in the Kapton film, but the first pinhole formed was not the site for all subsequent discharges, even over a small area. The discharges were accompanied by visible

light flashes, and photographs showed that they occurred exactly at points where pinholes were found, and that one or several pinholes may be involved in a particular discharge. Repeated discharging may take place at a given pinhole but not necessarily successively at the same hole. For all of the samples examined the pinholes and other damage occurred within the unaluminised zone or at the adjacent edge of the aluminium collector, indicating that discharges are initiated in those regions where the voltage stress is greatest. The pinholes were surrounded by a region of charred polymer, and usually by a network of visible discharge tracks. More extensive damage arose when discharges occurred in aluminised areas, and they sometimes produced holes of up to 1 mm diameter due to complete vaporisation of Kapton and loss of aluminium from a further 1 mm strip around the hole. This damage had resulted from discharges of an area of at most 100 cm^2 and involving $<0.1 \text{ J}$ of energy. Since the area of dielectric surface on a satellite can be up to several m^2 , and scaling experiments have shown⁽⁹⁾ that the maximum energy in discharges is proportional to the function (area of dielectric)^{1.5} then it is apparent that discharges of tens of Joules of energy can occur and cause considerable damage to the satellite in addition to giving rise to electrical interference.

(c) Influence of Temperature

The temperature at which Kapton is irradiated has a significant influence on its behaviour. When irradiated with 30 keV electrons at a flux of 5 nA.cm^{-2} standard $51 \mu\text{m}$ thick samples showed at most one discharge per hour at 80°C . At 25°C the rate was initially about 2 per minute, while at -180°C it was about 4 per minute. Moreover, the charge associated with each pulse was on average several fold greater at -180°C than at 25°C , and as the irradiation proceeded there was a much slower fall in the rate of discharging at the lower temperature.

The volume resistivity of Kapton is greater at lower temperatures⁽⁸⁾ and this should lead to reductions in the leakage currents and increases in the surface voltages as the temperature is reduced. The data in Table 1 show that the voltages at the side (unaluminised region) and in the centre of standard $51 \mu\text{m}$ thick Kapton samples do indeed increase as the temperature is reduced, and at the same time the leakage current falls. However, the decrease in the latter is much smaller than would be predicted from the volume resistivity, which decreases nearly 10-fold between 25° and 70°C ⁽⁸⁾, so that presumably radiation-induced conductivity makes a much greater contribution than ohmic conductivity. Nevertheless the latter probably determines the effect of temperature, since the radiation-induced effect would not be expected to vary with the temperature. The data given in Table 1 were measured under conditions where little or no discharging occurred so that the voltages represent equilibrium values rather than the breakdown voltages of the sample.

TABLE 1. Effect of Temperature on Surface Voltage of Irradiated Kapton

Electron energy keV Beam flux nA.cm^{-2}	80°C			25°C			-180°C		
	Voltage at sample edge kV	Voltage at sample centre kV	Leakage current $\text{A} \times 10^{-7}$	Voltage at sample edge kV	Voltage at sample centre kV	Leakage current $\text{A} \times 10^{-7}$	Voltage at sample edge kV	Voltage at sample centre kV	Leakage current $\text{A} \times 10^{-7}$
15	10.3	8.7	2.4	11.1	9.3	2.5	12.5	11.8	1.5
20	9.7	9.2	3.5	11.3	9.1	3.0	14.0	12.4	1.9
25	-	-	-	-	-	-	≥ 13.4	11.8	3.0

4. THE ELECTROSTATIC BEHAVIOUR OF OTHER SPACECRAFT MATERIALS AND COMPONENTS

(a) Composite Kapton Systems

The first material examined consisted of a laminate of $25 \mu\text{m}$ of aluminium bonded to $75 \mu\text{m}$ thick Kapton with a polyester adhesive: this had been proposed as a VHF shield on the OIS satellite⁽¹⁰⁾. When irradiated on the Kapton side with 30 keV electrons at a beam flux of 12 nA.cm^{-2} this material exhibited considerable discharging at 70°C (Table 2), although the rate of discharging fell rapidly as irradiation continued. At low temperature (-180°C) it showed even higher rates of discharging, which decreased only slightly on continued exposure. In spite of the discharges the samples irradiated at 70°C suffered no physical damage, but those irradiated at -180°C all had holes (up to 17 of $\leq 1 \text{ mm}$ diameter) blown completely through the Kapton into the aluminium by the discharges, although they did not penetrate the thick aluminium layer completely. These results demonstrate that this laminated material is much more susceptible to electrostatic effects than the thinner ($51 \mu\text{m}$) Kapton coated with vacuum-deposited aluminium, but the thicker aluminium layer was able to withstand the discharges which occurred.

TABLE 2. Irradiation of Kapton-Aluminium Laminate with 30 keV Electrons

Temperature $^\circ\text{C}$	Initial discharge frequency (per min.)	Final discharge frequency (per min.)	Duration of run (min.)	Total number of discharges	Maximum discharge $\times 10^{-7} \text{ C}$
70	4.3	0.15	185	280	34.2
70	4.7	0	188	275	53.1
-180	6.5	4.9	205	-	73.9
-180	5.6	3.7	174	740	42.8
-180	8.2	5.7	218	1255	46.4

More recently Kapton having a transparent conductive coating has become commercially available (Sheldahl Inc.), and a sample of 76 μ m thick Kapton with vacuum-deposited aluminium on the rear surface and a coating of indium-tin oxide on the front surface has been tested. The two surface coatings were connected electrically by painting Chemglaze L300 paint (Hughson Chemicals Inc., Erie, Pa) around the edge of the sample, which was irradiated with a flux of 10 nA.cm⁻² of electrons, the energy of which was increased in 5 keV steps up to 30 keV. Throughout two series of irradiations, at ambient temperature and then at -180°C, the surface voltage remained at less than 5 V. The total current collected from the two surfaces was usually 70-80% of the incident flux, although it exhibited a minimum of 50% for 15 keV electrons at each temperature. At 25°C the sample exhibited a few microdischarges (<1% fsd on the electrometer: sensitivity 10⁻⁵A fsd) with 25 keV electrons and similar pulses at a rate of 14/min with 30 keV electrons. At -180°C the first few discharges occurred with 20 keV electrons, but at the higher energies the behaviour was similar to that at 25°C. The results described above for indium-tin oxide coated Kapton confirm and extend earlier observations⁽¹⁰⁾ of its essential freedom from electrostatic effects. The suitability of the material for use on the outer surface of spacecraft will therefore depend primarily on the mechanical and thermal properties of the coating and on the difficulty in confirming the integrity of the invisible film over the whole exposed area of the material when installed on a spacecraft.

Two "Minco" pad heaters have also been tested for their electrostatic behaviour at 25°C, but since they gave similar results only one test is described here. The heater consisted of a 275 Ω element sandwiched between Kapton discs (65 mm diameter; 76 μ m thick) to give an overall thickness of 157 μ m. The lower disc was extended into a tongue to support and insulate the heater connection tabs. The current from the heating element to earth was monitored with an electrometer, and the sample was surrounded by an earthed metal plate which overlapped the edge of the heater by about 1 mm, but was insulated from it. The sample was irradiated with an electron flux of 5 nA.cm⁻², the electron energy being increased in 5 keV steps to 30 keV.

The surface voltages, leakage currents and sizes of the discharges observed are summarized in Table 3. Discharging commenced with 20 keV electrons, and at the higher energies the peak currents reached 0.8 μ A and the discharges decayed completely with 1 μ sec. The data show that up to 20 keV electron energy the surface voltages are consistent with those for Kapton given in Figure 4. The voltage profiles were stable at 5 keV energy up to 15 keV, but at 20 keV a voltage level of \approx 7 kV was recorded over the whole sample at the time of discharge. Due to the more frequent discharging with 25 and 30 keV electrons all of the profiles at these energies were different, but in no case did the surface voltage fall below 5 kV. The leakage current to the heating element increased with the electron energy, and although the rate of discharging with 30 keV electrons was lower than at 25 keV this probably only reflects the usual decrease in discharge rates with prolonged exposure at 25°C. The mean charge flow involved in the pulses decreased with electron energy from 20 to 30 keV in a similar manner to that quoted above for 25 μ m thick Kapton.

After completion of the above irradiation examination of the heater showed 9 pinholes punched through the Kapton from the irradiated surface to the heating element by the discharges. Thus, in all respects the behaviour of this type of pad heater is in accord with that expected from the data presented for the electrostatic behaviour of aluminised Kapton.

TABLE 3. Irradiation of a Pad Heater at 25°C

Electron Energy keV	Maximum surface voltage kV	Leakage current $\times 10^{-7}$ A	Mean discharge rate per min.	Mean discharge size $\times 10^{-6}$ C
5	2.7	≤ 0.02	-	-
10	7.15	≤ 0.02	-	-
15	11.4	0.05	-	-
20	15.8	0.50	0.11	6.1
25	11.4*	0.8	0.42	2.6
30	10.3*	0.8 \pm 0.3	0.27	1.7

*low levels due to discharging

(1) Aluminised Teflon

Self-adhesive aluminised Teflon tape is used for thermal control purposes on spacecraft, and it is therefore necessary to examine its electrostatic behaviour under electron irradiation. The material is commonly employed with the aluminised layer electrically floating, the strips of tape being stuck to the substrate with their edges as close together as possible. Samples were prepared from 125 μ m thick Teflon tape (Sheldahl, G400800) in the form of two semicircular pieces of radius 65 mm stuck closely together on 1.5 mm thick aluminium plate, and an earthed shield, separate from the sample, limited the area of the sample exposed to the electron beam to a circle of 111 mm diameter. The following results are for a sample of this kind irradiated at 25°C with a flux of electrons of 5 nA.cm⁻² at energies increasing in 5 keV steps up to 30 keV.

The maximum surface voltages attained at each energy, are given in Table 4, and extrapolation of the data for the three lowest energies indicates the second crossover for secondary emission from Teflon at 25°C lies at 3.5 kV. However, a duplicate sample gave an intercept of only 2.0 kV, nevertheless on average the second crossover for Teflon is somewhat higher than that for Kapton. Each profile showed a pronounced dip at the centre of the scan where the surface voltage probe passed over the join between the two halves of the sample, and for electron energies up to 15 keV stable equilibrium profiles which were symmetrical about the central dip were obtained, but above this energy every profile recorded was different due to the frequent discharging of the sample. No leakage currents were observed from the sample at energies up to 15 keV, and this is consistent with the fact that the Teflon was 125 μ m thick and the

non-conductive adhesive was about $50\mu\text{m}$ thick. When a discharge occurred the electrometer monitoring the current from the substrate plate showed a sharp displacement of 1 to 40 fsd (sensitivity 10^{-6} A fsd) and returned towards zero over a period of up to two minutes, but subsequent discharges often occurred before the current had reached its stable zero level, and in most instances, small ($<2\%$ fsd) negative-going pulses were superimposed on the decaying current. Very similar behaviour occurred with 25 and 30 keV electrons, except that the pulse rates were greater, so that subsequent discharges occurred much sooner on the current decay curve, i.e. the current rarely reached zero between discharges. The discharge rates were constant during the irradiations, and they are given together with the charge flow associated with the discharges in Table 4. At each energy, the sizes of the discharges varied widely, the smallest peak recorded by the transient recorder corresponding to $1.1 \times 10^{-5}\text{C}$. With 20 keV electrons the discharges resulted in the surface voltage across the full width of the sample falling to levels over the range 1.5 to 6.5 kV, but with 25 keV electrons the lowest levels recorded immediately after a discharge were 3 kV, the full width of the sample again falling in voltage, and with 30 keV electrons voltages as low as 1.5 kV were again observed immediately after discharges. The initial stage of a discharge was quite short, the current rising to as high as 68A and decaying within 0.8 μs to a level which appeared constant on the oscilloscope, but which was shown by the electrometer to slowly decline for about a further 2 minutes.

Photographs taken for periods of 30 seconds during the irradiation showed point flashes of light, the majority of which appeared along the joint between the two sections of the sample, but there were also some at other points across the sample. On completing the irradiation the sample showed evaporation of the vacuum deposited aluminium along about a 0.5 mm wide strip on each side of the joint and also over 1 mm diameter circles at some other points across the sample. In each case the exposed surface of the Teflon film was unamaged. Moreover, no damage occurred around the shielded circumference of the sample, so that much of the discharging appears to be initiated by the voltage stresses present at the joint. When preparing the sample a crease was made in the tape near the end of one of the semi-circles, and it was found that vaporisation of aluminium had occurred along the full length of the crease, so that care must be taken to avoid such defects when applying the material.

TABLE 4. Irradiation of $125\mu\text{m}$ Thick Aluminised Teflon at 25°C

Electron energy keV	Maximum surface voltage kV	Discharge rate per min.	Mean discharge size $\times 10^{-5}\text{C}$	Maximum discharge size $\times 10^{-5}\text{C}$
5	1.4	-	-	-
10	5.8	-	-	-
15	10.5	-	-	-
20	12.7*	1.36	1.31	1.90
25	12.6*	0.91	1.15	3.13
30	18.4*	0.47	1.18	4.14

*Sample discharging frequently

Thinner ($50\mu\text{m}$) samples of aluminised Teflon, were irradiated at 25°C with 5 keV electrons at a beam flux of 12 nA.cm^{-2} , and these also exhibited considerable discharging, but, as expected from the higher temperature and the thinner polymer film, the charge flow in the discharges was smaller under these conditions, the maximum discharge recorded involving $3.8 \times 10^{-6}\text{C}$.

(c) Thermal Control Paints

The black thermal control paint Chemlaze L90 (Hughson Chemicals, Erie, Pa) has been examined in the form of a film cast on mercury to give a coherent sheet $70 \pm 4\mu\text{m}$ thick, which was then aluminised in the same way as described for Kapton. The sample was irradiated at $+20^\circ\text{C}$ and subsequently at -80°C with a flux of 5 nA.cm^{-2} of electrons of up to 30 keV energy. Under all conditions zero surface voltage was recorded, and at -180°C the leakage current to the aluminised collector accounted for 30 + 1% of the incident flux. On continuing the irradiation at $+80^\circ\text{C}$ the current progressively decreased to a limiting value of 6% of the incident flux, which may reflect a change in the bulk resistivity of the material with increasing radiation dose.

The white thermal control paint Chemlaze A276 was applied to aluminium plate and to $5\mu\text{m}$ thick Kapton, and its behaviour at high and low temperature when exposed to 30 keV electrons is summarized in Table 5. For the aluminium substrate discharges were only observed at the lower temperature, and the rather variable performance may be due to incorporation of defects (e.g. dust particles) in the film during curing in the atmosphere. When applied to Kapton significant discharging was also observed initially at $+4^\circ\text{C}$, in contrast to the results with Kapton itself at this temperature, yet at -180°C the discharging activity was very similar to that for Kapton alone, so that the behaviour of the composite material is not an additive function of that of the individual components. For the paint film on aluminium at 25°C the surface voltages attained were very low, the maximum being 1.7 kV with 5 keV electrons, and lower values were observed at the higher electron energies. At low temperature the surface voltage reached 4.4 kV with 5 keV electrons and correspondingly high values with the other electron energies. However, the leakage currents at the two temperatures were very similar at most energies, so that variation in volume resistivity with temperature does not appear to be an important factor for this material.

TABLE 5. Irradiation of Thermal Control Coatings with 30 keV Electrons at a Beam Flux of 12 nA.cm^{-2}

Material	Temperature °C	Initial discharge frequency (per min.)	Duration of run (min.)	Total No. of discharges	Maximum discharge $\times 10^{-7} \text{C}$
(69.7	0	245	0	0
Chemglaze A276 (69.7	0	174	0	0
paint on (-180	0.4	206	178	53
aluminium (-180	4.4	180	202	14
plate (-180	1.9	183	343	9.8
(73	6.9	212	352*	3.6
(73	3.2	194	127*	8.0
Chemglaze A276 (73	5.1	211	231*	10.7
paint on (-180	4.3	192	915	110
51 μm thick (-180	3.0	215	308	32
Kapton (-180	7.4	225	1040	45
(-180	3.9	288	995	347

*Final discharge frequency zero

(d) Solar Cell Arrays

Solar cell modules having the construction illustrated in Figure 8 were assembled, and their susceptibility to electrostatic discharging at low temperature was investigated by irradiating them with electrons of up to 30 keV energy at a beam flux of 5 nA.cm^{-2} .

The first module incorporated solar cells without any coverslides, the cells being mounted on 25.4 μm thick Kapton using Dow Corning 3145RTV silicone adhesive. The module was secured to the sample holder with the low bond strength adhesive, the cells facing upwards for the initial irradiations, in which the sample holder was cooled by liquid nitrogen. The Kapton film was therefore at about -180°C , but the temperature of the exposed surface of the cells was not known. The negative lead from the top surface of the cells in the module was connected to earth via an electrometer, and the discharges were recorded by the pulse monitor coupled to this lead; the positive lead was also earthed.

During irradiation the conductivity of the cells held their surface potential below about -200 V , but the exposed Kapton around the outside of the module reached nearly -4 kV with 10 keV incident electrons, and gave small discharges (peak current 0.4A), whereas aluminised Kapton of this thickness produces no discharges at this energy, and only very small ones with 15 keV electrons. Clearly the voltage stress between the exposed polymer surface and the solar cells is a source of discharges in such an assembly if it is not exposed to sunlight. Nevertheless, even for 30 keV electrons the discharges were still small (peak current $\leq 0.8\text{A}$) and localised. When the assembly was irradiated from the substrate side the behaviour with 5 and 10 keV electrons was essentially that expected for plain Kapton film, the surface charging up to 4.2 and 9.1 kV respectively. With 15 keV electrons the Kapton attained 11 kV, which is about twice the level attained by aluminised 25 μm thick Kapton. Clearly the leakage current to the solar cells was very low, due to the additional insulation provided by the adhesive, but eventually breakdown discharges occurred, although they were not very large (peak current $\leq 1\text{A}$). With 20 keV electrons the surface even reached 18.2 kV before the first discharge occurred. Subsequently, at this and higher energies, the surface discharged from about 10 kV, and the discharges were of about the same size as above, but occurred at high rates, of up to 6.6/min. Thus, under operational conditions an array of this type would be subjected to large numbers of small discharges from the Kapton film to the solar cells.

For a module comprising solar cells with 50 μm thick cerium doped (CMX) coverslides and 51 μm thick Kapton irradiation with 5 and 10 keV electrons gave surface potentials about 2.5 kV below the energy of the incident electrons, indicating the charging of the surface of the coverslides. Small discharges occurred with 10 keV electrons, (peak current $\leq 0.6\text{A}$; maximum charge associated with pulse $1.5 \times 10^{-7}\text{C}$), however, with 15 keV electrons the discharges were quite large (peak current $\leq 6\text{A}$, charge $\leq 20 \times 10^{-7}\text{C}$). As the electron energy was further increased the discharges remained at a comparable size, with the peak currents reaching 8A, and the pulse rates being up to 8.4/min. The changes in surface voltage showed that several solar cells could be discharged in a single event, but in no case did the whole assembly discharge, so that the total charge involved was less than that from the discharge of a comparable area of Kapton. Moreover, for an array of solar cells having cover slips, which themselves charge up, the charging of the exposed Kapton surrounding them is of less significance in the electrostatic behaviour of the assembly.

When this module was irradiated from the substrate side the behaviour up to 15 keV was essentially that expected for plain Kapton, apart from a few discharges at 15 keV. At higher energies the polymer surface always reached the same limiting voltage of about 14.5 kV, which presumably represented the breakdown voltage to the solar cells, since it showed discharges at rates of up to 1.8/min, which reduced much of the sample surface to nearly zero volts, and resulted in physical damage to the polymer film. Thus, under operational conditions an array of this kind would be subjected to significant electrostatic discharging.

Inspection of this assembly after it had been irradiated in each orientation showed a considerable number of discharge sites in the form of charred pinholes. When irradiated with the solar cells exposed to the electron beam the damage was confined to the Kapton adjacent to the edges of the solar cells, and when irradiated from the Kapton side the damage was always within the area of each cell.

The electrical characteristics of the solar cell module were measured before and after irradiation, and it was found that the exposure to the low energy electron beam caused no changes. This is consistent with the fact that the electron ranges were less than the thickness of the coverslides or of the Kapton substrate.

A solar cell module incorporating 'frosted' silica coverslides has also been irradiated. With the electron beam incident on the coverslides the surface voltage equilibrated at 1-5 kV for electron energies up to 15 keV, but exhibited surface voltages from 0.5 to 7.5 kV at the higher electron energies, due to discharging. Although the thicker (150 μ m) 'frosted' coverslides were at a higher temperature than the CMX glasses due to a different mounting technique being used, this would have been insufficient to account for the much lower voltages observed. However, the threshold at which discharging occurred was higher, at 20 keV, for this module, compared with 10 keV for the CMX assembly. Discharge frequencies and peak currents for the frosted module were fairly similar to those for the CMX system.

On exposing the reverse side of the above assembly to the electron beam the surface voltages behaved in a very similar way to those observed on aluminised Kapton. Discharging through the Kapton and adhesive to the rear of the solar cells commenced at 15 keV electron energy, and the discharge pulses reached peak currents up to 5A. On the 'frosted' system the discharges produced a large number (61) of pinholes in the Kapton regions behind the cells, and these were usually associated with some volatilisation of metal from the rear surface of the cell and interconnections. The maximum dimension of the damaged area was 1 mm.

Other workers^(1, 11) have found similar results for the irradiation of flexible solar arrays based on a 76 μ m thick Kapton-fibreglass substrate with electrons of up to 20 keV energy at fluxes of 1-10 nA.cm⁻². When the substrate side was exposed to the beam the majority of discharges occurred at the edges of cells, due to dielectric breakdown to the cell interconnects when the surface potential reached 10 \pm 2 kV. For a rigid array, with the cells mounted on Kapton⁽¹¹⁾, irradiation from the cell side produced voltage profiles showing similar features to the present observations, with the highest voltages arising on the exposed Kapton border surrounding the cells. The discharges in this case also originated at the edges of the coverslides.

REFERENCES

1. Stevens, N.J., Berkopec, F.D., Staskus, J.V., Bloch, R.A. and Narciso, S.J.: Testing of Typical Spacecraft Materials in a Simulated Substorm Environment. Proc. Spacecraft Charging Technol. Conf., 1977, AFGL-TR-77-0051, NASA TM X-73537, pp. 431-457.
2. Treble, F.: The RAE Lightweight Solar Array, 1974, RAE Tech. Rep. 73172.
3. Davies, D.K.: Charges and Vacuum Flashover. Nature 262, 1976, p. 270.
4. Davies, D.K.: The Charging and Discharging of Spacecraft Dielectrics. Proc. ESA Symposium "Spacecraft Materials in Space Environment", 1979, ESA SP-145, pp. 217-221.
5. Hedvig, P.: The Radiation Chemistry of Macromolecules, Ed. M. Dole, Academic Press, 1972, Vol. 1, pp. 127-142.
6. Spencer, L.V.: Energy Dissipation by Fast Electrons, 1959, N.B.S. Monograph No. 1.
7. Fellas, C.N.: An Arc-Free Thermal Blanket for Spacecraft Use. IEEE 1980 Conf. on Nucl. and Space Radiation Effects. Paper H.9.
8. Technical Information Bulletin H-4. Film Department, Electrical Insulation Products Division. Du Pont de Nemours Inc.
9. Blamain, K.G.: Scaling Laws and Edge Effects for Polymer Surface Discharges. Proc. Spacecraft Charging Technol. Conf. 1979, AFGL-TR-79-0082, pp. 646-656.
10. Bosma, J. and Levadou, F.: Electrostatic Charging and Space Materials. Proc. ESA Symposium "Spacecraft Materials in Space Environment", 1979, ESA SP-145, pp. 189-207.
11. Stevens, N.J. and Lovell, R.R.: Spacecraft Charging Investigation for the CTS Project, 1975, NASA TMX-71795.

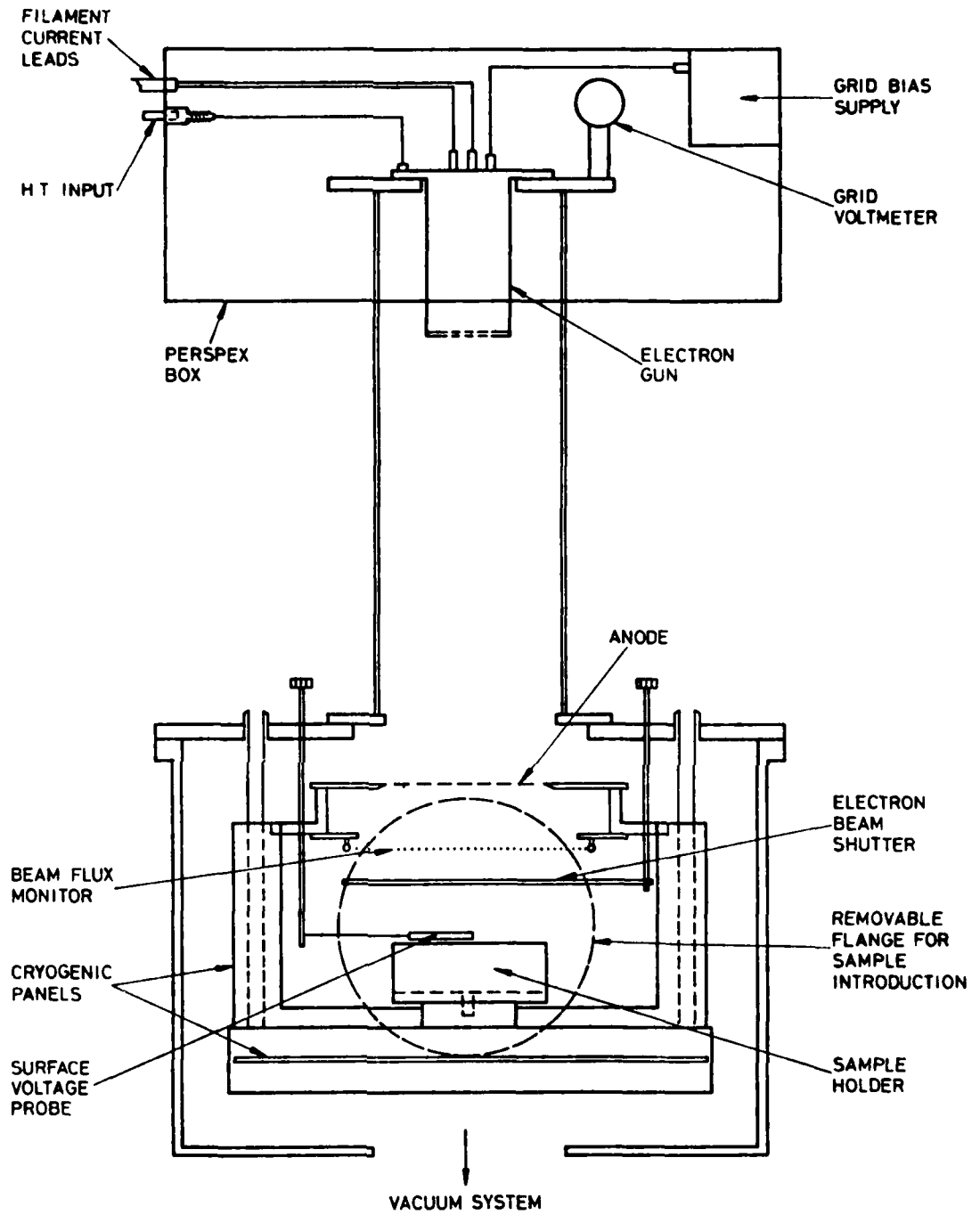
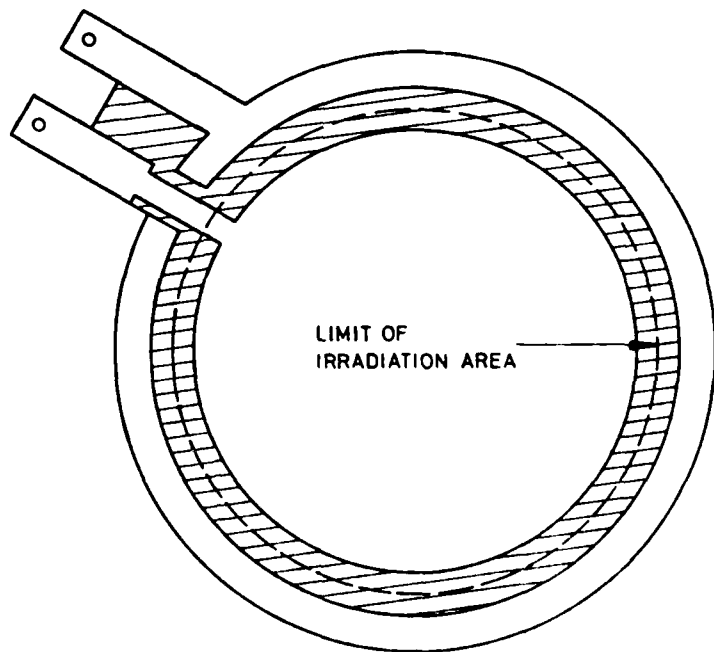


FIG.1. IRRADIATION CHAMBER AND ELECTRON GUN ASSEMBLY




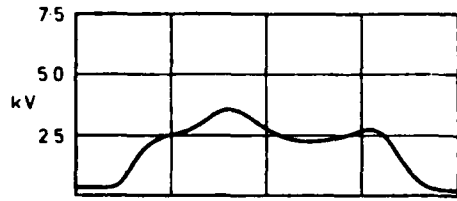
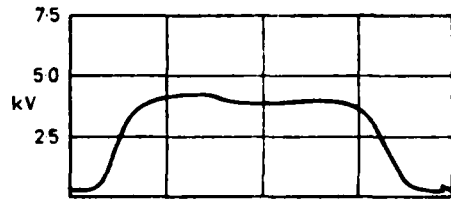
 KAPTON ALUMINISED ON LOWER SURFACE
UNALUMINISED KAPTON

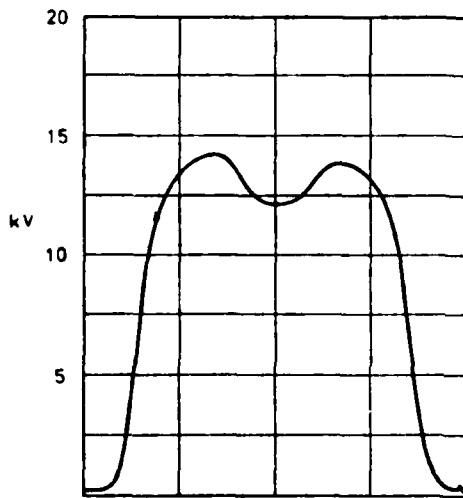
FIG. 2. "STANDARD" ALUMINISED KAPTON SAMPLE



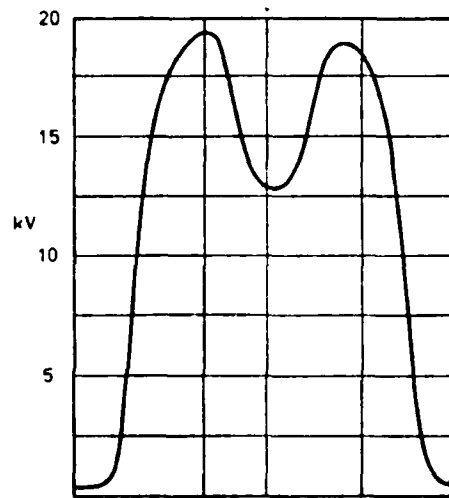
ELECTRON ENERGY 5 KeV
IRRADIATION TIME 30 SEC



ELECTRON ENERGY 5 keV
IRRADIATION TIME 10 MIN



ELECTRON ENERGY 15 keV
IRRADIATION TIME 10 MIN



ELECTRON ENERGY 20 keV
IRRADIATION TIME 3 MIN

Kapton thickness 50 μ m
Beam flux 5 nA cm⁻²
Diameter of irradiated zone 111mm
Current collector diameter 32mm

FIG. 3. SURFACE VOLTAGE PROFILES FOR ELECTRON IRRADIATION OF KAPTON

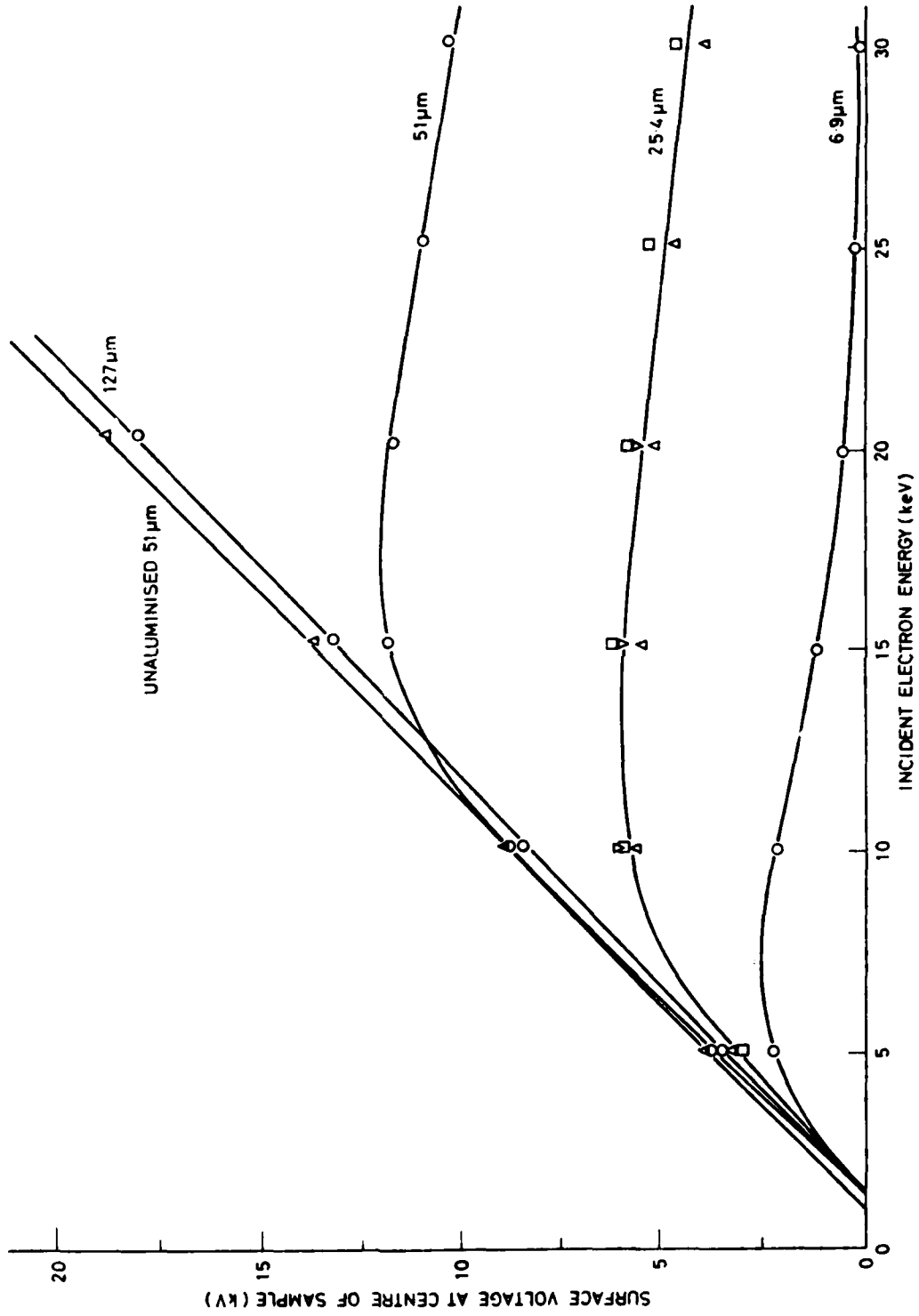


FIG. 4. SURFACE VOLTAGE AS A FUNCTION OF INCIDENT ELECTRON ENERGY FOR DIFFERENT THICKNESSES OF KAPTON IRRADIATED AT -180°C

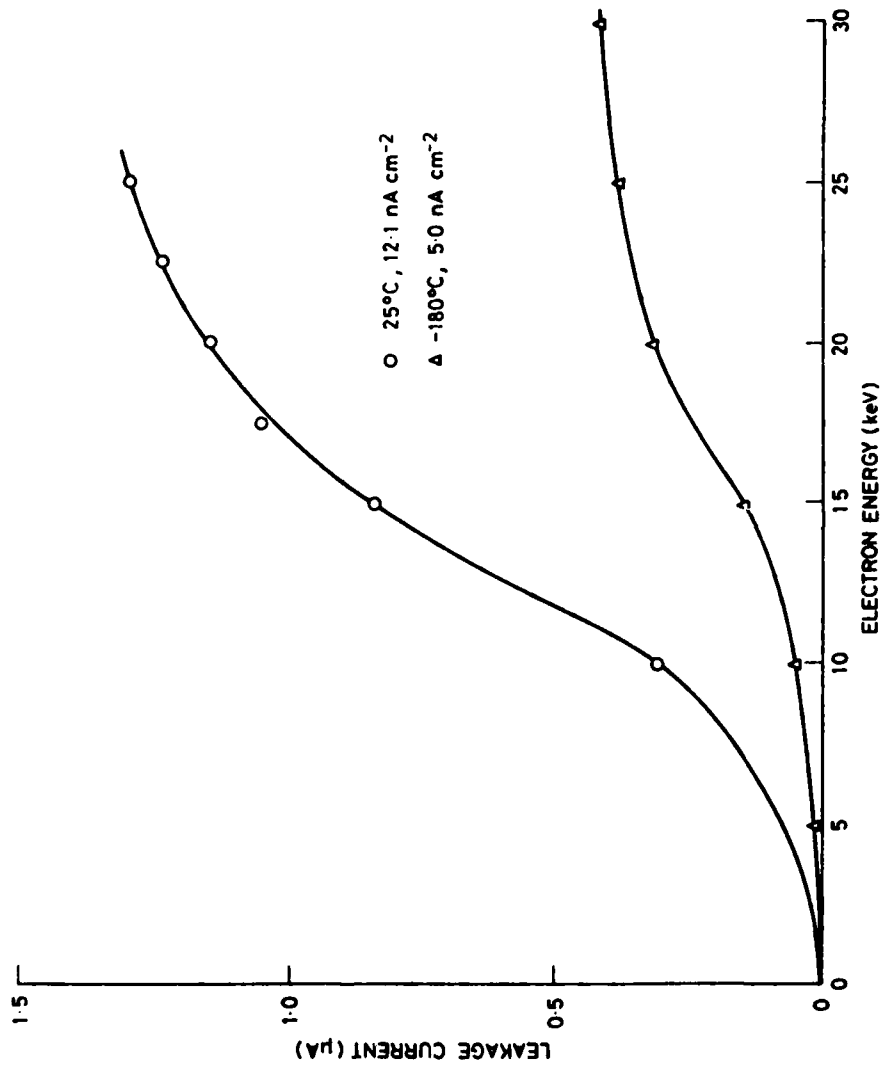


FIG. 5. VARIATION OF LEAKAGE CURRENT WITH ELECTRON ENERGY FOR
51 μm THICK KAPTON

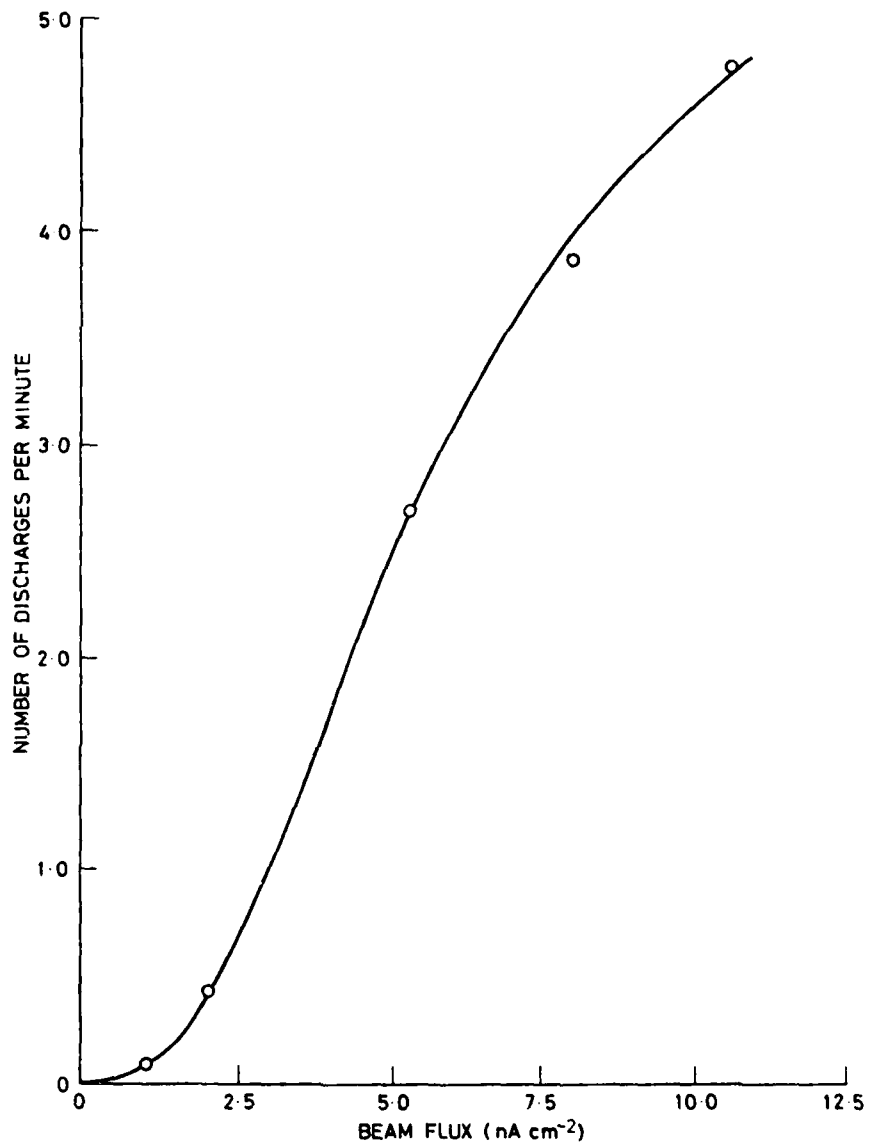


FIG. 6. VARIATION OF DISCHARGE RATE WITH BEAM FLUX FOR 51 μm THICK KAPTON AT 25°C

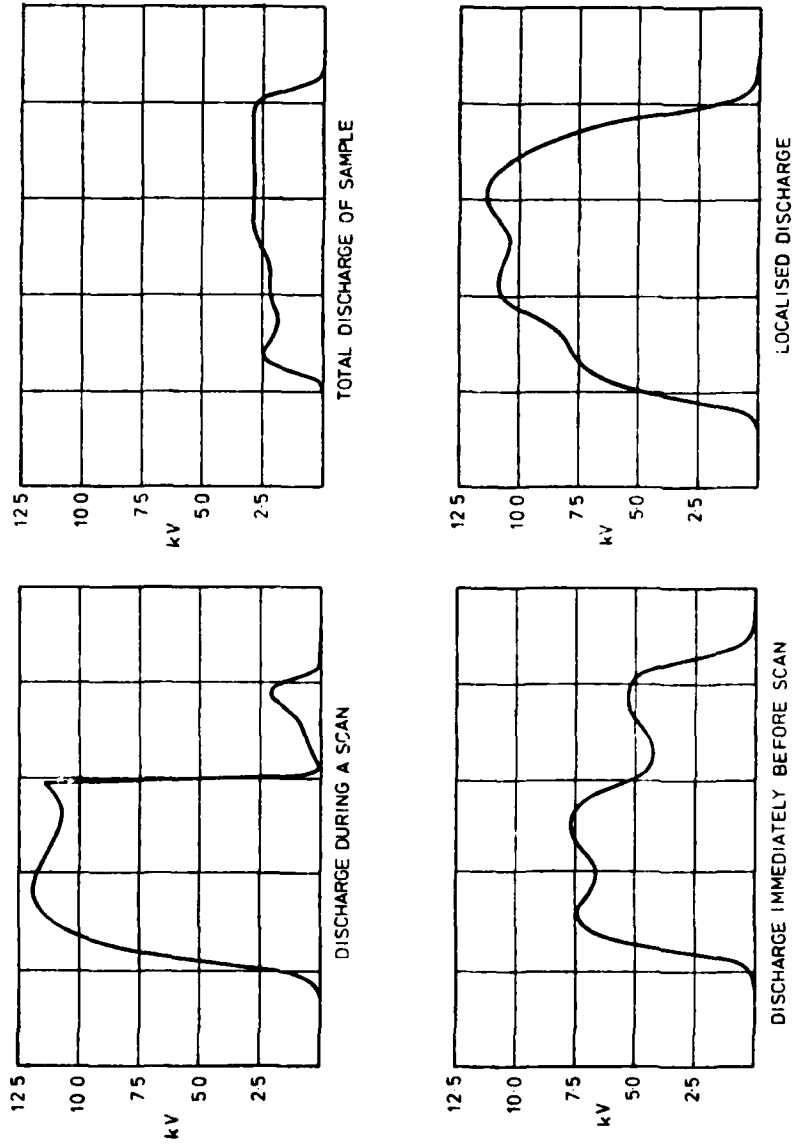


FIG. 7. EFFECT OF DISCHARGES ON SURFACE VOLTAGE PROFILES OF KAPTON

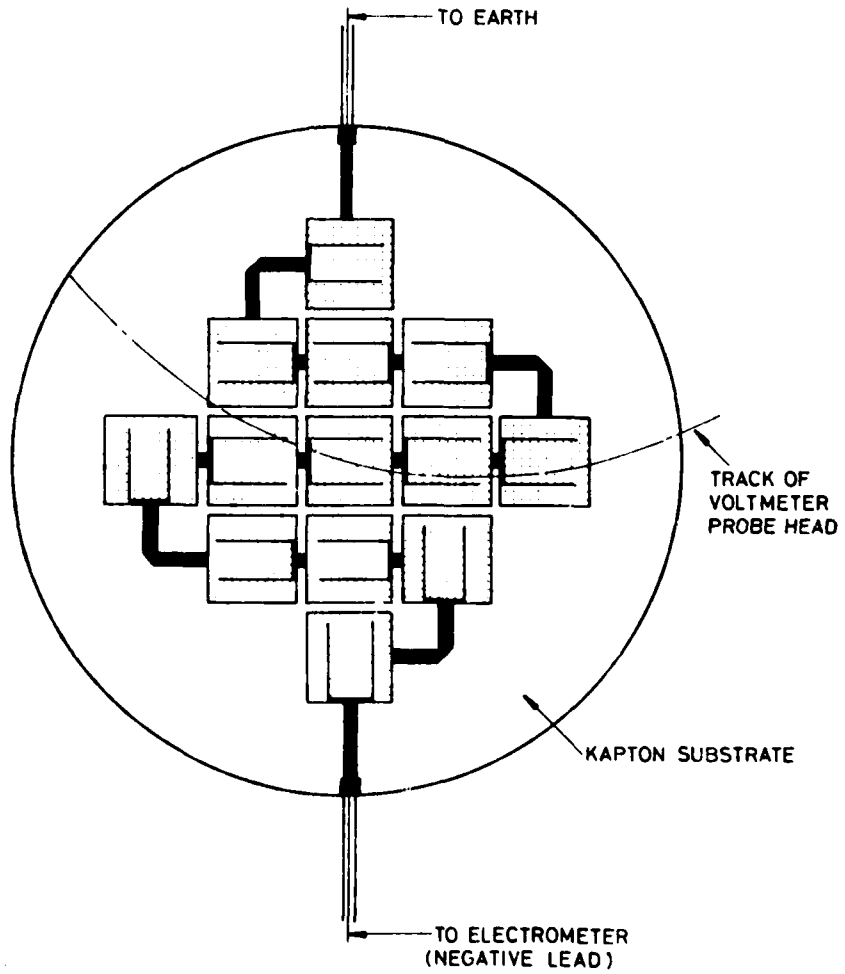


FIG 8. SOLAR CELL MODULE

RECORDER'S REPORT

SESSION II - ENVIRONMENT AND ENVIRONMENTAL EFFECTS

by

D.R.Tenney
 NASA-Langley Research Center
 Hampton, Virginia 23665
 USA

Five papers were presented on space environmental effects on materials. Professor Tennyson discussed a program he is conducting at the University of Toronto on the effect of the space environment on the thermal distortion of polymer matrix composites. The objectives of their program were presented and the facilities at the university for studying space environmental effects on materials were discussed. Experimental data were presented for both graphite/epoxy and Kevlar/epoxy systems. Thermal cycling studies, over the temperature range 24°C to 95°C, showed only small changes in the coefficient of thermal expansion (CTE) up to 50 cycles after an initial change during the first few cycles. The effects of UV and electron exposure on the CTE of composites were also investigated. UV exposure of up to 160 days and electron exposure up to 10^{10} rads had no significant effect on the CTE. However, electron exposure did cause considerable scatter in the data. Linear elastic and viscoelastic models were used to predict the thermal expansion and creep response of composite laminates. In general the agreement between predictions and experimental data was good. Data presented on the creep response pointed out that viscoelastic effects need to be considered for space applications when designing with angle ply composites. In addition, a discussion was presented on bonded strain gages which indicated that at low dose levels radiation exposure did not significantly alter strain gage response and therefore could be used in an environmental chamber for strain measurement at low-dose levels.

Dr Tenney presented an overview paper on the long term durability of composite materials in space. Major topic areas covered included radiation degradation of polymer matrix composites, dimensional stability of graphite reinforced polymer composites, and thermal control coatings. Experimental data on the radiation stability of epoxies and polysulfones showed significant changes in the chemical structure of the polymers. However, significant mechanical property changes of the composite were not observed at the dose levels (5×10^9 rads) being considered. These results were obtained using high dose rates to simulate a 30-year exposure with 30-60 hours of testing. The need for longer-term, low-dose rate tests, which more closely simulates the space environment, was identified. Data were also presented on the effect of microcracks on the CTE of graphite/epoxy composites, showing that cracks in the 90° plies reduce the CTE. Experimental data compared favorably with a finite element analysis used to predict the effect. Work on the development of high toughness matrix resins was also discussed. Use of these resins, which have a higher strain-to-failure than currently available epoxy resins, may eliminate matrix microcracking caused by thermal cycling. Dr Tenney also presented an overview of the requirements for thermal control coatings and an assessment of the status of currently available coatings. Experimental flight data were presented showing the increase in solar absorptance with flight exposure years of typical white paint coatings and second surface mirrors. Experimental data were also presented on two new polymer systems which look promising for thermal control coating development. A new colorless polyimide is being evaluated for second surface mirror applications and high conductivity polymer films may help to eliminate spacecraft charging.

Dr Bourguin discussed results of a program to simulate the acoustic environment of the Ariane launcher and measure the high level and wide-band frequency vibrations that are transmitted to the payload and equipment. Electrodynamic shakers were used to force vibrations in the launcher wall at the shroud which shelters the satellite. The proper simulation was achieved when measured responses at the wall exhibited spectral distributions and overall RMS levels close to the predicted flight values. The noise level inside the shroud of the Ariane vehicle and the vibrations transmitted to the payload were judged to be very close to those expected for flight conditions. The results were encouraging and demonstrated that the simulation method used could reproduce the random vibrations expected in the real environment with a high degree of reliability.

Mr Saylor reported the results of the experimental program conducted at General Electric on space environmental effects on composite materials. It was a very extensive program and included evaluation of Kevlar 49/5209, P75-S/CE339, GY70/X-30, and T300/934. Several different laminate orientations were fabricated and specimens were individually exposed to high-energy electrons in a vacuum chamber especially designed for use with the Van de Graaff located at the University of Illinois. Three levels of radiation were examined as well as specimens in both moist and dry conditions. Extensive mechanical and thermophysical property measurements were made on the

materials before and after exposure. Mechanical property tests were conducted over a large temperature range (-185°C to +120°C). Experimental data on some of the materials showed that the moisture saturation level increased by a factor of 2 due to electron radiation. Data also showed that the CTE for unidirectional graphite/epoxy laminates changed at elevated temperatures due to radiation exposure. The thermal conductivity of the graphite/epoxy material systems was not significantly affected by the radiation. In general, the Kevlar materials were much more sensitive to the space environmental exposure than were the graphite/epoxy materials.

Mr Dollery presented experimental results on the electrostatic discharging behavior of Kapton, Kapton-Aluminum laminate (25 μm Aluminum/75 μm Kapton), aluminized Teflon, a black thermal control paint (Chemglaze L300), a white thermal control paint (Chemglaze A276), and solar cell cover glasses under similar conditions. Samples were irradiated in vacuum with mono-energetic electrons of 5 to 30 Kev energy at temperatures from

180 to 70°C. Characterization of the electrostatic behavior included measurement of the maximum surface voltage, leakage current, mean discharge rate, mean discharge size, and maximum discharge size. Surface voltage profiles for Kapton irradiated with different energy electrons were presented and examples of the effect of discharges on surface voltage profiles were illustrated. In some cases electrical discharge resulted in physical damage (pinholes) to the Kapton film. One of the key conclusions reached in the paper was that use of the thinnest Kapton films available (thinnest studied 6-9 μm) as the outer component of thermal blankets would facilitate the removal of lower energy incident electrons, and thus reduce the susceptibility to dielectric breakdown by arc discharge.

Subsequent general discussions at the end of the session focused on the importance of having a good understanding of the long-term behavior of composite materials in the space environment. The need for such data was stated by materials researchers present and by a number of spacecraft designers who indicated that the design lifetimes of future spacecraft will likely be extended to a 15-20 year range. There was a consensus that general scarcity of good experimental data was a problem for the spacecraft designers in trying to insure long operational lives. Considerable discussion pursued as to the outlook for making significant improvements in space materials. Several examples of new materials development currently underway that hold promise for future space use were discussed. In general, the area of space environmental effects on materials was considered to be an important area of research and should be pursued vigorously in the future.

CANDIDATE MATERIALS FOR PRETENSIONED MEMBRANES OF FIBRE COMPOSITE MATERIALS FOR SPACE APPLICATION

by

W. Buchs

Messerschmitt-Bölkow-Blohm GmbH

Postfach 801140

8000 München 80 Germany

ABSTRACT

In recent years pretensioned membranes of fibre composite materials have become increasingly under consideration for use as solar cell substrates, thermal shields etc.

Various particular areas of investigation arose from loads (launch vibrations) and environmental conditions (vacuum, temperature, irradiation).

Glass-, Carbon- and Aramidfabric composite materials were analyzed with respect to the requirements and the interfaces determined by the tensioning frame.

Sections and full-scale samples of some membranes were manufactured and tested with methods, which in several cases had to be specifically developed for these purposes.

Special attention has been paid to the decrease of characteristics of aramid-fibre composites under UV-irradiation.

Analysis results are presented as well as test data and manufacturing experience.

1. INTRODUCTION

Compared to sandwich structures, which are in use in spacecraft subsystem structures with a mass per unit area of 1.1 to 1.4 kg/m² in composite construction, the use of pretensioned membranes plus frames was calculated to end up with the amount of 0.7 to 0.9 kg/m². This promising benefit combined with high packing density should be taken into account specially when talking about large spacecraft structures such as solar array structures for directly broadcasting satellites. The design details in the following pages are taken from the development of membranes for the Ultra-Light-Panel solar array (ULP).

The results concerning material selection, however, should be also valid for similar applications such as for thermal shields, plain reflecting layers etc.

Figure 1 shows the whole assembly of the ULP solar array at the MBB test facility. /1/ gives detailed information about development and qualification of the whole subsystem.



Fig. 1 ULP solar array with Carbon-Fibre Composite (CFC) frames and pretensioned membranes covered with solar cells

2. TYPICAL DESIGN REQUIREMENTS

The main design requirements relevant for the membrane and its interface to the frame are typically the followings

- withstand the static launch loads
- withstand the launch vibrations from sinusoidal, random and acoustic vibration with limited amplitude (two neighboured membranes may not touch in the stowed array due to vibrations)
- show a first natural frequency of above 20 Hz, in order not to interfere with the first natural frequency of the spacecraft
- withstand deployment shocks
- withstand temperatures from -180°C up to 100°C
- withstand irradiation from 7 years geostationary orbit without a decrease of characteristics, which could prevent function in orbit
- have provisions for electrostatic discharge

3. DESIGN DESCRIPTION

3.1 Membrane suspension

In order to meet the static and dynamic launch requirements, a membrane suspension in one axis providing a global (including frame stiffness) equivalent spring constant of about 200 N/mm was chosen.

This spring constant mainly is provided by an appropriate bending stiffness of the suspension beam. The bending line of these two beams is compensated by individual packages of cup springs at 11 suspension points.

The two not suspended edges are basically free, a so-called "fishing-line", however, limits the edge amplitudes.

Fig. 2 illustrates the arrangement of the outermost spring-package (in suspension beam) bracket at the end stringer of the membrane and the "fishing-line" at the free membrane edge.



Fig. 2 Membrane suspension in high modulus CFC frame (white cabling is test cabling)

At 7 lines over the panel the membrane furthermore is guided between two auxiliary beams of high modulus CFC in a sliding manner. This, too, is for raising the membrane's first natural frequency and lowering the amplitudes.

More details about the structure design, specially of the frame, are given in /2/.

3.2 Membrane components

The load carrying part is a 1 layer composite structure of fibres and epoxy resin. It is covered at the cell-side by a thin plastic film, which acts as bonding surface for solar cells and electrical isolation, when using carbon-fibres in the composite.

The suspension edge shows an end stringer with unidirectional CFC, suitable for joining the suspension brackets (see figure 2).

The "fishing-line" is joined by tab elements of composite. In the sliding area between the auxiliary beams stiffeners of composite material are bonded to the basic membrane.

4. MATERIAL SELECTION

4.1 Beams

All beams are designed in high modulus CFC, in order to meet the frequency requirements.

4.2 Suspension elements

Cup springs are of steel, coated with nickel, the bolts are of inoxidable steel, coated with chromium. The bracket elements are made of anodized aluminium. The reasons for these materials were mainly to avoid galvanic und wear problems.

4.3 End stringers, stiffeners, tabs

In general the same materials as in the basic membrane are used. The preferred fibre orientation in the end stringers is unidirectional, the one in the stiffeners and tabs $0^\circ/90^\circ$ (tensile-stiffness and strength in plain required).

4.4 Basic membrane

Calculations showed that very light fabrics (in plain weave in order to avoid "curling" after curing at elevated temperatures) or filament wound skins would be desirable from frequency point of view. In order not to cause unacceptable distortions of the panel at the deep temperature extreme (-180°C), the basic membrane should have a coefficient of thermal expansion close to the one of the frame - i.e. close to zero - and a low inplain tensile stiffness $E \cdot t$.

Investigations showed that plain weave fabrics were commercially available as
 glassfibre fabric with 26 g/m^2
 aramidfibre fabric with 60 g/m^2
 carbonfibre fabric with 66 g/m^2 .

Although offering the lowest mass (55 g/m^2) and tensile stiffness (1930 N/mm), the glassfibre composite (GFC) had to be rejected because of the high coefficient of thermal expansion ($\alpha = 11,2 \cdot 10^{-6} \text{ m/mK}$).

The filament winding of (high modulus) carbon fibre was rejected because of the high costs: a huge mandrel would have been necessary.

From the commercially available fabrics the high tensile CFC with a mass of 115 g/m^2 , a stiffness of 4100 N/mm and a coefficient of thermal expansion of $3,5 \cdot 10^{-6} \text{ m/mK}$ seemed to be the best compromise. Therefore, the first membranes were manufactured in CFC.

The suitable matrix material was epoxy resin with a curing temperature of 120°C , the suitable plastic foil material seemed to be a polyimid foil with $12,5 \mu\text{m}$ thickness.

Later negotiations with a fabric weaver, however, brought a unidirectional aramid-fibre fabric composite (AFC) into discussion with a completed mass (i.e. including epoxy and polyimidfoil) of 88 g/my of a stiffness of 2830 N/mm and a coefficient of thermal expansion of $1,3 \cdot 10^{-6} \text{ m/mK}$.

As this membrane revealed superior the one of CFC it was decided to manufacture and test one further membrane of this kind.

4.5 Adhesives

Room temperature curing epoxies and epoxy resins curing at 120°C were chosen as adhesives, because experiences from other programs were available on these.

5. MANUFACTURING EXPERIENCE

The first manufacturing step is unrolling the polyimid film on a table and cleaning it. Figure 3 shows a check to local defects by a high voltage test device, the so-called "wet-sponge" test.

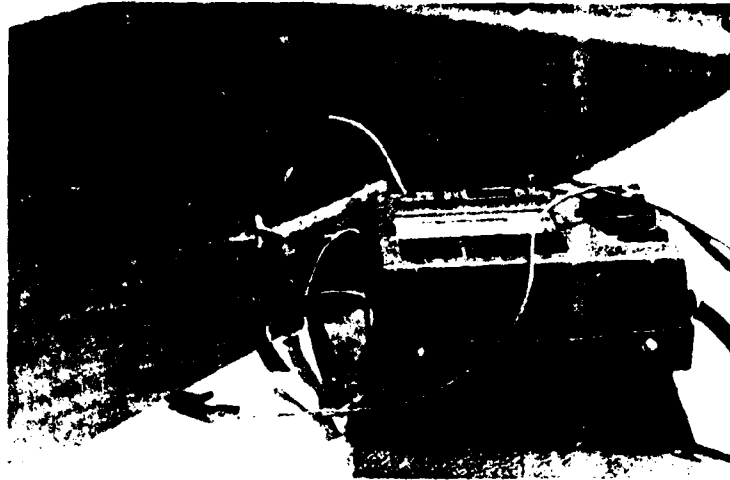


Fig. 3 "Wet-sponge" test for local defects of polyimide film

Then the polyimide film is wetted with resin + hardener and the dry fabric is positioned on it and impregnated with rollers.

The vacuum lay-up is applied and curing in the autoclave is performed (autoclave yields high fibre volume content).

After unpacking besides of the standard inspection criteria (e.g. to fibre misalignments) the "wet-sponge" test is repeated.

At this step the intended 12,5 μm thick polyimide film showed much more defects (i.e. was penetrated by carbon fibres) than at the initial inspection. Therefore, a 25 μm thick polyimide film had to be taken for CFC membranes, which now had a mass of 135 g/m^2 instead of 115 g/m^2 before.

After this inspection the basic membrane is cut to size and prepared for assembly with the stiffeners, stringers and tabs, which had been prepared in separate press-moulds.

The assembly is performed on a special bonding table, which allows exact positioning of all components to be bonded.

6. TESTING

6.1 Outgassing

Shortly after the selection of materials the outgassing behaviour had to be proven. For the CFC basic membrane a total weight loss (TWL) 0.32% and an amount of volatile condensable material (VCM) of 0.03% was determined. For the basic AFC membrane the corresponding figures were: TWL 0.96%, VCM 0.04%.

The comparatively high amount of TWL at the AFC membrane was found to be water.

6.2 UV-Irradiation

In a previous program the influence of space irradiation on CFC was investigated and no degradation was detectable. Therefore, no irradiation test was performed with the CFC membrane.

From numerous publications, however, the decrease of strength of unprotected AFC under UV-irradiation is known.

Initial measurements with polyimide films even thinner than 12.5 μm had shown, that in the range of wavelengths about 200 nm ("hard" irradiation) the transmission of UV-light was below 1%, in the range of 450 nm between 5% and 10%.

A 1000 h irradiation test with 6 + 2 solar constants at 60°C was performed in order to verify that the protection by the 12,5 μm thick polyimide film was sufficient.

The result was: no influence on stiffness detectable comparing irradiated (series III) to untreated specimen (series I). An increase in stiffness was measured at the specimen treated with 60°C for 1000 h (series II), which was assumed as post-curing effect.

Figure 4 shows measured stiffness data of the three series.

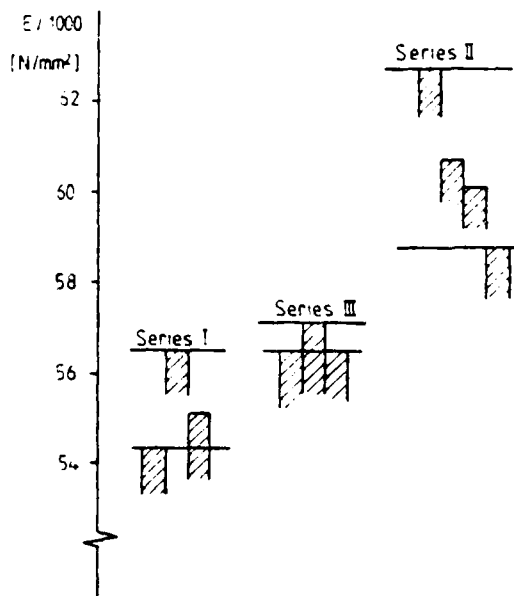


Fig. 4 Measured stiffness data after UV-irradiation

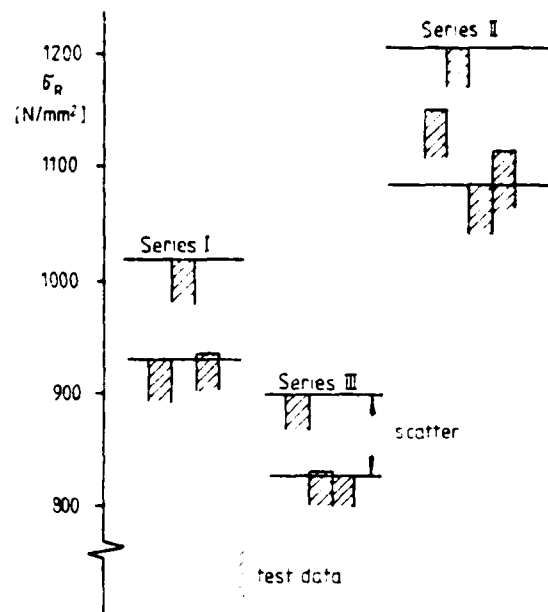


Fig. 5 Measured rupture strength after UV-irradiation

Concerning strength, a decrease of 11% was measured (see Figure 5), and again a postcuring effect could be postulated.

Extrapolating the initial decrease to 7 years orbit lifetime, it was stated that no risk for the mission exists by the expected degradation of the strength.

It should, however, be kept in mind that the number of test specimen due to the expensive irradiation tests was limited to 3 and 4 per measuring point, respectively. The figure of 11% degradation thus should be more regarded as a trend information which has to be substantiated by further tests.

6.3 Stiffness and strength

For the stiffness and strength measurement a special test method had to be developed for the basic substrate as commercially available strain gauges turned out to be too large compared to the fine yarns of the substrate.

Figure 6 shows the test specimen and the test equipment: a tensile test specimen 300 x 15 mm with aluminium doublers is suspended soft against bending in the test machine. Mechanical elongation gauges (200 mm length) take the edges of the aluminium doublers as referred elongation length.

For strength tests the mechanical elongation device is removed.

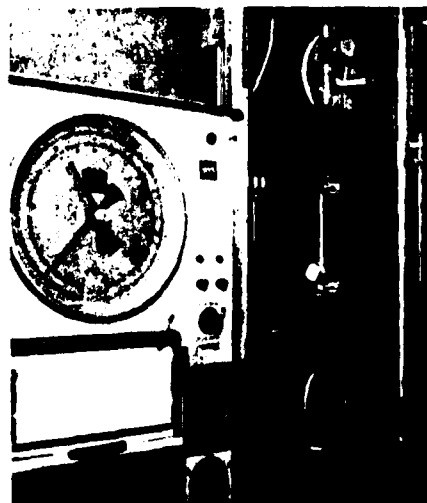


Fig. 6 Test specimen and test equipment for stiffness and strength determination of basic substrate

The strength of the stringer bondings was determined in a further test series with representative "mini-membranes" in representative suspension. All specimen showed high margins of safety referred to the acting loads during the mission. In several cases the load introduction bracket failed - see figure 7.

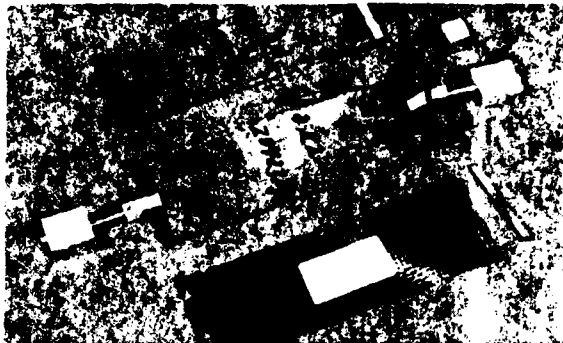


Fig. 7 Three types of failures at suspension load introduction: failures of matrix to fibre adhesion (above), failure of bracket (center), failure of end stringer bonding (bottom)

7. CONCLUSIONS

The manufacturing of several full-scale membranes and the performed environmental and mechanical testing showed that both carbonfibre and aramidfibre composite membranes are suitable for geostationary orbit missions. For mass reasons, not existing of isolation problems and minimization of suspension frame distortions at deep temperature extremes the aramidfibre membrane can be recommended for further applications.

LITERATURE

- /1/ Schneider, K.: Development and Testing of the ULP Solar Array ESA SP - 140, November 1978
- /2/ Bansemir, H.
Buch, W.: Leichtbaustrukturen aus CFK für Satellitensolargeneratoren verschiedener Größe
DGLR - Vortrag Nr. 81-080, Aachen, 1981

EFFECTS OF LONG DURATION EXPOSURE TO SIMULATED SPACE ENVIRONMENT ON NONMETALLIC MATERIAL PROPERTIES

by

Charles L. Peacock, Jr. and Ann F. Whitaker
NASA - Marshall Space Flight Center
Marshall Space Flight Center, Alabama, U. S. A. 35812

SUMMARY

Nonmetallic materials specimens from the Viking program were tested *in situ* *in vacuo* after continuous thermal-vacuum exposure from 1971/1972 to the present. Eleven ASTM based tests were done on appropriate specimens of 30 materials; however, no single material received all the tests. Some specimens also were exposed to 1 or 2.5 MeV electrons at differing fluences before testing. Baseline exposure data is reported here for graphite/epoxy specimens that had been exposed to vacuum since 1974. These materials have been transferred to the thermal vacuum storage facility for future *in situ* testing and irradiation.

Thin G/E specimens were tensile tested after thermal-vacuum cycling exposure. Photomicrographic examinations and SEM analyses were done on the failed specimens.

INTRODUCTION

The space structures and advanced space transportation systems that are envisioned for space flight in the next several decades must be fabricated from long-life, low-cost, environment-resistant materials in order to be economically feasible and to meet mission goals. Materials technology must be advanced through studies to identify degradation and changes in properties of materials induced by environmental exposure, to define degradation mechanisms by which environmental parameters interact with the materials, to determine accelerated test methodology, and to derive accurate degradation prediction modeling techniques. Since previous work has shown that it takes a decade or more to bring a material concept to engineering readiness, NASA has emphasized a strong space materials durability research and technology program to develop new and improved materials.

Composite materials show great promise for structural applications in future space systems and are being used today in critical structural elements of space systems, such as the graphite-epoxy metering truss, focal plane structure, and optical bench structures of the Space Telescope. Fiber resin composites such as graphite-epoxy, boron-epoxy, graphite-polyimide, and graphite-Kevlar-epoxy are being proposed as primary structural materials in design studies of future long-life large space systems. The improved performance characteristics of fiber-metallic matrix composites make them highly attractive structural and engineering materials for specialized applications in space systems. Consequently, there exists a great need for increased research and technology development of environmentally resistant advanced composites. Comprehensive environmental testing of composite materials is vitally required because of the complex and varied degradation effects that are induced in composites by long duration exposure to the different external and internal environmental parameters of space systems.

At the conclusion of the Viking Mars Lander program, a number of samples of a wide variety of materials that had passed the initial screening tests remained in thermal-vacuum exposure at the Martin-Marietta Corporation (MMC). The decision was made at that time to continue the thermal-vacuum exposure of these materials with the plan of reestablishing a test program to measure the effects of long duration exposure on the properties of these materials in the future. In 1979, MMC and the Materials and Processes Laboratory at the Marshall Space Flight Center (MSFC) decided that sufficient exposure had occurred to warrant testing some of the specimens to obtain data on nominally nine years exposure. Over 150 specimens of 30 of these materials were evaluated including some with electron exposure in the present program.

In 1973 test specimens from 12 different graphite-epoxy samples that had been fabricated at MSFC were put into long duration vacuum exposure following baseline materials properties measurements. These specimens were transferred *in vacuo* to MMC for *in situ* testing and inclusion in the irradiation testing with the Viking specimens.

Specimens from 10 sets of samples of thin 150 μm to 560 μm graphite-epoxy composites fabricated by Hercules Aerospace Division in 1980 have undergone baseline testing and thermal-vacuum cycling testing. Long duration thermal-vacuum exposure of some of these specimens has been started at MMC.

This paper describes the results of evaluations of a variety of long term (since 1971 and 1973) thermal-vacuum exposed materials and short term (1982) thermal-vacuum cycled thin graphite-epoxy materials. The materials reported on here along with their descriptions are shown in Tables 1-a and 1-b.

TEST FACILITIES

The testing and evaluation work reported herein was accomplished jointly at Marshall Space Flight Center (MSFC) and Martin-Marietta Corporation (MMC), Denver Aerospace Division. The unique *in situ* vacuum test chambers and thermal-vacuum exposure systems at MMC were complemented with the Van de Graaff accelerators at MSFC to achieve

the desired tests and environmental exposures.

Thermal-Vacuum Exposure Facility (MMC)

The long-term vacuum exposures were accomplished at MMC in individual canisters connected to ion pumps. Four canisters are coupled directly to 50 ℓ/s ion pumps and the remaining 28 are connected to seven-canister plenums, with each plenum attached to a 400 ℓ/s ion pump. Each system is capable of maintaining pressures in the 10^{-5} to 10^{-6} pascal (10^{-7} to 10^{-8} torr) range. Each canister is constructed of 300-series stainless steel, with a double wall for circulating water and maintaining the required thermal conditions in the canisters. A Marman clamp seals the lid to simplify remote opening and closing of the canisters in the test chamber. Two vacuum valves between the canister and vacuum plenum permit the canister to be removed from the pumping system and transferred to the test chamber without altering the pressure in the canister or plenum. A recirculating hot water heater maintains canister temperatures between ambient and 66°C.

Vacuum In Situ Test Facility (MMC)

The Vacuum In Situ Test Chamber at MMC is constructed of 300-series stainless steel and consists of two individual vacuum chambers separated by a sliding gate valve. The main chamber is a nominal 1.5 meters (5 feet) in diameter and 2.1 meters (7 feet) long. The pumping portion of the main chamber consists of two 7.9 cm (20-inch) diffusion pumps with a multicoolant baffle and a valve isolating the pump from the chamber. The airlock pumping system consists of a 2.4 cm (6-inch) diffusion pump with a multicoolant baffle and isolation valve. The .55-square-meter (6-square-foot) chamber window has three tempered glass sections. A door on one end provides easy access to the entire chamber interior.

The unique feature of this system is the master/slave manipulation capability in the main chamber. Three manipulators provide six degrees-of-freedom and have electric indexing in two axes for displacement of the master arm relative to the slave arm. All other motions are mechanical, with a one-to-one force ratio between the master arm and the slave arm except for the friction of the motion rods within the seal tube assembly.

A Universal test machine is coupled to the main chamber. The columns are shock-isolated from the chamber with bellows and a moving crosshead pull rod is attached to the bellows. Tensile, compression, flexure, and shear tests have been performed in this chamber. Electrical property tests, including dielectric strength, dielectric constant, and surface and volume resistivity, are conducted with the aid of special fixturing developed by MMC for use in vacuum with the master/slave manipulators.

Radiation Effects Facility (MSFC)

The Radiation Effects Facility of the Materials and Processes Laboratory located at MSFC includes two Van de Graaff accelerators, a Model A-2500 and a Model A-400 in a shielded irradiation room with an associated control room. The irradiations that were performed for this work were done with the A-2500 accelerator operating in the negative mode producing electrons with energies of either 1.0 MeV or 2.5 MeV as required for the different specimens. An electromagnet is used to deflect the electron beam into the irradiation vacuum canister and to provide a monoenergetic electron flux. A 19 μm (0.75 mil) thick aluminum foil was used to spread the electron beam to cover the desired irradiation area without significantly degrading the energy of the electrons. The electron beam fluxes were kept low, of the order of 10 to 15 μA , for all irradiations to minimize thermal effects in the specimens. Faraday cups were mounted inside the canisters to monitor the electron beam during the irradiations.

DISCUSSION OF RESULTS

Viking Mars Lander Materials

For the Viking Mars Lander program, MMC performed a series of screening and qualification tests on the candidate materials proposed for the lander capsule. All proposed materials were screened initially by thermogravimetric analysis (TGA) with materials that showed relatively high weight loss and a relatively low decomposition temperature being rejected at this time. The materials that passed the screening tests were subjected to more detailed TGA/RGA, heat compatibility, and physical properties tests before and after thermal-vacuum exposure to qualify them for use in the lander (Ref. 1 & 2).

The residual material specimens that were not used during the Viking program have been maintained in a controlled thermal-vacuum environment in the vacuum exposure system at MMC since 1971. Some 150 specimens of 30 of these materials were selected for testing after nominally 9 years exposure at 66°C (150°F) temperature and 10^{-4} pascal (10^{-6} torr) vacuum. The tests selected for a particular material were determined by the baseline and short term tests that were originally done on that material in 1971/1972. All tests were done *in situ* in vacuo in the MMC Vacuum In Situ Test Facility. The specimens were kept in a vacuum environment at all times during transfer and testing through the use of the portable vacuum canisters and the chamber airlocks.

A limited number of specimens were irradiated with electrons at the MSFC Radiation Effects Facility. These specimens were maintained constantly in a vacuum environment at all times during transfer between Denver, CO, and Huntsville, AL, and during irradiation. The lap shear specimens were exposed to a fluence of 1×10^{15} e^-/cm^2 of 2.5 MeV electrons. All other specimens were irradiated with 1 MeV electrons to a fluence of 1×10^{14} e^-/cm^2 except for the initial irradiation test in which a fluence of 1×10^{15} e^-/cm^2 was used. Some of these specimens were degraded to the extent that they broke while being removed from the canister at MMC; therefore, the lower fluence was selected for subsequent irradiations.

The Viking program materials that were tested are identified in Table 1-a along with their manufacturer. Table 2 lists the materials tests that were done *in situ* in the vacuum chamber and the ASTM test procedure that was followed (Ref. 3).

The results of the tests, the number of specimens, and the date the tests were performed are given in Tables 3 through 11. The average value and the range of values are listed. The tensile data given in Table 3 show that the tensile strength of most nonmetallic materials will be affected significantly by thermal-vacuum exposure with Kapton being the least affected. The initial short exposure usually, but not always, produced a sharp decrease in strength and the longer exposure gave a slight recovery. The effect of electron irradiation, however, was to reverse the effects of the thermal-vacuum exposure.

The lap shear strength data given in Table 4 for adhesives and coatings generally showed an increase in strength for short duration thermal-vacuum exposure, but a large decrease for the long duration exposure. All of the electron irradiated specimens showed a relative increase in strength. Thus, the electron radiation tended to reverse the effect of the long thermal vacuum exposure on the lap shear strength of the adhesives tested.

The flexure strength data in Table 5 and the compression strength measurement in Table 6 indicate that the effect of the long thermal-vacuum exposure is a continuation of the effect of the short exposure for the tested materials on these parameters. The 180-degree peel strength data in Table 7 also shows a similar trend for two of the materials. The overlap of the data for the PC board indicates no significant change occurred for this material. Likewise the hardness measurement given in Table 8 shows no significant change for the various environments.

The dielectric strength data in Table 9 reveals that for all materials tested the dielectric strength is reduced significantly by short duration thermal-vacuum exposure; however, some materials tend to recover with long exposures, but other materials continue to decrease. The dielectric constant and dissipation factor data in Table 10 and the volume resistivity data in Table 11 show similar responses.

Thermogravimetric Analysis

A useful technique for predicting polymer system degradation kinetics at moderate temperatures is high temperature thermogravimetric analysis (TGA) in conjunction with mass spectral analysis with a residual gas analyzer (RGA). In TGA a small sample of material is taken through total decomposition by increasing the temperature of the sample at a constant rate (e.g., 10°C/min.) in vacuum while continuously measuring the weight loss of the sample.

The variation of the rate constant with temperature is represented by the Arrhenius equation

$$k = A e^{-\frac{\Delta E}{RT}}$$

where k is the reaction rate constant, T is the absolute temperature, R is the gas constant, ΔE is the energy of activation, and A is an integration constant. Generally the thermal degradation reaction is a first order reaction with the degradation rate proportional to the concentration of the reacting material

$$-\frac{dc}{dt} = kC$$

where C is the concentration of the reaction species, and t is time.

Thus the activation energy is given by

and the rate constant is determined from

$$k = \frac{1}{a-x} \frac{dx}{dt}$$

where a is the initial weight of the sample, x is the weight loss after time t , and $\frac{dx}{dt}$ is the rate of weight loss.

Figure 1 shows a schematic multistage (here two-stage) TGA curve. In Table 12 the number 2 in the column headed "Stages in the TGA Curve" refers to curves similar to that depicted in Figure 1. The number 1 indicates that only a one-stage degradation takes place through total decomposition, and the number 3 indicates an even more complex degradation than depicted in Figure 4, that is, a three-stage degradation through total decomposition. With multistage decompositions only the lowest temperature degradations (i.e., stage 1) were analyzed since this would be the one expected to dominate the near normal-use temperature isothermal decompositions. In the column labeled "Reaction Mechanism in Stage 1," the a_0 is the so-called "active component" in chemical kinetics terminology, and B represents the chemical component resulting from the degradation of a_0 . Some materials show a simple mechanism, $a_0 \rightarrow B$, of degradation while others show a complex mechanism, $a_0 \rightarrow \frac{B}{C}$ where a_0 decomposes to B at the lower temperatures and $a_0 \rightarrow C$ as the temperature increases within stage 1. Thus materials labeled 1 (i.e., single stage) a_0 decomposes to B at the lower temperature and $a_0 \rightarrow C$ as the temperature increases within stage 1. Thus, materials labeled 1 (i.e., single stage) and $a_0 \rightarrow B$ have a simple reaction mechanism through total degradation. Materials labeled as multistage (i.e., 2 or 3) and $a_0 \rightarrow \frac{B}{C}$ will have an exceedingly complex degradation since the decomposition stage (or stages) at higher temperatures, which were not analyzed for the present study, may also degrade by complex routes such as $(d_0) \rightarrow \frac{E}{F}$.

Graphite/Epoxy Composites

In 1973 graphite/epoxy samples were fabricated by the Materials and Processes Laboratory at MSFC using High Modulus Surface-treat (HMS) graphite fibers at orientation angle increments of 45° and 60° in types 5208, 3501, and BP-907 epoxy resins in the combinations shown in Table 1-b. Tensile test specimens were cut from these samples. Baseline tensile test data were taken, and a set of specimens from the 0.8 mm (30 mil) and 1.0 mm (40 mil) thick samples were exposed to a fluence of $2.63 \times 10^{16} \text{ e}^-/\text{cm}^2$ of 2.0 MeV electrons. A second set of these tensile specimens were exposed in vacuum to ultraviolet light from a solar simulator using a xenon lamp source for 2000 ESH. This data, shown in Table 13 has considerable overlap between the range of electron or UV irradiated values and the range of the baseline data, and indicates no significant degradation was induced by these levels of radiation (Ref. 4).

The remaining specimens were placed in a vacuum chamber at MSFC for long duration vacuum exposure. In 1981 the specimens were transferred to one of the vacuum storage canisters and transferred to MMC in the MSFC mobile vacuum system van. In situ testing and irradiation of these graphite/epoxy specimens is in progress.

Thin Graphite/Epoxy Materials

Tensile and shear specimens of thin graphite/epoxy materials were obtained from Hercules, Inc. for environmental testing. Hercules used their HMS/3501-6 graphite prepreg tape to fabricate high modulus specimens. Unidirectional layups of 2, 3 and 8 plies and $\pm 45^\circ$ layups of 4 and 8 plies in a $(+45^\circ, -45^\circ, -45^\circ, +45^\circ)$ pattern were prepared. With a nominal tape thickness of 7.5 mm (3 mil), the specimens ranged from about 15 mm (7 mil) to nearly 60 mm (22 mil) in thickness. Top and bottom caul plates as well as special processing of the laminate sheets were used by Hercules to achieve improved surface flatness and consistent thickness of the specimens. Data generated only on the $\pm 45^\circ$ layups are reported on here.

Specimens of the HMS/3501-6 $\pm 45^\circ$ layup material were thermally cycled in the thermal vacuum chamber from -73°C (-100°F) to 149°C (300°F) in a vacuum of the order of 10^{-2} pascal (10^{-4} torr) with each thermal cycle lasting about an hour. The tensile data are shown in Figure 2 for specimens removed after 104, 522, and 2003 cycles. The anomalous behavior of the 8 ply specimens after 522 cycles as yet has not been determined.

After the tensile and flexure testing was completed the specimens were cut in half using a diamond saw. One section was used for SEM examination of the surface and the other section was mounted for photomicrographic examination. The tensile specimens were cut near the failed area and the filament density of that cross-section was measured. No correlation was found between the tensile data and the filament density.

The specimens were examined by SEM on one surface to determine presence of cracks and other anomalous conditions. Photomicrographic examinations were made on cross-sectioned specimens to evaluate sub-surface cracking, delamination filament distribution and other conditions. The control sample illustrated conditions representative of all the samples, such as missing fibers in one laminate and a surface pattern created by the woven "bleeder" cloth used when pressing the laminates and not associated with the graphite fiber layup. No cracks were found in either of the control samples. Examples of the microcracking are seen in Figure 3 for specimens after 104, 522 and 2003 thermal vacuum cycles. Samples thermal cycled 104 times had cracks both surface and sub-surface (Figures 3a & b). The surface cracks were oriented parallel to the layer of fibers immediately below the surface and were relatively uniformly spaced at intervals of approximately 35 mm (0.014 in.) over the surface. The sub-surface cracks occurred in the matrix between the laminates and at the fiber-matrix interface perpendicular to the line of the composite sheet. After 522 cycles the surface cracks became more numerous and wider (Figures 3c & d), with spacings on the order of 30 mm (0.012 in.) to 6 mm (0.0025 in.) and some cross-cracks started to appear at 90° to the predominant crack direction. Internal cracks became longer and extended across two or more plies. With further cycling to 2003 cycles the surface crack spacing remained about the same as at 522 cycles but were more pronounced (Figures 3e & f), both parallel and perpendicular to the first sub-surface laminate. The extent of cracks perpendicular to the laminates seen on the cross sections were about the same as at 522 cycles but there was considerable more cracks parallel to the laminates.

Examinations of the thermal cycled samples showed that the primary degradation due to cycling was crack formation in the epoxy matrix and this degradation increased with increasing number of cycles. Initially the cracks were predominantly perpendicular to the plane surface of the composite and, with increased cycling, also occurred parallel to the surface. Internal cracks were mostly at the interface between the graphite filaments and epoxy. The cracks observed on the surface were mostly parallel to the outer laminate filaments and generally increased in width up to 522 cycles. This is probably due to shrinkage of the epoxy as a result of continued curing due to heating during cycling and this fact may account for the observed increases in strength at 522 cycles. This "post-curing" may have masked the degradation due to cycling until further damage was caused by cycling up to 2003 cycles.

CONCLUSIONS

The data reported herein for the Viking materials shows that the effect of long duration exposure to space environments on some of the properties of many nonmetallic materials is not predictable from the response of those materials to short duration exposures. Electrical insulating materials, for example, often showed a recovery after long exposure of the electrical properties that were degraded during short exposure. A surprising result is that electron irradiation sometimes reverses or reduces the change in material properties that was induced by vacuum exposure.

These results confirm the need for continued testing and evaluation of materials exposed for long durations to simulated space environments in order to identify acceptable materials for long-lived spacecraft. The wide variance in the

patterns of this data exceeds the capability of current models to predict the degradation and verifies the necessity for more advanced studies of degradation mechanism modeling techniques.

REFERENCES

1. Martin-Marietta Corporation, Handbook-Nonmetallic Materials, 1974, NASA CR-132673.
2. Martin-Marietta Corporation, unpublished data, 1974.
3. Martin-Marietta Corporation, Final Report - Evaluation and Prediction of Long-Term Environmental Effects on Non-metallic Materials, 1982, MCR-82-530.
4. C. L. Peacock, Jr., George C. Marshall Space Flight Center, Proceedings of the Second Annual Research and Technology Review, 1974, Pages 184-193.

ACKNOWLEDGEMENTS

This report presents the work of many persons of whom only a few key individuals can be mentioned. At MSFC, over the past three years, the electron irradiations were performed by D. Gregory and C. D. Stocks. The thermal cycling testing was done by B. E. Cothren and L. M. Thompson. The photomicrographs were prepared by J. A. Burka. The base-line data was provided by Dr. J. M. Stuckey.

The in situ testing at MMC was accomplished by J. A. Shepic, R. F. Geisendorfer, H. A. Papazian and J. C. LeBeau.

The typing of this manuscript by Ms. Barbara Simms is especially appreciated.

TABLE 1-a - VIKING MATERIALS LIST

Material	Classification	Manufacturer
Abefilm 501	Film Adhesive	Ablestik Labs
Adlock 851	Phenolic Laminate	Am Reinforced Plastics
Choseal 1224	Conductive Elastomer	Chromerics Inc.
Choseal 1236	Conductive Elastomer	Chromerics Inc.
DC93-500	Silicone Encapsulant	Dow Corning Corp.
DC6-1106	Sealant	Dow Corning Corp.
Diall FS-80, Type G01-30	Molding Compound	Miro Plastics Inc.
EA 934	Structural Adhesive	Hysol
EA 956	Structural Adhesive	Hysol
EA 9414	Structural Adhesive	Hysol
EC 2216	Structural Adhesive	3M
Eccofoam FPH	Structural Adhesive	Emerson and Cuming, Inc.
FM 96U	Structural Adhesive	Am. Cyanamid Co.
HT 424	Structural Adhesive	Am. Cyanamid Co.
HT 435	Film Adhesive	Am. Cyanamid Co.
C7-4248	Epoxy Resin	Hysol
Kapton F, 011	Electrical Insulation	E. I. duPont
Kapton F, 919	Electrical Insulation	E. I. duPont
Kynar Tubing	Heat Shrinkable Tubing	Raychem Corp.
Lexan	Polycarbonate	GE
Lucite	Acrylic	E. I. duPont
Nylon	Polyamide	General Electric Co.
Polyethylene	Polyethylene	E. I. duPont
Polythermalese Wire	Magnet Wire Insulation	-
Polyurethane	Polyurethane	Belden
Printed Circuit Board-Type GF	Laminated Sheet	-
Solithane 113	Polyurethane Coating	Synthane-Taylor Corp.
Stycast 1090	Epoxy Encapsulant	Thiokol Chem Corp.
Therm-Amid Wire	Magnet Wire Insulation	Emerson and Cuming, Inc.
Vespel SP-1	Polyimide	Rea Magnet Wire Co. E. I. duPont

TABLE 1-b - MSFC GRAPHITE/EPOXY MATERIALS

<u>Sample</u>	<u>Manufacturer</u>	<u>Fiber</u>	<u>Resin</u>	<u>Fiber Orientation</u>	<u>Number of Plies</u>
T-22	MSFC	MOD I	5208	$\pm 45/90$	8
T-24	MSFC	MOD I	5208	$\pm 45/90$	16
T-26	MSFC	HMS	3501	$\pm 45/90$	16
T-27	MSFC	HMS	3501	$\pm 45/90$	8
T-35	MSFC	HMS	BP907	± 60	6
T-36	MSFC	HMS	BP907	$\pm 45/90$	8
T-37	MSFC	HMS	BP907	± 60	12
T-38	MSFC	HMS	BP907	$\pm 45/90$	16
T-40	MSFC	MOD I	5208	± 60	12
T-41	MSFC	MOD I	5208	± 60	6
T-42	MSFC	HMS	3501	± 60	12
T-43	MSFC	HMS	3501	± 60	6
H-9	Hercules	HMS	3501-6	± 45	4
H-10	Hercules	HMS	3501-6	± 45	8

TABLE 2 - TEST METHODS UTILIZED TO EVALUATE MATERIALS

<u>Test</u>	<u>ASTM</u>
1. Tensile Strength	D638, D882
2. Lap Shear Strength	D1002
3. Flexure Strength	D790, C393
4. Compression Strength	D695, D3410
5. 180-deg Peel Strength	D1967, D903
6. Hardness	D785
7. Dielectric Strength	D149
8. Dielectric Constant	D150
9. Dissipation Factor	D150
10. Volume Resistivity	D257
11. Thermal Degradation	See Text

TABLE 3 - MATERIALS EVALUATION - ULTIMATE TENSILE STRENGTH IN MPa,
NUMBER OF SPECIMENS, AND DATE TESTED

Material	Baseline	1 Mo/3 Mo	Long-Term	After Irrad
Adlock 851	184 +80 -70 (5) 06/71		234 +33 -45 (5) 07/80	
Vespel SP-1	124 +5.0 -7.0 (5) 10/71	124 +8.0 -11.0 (5) 11/71	139 +2.0 -2.0 (5) 01/80	139 +2.0 -36 (3) 05/81
Kapton F, 919	103 +10.3 -15.8 (5) 11/71		109 +18.6 -36.5 (5) 05/80	
Kapton F, 011	93.4 +20.7 -22.1 (5) 11/71		84 +19.3 -26.2 (5) 05/80	
Lucite	88.9 +1.4 -4.9 (5) 03/72	68.9 +6.1 -4.6 (3) 06/72	77.1 +1.2 -2.9 (4) 05/80	64.6 (1) 05/81
Lexan	66.7 +5.3 -4.2 (5) 03/72	62.4 +2.3 -1.2 (4) 09/72	58.5 +0.6 -0.3 (4) 05/80	62.6 +2.0 -2.8 (4) 05/81
Polyurethane	56.1 +2.3 -2.4 (5) 03/72		55.3 +5.9 -2.3 (4) 05/80	47.4 +1.5 -0.8 (3) 05/81
Nylon	59.3 +2.7 -0.9 (5) 03/72	56.5 +1.5 -1.9 (4) 09/72	77.2 +1.4 -1.4 (3) 05/80	86.8 +1.4 -0.6 (4) 05/81
Polyethylene	14.5 +1.6 -2.4 (5) 03/72	9.78 +0.05 -0.05 (4) 09/72	10.5 +3.30 -1.80 (4) 05/80	15.4 +0.20 -0.10 (3) 02/82

TABLE 4 — MATERIALS EVALUATION - LAP SHEAR STRENGTH[†] IN MPa,
NUMBER OF SPECIMENS, AND DATE TESTED

Material	Baseline	1 Mo/3 Mo	Long-Term	After Irrad
Ablefilm 501	25.1 +2.07 -2.76 (5) 08/72	30.6 +0.96 -1.31 (5) 11/72	27.1 +3.04 -0.34 (5) 03/80	
EC 2216	27.9 +0.34 -0.83 (5) 10/71	28.1 +3.1 -3.2 (5) 01/72	32.7 +1.24 -1.45 (5) 01/80	
EA 934	16.7 +1.31 -1.79 (10) 10/71	16.9 +1.45 -1.10 (5) 11/71	15.8 +0.55 -1.17 (5) 01/80	16.1 +0.69 -0.83 (5) 05/81
EA 956	14.5 +1.0 -0.4 (3) 08/72		14.9 +0.70 -0.30 (3) 05/80	
EA 9414	36.6 +2.3 -2.2 (3) 08/72		42.6 +1.1 -2.2 (3) 05/80	
FM 96U	22.6 +0.83 -0.47 (5) 11/71	23.5 +1.38 -1.38 (5) 01/72	21.8 +2.40 -3.90 (5) 01/80	22.3 +0.70 -0.70 (3) 02/82
HT 424	21.8 +0.76 -0.83 (5) 11/71	25.3 +0.48 -0.55 (5) 01/72	23.7 +1.10 -0.96 (5) 01/80	21.7 +1.90 -3.5 (3) 02/82
HT 435	16.9 +0.83 -0.48 (5) 11/71	15.8 +0.90 -0.83 (5) 01/72	13.5 +0.69 -0.75 (5) 01/80	15.1 +0.50 -1.0 (3) 02/82
HT 435 with Adlock 851 Adherends	14.1 +0.83 -0.69 (5) 11/71	14.5 +0.69 -0.69 (5) 01/72	13.1 +1.10 -1.10 (5) 01/80	
Solithane 113	2.07 +0.48 -0.48 (5) 09/71	1.73 +0.14 -0.14 (4) 12/72	2.28 +0.15 -0.10 (5) 01/80	

[†] All with 0.16 cm (0.063 in.) aluminum adherends (except as noted).

TABLE 5 — MATERIALS EVALUATION - FLEXURE STRENGTH IN MPa,
NUMBER OF SPECIMENS, AND DATE TESTED

Material	Baseline	1 Mo/3 Mo	Long-Term	After Irrad
Vespel SP-1	132 +4.1 -4.1 (5) 10/71		118 +3.4 -4.1 (5) 01/80	
PC Board Copper-Clad Laminate	386 +22.0 -10.3 (5) 02/72	445 +9.0 -6.2 (5) 03/72	457 +13.1 -11.0 (5) 06/80	
Adlock 851	407 +9 -8 (5) 10/71	600 +23 -39 (5) 11/71	704 +21 -16 (5) 04/80	

TABLE 6 — MATERIALS EVALUATION - COMPRESSION STRENGTH IN MPa,
NUMBER OF SPECIMENS, AND DATE TESTED

Material	Baseline	1 Mo/3 Mo	Long-Term	After Irrad
Hysol C7-4248	217 +15.2 -15.8 (4) 01/72	129 +13.8 -42.0 (5) 02/72	115 +41 -43 (5) 01/80	

TABLE 7 — MATERIALS EVALUATION - 180-DEGREE PEEL STRENGTH IN N/m X 10⁻³,
NUMBER OF SPECIMENS, AND DATE TESTED

Material	Baseline	1 Mo/3 Mo	Long-Term	After Irrad
DC6-1106	4.9 +2.8 -1.8 (5) 09/71	2.7 +0.37 -0.16 (5) 10/71	2.4 +0.26 -0.26 (5) 05/80	
EC-2216	6.47 +1.22 -1.58 (10) 07/71		3.33 +1.22 -2.10 (5) 01/80	1.66 +0.44 -0.26 (3) 05/81
PC Board Copper Peel	0.32 +0.09 -0.05 (11) 02/72	0.27 +0.01 -0.05 (12) 03/72	0.30 +0.07 -0.03 (20) 06/80	

TABLE 8 — MATERIALS EVALUATION - HARDNESS, NUMBER OF SPECIMENS,
AND DATE TESTED

Material	Baseline	1 Mo/3 Mo	Long-Term	After Irrad
Vespel SP-1				
Rockwell-M	88.2 +0.8 -1.2	89.6 +0.4 -2.6	87.2 +1.8 -2.2	
Shore-D	86 +0 -1.0 (5) 10/71	85 +1 -0 (5) 11/71	87 +1 -1 (4) 01/80	86 +1 -0 (3) 05/81

Note: Rockwell-M tester could not be used in situ - Rockwell tests carried out after Shore-D test.

TABLE 9 - MATERIALS EVALUATION - DIELECTRIC STRENGTH, NUMBER OF SPECIMENS, AND DATE TESTED

Material	Baseline	1 Mo/3 Mo	Long-Term	After Irrad
Vespel SP-1 V/m (10^{-7})	2.7 +0.1 -0.1 (5) 12/71	1.9 +0.2 -0.4 (5) 01/72	1.6 +0.1 -0.1 (5) 06/80	
Hysol C7-4248 V/m (10^{-4})	9.1 +0.73 -1.70 (5) 05/72	7.6 +1.25 -0.90 (5) 06/72	8.0 +0.06 -0.12 (3) 03/80	
Kynnar Tubing V/m (10^{-4})	5.4 +0.14 -0.07 (5) 05/72	2.78 +0.13 -0.22 (5) 07/72	1.89 +0.08 -0.12 (5) 03/80	
Polythermalese Wire AWG 20 KV	9.5 +1.7 -1.4	8.7 +3.0 -1.5	14.3 +2.2 -2.3	
AWG 30	8.8 +2.3 -1.8 (3) 05/72	6.8 +0.4 -0.3 (3) 06/72	8.7 +0.8 -0.7 (3) 07/80	
Therm-Amid Wire AWG 20 KV	12.7 +1.8 -1.7	7.5 +0 -0.1	11.3 +0.2 -0.3	
AWG 30	8.0 +1.5 -1.0 (3) 05/72	6.5 +0 -0.1 (3) 06/72	10.8 +0.7 -0.8 (3) 07/80	

TABLE 10 - MATERIALS EVALUATION - DIELECTRIC CONSTANT, DISSIPATION FACTOR, NUMBER OF SPECIMENS, AND DATE TESTED

Material	Baseline	1 Mo/3 Mo	Long-Term	After Irrad
Vespel SP-1	2.94 0.00046 (3) 12/71	2.87 0.00016 (3) 01/72	2.44 0.0013 (3) 04/80	2.52 0.0024 (3) 03/81
Ecco Foam FPH			1.14 0.004 (3) 06/80	1.095 0.0077 (3) 03/82
Hysol C7-4248		2.997 ----- (3) 12/71	3.065 0.0084 (2) 04/80	3.238 0.0047 (1) 03/81
Diall FS-80	3.79 0.012 (3) 06/72	3.43 0.002 (3) 07/72	3.49 0.004 (2) 04/80	
Stycast 1090	2.89 ----- (3) 10/72	2.75 ----- (3) 04/72	3.17 ----- (3) 04/80	
DC 93-500	2.79 ----- (2) 12/71	2.76 ----- (4) 03/72	2.70 0.0043 (3) 04/80	1.985 0.0026 (1) 03/81

TABLE 11 — MATERIALS EVALUATION - VOLUME RESISTIVITY IN OHM-CM X 10⁻¹⁴,
NUMBER OF SPECIMENS, AND DATE TESTED

Material	Baseline	1 Mo/3 Mo	Long-Term	After Irrad
Choseal 1224	6.2 +3.6 -3.2 (3) 12/71	4.8 +0.1 -0.3 (3) 01/72	9.0 +4.7 -3.1 (3) 04/80	
Vespel SP-1	6.67 +3.33 -1.67 (3) 12/71	3.01 +0.13 -0.27 (3) 01/72		

TABLE 12 — MATERIALS EVALUATION - THERMAL DECOMPOSITION

Material	Stages in TGA Curve	Reaction Mechanism in Stage 1	Stage 1 Temp Range, °C	Activation Energy, kcal, (kJ)		
				Baseline	Long-Term	After Irrad
Solithane	3	○ → B	25-250	23 (96)	26 (109)	
EA 934	2	○ → B	25-400	70 (293)	73 (305)	
HT 424	1	○ → B ○ → C	25-500	11 (46)	18 (75)	
Vespel SP-1	1	○ → B ○ → C	450-650		86 (360)	108 (450)
Kapton F, 919	2	○ → B	300-550		52 (218)	
Adlock 851	1	○ → B	250-650	14 (59)	16 (62)	
Kynar Tubing	2	○ → B	300-450		48 (201)	
DC 93-500	3	○ → B	25-550			25 (105)
DC 6-1106	2	○ → B	25-550	25 (105)		
Choseal 1224	1	○ → B	330-720	24 (100)		
Lucite	1	○ → B	125-400	43 (180)	42 (176)	41 (171)
Nylon	1	○ → B	200-400		65 (272)	46 (192)
Lexan	1	○ → B	200-500	52 (218)	48 (201)	
	2	○ → B ○ → C	140-450			59 (247)
Polyurethane	2	○ → B	125-250		24 (100)	34 (142)
Polyethylene	3	○ → B	150-400		118 (490)	
GFE 010/049	1	○ → B ○ → C	25-450	23 (96)		
005/063	1	○ → B ○ → C	25-450	23 (96)		
009/055	1	○ → B ○ → C	25-450	18 (75)		
004/044	1	○ → B ○ → C	25-450	18 (75)		

TABLE 13 — GRAPHITE/EPOXY SPECIMENS IRRADIATED WITH ELECTRONS
AND UV TENSILE TEST DATA IN MPa

Sample	Baseline MPa	Electron Irradiation	UV Irradiation
T-22	258 ± 20	225 ± 26	223 ± 27
T-41	312 ± 40	235 ± 42	230 ± 59
T-27	330 ± 18	325 ± 25	305 ± 18
T-43	399 ± 61	422 ± 26	341 ± 48
T-36	221 ± 25	242 ± 32	184 ± 31
T-35	216 ± 31	256 ± 12	194 ± 37

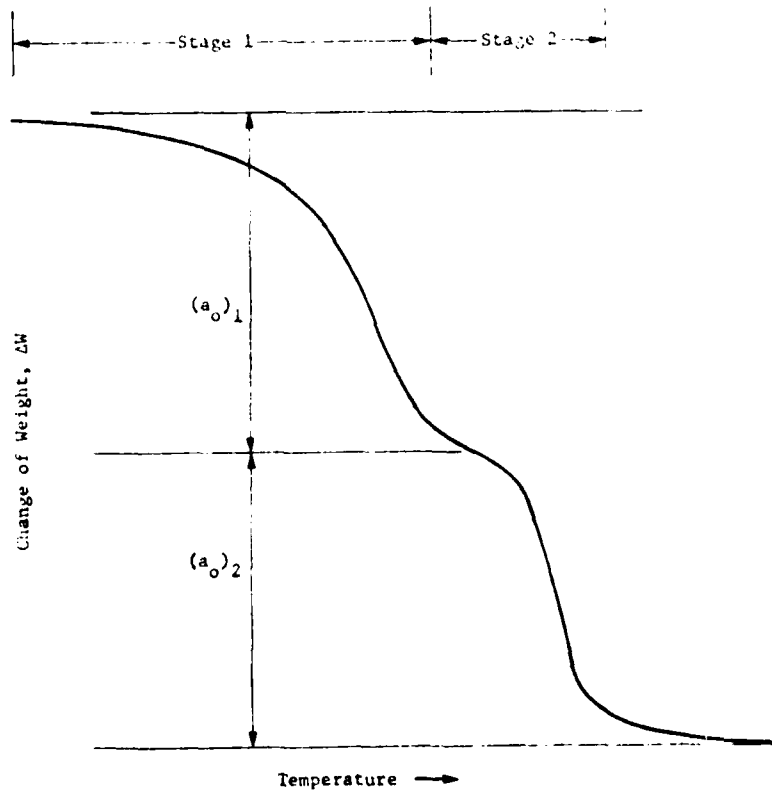
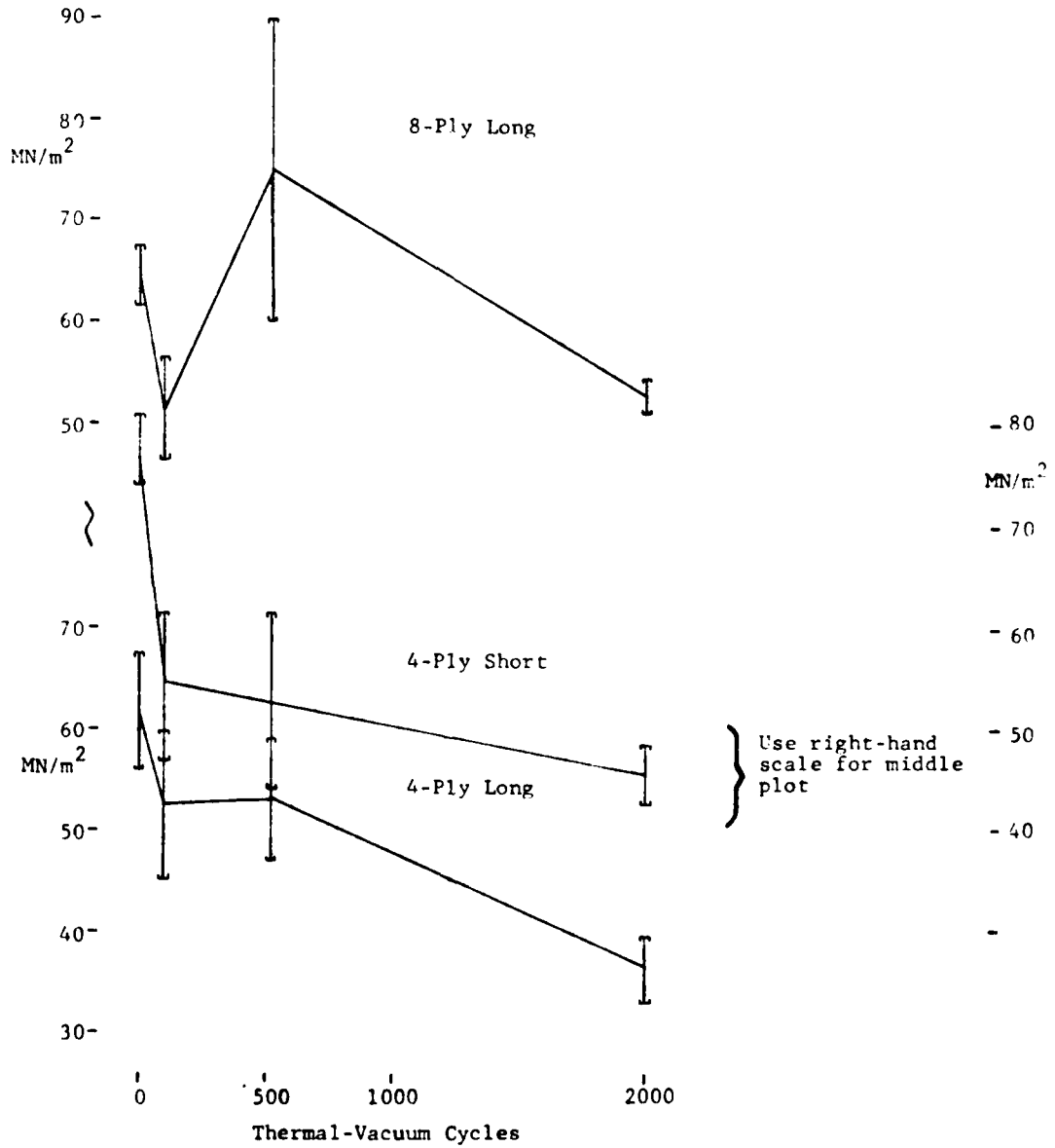
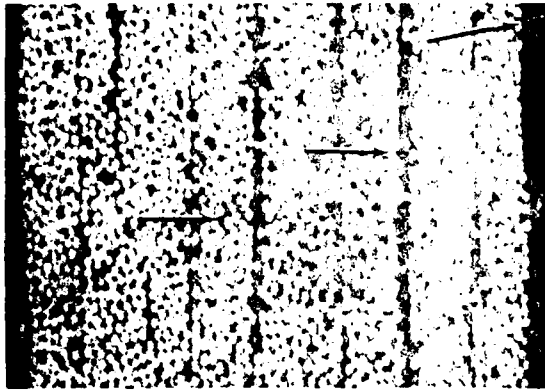


Figure 1 Schematic TGA Curve with a Two-Stage Decomposition

Figure 2. Tensile Strength of HMS/3501-6 after Thermal-Vacuum Cycling

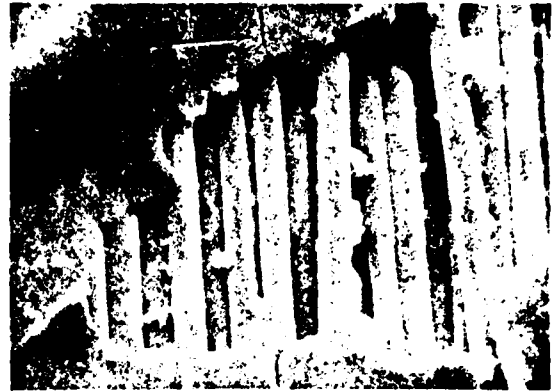


104 Cycles



a

100X

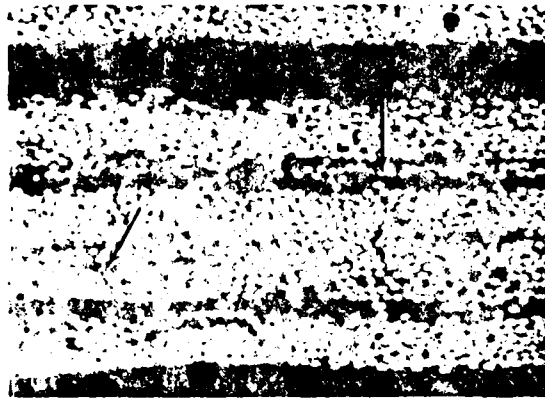


b

SEM

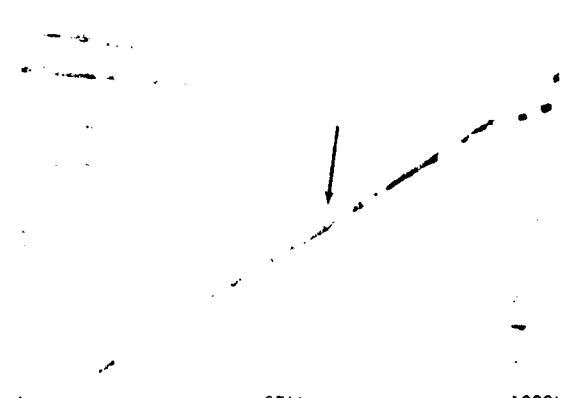
1000X

522 Cycles



c

100X

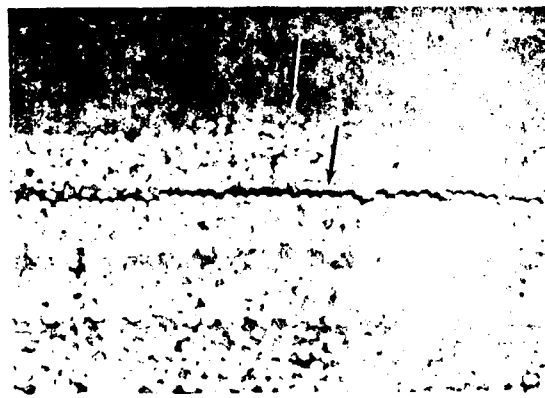


d

SEM

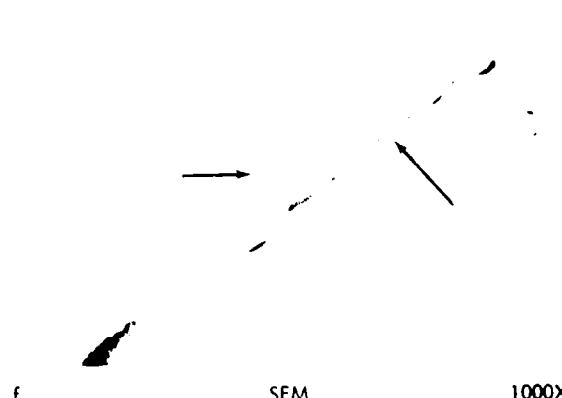
1000X

2003 Cycles



e

100X



f

SEM

1000X

Figure 3. HMS/3501-6 Microcracking After Thermal-Vacuum Cycling

STRUCTURAL DAMPING OF COMPOSITE MATERIALS FOR SPACE APPLICATIONS

by

Luigi BALIS CREMA, Renato BARBONI, Antonio CASTELLANI
Istituto di Tecnologia Aerospaziale
Via Eudossiana, 16 - 00184 Roma - Italy

SUMMARY

A series of experimental tests carried out on specimens of composite materials is presented. The measured damping ratios were obtained, in a vacuum chamber (10^{-6} torr), from the three first bending modes resonance (frequency range between 15 and 1400 Hz). The influence of the following parameters is considered: vibration amplitudes, frequency, air pressure, laminae number and mode shape.

The tests are performed with an electromagnetic exciter and a vibration detector; the measurements of the damping coefficient is worked by the frequency sweep and the decay transient method.

INTRODUCTION

The importance of damping prediction in aerospace composite structures is shown by recent research activities carried out in this field [1, 2, 3, 4]. As a matter of fact, experience with damping characteristics obtained for metal structures should not be translated directly to composite structures.

Actually parameters influencing damping are different and additional effects, peculiar for composite materials, must be considered. So to-day only a preliminary knowledge of damping properties of composite materials is available.

In the future, essential items will be:

- i) extensive tests;
- ii) theoretical and semi-empirical models of damping;
- iii) correlation of stiffness and damping qualities;
- iv) nonlinear damping.

In this paper a series of tests carried out at pressure until 10^{-6} torr is discussed; different specimens in carbon fiber and glass fiber have been considered. The experimental work represents a preliminary investigation to determine the behavior of composite materials in space environment by using the testing facilities presently available at Institute of Aerospace Technology (University of Rome).

1. DESCRIPTION OF SPECIMENS

A series of specimens made in composite at the Italian Industry AGUSTA (Cascina Costa, Varese) has been tested at the Institute of Aerospace Technology to evaluate the damping characteristics.

Two materials have been utilized: carbon fiber and glass fiber; for each material nine sets of specimens have been used.

In Table 1 the specifications of all the specimens are summarized.

TABLE 1

SPECIMEN		number of laminae	length (mm)
carbon fiber	glass fiber		
CCL4	GGL4	16	220
CCL2	GGL2	8	220
CCL1	GGL1	4	220
CL4	GL4	16	200
CL2	GL2	8	200
CL1	GL1	4	200
CS4	GS4	16	150
CS2	GS2	8	150
CS1	GS1	4	150

All the specimens have a width of 15 mm; the nominal thickness for 4 laminae of carbon fiber is 0.75 mm and for 4 laminae of glass fiber is 0.85 mm.

The specimens named CC-, GG- are clamped on the two ends, while the specimens named C-, G- are clamped on one end, as shown in Fig. 1.

The properties of the laminates are as shown in Table 2.

The lay-up sequence is, for both the materials, 0/90/90/0.

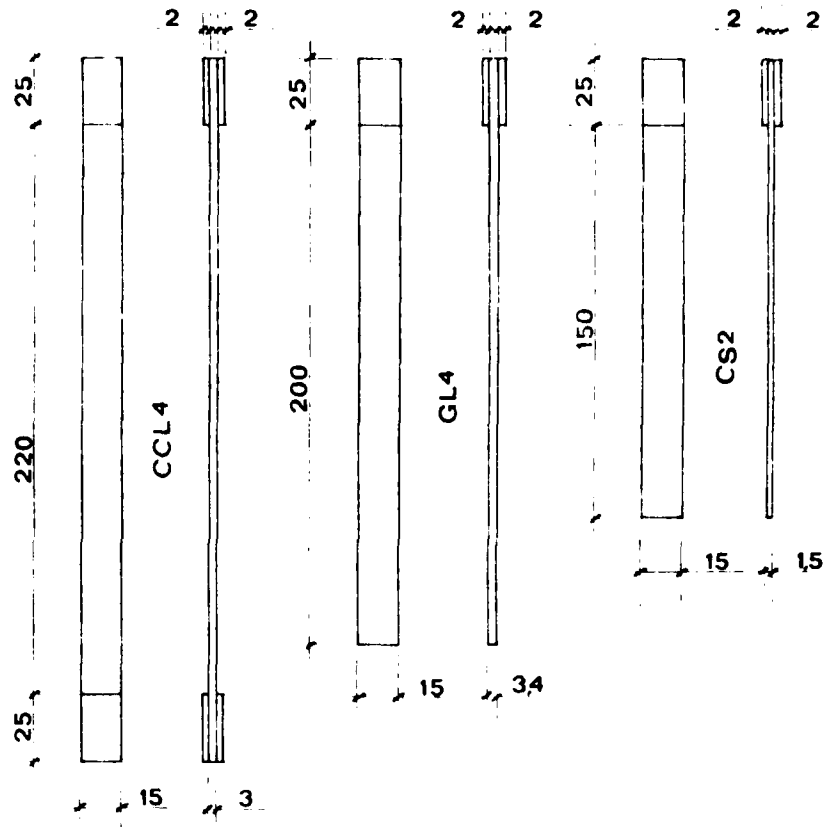


Fig. 1 Details of test specimens

TABLE 2

PROPERTIES	CARBON FIBER	GLASS FIBER
Fiber volume (%)	60	60
Density (kg.m^{-3})	1530	1890
Elastic modulus (GPa)	75	30

2. MEASUREMENT METHOD AND TEST PROCEDURE

The testing equipment used to evaluate damping is composed by the system shown in Fig. 2 and consists of the following instruments: oscillator, vibration exciter, capacitive detector, amplifier and recorder [5, 6].

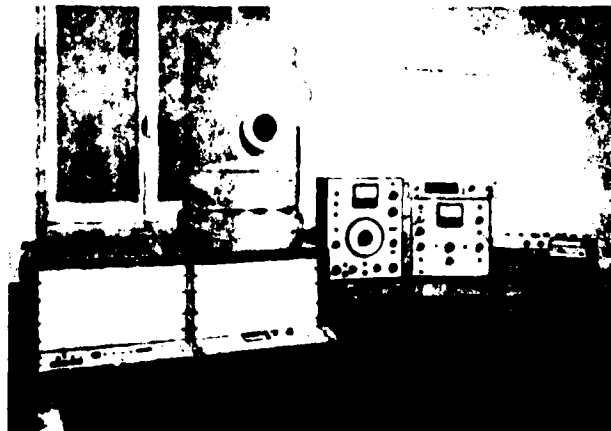


Fig. 2 Experimental set-up

The specimen is clamped on a mounting, while the electromagnetic exciter and the vibration detector can move along a slide which is fixed on the same mounting. A frequency range between 2 and 2000 Hz can be examined; a digital frequencymeter and an oscilloscope allow to determine resonant frequencies correctly. It is well known that several difficulties are involved since measurement is influenced by vibration amplitudes, transducers position, clamping pressure, specimen characteristics, and so on.

Experiments have been carried out making any possible effort to maintain identical conditions, in order to obtain repetitive and comparable results; particular attention has been given to keep comparable vibration amplitudes.

Non dimensional damping coefficients vs. specimen vibration amplitude (peak-peak) w , normalized to the specimen thickness h , are reported in Fig. 3, which refers to normal test conditions; it can be noticed that the vibration amplitude has no effects in working conditions selected.

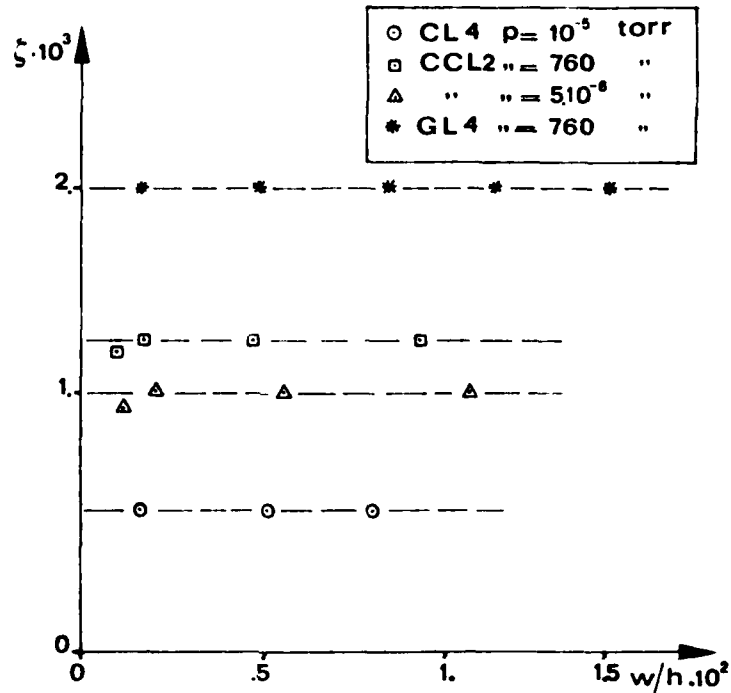


Fig. 3 - Damping coefficient versus w/h

The tests are carried out in the vacuum chamber available at the Institute of Aerospace Technology: its diameter is 457 mm and its height 762 mm.

3. EXPERIMENTAL RESULTS

A series of tests referred to the excitation of the first bending mode, has been made in the frequency range between 15 and 400 Hz and the damping coefficients versus pressure are reported in Fig. 4 to Fig. 9. The pressure range is from 760 torr to 10^{-6} torr to simulate, as possible, the space conditions.

The Figs. 4 and 5 refer to one laminate specimens, the Figs. 6 and 7 to two laminate specimens, the Figs. 8 and 9 to four laminate specimens.

A series of tests referred to the excitation of the second bending mode has been made in the frequency range between 90 and 600 Hz. The experimental results are presented in Figs. 10 and 11, respectively for carbon fiber and glass fiber specimens.

Finally in Figs. 12 and 13 the results referred to the excitation of the third bending mode are reported.

4. ANALYSIS OF RESULTS

As pointed out before, the present research is the first step to evaluate the damping properties of composite materials in space environment.

In the above tests the pressure and frequency effect was investigated, while the temperature effect shall be considered in future.

- **Pressure effect:** Figs. 4 to 13 show a decrease of damping coefficient versus pressure from atmospheric pressure to 10^{-6} torr.

This effect is more relevant for the thinner specimens that get to a decrease until the 25 per cent of the value at the atmospheric pressure.

The numerical values of this decrease are shown in Figs. 14 and 15, respectively for carbon fiber and glass fiber, where ξ/ξ_0 ratio (ξ_0 is the damping coefficient at the atmospheric pressure and ξ is the damping value obtained at 10^{-6} torr pressure) versus frequency is reported.

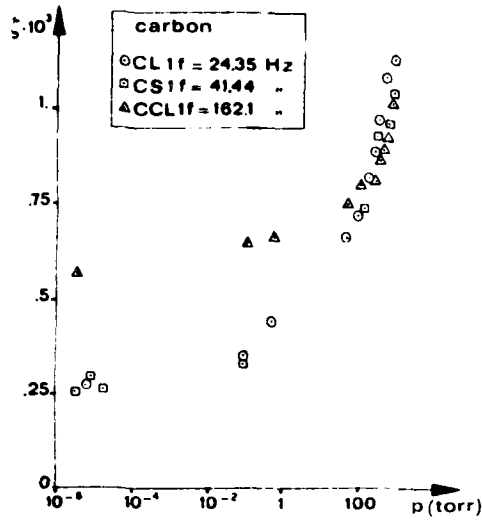


Fig. 4 - Damping coefficients vs. pressure

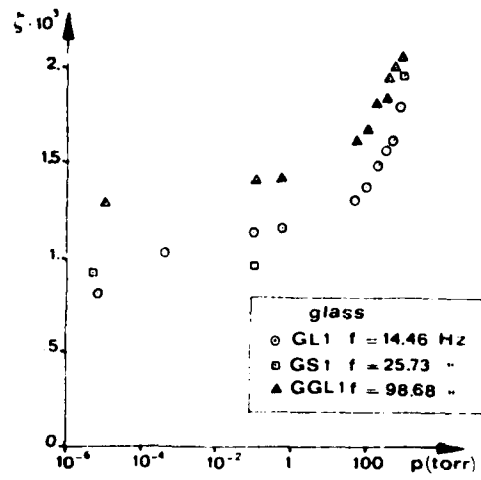


Fig. 5 - Damping coefficients vs. pressure

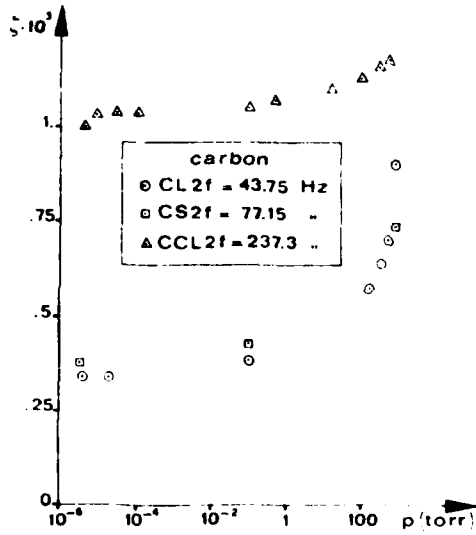


Fig. 6 - Damping coefficients vs. pressure

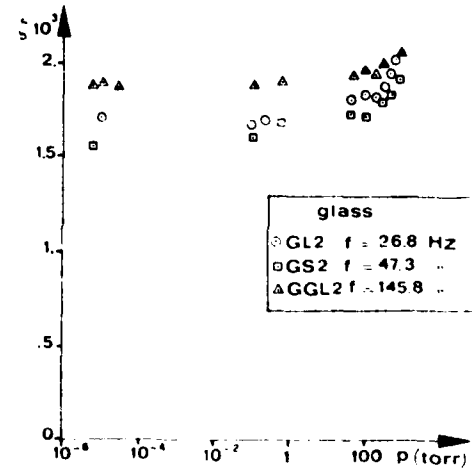


Fig. 7 - Damping coefficients vs. pressure

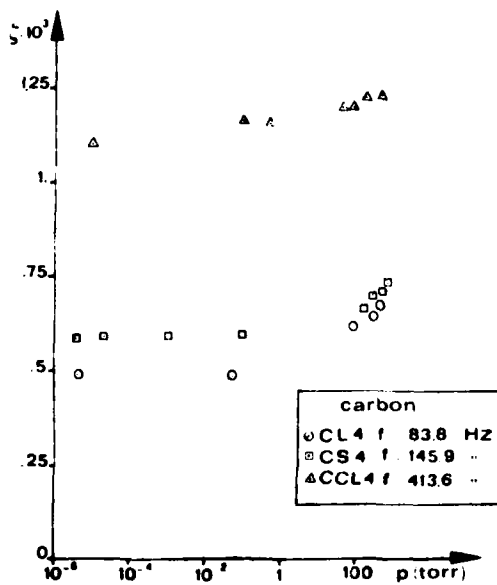


Fig. 8 - Damping coefficients vs. pressure

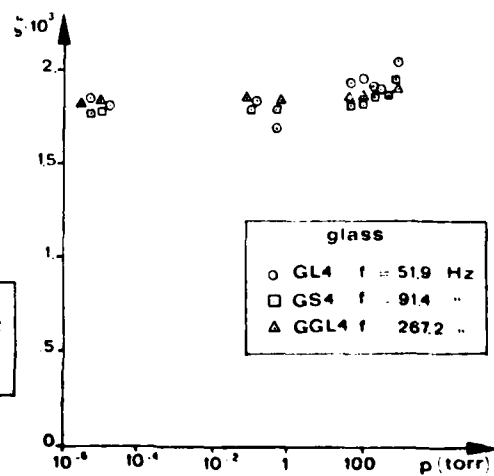


Fig. 9 - Damping coefficients vs. pressure

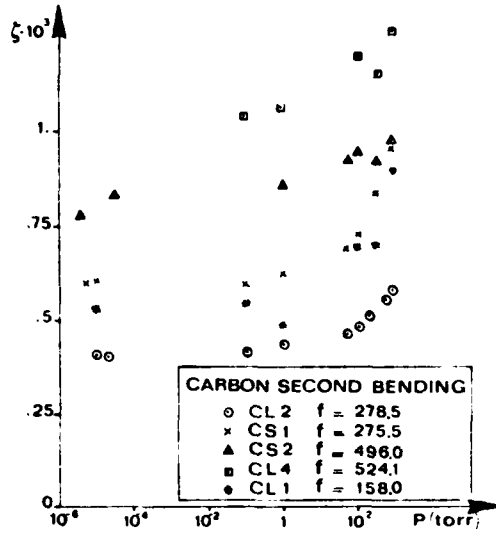


Fig. 11 - Second bending mode damping coefficients

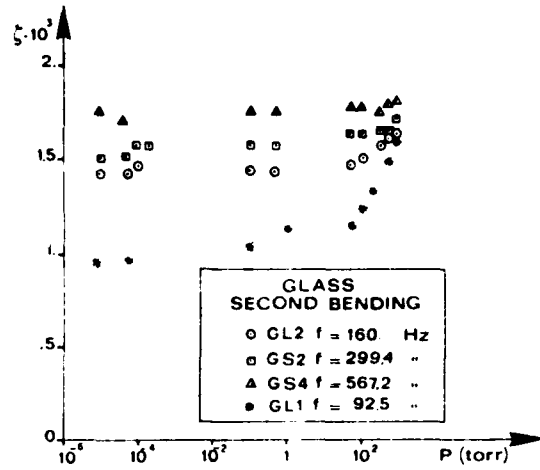


Fig. 10 - Second bending mode damping coefficients

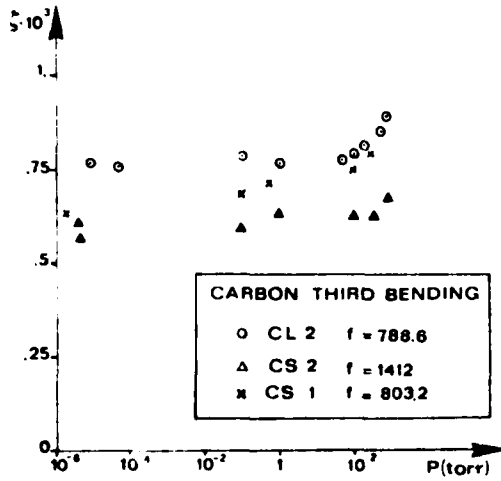


Fig. 12 - Third bending mode damping coefficients

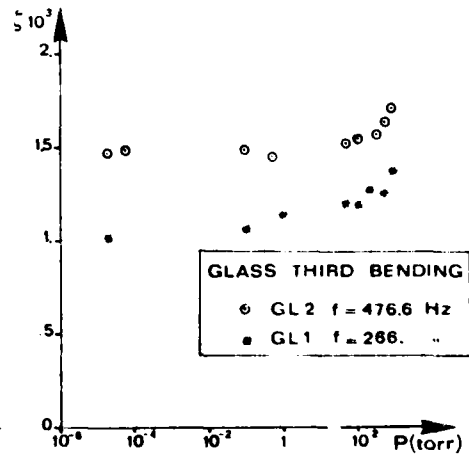


Fig. 13 - Third bending mode damping coefficients

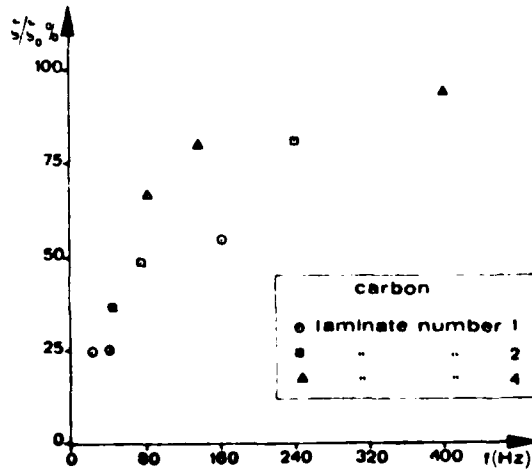


Fig. 14 - Damping change in the vacuum

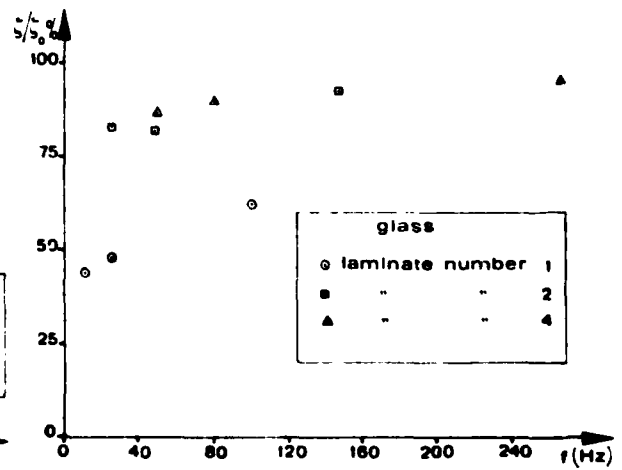


Fig. 15 - Damping change in the vacuum

The pressure variation causes also a frequency shift.

The frequency increase with the pressure decrease, due to the aerodynamic effect is shown in Fig. 16, where the $\Delta f/f$ ratio (Δf is the frequency increase and f is the frequency at 10^{-6} torr pressure) versus frequency is reported.

Frequency effect: In Figs. 17 and 18 the damping coefficients, for the two materials, in the first bending mode, versus frequency (in the 15 and 400 Hz range) are shown at 10^{-6} torr pressure.

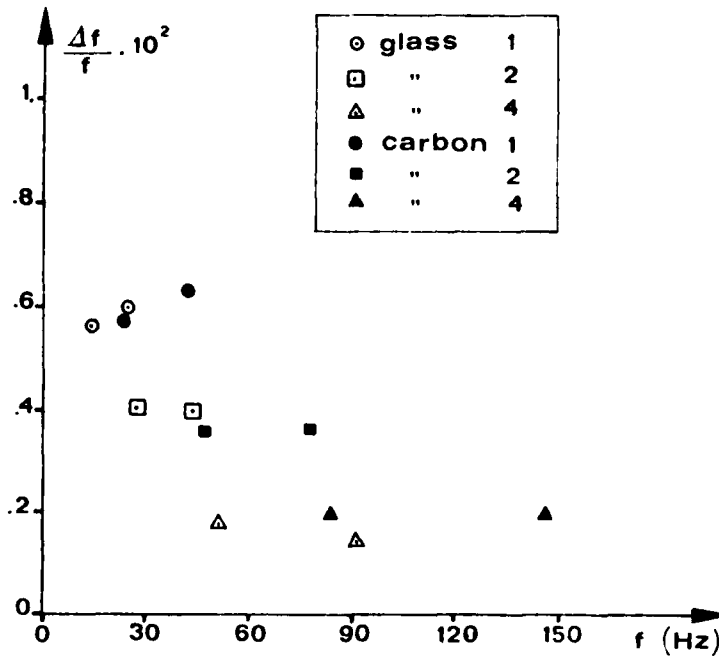


Fig. 16 - $\Delta f/f$ ratio vs. frequency

It appears that frequency effect on the damping coefficient is less remarkable for the glass fiber, while the carbon fiber damping coefficient increases, at least for a first range (about until 200 Hz), according to a nearly linear trend.

The test analysis shows that the damping coefficient for the carbon fiber is, for the whole range of investigated frequencies, lower than the damping coefficient for the glass fiber.

A comparison with results obtained in previous tests [6, 7] on aluminium alloys specimens shows that, at least for the carbon fiber here employed, the damping coefficient is also lower for carbon fiber than for aluminium alloys (Fig. 19).

These values can suggest a correlation between damping coefficient and stiffness characteristics (Fig. 20).

Mode effect: in Figs. 21 and 22 (at 10^{-6} torr pressure) damping coefficients versus frequency for the three first vibration modes are shown.

It appears that the mode effect on the damping coefficient for the carbon fiber is a significant increase versus mode order, similarly to the frequency effect; for the glass fiber these effects are less remarkable.

5. CONCLUSIONS

The analysis of the results obtained for glass fiber and carbon fiber specimens shows that it is possible to get significant data by means of normal test facilities.

For a development of the study on composite materials damping characteristics in space environment it needs to foresee further investigations, namely:

- i) evaluation of the temperature effect in the vacuum;
- ii) effect of the laminae orientation;
- iii) investigation in low frequency range (≤ 5 Hz);
- iv) extensive tests on the effect of the mode order;
- v) predictions of effective mechanical properties and structural response in terms of constitutive property of the phases.

The presented and proposed damping tests represent an attempt of collecting experimental data with the aim of getting a prediction of structural damping in aerospace composite structures.

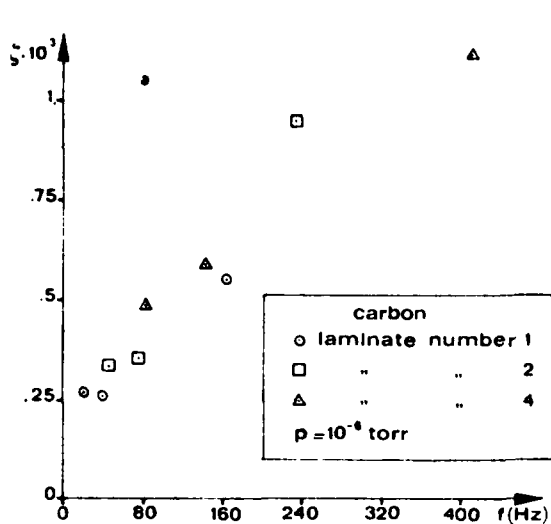


Fig. 17 Damping coefficients vs. frequency

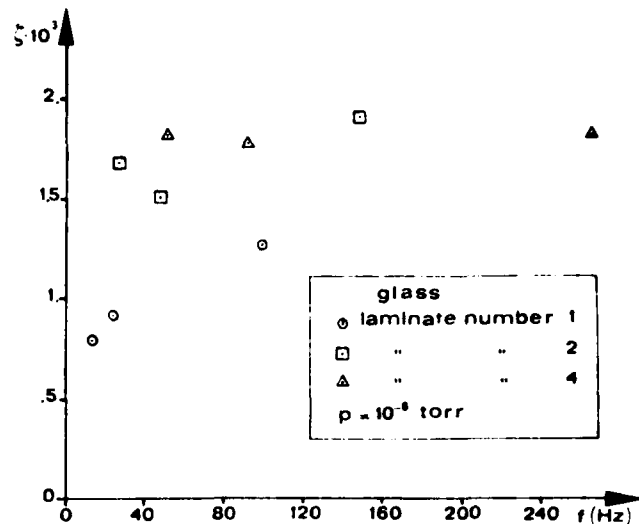


Fig. 18 Damping coefficients vs. frequency

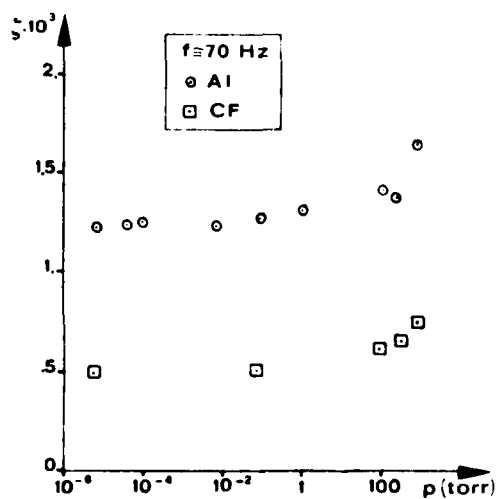


Fig. 19 - Comparison between Al and CF damping coefficient

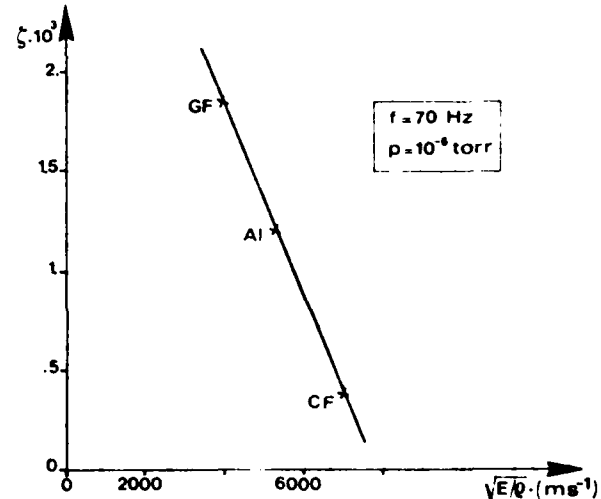


Fig. 20 - Damping coefficients vs. stiffness characteristics

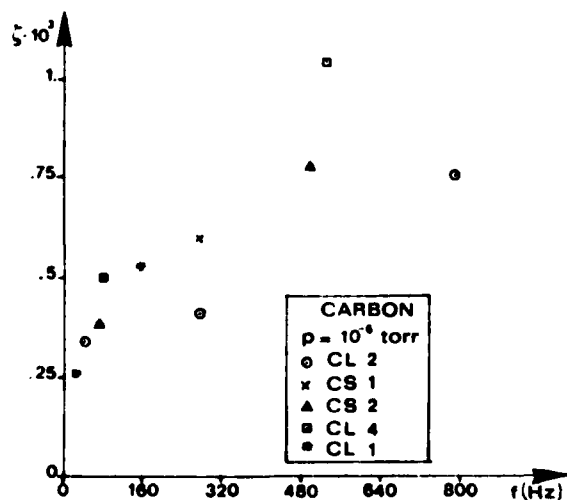


Fig. 21 - Damping coefficients vs. frequency

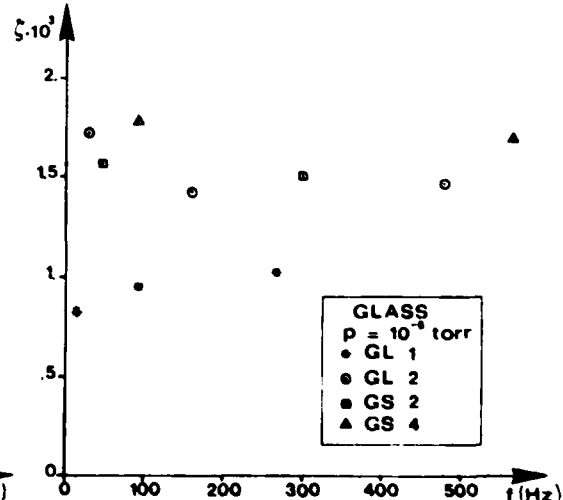


Fig. 22 - Damping coefficients vs. frequency

REFERENCES

- [1] H. GEORGI: "Dynamic Damping Investigations on Composites", AGARD CP 277, 1979.
- [2] R. BARBONI, M. MARCIETTI, I. PERONI: "Effects Connected with the Space Environment on Composite Materials", AGARD CP 288, 1980.
- [3] R. BARBONI, A. NAPPI, I. PERONI: "Composite Materials for Space Applications - A Scientific and Technological Survey", 44th AGARD-SMP Meeting, Lisbon, 1977.
- [4] L. ROGERS: "Conference on Aerospace Polymeric Viscoelastic Damping Technology for the 1980's", AFFDL-IM-78-FBA, July, 1978.
- [5] R. BARBONI, L. BALIS CREMA: "Determinazione sperimentale delle Caratteristiche Viscoelastiche", L'Aerotecnica Missili e Spazio, N. 2, 1972, pp.117-127.
- [6] L. BALIS CREMA, A. CASTELLANI, A. NAPPI: "Damping Effects in Joints and Experimental Tests on Riveted Specimens", AGARD CP 277, 1979.
- [7] L. BALIS CREMA, A. CASTELLANI, A. NAPPI: "Influenza della temperatura e del vuoto sul coefficiente di smorzamento in giunti rivettati", L'Aerotecnica Missili e Spazio, N. 4, 1979, pp. 183-187.

ACKNOWLEDGMENTS

This work was sponsored, in part, by the Ministero Pubblica Istruzione, under Contract for the year 1981.

The authors would like to acknowledge for helpful criticisms received from prof. P. Santini and for his kind presentation of this work in the SMP Meeting at Toronto.

The authors are indebted with the AGUSTA S.p.A. for the cooperation in the specimens supply.

SILICON SOLAR CELL CHARACTERIZATION AT LOW TEMPERATURES AND LOW ILLUMINATION AS A FUNCTION OF PARTICULATE IRRADIATION

by

Ann F. Whitaker, Sally A. Little and Charles L. Peacock, Jr.
NASA - Marshall Space Flight Center
Marshall Space Flight Center, Alabama, U. S. A. 35812

SUMMARY

Various configurations of Back Surface Reflector silicon solar cells including small (2 x 2) cm and large (~6 x 6) cm cells with conventional and wraparound contacts have been subjected to 1 MeV electron irradiation and characterized under both earth orbital and deep space conditions of temperatures and illuminations. Current-Voltage (I-V) data were generated from +65°C to -150°C and at incident illuminations from 135.3 mW/cm² to 5.4 mW/cm² for these cells. Degradation in cell performance which is manifested only under deep space conditions is emphasized. In addition, the effect of particle irradiation on the high temperature and high intensity and low temperature and low intensity performance of the cells is described. The cells with wraparound contacts were found to have lower efficiencies at earth orbital conditions than the cells with conventional contacts.

INTRODUCTION

Solar cells, the most critical and costly components of solar arrays, will have long life requirements in the space structures of the 1980's and 90's. Cost and space environmental durability of these cells are major concerns. Much emphasis is being placed on reducing costs through development of large cells (~6 x 6) cm which, in addition to being produced almost as cheaply as smaller cells, reduce array complexity and conserve array area and volume through efficient packing. Space environmental durability of solar cells has always been a critical issue with high end-of-life efficiencies desirable. In the last several years silicon solar cell technology has concentrated on improving cell efficiencies and radiation resistance by incorporating into the cell design such features as back surface field (BSF), back surface reflector (BSR), shallow junction, textured surface, reduced thickness, and new/improved covers and antireflective (AR) coatings.

Both solar cell design and performance differ depending on the cell's application to earth orbit or deep space missions. In earth orbit cells must accommodate high temperatures and high intensities in addition to more intense solar particle irradiations. Nominally earth orbital environments are considered to have an intensity of one solar constant (135.3 mW/cm²) and to produce temperatures ranging from +50°C to +80°C in operational cells. In deep space near Jupiter's orbit where temperature and intensity are low, incident illumination is as low as 0.04 solar constant (5.4 mW/cm²) and ambient temperatures are -120°C to -160°C. Each of these regions imposes operational difficulties on cells. High temperatures reduce cell voltage output and high intensities can lead to problems with series resistance. Low temperatures and low intensities (LILT) require a cell to have high junction perfection since shunt resistance can dominate performance under these conditions. Solar cells manufactured for space use to date have been designed for earth orbital applications.

Deep space missions requiring solar array power have been considered twice in the last fifteen years. A proposed Jupiter mission in the late sixties resulted in the identification of several performance problems in cells not detectable under earth orbital conditions but present under LILT conditions. In 1979 at the time when solar electric propulsion was being considered for a series of earth orbital/near sun and deep space missions, the Materials and Processes Laboratory at the Marshall Space Flight Center began an extensive program to characterize state-of-the-art silicon solar cells to determine which cells possessed the best characteristics for deep space performance. Current and voltage data were generated on nine types of cells exposed to 9 intensities and 11 temperatures taken along a mission profile from earth orbit to deep space. These investigations showed that while a few of the LILT cell problems identified earlier were not present in the current cells, several severe performance problems exist in these cells and to some extent are peculiar to cell types. Further, these studies revealed the 2 ohm-cm Back Surface Reflector shallow junction cell to have the best yield and least problems at LILT. An attractive feature of this cell type is that it is one of the least costly.

This paper describes the extension of the previous work: the evaluation of the 2 ohm-cm BSR shallow junction cell in the 2 x 2 cm size and in the large cell size with conventional and wraparound contacts at LILT and earth orbital conditions prior to and following various levels of 1 MeV electron irradiation.

TEST PROGRAM

The BSR 2 ohm-cm silicon solar cells investigated are described in Table I. These are production run cells purchased from Applied Solar Energy Corporation. The 2 x 2 cm cells represent 1980 technology cells while the large area cells are late 1981 cells. The testing and evaluation of these cells occurred over a 14 month period. Some of the objectives of the 2 x 2 cm cells evaluation were different from those of the large cells and are reflected in the test matrix in Table II. However, data were generated at sufficient test conditions to provide cell performance comparisons. Most of the analysis is presented for the large cells since they are currently of more interest.

Cell characterization was performed utilizing a Spectrolab X-75 solar simulator. The spectral content of this simulator over the wavelengths of interest (~300-1200 mμ) is within a 5% match to the solar spectrum. A standard cell

was maintained in the cell vacuum test chamber at $28 \pm 1/2^\circ\text{C}$ to monitor incident intensity. Neutral density filters were used to vary illumination intensity. During measurements of cell current-voltage parameters the cell temperature was controlled to $\pm 1/2^\circ\text{C}$. Illumination uniformity over 230 cm^2 was within $\pm 2\%$.

Exposure of the cells to 1 MeV electrons was accomplished with a 2.5 MeV Van de Graaff accelerator. Cells were maintained at $25 \pm 2^\circ\text{C}$ during irradiation in vacuum. A Faraday Cup was used to determine incident fluxes and fluences of electrons on cells.

DISCUSSION OF RESULTS

Earth Orbital Characterization

Earth orbital performance at $+25^\circ\text{C}$ of the three series of the BSR 2 ohm-cm unirradiated cells are described in Table III. These production run cells which provide power densities of $17-18\text{ mW/cm}^2$ under an Air Mass Zero (AMO) spectrum consistently have efficiencies of 13+ percent. The wraparound contact (WAC) version of this cell is an exception with some cells having efficiencies as low as 12.4%. Series resistance ranging from about .02 to .05 ohm were measured in the WAC cells under these high intensity conditions. Current densities of about $33-34\text{ mA/cm}^2$ at the maximum power point result in a voltage drop of about 55 mV across the series resistance and reduce the maximum power available. No defects such as cracking of the dielectric material or poor coverage of the contact metallization on the wraparound edge were detected. While the WAC cells have high open circuit voltage (603 mV average) and short circuit current (1337 mA average) their fill factors are reduced (.75-.76) to a large extent by this series resistance. Average short circuit current densities of $37-38\text{ mA/cm}^2$ in all of these 8-10 mils (.020-.025 cm) thick cells are indicative of the effectiveness of the shallow junction, BSR and minimum defect silicon.

Temperature coefficients of Short Circuit Current (ISC), Open Circuit Voltage (VOC) and Maximum Power (MP) prior to and following 1 MeV electron irradiation are shown in Tables IV and V (temperature coefficient data were not generated on the small cells following irradiation). The voltage temperature coefficients of -2.1 to $-2.2\text{ mV}/^\circ\text{C}$ remain unchanged for both the unirradiated and irradiated cases from -100°C to $+80^\circ\text{C}$. Data obtained by others on small area 2 ohm-cm cells have shown similar results over the temperature range from -20°C to $+40^\circ\text{C}$. Positive changes in current with temperature showed slight deviations from linearity over the entire range evaluated. As a result coefficients were generated above and below $+25^\circ\text{C}$ prior to irradiation. Coefficients were slightly larger above $+25^\circ\text{C}$ except for an unexplained decrease in the coefficient of the small area cells. The normalized values of $d\text{ISC}/dt$ were found to be .04 to .06%/°C in the large cells which is similar to that found in other unirradiated cells. These cell current variations with temperature are attributed to temperature variations of the absorption coefficient and minority carrier diffusion length.

The small variations of current coefficients above and below $+25^\circ\text{C}$ could not be separated from the irradiation effects. Thus only one coefficient was generated for the full temperature range after each irradiation. These temperature coefficients of current increase dramatically with irradiation by a factor as large as 2.5 for 1 MeV electron fluences to $2.6 \times 10^{14}\text{ e}^-/\text{cm}^2$. These increases are a result of irradiation caused changes in minority carrier diffusion length.

The large and negative values of $d\text{VOC}/dt$ determine the trend of the maximum power coefficient to large negative values. The magnitude of these values are influenced by the current capabilities of the cells. Normalized values were approximately $-.4\%/^\circ\text{C}$ for the unirradiated large cells and $-.3\%/^\circ\text{C}$ and $-.5\%/^\circ\text{C}$ above and below $+25^\circ\text{C}$, respectively, for the small cells. Maximum power coefficients of the large cells decrease by about 15% from the unirradiated condition to 1 MeV fluences of $2.6 \times 10^{14}\text{ e}^-/\text{cm}^2$. These decreases are a result of changes in minority carrier diffusion length reflected in reduced current output. Figure 1 shows a plot of normalized values of VOC, ISC and MP as a function of 1 MeV electron irradiation with characterization at 1 solar constant/ $+25^\circ\text{C}$. At $1 \times 10^{14}\text{ e}^-/\text{cm}^2$, the VOC, ISC and MP parameters of the large cells are reduced by approximately 2%, 6.5-8%, and 8-9.5%, respectively. At $2.6 \times 10^{14}\text{ e}^-/\text{cm}^2$, these parameters are decreased by about 4%, 11-12% and 16-17%, respectively. Current and maximum power reductions were less for the small cells even though they were nominally .0005 cm (2 mils) thicker. These decreases in cell electrical parameters were gradual changes as a function of irradiation. No discernible change in series resistance with irradiation was noted in the WAC cells. A five year mission of a space platform would be expected to accumulate cell radiation equivalent to about 1 MeV electron fluence of $1 \times 10^{14}\text{ e}^-/\text{cm}^2$.

Under earth orbital conditions these BSR 2 ohm-cm cells behave similarly. The performance characteristics of the WAC cells show a small series resistance which reduces the power output. In addition there is wide variability in the output of the WAC cells due mainly to a spread in current output. This is reflected in the cell efficiencies which vary from 12.4 to 13.4%.

Low Intensity Low Temperature Characterization

The operational problems of solar cells are more severe under deep space conditions of low temperature and low intensities than under high temperatures and intensities. Our previous investigations revealed two major performance problems at LILT in nine types of cells. These are: (1) the double slope, flat spot or non-ohmic shunt in Back Surface Reflector cells and (2) the ohmic shunt peculiar to the Back Surface Field cells. Plots of cell current-voltage curves (Figure 2) show examples of these problems which are manifested only under LILT conditions. The BSR 2 ohm-cm cells investigated here indicate approximately 50% have the non-ohmic shunt defect which results in reduced current and voltage output around the performance curve maximum power point. The reduced cell performance resulting from this defect begins to appear as the temperature is lowered below 0°C at low illuminations and becomes more pronounced as temperatures and illuminations are further reduced. No additional LILT problems were observed in the performance of these cells. Comparative evaluations of these cells are provided at LILT conditions of 0.086 solar constant (11.6 mW/cm^2)

and -100°C since this is an environmental condition at which spacecraft on deep space missions would spend considerable mission time.

Deep space electrical characteristics are shown in Tables VI, VII, VIII and in Figure 3. Short circuit current outputs were proportional to incident illumination which is characteristic of good cells and open circuit voltage shows increases with decreasing temperature at a rate of $-2.2\text{ mV}/^{\circ}\text{C}$ which is typical for 2 ohm-cm cells. Reduced output in these cells is reflected in the variability of the maximum power values and in the efficiencies and is associated with the non-ohmic shunt problem. Cell MP outputs were reduced by as much as 30% as a result of this LILT problem. The flat spot effect responsible for these reductions has been determined to be caused by localized defects in the front metallization in which highly conductive metal-silicide regions extend through the junction to the base region of the cell. This defect is considered to be brought about during the processing of the cell metallization.

The changes in temperature coefficients as a function of irradiation under LILT characterization varies somewhat from those generated at earth orbital conditions even though the temperature ranges covered are approximately the same. Current coefficients which are low simply by virtue of the low illumination show an increase with irradiation by a factor of only 1.5 for 1 MeV fluences to $2.6 \times 10^{14}\text{ e}^{-}/\text{cm}^2$. Further, a slight increase in the voltage coefficient with irradiation was noted. Maximum power coefficients decrease with irradiation similar to those seen at earth orbital conditions; the spread in these data is attributed to the magnitudes of the flat spot phenomena in the cells. Normalized parameters for the large cells shown as a function of irradiation indicate degradation of VOC, ISC and MP at 1 MeV electron fluence of $1 \times 10^{14}\text{ e}^{-}/\text{cm}^2$ to be 1.5%, 9.5% and 10%, respectively. At a higher fluence of $2.6 \times 10^{14}\text{ e}^{-}/\text{cm}^2$ these values are decreased to 2%, 14% and 17%, respectively.

CONCLUSIONS

The capabilities of the three types of cells investigated in terms of photoconductivity (current density) and developed voltage generally were as expected from production run cells. However, some of the WAC cells had high open circuit voltage output (607 mV) at $135.3\text{ mW}/+25^{\circ}\text{C}$. The performance spread of the WAC cells was large with efficiencies ranging from 12.4% to 13.4% under earth orbital conditions; small series resistance contributed to some reduced output in these cells. The LILT flat spot performance problem identified earlier in BSR cells was found in the large cells in approximately the same severity and percentage of affected cells.

The large cells showed less resistance to 1 MeV electron irradiation than the $2 \times 2\text{ cm}$ cells in terms of decreased current and maximum power output. The degradation shown by normalized current-voltage parameters as a function of irradiation is equal or slightly greater under LILT conditions than under high temperatures and intensities. The percentage change in current-voltage temperature coefficients with the exception of voltage was less at LILT conditions. Possibly some synergistic effects involving characterization temperatures, particle irradiation, LILT and high temperature and intensity performance defects and large area, highly doped silicon wafer metallurgy are responsible for the differences in normalized cell electrical parameters and temperature coefficients found at the two space environmental conditions addressed here. Characterization of considerably more large cells is required to substantiate these differences.

REFERENCES

1. Miller, J. L.: The Swing to Concentrator Arrays, to be published in the proceedings of the 3rd European Symposium on Photovoltaic Generators in Space, May 1982.
2. Hovel, H. J.: Solar Cells, Semiconductors and Semimetals, 11 Academic Press, London, 1975.
3. Payne, P.: Research and Development of Silicon Solar Cells for Low Solar Intensity and Low Temperature Applications. Final Report NAS2-5519, 1970.
4. Bartels, F., Ho, J. and Kirkpatrick, A.: Silicon Solar Cell Development for Low Temperature and Low Illumination Intensity Operation, Vol. I, Analysis Report, NAS2-5516, 1970.
5. Whitaker, A. F., Little, S. A., Smith, C. F., Jr., and Wooden, V. A.: Characterization of Three Types of Silicon Solar Cells for SEPS Deep Space Missions, Vol. I, NASA TM-78253, 1979.
6. Whitaker, A. F., Little, S. A., and Wooden, V. A.: Characterization of Three Types of Silicon Solar Cells for SEPS Deep Space Missions, Vol. II, NASA TM-78272.
7. Whitaker, A. F., Little, S. A., Wooden, V. A., Carter, D. E., Cothren, B. E., and Torstenson, A. A.: Characterization of Three Types of Silicon Solar Cells for SEPS Deep Space Missions, Vol. III, NASA TM-78305.
8. Weizer, V. A. and Broder, J. D.: On the cause of the Flat Spot Phenomenon Observed in Silicon Solar Cells at Low Temperatures and Low Intensities, paper presented at 15th IEEE Photovoltaic Specialist's Conf., May 1981.
9. Space Photovoltaic Research and Technology 1980, NASA CP 2169, 1980.
10. Rauschenbach, H. S., Solar Cell Array Design Handbook, 1 TRW DSSG, July 1976.
11. Tada, H. Y. and Carter, J. R., Jr.: Solar Cell Radiation Handbook, JPL Publication 77-56, November 1977.

ACKNOWLEDGEMENTS

The authors wish to thank Ms. Valerie Wooden for data reduction and Ms. Barbara Simms for typing the paper.

TABLE I — BSR 2 OHM-CM TEST CELLS DESCRIPTIONS

Cell Identification	(2 x 2) cm	(5.7 x 5.4) cm	(5.9 x 5.9) cm
Number of Cells	22	6	6
Type	N/P BSR 2 ohm-cm	N/P BSR 2 ohm-cm	N/P BSR 2 ohm-cm
Thickness	.025 cm (10 mils)	.020 cm (8 mils)	.020 cm (8 mils)
Junction Depth	Shallow (0.15 to .25 μ m)	Shallow (0.15 to 0.25 μ m)	Shallow (0.15 to .25 μ m)
Contacts	Ti-Pd-Ag	Ti-Pd-Ag	Ti-Pd-Ag
Back Surface Reflector	Aluminum	Aluminum	Aluminum
Grids	Fine Line (3/15)	Fine Line	Fine Line
Cover Glass	FS 0.35 Cut-on .015 cm (6 mil)	FS 0.35 Cut-on .015 cm (6 mil)	FS 0.35 Cut-on 0.015 cm (6 mil)
Cover Glass Adhesive	DC 93-500	DC 93-500	DC 93-500
Grade of Cell	Production Run	Production Run	Production Run

TABLE II — CELL TEST MATRIX

Cell Exposures Cell I.D.	Cell Characterization Intensity (SC)/Temperature ($^{\circ}$ C)	1 MeV Electron Irradiation Fluences (e^{-}/cm^2)
(2 x 2) cm	1 SC/+50 $^{\circ}$ C, 25 $^{\circ}$ C, 0 $^{\circ}$ C 0.174 SC/-50 $^{\circ}$ C, 0.086 SC/-100 $^{\circ}$ C, 0.040 SC/-150 $^{\circ}$ C	1×10^{12} , 1.1×10^{13} , 6.1×10^{13} , 1.61×10^{14} , 6.6×10^{14} , 1.66×10^{15} , 2.66×10^{15}
(5.7 x 5.4) cm	1 SC/+80 $^{\circ}$ C, 65 $^{\circ}$ C, 55 $^{\circ}$ C, 25 $^{\circ}$ C, 0 $^{\circ}$ C, -50 $^{\circ}$ C, -100 $^{\circ}$ C 0.174 SC/-50 $^{\circ}$ C, 0.086 SC/+25 $^{\circ}$ C, -100 $^{\circ}$ C 0.040 SC/-150 $^{\circ}$ C	1×10^{13} , 6×10^{13} , 1.2×10^{14} , 2.6×10^{14}
(5.9 x 5.9) cm	" "	" " " "

TABLE III — CELL PARAMETERS FOR BSR 2 OHM-CM UNIRRADIATED CELLS
AT 1 SOLAR CONSTANT (135.3 mW/cm^2)/ $+25^\circ\text{C}$

Cell Parameters	Cell I.D. (2 x 2) cm Conv C	(5.7 x 5.4) cm Conv C	(5.9 x 5.9) cm WAC
ISC Density, mA/cm^2	38.3 [37.8 - 39.6]	37.5 [36.7 - 38.0]	38.4 [37.2 - 39.3]
Avg. VOC	596 [589 - 602]	597 [592 - 599]	603 [599 - 607]
MP Density, mW/cm^2	18.0 [17.6 - 18.5]	18.2 [17.9 - 18.6]	17.6 [17.4 - 18.2]
Fill Factor	[.78 - .80]	[.80 - .81]	[.75 - .76]
Avg. Efficiency	13.3% [12.9 - 13.5]	13.3% [13.1 - 13.7]	12.9% [12.4 - 13.4]

TABLE IV — AVERAGE TEMPERATURE COEFFICIENTS[†] FOR BSR 2 OHM-CM
UNIRRADIATED CELLS AT HIGH INTENSITY (135.3 mW/cm^2)

Cell Parameter	Cell Type (2 x 2) cm Conv C	(5.7 x 5.4) cm Conv C	(5.9 x 5.9) cm WAC
<u>Current:</u>			
$\frac{d \text{ISC}}{dt}$, $\text{mA}/^\circ\text{C}$.160	.59	.56
	-.09	.67	.73
$\frac{d \text{ISC}}{\text{ISC}_r}/dt$, $\%/^\circ\text{C}$.10	.05	.04
	-.06	.06	.05
<u>Voltage:</u>			
$\frac{d \text{VOC}}{dt}$, $\text{mV}/^\circ\text{C}$	-2.2	-2.1	-2.1
<u>Power:</u>			
$\frac{d \text{MP}}{dt}$, $\text{mW}/^\circ\text{C}$	-.22	-2.1	-2.3
	-.38	-2.2	-2.7
$\frac{d \text{MP}}{\text{MP}_r}/dt$, $\%/^\circ\text{C}$	-.5	-.4	-.4
	-.3		

[†] Coefficients on 2 x 2 cm cells determined from 0°C to $+25^\circ\text{C}$ and $+50^\circ$ to $+25^\circ\text{C}$.
Coefficients on large cells determined from -100°C to $+25^\circ\text{C}$ and $+80^\circ$ to $+25^\circ\text{C}$.
Reference parameters taken at 25°C .

TABLE V — TEMPERATURE COEFFICIENTS* FOR LARGE BSR 2 OHM-CM CELLS AT HIGH INTENSITY (135.3 mW/cm^2) AS A FUNCTION OF 1 MEV ELECTRON IRRADIATION

1 MeV Electron Fluence	Cell Parameters		$\frac{dISC}{dt}, \text{ mA/}^\circ\text{C}$		$\frac{dVOC}{dt}, \text{ mV/}^\circ\text{C}$		$\frac{dMP}{dt}, \text{ mW/}^\circ\text{C}$	
	Conv C ⁺	WAC ⁺	Conv C	WAC	Conv C	WAC	Conv C	WAC
Unirradiated	.50 to .67	.38 to .72	-2.1	-2.0 to -2.3	-2.1 to -2.3	-2.6 to -2.7		
$1 \times 10^{13} \text{ e}^-/\text{cm}^2$.52 to .67	.38 to .71	-2.1	-2.0 to -2.1	-2.0 to -2.1	-2.4 to -2.6		
$6 \times 10^{13} \text{ e}^-/\text{cm}^2$.65 to .70	.56 to .90	-2.1	-2.1	-1.9 to -2.0	-2.3 to -2.5		
$1.2 \times 10^{14} \text{ e}^-/\text{cm}^2$.58 to .76	— to .99	-2.1	-2.1	-1.8 to -2.1	— to -2.2		
$2.6 \times 10^{14} \text{ e}^-/\text{cm}^2$.85 to 1.05	.91 to .96	-2.1	-2.1	-1.7 to 1.9	-2.2 to -2.4		

* Coefficients determined from -100°C to $+80^\circ\text{C}$; Reference parameters taken at -100°C .

⁺ Conventional contacts cells (conv c) have areas $\sim(5.7 \times 5.4) \text{ cm}$.

Wraparound contacts cells (WAC) have areas $\sim(5.9 \times 5.9) \text{ cm}$.

TABLE VI — CELL PARAMETERS FOR BSR 2 OHM-CM UNIRRADIATED CELLS AT 0.086 SOLAR CONSTANT (11.6 mW/cm^2)/ -100°C

Cell Parameters	Cell I.D.	(2×2) cm	(5.7×5.4) cm	(5.9×5.9) cm
		Conv C	Conv C	WAC
ISC Density, mA/cm^2	3.3	[3.2 - 3.5]	3.1	[3.0 - 3.1]
Avg. VOC	817	[811 - 822]	813	[810 - 814]
MP Density, mW/cm^2	2.3	[2.1 - 2.4]	1.7	[1.4 - 1.9]
Fill Factor	.78	[.78 - .88]	.56	[.56 - .75]
Avg. Efficiency	19.6%	[18.2 - 20.4]	14.8%	[11.6 - 16.2]
			16.3%	[15.0 - 17.8]

TABLE VII — AVERAGE TEMPERATURE COEFFICIENTS* FOR BSR 2 OHM-CM UNIRRADIATED CELLS AT LOW INTENSITY (0.086 SC/11.6 mW/cm²)

Cell Parameter \ Cell Type	(2 x 2) cm Conv C	(5.7 x 5.4) cm Conv C	(5.9 x 5.9) cm WAC
<u>Current:</u>			
$\frac{d ISC}{dt}$, mA/°C	.01	.04	.05
$\frac{d ISC}{ISC_r} / dt$, %/°C	.06	.04	.04
<u>Voltage:</u>			
$\frac{d VOC}{dt}$, mV/°C	-2.2	-2.2	-2.2
<u>Power:</u>			
$\frac{d MP}{dt}$, mW/°C	-.02	-.08	-.15
$\frac{d MP}{MP_r} / dt$, %/°C	-.24	-.19	-.25

* Coefficients on 2 x 2 cm determined from -150°C to -25°C.
 Coefficients on large cells determined from -100°C to +25°C.
 Reference parameters at lowest temperature.

TABLE VIII — TEMPERATURE COEFFICIENTS* FOR LARGE BSR 2 OHM-CM CELLS AT LOW INTENSITY (11.6 mW/cm²) AS A FUNCTION OF 1 MEV ELECTRON IRRADIATION

1 MeV Electron Fluence	$\frac{d ISC}{dt}$, mA/°C		$\frac{d VOC}{dt}$, mV/°C		$\frac{d MP}{dt}$, mW/°C	
	Conv C ⁺	WAC ⁺	Conv C	WAC	Conv C	WAC
Unirradiated	.04	.05	-2.2	-2.2	-.03 to -.12	-.14 to -.16
$1 \times 10^{13} e^- / cm^2$.04 to .05	.04 to .05	-2.25	-2.2	-.03 to -.11	-.14 to -.15
$6 \times 10^{13} e^- / cm^2$.06	.06	-2.25	-2.3	-.03 to -.10	-.12 to -.15
$1.2 \times 10^{14} e^- / cm^2$.06	—	-2.3	—	-.04 to -.10	—
$2.6 \times 10^{14} e^- / cm^2$.06	.07	-2.37	-2.3 to -2.4	-.04 to -.10	-.10 to -.13

* Coefficients determined from -100°C to +25°C; Reference temperature is -100°C.
⁺ Conventional contact cells (conv c) have areas~(5.7 x 5.4) cm.
 Wraparound contact cells (WAC) have areas~(5.9 x 5.9) cm.

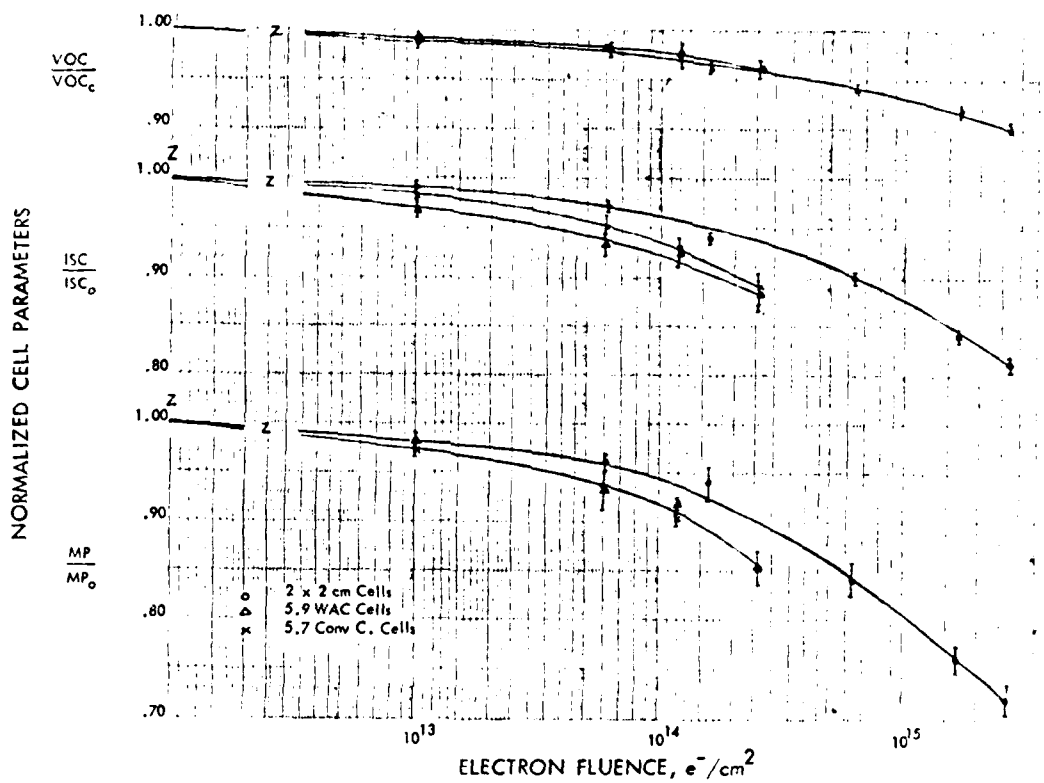


Figure 1. Normalized cell current-voltage parameters at $135.3 \text{ mW/cm}^2 / +25^\circ\text{C}$ as a function of 1 MeV electron irradiation.

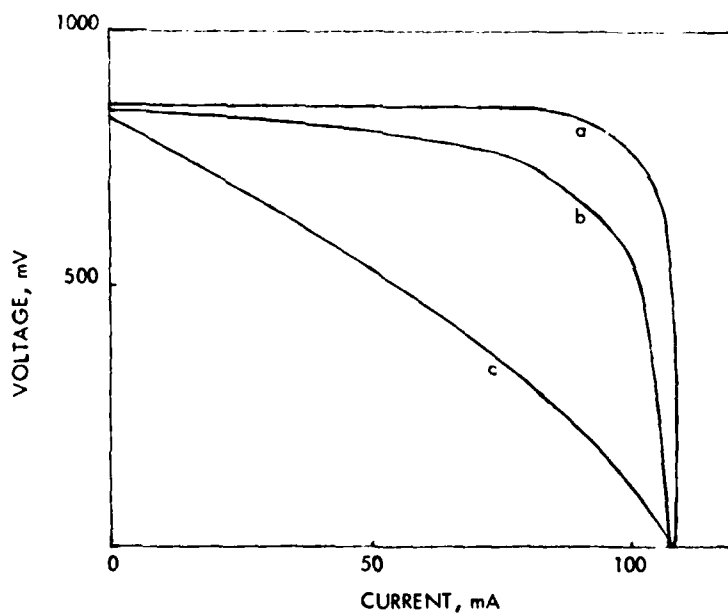


Figure 2. Current-Voltage characteristics of three cells exhibiting different behaviors at $0.086 \text{ SC}/-100^\circ\text{C}$; (a) insignificant shunt, (b) non-ohmic shunt, and (c) ohmic shunt.

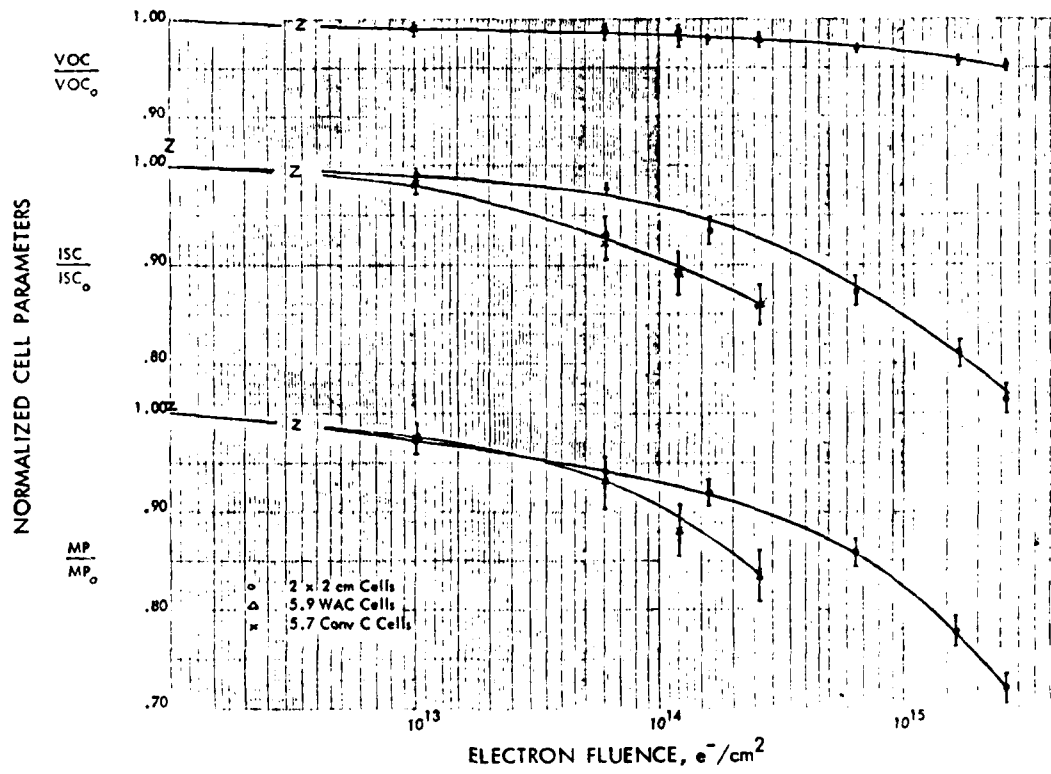


Figure 3. Normalized cell current-voltage parameters at $11.6 \text{ mW/cm}^2/-100^\circ\text{C}$ as a function of 1 MeV electron irradiation.

THE EFFECT OF SPACE ENVIRONMENT
ON THE DAMPING OF POLYMER MATRIX COMPOSITES

by

R. C. Tennyson, W. D. Morison and G. E. Mabson
University of Toronto
Institute for Aerospace Studies
4925 Dufferin Street
Downsview, Ontario, Canada
M3H 5T6

SUMMARY

A combined experimental and analytical investigation has been undertaken to evaluate material damping of laminated composites. Particular emphasis has been given to the effect of thermal-vacuum exposure and U.V. radiation on the change in damping response. A laminate analysis was developed for predicting material damping utilizing experimentally determined 'principal' damping coefficients. Results are presented based on flexural vibration and creep compliance tests performed on graphite/epoxy laminates at ambient conditions and in a space simulator.

LIST OF SYMBOLS

A_{ij}, D_{ij}	$\int_{-h/2}^{h/2} (\bar{Q}_{ij})_k(1, z^2) dz$
E_{11}, E_{22}	orthotropic moduli of elasticity measured in the 1 and 2 directions, respectively
G_{12}	shear modulus of elasticity measured in the 1-2 plane
h	total laminate thickness
\bar{Q}_{11}	$Q_{11}m^4 + 2(Q_{12} + 2Q_{66})n^2m^2 + Q_{22}n^4$
\bar{Q}_{22}	$Q_{11}n^4 + 2(Q_{12} + 2Q_{66})n^2m^2 + Q_{22}m^4$
\bar{Q}_{12}	$(Q_{11} + Q_{22} - 4Q_{66})n^2m^2 + Q_{12}(m^4 + n^4)$
\bar{Q}_{66}	$(Q_{11} + Q_{22} - 2Q_{12} - 2Q_{66})n^2m^2 + Q_{66}(m^4 + n^4)$
\bar{Q}_{16}	$(Q_{11} - Q_{12} - 2Q_{66})nm^3 + (Q_{12} - Q_{22} + 2Q_{66})n^3m$
\bar{Q}_{26}	$(Q_{11} - Q_{12} - 2Q_{66})n^3m + (Q_{12} - Q_{22} + 2Q_{66})nm^3$
Q_{11}	$E_{11}/(1 - \nu_{12}\nu_{21})$
Q_{22}	$E_{22}/(1 - \nu_{12}\nu_{21})$
Q_{12}	$\nu_{21}E_{11}/(1 - \nu_{12}\nu_{21}) = \nu_{12}E_{22}/(1 - \nu_{12}\nu_{21})$
Q_{66}	G_{12}
ν	Poisson's ratio

1. INTRODUCTION

The recent successful flights of the space shuttle usher in an age in which very large scale structures may be constructed in space. Because the useful lifetime of such structures must necessarily be quite long, the materials used will have to withstand the space environment for decades without severe degradation. Polymer matrix fiber reinforced composites are among the leading candidates for use in these space structures because of their high strength and stiffness-to-weight ratios and because of the possibility of designing dimensionally stable structures. Unfortunately, the organic components of these materials are potentially much more sensitive to many space environmental factors than are metals.

One aspect of composite design that has received little attention in the literature is that of optimizing material damping. From a structural dynamics viewpoint, material damping plays an important role in assessing cyclic stresses, fatigue life, oscillatory amplitudes and decay times. For some spacecraft applications, damping will be essential to ensure successful stabilization of large flexible appendages. In a recent report on passive damping mechanisms in large space structures [1], it was noted that for 'beam' type configurations it might not be possible to stabilize all flexural modes without using structural damping, except by the judicious co-location of sensors and controls. Clearly such devices lead to weight penalties and may well be impractical for very large structures.

Although a large body of literature exists on material damping (see Refs. 2 and 3, for example), it would appear that the most successful models are those which approach the problem phenomenologically - that is, damping is viewed macroscopically as the result of a number of unknown micromechanical processes whose net effect can be characterized. Specifically, in terms of viscoelastic composites, a variety of methods have been taken with varying degrees of success.

In 1968 Schultz and Tsai [4] reported the results of dynamic moduli and damping ratio measurements of unidirectional glass-reinforced epoxy. Although a simple Bernoulli-Euler beam subject to an external damping stress was introduced as an artifice to aid in interpretation of the data, the "model" was based on laminate constitutive relations. A complex modulus representation of the dynamic response was intro-

duced and invariants of the compliance matrix used to predict modulus values of one laminate based on three other experimental values. Moduli were predicted to within approximately 5 percent; however, the transformation of damping ratios achieved accuracies of only 14 to 32 percent. Further work [5] involving quasi-isotropic laminates failed to improve the accuracy of the damping predictions.

In 1970, Hashin [6,7] developed a model for the complex moduli of both particulate and fiber reinforced materials. Using rigorous expressions for effective material constants, upper and lower bounds on complex quantities were derived using a correspondence principle. This principle related elastic material properties to complex material properties. Although the method gave an accurate prediction of modulus, for the one example quoted, the mathematics are made cumbersome by the requirement of a knowledge of the geometry of the phases in the composite and the need for rigorous expressions for effective material properties. Furthermore, an assumption of locally homogeneous stress and strain fields for the purpose of relating stress and strain on a macroscale renders predictions invalid outside of a certain frequency range. This latter problem is a severe impediment if one wishes to express the loss factor in the preferred notation of the frequency domain.

In 1972, Abarcar and Cunniff [8] conducted experiments involving the vibration of unidirectional graphite-epoxy and boron-epoxy beams. A lumped mass approximation to the orthotropic beam vibration was used to predict natural frequencies for bending and twisting modes. Very good agreement was achieved in predicting the frequencies; however, no extension to complex moduli or loss factors was made.

In 1973 Adams and Bacon [9] published a theory for material damping based on the laminate constitutive relations. The theory arrives at an expression for the damping in a general state of stress/strain for a laminate in terms of the specific damping capacity (ratio of energy dissipated to the strain energy per cycle). The advantage of this approach is that the damping is viewed as being a function of two normal in-plane damping components and one shear damping component. Thus, the damping is geometry independent. Comparison with experimental results for free flexure/torsion tests on unidirectional beam specimens gave good agreement with complex modulus values, but only fair agreement with damping predictions. Experimental technique was reported to be the main difficulty. However, further experiments with (± 9) and cross-ply laminates failed to improve the accuracy of the damping capacity predictions.

In 1975 Paxson [10] conducted transverse beam vibration tests on boron reinforced plastic. The phase lag between root and tip displacements of cantilever beams was used to compute complex moduli and resonance curves were plotted. Values of the loss factor were compared using the bandwidth, log decrement and ratio of loss to storage modulus methods. However, the agreement was poor and the results rendered inconclusive.

In 1976 Gibson and Plunkett [11] used an extension of the method of Hashin to compare theoretical predictions of loss and storage moduli to experimentally derived values. Due to a combination of analytical and experimental weaknesses, prediction of loss moduli were in error by 50-80%, although storage moduli were in good agreement. The values of the loss factor were not computed (they would be at least as much in error) although a strain level dependence was reported.

In 1979-1982 Morison and Bjarnason [12-14] conducted beam vibration experiments in-vacua using a free vibration decay technique. Log decrement values were compared to predictions from a modified version of the theory of Adams and Bacon. Fairly good agreement was achieved despite using static values of material properties in the analysis. These results were also reported by Tennyson [15,16].

In 1980 Bagley and Torvik [17] introduced a model of viscoelastic damping based on a fractional calculus approach. Since viscoelastic properties are, in general, proportional to fractional powers of time or stress, a finite element (FE) dynamics model of a damped structure was derived on that basis. Agreement between FE predictions and experiment was quite reasonable; however, the model encompasses only isotropic viscoelastic materials at present.

As far as environmental influences are concerned, extensive effort has been directed recently towards determining the effects of temperature, moisture and frequency on the damping of graphite/epoxy laminates [18]. However, little has been published regarding space environmental effects. The relevant parameters of interest include outgassing resulting from exposure to hard vacuum ($10^{-6} \sim 10^{-7}$ torr), thermal-cycling, and radiation (U.V. and high energy electrons).

Thus, the present investigation has three objectives in mind:

- development of a composite laminate damping model;
- experimental validation of model;
- determination of the effect of space environment exposure on composite damping parameters.

Other internal dissipation mechanisms such as joints and bearings are not considered. It might be noted though that the analysis procedure can also be applied to 'constrained viscoelastic layers' that are often utilized for damping purposes [3].

2. LAMINATE DAMPING ANALYSIS

Although several experimental techniques are available for characterizing a material's damping response [3], analytical methods are required to determine the damping behaviour of arbitrary laminated structures. One approach involves a finite element solution for the dynamic viscoelastic response of the composite structure, from which modal damping factors and frequencies are obtained (see Ref. 20, for example). In this case, test data are necessary to construct the appropriate viscoelastic model.

Another analytical model can be formulated in terms of a matrix of 'damping coefficients' derived from strain energy considerations [9]. This method yields a direct solution for the specific damping capacity

(SDC) ψ for any laminate in terms of lamina material properties [see Eq. (A-14), Appendix A]. It should be noted that the SDC can be readily replaced by other commonly used damping parameters such as the logarithmic decay rate, defined by $\delta = \psi/2$, or the loss factor, $\eta = \psi/2\pi$.

One of the simplest cases to investigate experimentally is that of flexural vibration. Thus Eq. (A-14) can be reduced to Eq. (A-18). For transitory decay of free vibration, the logarithmic decrement is frequently used. The definition of log decrement inherently assumes the damping has no strain dependence or, at best, allows that damping be defined as a function of an initial value of strain. Using Eq. (A-18), the SDC can be rewritten in an experimentally useful form - the log decrement in free flexure,

$$\delta_{FF} = \frac{\sum_{k=1}^n [D'_{11}, D'_{12}, D'_{16}] [T']^T [\delta] [Q]_k [T']_k \begin{bmatrix} D'_{11} \\ D'_{12} \\ D'_{16} \end{bmatrix}}{6D'_{11}} \quad (1)$$

where

$$\delta = \begin{bmatrix} \delta_{11} & \delta_{12} & 0 \\ \delta_{12} & \delta_{22} & 0 \\ 0 & 0 & \delta_{66} \end{bmatrix} \quad (2)$$

The δ_{ij} are referred to as the 'fundamental' log decrements.

It can be shown that Eq. (1) can be expanded in the form,

$$\delta_{FF} = K_{11}\delta_{11} + K_{12}\delta_{12} + K_{22}\delta_{22} + K_{66}\delta_{66} \quad (3)$$

where the K_{ij} are coefficients dependent upon laminate geometry and material elastic properties. Clearly, for a given laminate, Eq. (3) is linear in four unknowns with constant coefficients. Provided that the K_{ij} are well behaved functions of laminate configuration, a set of four equations like Eq. (3) is sufficient to establish the values of the δ_{ij} . Furthermore, if the δ_{FF} and K_{ij} are known functions of some variable, such as frequency, temperature or moisture content, the dependence of the δ_{ij} on the independent variable is also defined. This formulation was used to predict composite material damping for several environmental conditions.

Viscoelastic creep tests can also be employed to obtain the principal damping parameters by means of the complex compliance functions. These values immediately yield the loss factor (η) which is given by the ratio of the (imag./real) parts. However, because of the relaxation times involved, data are usually obtained over a low frequency range ($f \leq 0.1$ Hz). Moreover, from an analytical viewpoint, considerable effort is required since the creep compliance functions $S(t)$ must first be derived from experimental strain/time data. For example, assuming linear viscoelastic behaviour, the strain at any time 't' (after removal of a stress ' σ_0 ' applied for some time ' t_0 ') is given by,

$$\epsilon(t) = \sigma_0 \sum_{i=1}^N S_i e^{-t/\tau_i} \left(e^{-t_0/\tau_i} - 1 \right) \quad (4)$$

where $S(t)$ is assumed to have the form

$$S(t) = S_\infty + \sum_{i=1}^N S_i e^{-t/\tau_i} \quad (5)$$

Based on experimental $\epsilon(t)$ curves, a collocation solution is used to calculate the S_i values. Both the collocation times (t_j) and the time constants (τ_i) were selected at one decade intervals. The following system of linear equations results;

$$\sum_{i=1}^N S_i e^{-t_j/\tau_i} \left(e^{-t_0/\tau_i} - 1 \right) = \frac{\epsilon(t_j) - \epsilon_\infty}{\sigma_0} \quad j = 1, \dots, N \quad (6)$$

It then remains to transform from the time domain to the frequency domain to obtain the complex creep compliances. Further details of the analytical procedures can be found in Ref. 20.

3. MATERIAL DAMPING EXPERIMENTS

The objectives of the experiments were: (i) to validate the laminate damping model; (ii) to evaluate the effects of space environment using ground based simulators.

In meeting these objectives, three types of experiments were conducted: (i) cantilever plate driven by a heterodyne system sweeping through the frequency domain, up to five modes; (ii) cantilever plate subject to step loading, transient decay at fixed frequency; (iii) axial creep compliance tests, low frequency spectrum.

3.1 HETERODYNE ANALYSER TESTS WITH CANTILEVER PLATES

To properly characterize the vibration response, a variety of 4-ply balanced symmetric laminates were selected for testing. The specimens were manufactured into plates, nominally 17.8 cm long by 5 cm wide and 0.5 mm thick. Since all samples could not be fabricated in the same cure cycle, an effort was made to account for batch effects by including (0)° and (90)° laminates in each cure cycle. All samples were made

from 3M SP 288 T300 graphite/epoxy tape.

Specimens were mounted on a Bruel & Kjaer (B&K) Complex Modulus Apparatus (Type 3930) which uses two magnetic transducers (B&K Type MN0002), one acting as an 'exciter', the other acting as a 'pickup'. High magnetic permeability discs were positioned opposite the transducers on the non-ferro-magnetic G&E samples. They were then connected to a B&K Heterodyne Analyser (Type 2010) which employed a beat frequency oscillator to drive the exciter transducer, and an analyser to process the signal from the pickup transducer. This system allowed manual or automatic sweep of the driving frequency through a range of 2 Hz to 200 KHz. The various natural frequencies of vibration were indicated as amplitude peaks on the printout of the B&K Recorder (Type 2305) (see Fig. 1). To determine the specimen damping characteristics, one could employ either the phase lag between input/output signals, which is directly related to the material loss factor, or the reverberation decay technique which provides a measure of the log decrement. In this latter method, the oscillator cutoff was activated at each mode of vibration, and the resonance peak was allowed to decay. The resulting decay appeared as a nearly straight line on the recorder. This system was used to validate the laminate model at ambient conditions, and it is presently being modified to operate in a space simulator.

3.2 SPACE SIMULATOR TESTS

Two space simulators were assembled to study the effects of thermal vacuum cycling and U.V. radiation on the damping of graphite/epoxy material. In one simulator, an electrically-driven travelling arm apparatus was designed to retract by remote control, thus providing a step-load to a cantilever plate specimen (Fig. 2). Bonded surface strain gauges, specially calibrated for thermal-vacuum exposure, provided the required transient decay damping output on an oscilloscope (see Fig. 3). From such traces one can calculate at any time t_1 , $\lambda = (1/t_1) \log(Y_0/Y_1)$ where (Y_0/Y_1) is the signal amplitude ratio. Knowing the frequency 'f', then the log decrement can readily be obtained from $\lambda = \pi/f$. This particular facility was used to study the effects of material batch and cure cycle variations as well as thermal-vacuum cycling.

The second simulator contained a 1000 watt Xenon D.C. arc lamp (Conrad-Hanovia, U.S.A.) capable of providing U.V. radiation in the wavelength range of 200 nm - 400 nm. In combination with a thermal-vacuum environment, it was possible to obtain creep compliance data for different U.V. exposures. Another feature included a carousel arrangement (see Fig. 4) which supported 30 flat coupons (about 2.54 cm in width), each of which could be rotated into a gimbal mounted load grip having 4500 N capacity. Each creep test consisted of subjecting a sample to a given tensile load for a certain length of time. Once the load was removed and the sample left unconstrained, the strain was recorded as a function of time.

For purposes of brevity, details on both space simulators can be found in Ref. 21.

4. EXPERIMENTAL RESULTS

4.1 VALIDATION OF LAMINATE DAMPING MODEL

Using the heterodyne analyser system, variations in principal damping values (log decrement in this case) were obtained as a function of frequency. These results are presented in Fig. 5 where the δ_{66} was derived from an off-axis test (δ_{xy}) in combination with the analysis of Appendix A.

Based on the above, it was then possible to predict the loss factor as a function of frequency for other GRE configurations. Comparisons with test data for $(\pm\theta)_s$ laminates are given in Figs. 6-9. In Fig. 10, one can readily see that the analysis holds for other stacking sequences as well. In all instances, agreement between predicted and measured responses is very good.

To illustrate how such damping data can be employed for design purposes, Figs. 11 and 12 were constructed for two quasi-isotropic laminates, (0, ± 60) and (0, ± 45 , 90). In both examples, the position of the 0° ply was varied. It is quite evident from these results that one can substantially change the damping values.

One additional feature inherent in using the heterodyne analyser is the ease with which one can obtain the frequencies associated with different modes of vibration. Using a cantilever plate vibration model, analyses of the various laminates were performed to estimate the change in mode frequencies with fiber angle. Figures 13-15 provide ample evidence of the excellent agreement one can achieve using laminate analysis, at least for flat cantilever plates. Note that these comparisons extend from the first to the fifth natural modes of vibration.

4.2 MATERIAL BATCH AND CURE CYCLE EFFECTS

One matter of importance arose concerning the effect of batch variations on the damping parameters. In measuring material damping it has been observed that it is essential for the test coupons to come from the same material batch and undergo the same cure cycle at the same time as the structural component being investigated. As can be seen in Fig. 16, not only can the principal damping values change (as might be expected), but their differences can have a substantial effect on the damping curves. For example, using the same graphite/epoxy material, two batches (M & B) were sampled and the resulting damping curves are shown in Fig. 16. However, material from the same batch but cured at different times also produced significant changes, as evidenced by batch M and the 'dry state' curves.

4.3 THERMAL-VACUUM CYCLING EFFECTS

For short term vacuum exposure, small changes in the principal damping parameters were obtained, as can be seen in Table 1. Using these data, predictions were made on the variation of δ with laminate ply angle, and the results compared to tests (Fig. 17). Agreement is rather good.

Long term space simulation results are shown in Fig. 18 based on damping measurements after 470 days exposure at 10^{-6} to 10^{-7} torr and 66 thermal cycles. The reference state was based on specimen data taken in the 'dry' state, again from duplicate samples prepared at the same time but relegated to a desiccator environment over the period of 470 days. The curves shown through the principal damping values are theoretical (but based on these values) and clearly demonstrate the effect of prolonged thermal-vacuum cycling.

4.4 EFFECT OF U.V. RADIATION IN A THERMAL-VACUUM ENVIRONMENT

Long term thermal-vacuum tests were conducted over a period of 180 equivalent sun days of U.V. radiation. Creep compliance measurements were made on graphite/epoxy (SP 288 T300) plate specimens at selected exposure intervals, the results of which can be found in Refs. 20 and 21. As outlined in Section 2, loss factors can then be determined from the complex compliance for any laminate once the principal values are known. Figure 19 shows the variation in loss factor for various $(\pm\theta)_s$ laminates as a function of fiber angle. Both ambient and vacuum-radiation exposure data are presented for a frequency of 0.1 Hz. Note that the maximum damping occurs around 45° which is consistent with the flexural damping results in Fig. 17 obtained from samples from the same material batch. The fact that this is near the 'zero' coefficient of thermal expansion angle (see Refs. 15 and 16) could prove useful in building dimensionally stable, highly damped structures. However, more than a 50% reduction in the maximum loss factor is observed after the material is subjected to the simulated space environment. Based on previous thermal-vacuum exposure data (Fig. 18), outgassing leads to a substantial reduction in material damping. Earlier work (Ref. 16) has shown that moisture comprises the bulk of the outgassing products.

To demonstrate the change in loss factor with frequency, Fig. 20 presents the calculated results for a $(\pm 45)_s$ laminate over a low frequency spectrum. As one would expect from the creep results, the loss factor generally increases in magnitude with a lowering of frequency in this range. This trend can also be seen in Figs. 6-9 for the low frequency end. The 'humps' correspond to similar behaviour evident in the original creep compliance curves. However, since the loss factor is related to the slope of these curves, it is quite sensitive to any inaccuracies in the creep data.

5. CONCLUSIONS

Sufficient data have been obtained to demonstrate that the laminate model can yield accurate predictions of the flexural damping values. Using a 'principal damping matrix' approach, optimum damping configurations can be derived. Loss factors have also been calculated from creep compliance experiments. However, more tests are required before the accuracy of this technique can be properly assessed.

Exposure to a thermal-vacuum environment of a polymer matrix composite leads to a significant reduction in the material damping, probably due to outgassing (mainly moisture). Additional exposure to U.V. radiation (up to 180 ESD) produced no substantial changes, at least for the graphite/epoxy material investigated. Finally, it was observed that material batch and cure cycle variations can result in large differences in principal damping values, thus seriously influencing damping predictions for a given structure.

REFERENCES

1. Ashley, H., "On Passive Damping Mechanisms in Large Space Structures", Proc. AIAA Structures, Structural Dynamics and Materials Conf., Paper No. 82-0639, 1982.
2. Graham, W. B., "Material Damping and Its Role in Linear Dynamic Equations", University of Toronto, Institute for Aerospace Studies, UTIAS Review No. 36, March 1973.
3. Torvik, P. J. (Ed.), "Damping Applications for Vibration Control", AMD-Vol. 38, Pub. ASME, 1980.
4. Schultz, A. B. and Tsai, S. W., "Dynamic Moduli and Damping Ratios in Fiber-Reinforced Composites", J. Composite Materials, Vol. 2, No. 3, July 1968.
5. Schultz, A. B. and Tsai, S. W., "Measurements of Complex Dynamic Moduli for Laminated Fiber-Reinforced Composites", J. Composite Materials, Vol. 3, July 1969.
6. Hashin, Z., "Complex Moduli of Viscoelastic Composites - I. General Theory and Application to Particulate Composites", Int. J. Solids Structures, Vol. 6, 1970.
7. Hashin, Z., "Complex Moduli of Viscoelastic Composites - II. Fiber Reinforced Materials", Int. J. Solids Structures, Vol. 6, 1970.
8. Abarcar, R. B. and Cunniff, P. F., "The Vibration of Cantilever Beams of Fiber Reinforced Material", J. Composite Materials, Vol. 6, Oct. 1972.
9. Adams, R. D. and Bacon, D. G. C., "Effect of Fibre Orientation and Laminate Geometry on the Dynamic Properties of CFRP", J. Composite Materials, Vol. 7, Oct. 1973.

10. Paxson, E. B., "Real and Imaginary Parts of the Complex Viscoelastic Modulus for Boron Fiber Reinforced Plastics (BFRP)", J. Acoust. Soc. Am., Vol. 57, No. 4, April 1975.
11. Gibson, R. F. and Plunkett, R., "Dynamic Mechanical Behavior of Fiber-Reinforced Composites: Measurement and Analysis", J. Composite Materials, Vol. 10, Oct. 1976.
12. Bjarnason, W. P. G., "The Effect of Space Environment on the Structural Damping of Laminated Composites", B.A.Sc. Thesis, University of Toronto, 1980.
13. Morison, W. D., "The Structural Damping and Thermal Response of Advanced Composites in a Simulated Space Environment", M.A.Sc. Thesis, University of Toronto, Institute for Aerospace Studies, 1980.
14. Morison, W. D., "The Prediction of Material Damping of Laminated Composites", Proc. Canadian Aeronautics and Space Institute, First Symposium Structures and Materials, Toronto, Canada, June 1982.
15. Tennyson, R. C., "Study of Space Environmental Effects on Polymer Matrix Composite Materials", Interim Reports submitted to AFOSR, Contract No. AFOSR-78-3694, A, B, Oct. 1979, 1980.
16. Tennyson, R. C., "Composite Materials in a Simulated Space Environment", Proc. 21st Structures, Dynamics and Materials Conf., AIAA/ASME/ASCE/AHS, Seattle, Wash., May 1980.
17. Bagley, R. L. and Torvik, P. J., "Fractional Calculus - A Different Approach to the Finite Element Analysis of Viscoelastically Damped Structures", Proc. 21st Structures, Dynamics and Materials Conf., AIAA/ASME/ASCE/AHS, Seattle, Wash., May 1980.
18. Briley, R. P. and Rehfield, L. W., "Influence of Environmental Conditions on Dynamic Behavior of Graphite/Epoxy Composites", Georgia Inst. Technology School of Aerospace Eng. Report, Jan. 1981.
19. Buhariwala, K. J. and Hansen, J. S., "Dynamic Response of Fiber Reinforced Viscoelastic Structures Using the Finite Element Method", Proc. Canadian Aeronautics and Astronautics 1st Symposium on Structures and Materials, Toronto, June 1982.
20. Smith, B. A. W., "Polymer Matrix Composite Materials in a Simulated Space Environment: UV and Vacuum Effects", M.A.Sc. Thesis, University of Toronto, Institute for Aerospace Studies, 1981.
21. Tennyson, R. C., Smith, B. A. W. and Hebert, L. P., "The Effect of Combined U.V. Radiation and High Energy Electrons on the Behaviour of Polymer Matrix Composites in Hard Vacuum", Proc. Specialist Meeting "Environmental Effects on Materials for Space Applications", AGARD, Sept. 1982.

ACKNOWLEDGEMENT

The authors wish to gratefully acknowledge the financial support for this research program received from the Natural Sciences and Engineering Research Council of Canada (Grant A-2783) and the United States Air Force Office of Scientific Research, Washington, D.C. (under Grant AFOSR-78 3694). Contributions to both the analytical and experimental programs were made by Mr. W. P. Bjarnason and Mr. G. Blom, research assistants at UTIAS.

TABLE 1
PRINCIPAL FLEXURAL DAMPING VALUES (LOG DECREMENT)
FOR GRAPHITE/EPOXY (9P288 T300)

Log Decrement δ (10^{-3})	Soft Vacuum* $\sim 10^{-2}$ torr	24 hrs. $\text{@ } \sim 10^{-6}$ torr	72 hrs. $\text{@ } \sim 10^{-6}$ torr
11	5.67	5.50	5.40
22	38.10	33.47	32.50
66	36.00	36.64	36.20

*No aerodynamic effects.

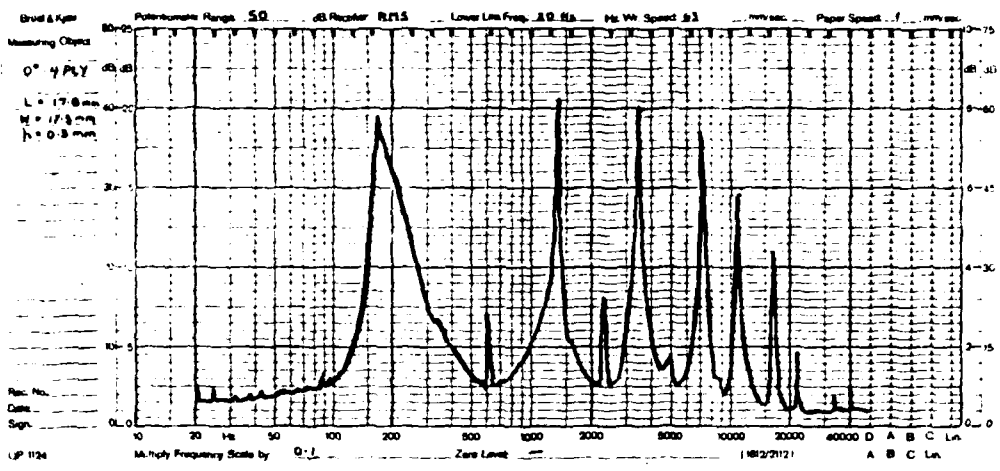


Figure 1 Sample Frequency Spectrum of Graphite/Epoxy Specimen

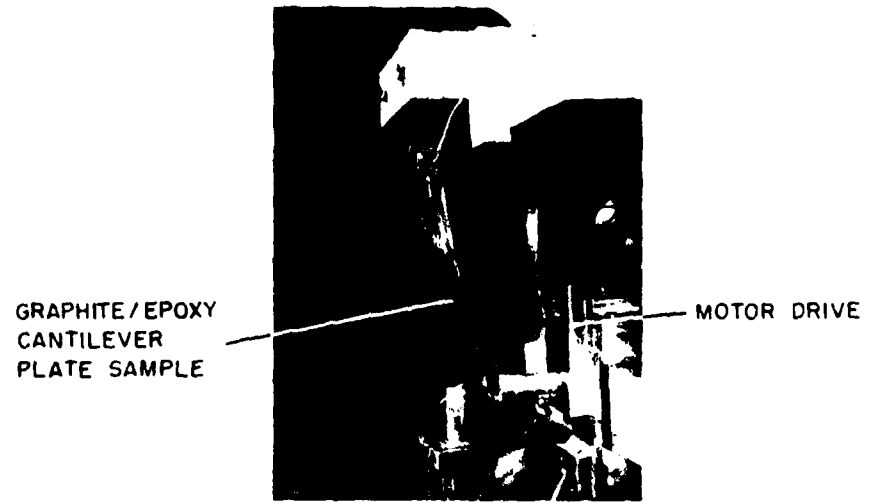


Figure 2 View of Remote Control Flexure Drive System

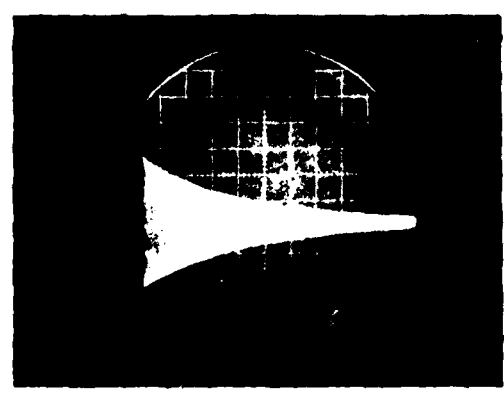


Figure 3 Strain Gauge Output from Damped Flexural Oscillation of Graphite/Epoxy Plate

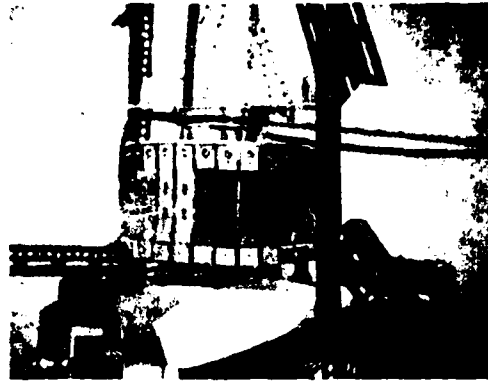


Figure 4 Carousel of Composite Samples

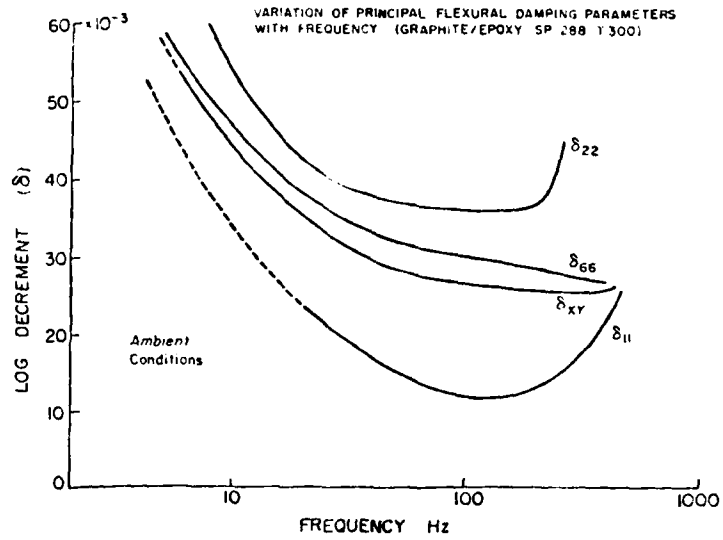


Figure 5

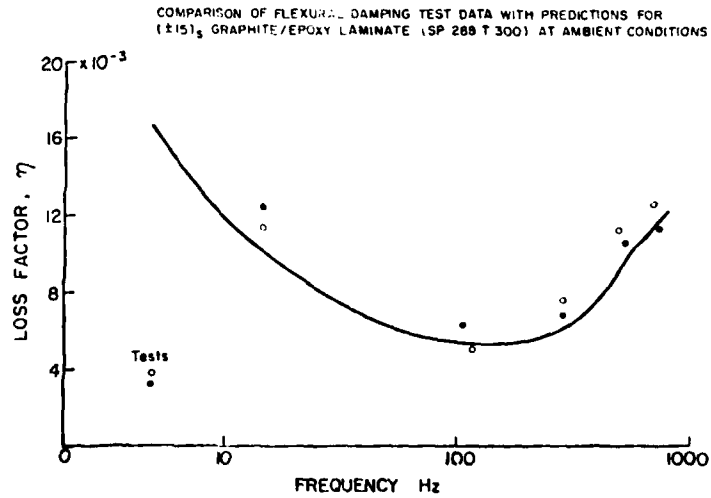


Figure 6

COMPARISON OF FLEXURAL DAMPING TEST DATA WITH PREDICTIONS FOR
(± 30)_g GRAPHITE/EPOXY LAMINATE (SP 288 T 300) AT AMBIENT CONDITIONS

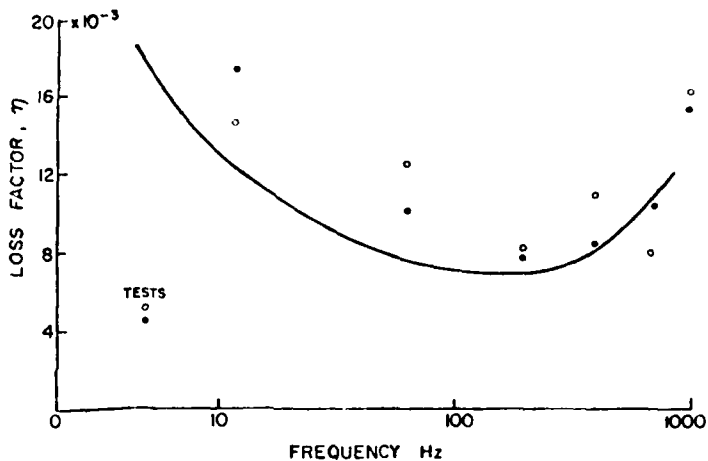


Figure 7

COMPARISON OF FLEXURAL DAMPING TEST DATA WITH PREDICTIONS FOR
(± 60)_g GRAPHITE/EPOXY LAMINATE (SP 288 T 300) AT AMBIENT CONDITIONS

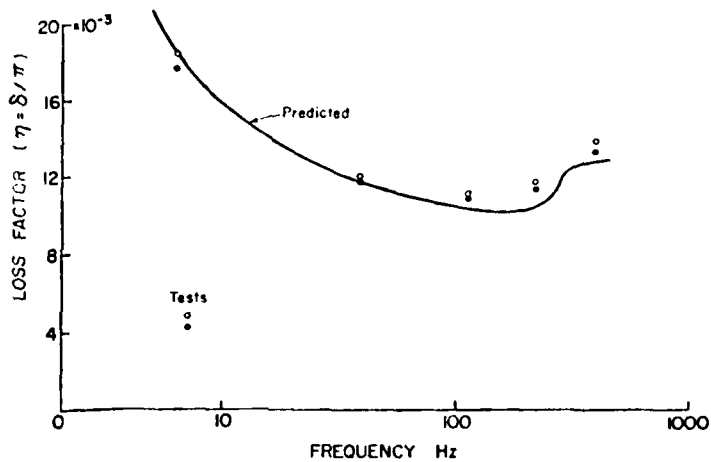


Figure 8

COMPARISON OF FLEXURAL DAMPING TEST DATA WITH PREDICTIONS FOR
(± 75)_g GRAPHITE/EPOXY LAMINATE (SP 288 T 300) AT AMBIENT CONDITIONS

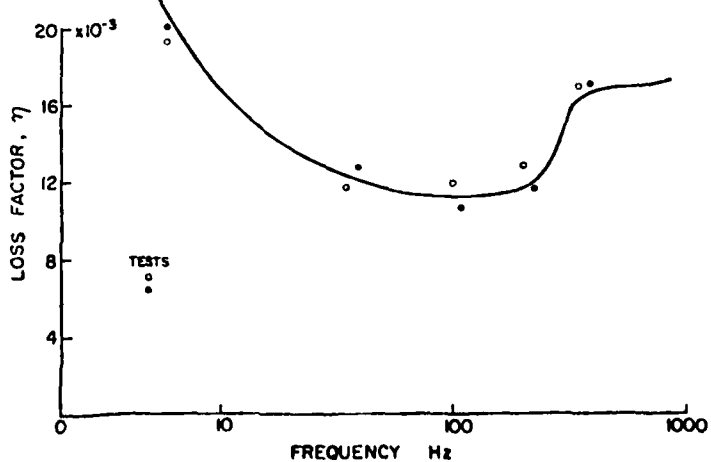


Figure 9

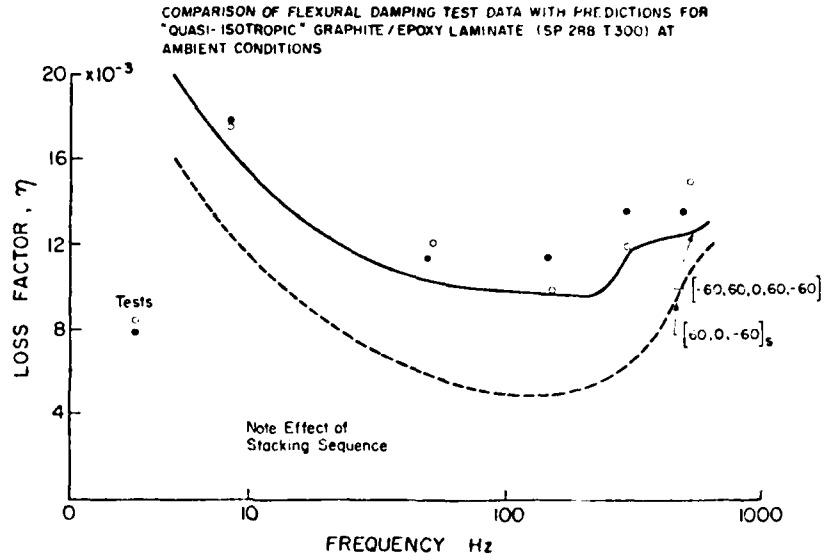
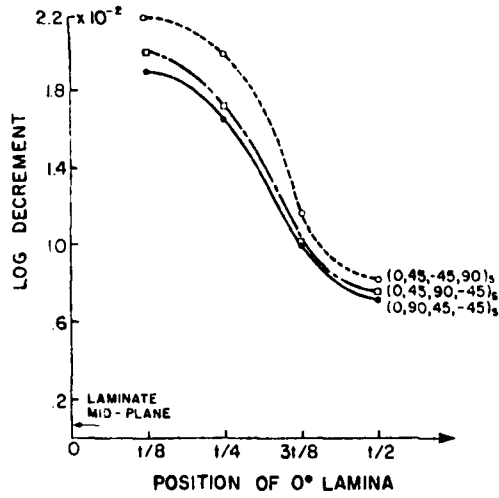
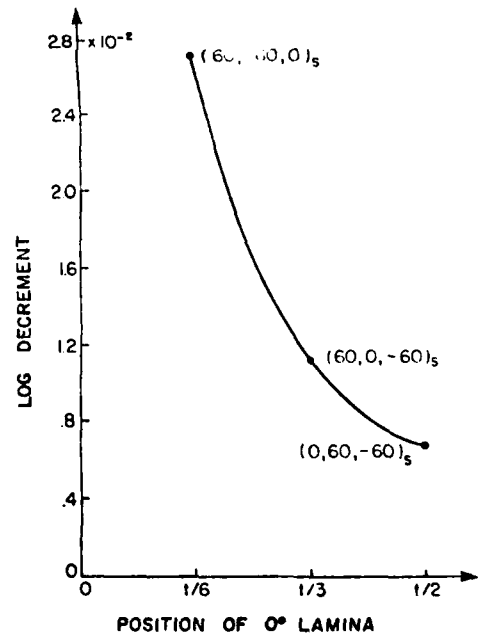


Figure 10



EFFECT OF VARYING PLY POSITIONS ON FLEXURAL DAMPING OF GRAPHITE/EPOXY LAMINATE (3M SP 288 T 300)

Figure 11



EFFECT OF VARYING PLY POSITIONS ON FLEXURAL DAMPING OF GRAPHITE/EPOXY LAMINATE (3M SP 288 T 300)

Figure 12

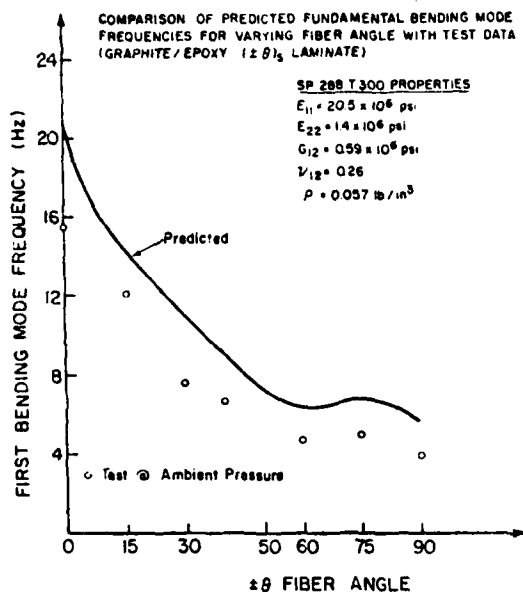


Figure 13

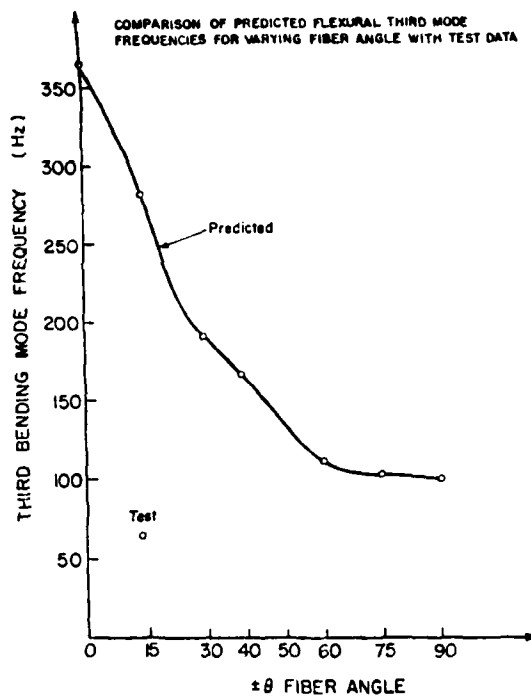


Figure 14

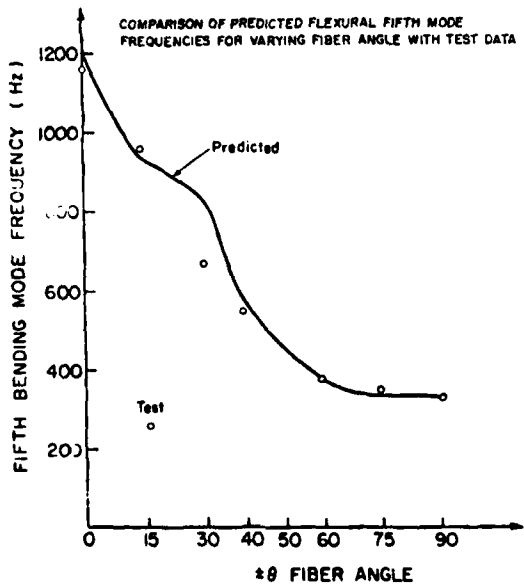


Figure 15

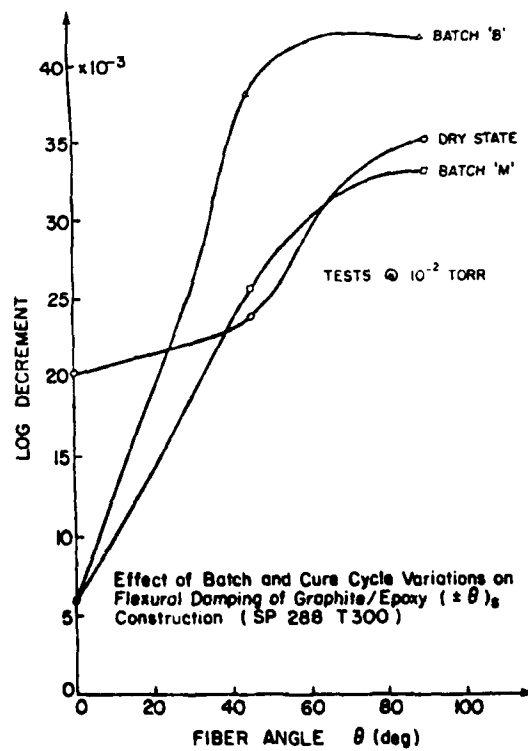


Figure 16

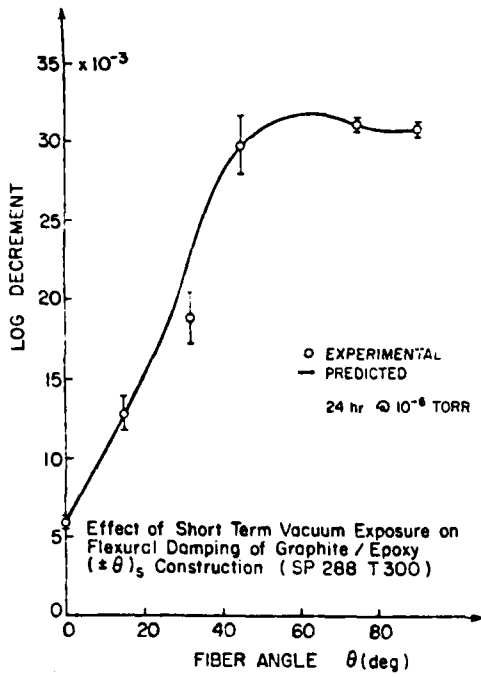


Figure 17

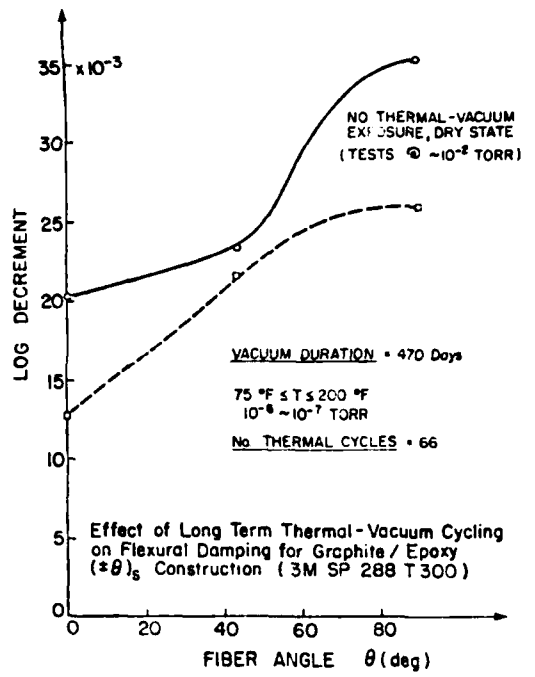


Figure 18

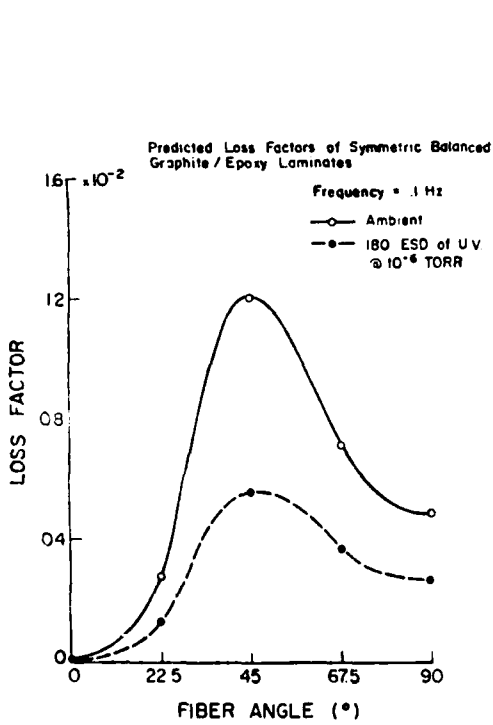


Figure 19

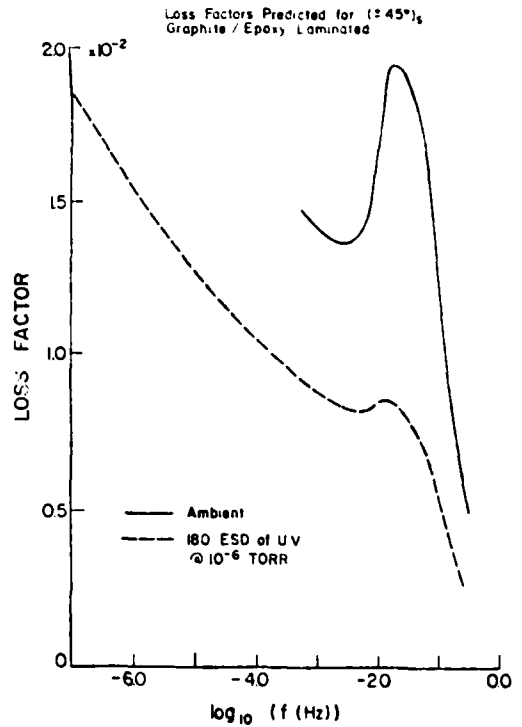


Figure 20

APPENDIX A

THEORETICAL PREDICTION OF LAMINATE MATERIAL DAMPING

Based on elastic strain energy considerations, a laminate damping analysis was developed in Ref. 9 for constant angle configurations. This analysis was extended for 'general' laminates, details of which are given in the following sections.

The material damping in composites is conveniently modelled as a dissipation of strain energy due to internal forces. The specific damping capacity (SDC) of a material is defined as,

$$\psi = \frac{\Delta U}{U} \quad (\text{A-1})$$

where U is the maximum strain energy in the laminate and ΔU is the strain energy dissipated during a strain cycle. Considering the k -th lamina of an arbitrary laminate which is of unit width and length, the strain energy is

$$U_k = \frac{1}{2} \int_{h_{k-1}}^{h_k} \{\epsilon\}_k^T \{\sigma\}_k dz \quad (\text{A-2})$$

where h_k and h_{k-1} represent, respectively, the upper and lower surface thickness (z) coordinates. The value of U_k is independent of the coordinate system; however, the most convenient system for beginning the damping analysis is the material (1-2) coordinate system where

$$\{\epsilon\}_k = \begin{bmatrix} \epsilon_1 \\ \epsilon_2 \\ \gamma_{12} \end{bmatrix}_k; \quad \{\sigma\}_k = \begin{bmatrix} \sigma_1 \\ \sigma_2 \\ \tau_{12} \end{bmatrix}_k \quad (\text{A-3})$$

Here ϵ_1 and ϵ_2 are normal strains, γ_{12} is the shear strain, σ_1 and σ_2 are normal stresses and τ_{12} is the shear stress, all in the lamina coordinates.

For an orthotropic lamina which exhibits a linear elastic stress-strain response, the strain energy can be separated into five components:

$$U_k = U_{11k} + U_{12k} + U_{21k} + U_{22k} + U_{66k} \quad (\text{A-4})$$

where

$$U_{11k} = \frac{1}{2} \int_{h_{k-1}}^{h_k} (Q_{11} \epsilon_1^2)_k dz$$

$$U_{22k} = \frac{1}{2} \int_{h_{k-1}}^{h_k} (Q_{22} \epsilon_2^2)_k dz$$

$$U_{66k} = \frac{1}{2} \int_{h_{k-1}}^{h_k} (Q_{66} \gamma_{12}^2)_k dz$$

and because of the elastic symmetry of the orthotropic lamina

$$U_{12k} = U_{21k} = \frac{1}{2} \int_{h_{k-1}}^{h_k} (Q_{12} \epsilon_1 \epsilon_2)_k dz \quad (\text{A-5})$$

This symmetry causes Eq. (A-4) to effectively collapse to only four terms. Following the definition of SDC, the total energy dissipated in this lamina is given by the sum of four components defined by

$$\Delta U_{11k} = \frac{1}{2} \int_{h_{k-1}}^{h_k} (\psi_{11} Q_{11} \epsilon_1^2)_k dz$$

$$\Delta U_{22k} = \frac{1}{2} \int_{h_{k-1}}^{h_k} (\psi_{22} Q_{22} \epsilon_2^2)_k dz$$

(A-6)
Contd...

Contd...

14-14

$$\Delta U_{66k} = \frac{1}{2} \int_{h_{k-1}}^{h_k} (\epsilon_{66} Q_{66} \gamma_{12}^2)_k dz \quad (A-6)$$

$$\Delta U_{12k} = \Delta U_{21k} = \frac{1}{2} \int_{h_{k-1}}^{h_k} (\psi_{12} Q_{12} \epsilon_1 \epsilon_2)_k dz$$

where the ψ_{ij} are generally nonlinear functions of strain. The total energy dissipation expression can be assembled as a matrix equation:

$$\Delta U_k = \frac{1}{2} \int_{h_{k-1}}^{h_k} \{ \epsilon \}_k \{ \psi \}_k \{ Q \}_k \{ \epsilon \}_k dz \quad (A-7)$$

where

$$\{ \epsilon \}_k = [\epsilon_1, \epsilon_2, \gamma_{12}]$$

and

$$\{ \psi \} = \begin{bmatrix} \psi_{11} & \psi_{12} & 0 \\ \psi_{12} & \psi_{22} & 0 \\ 0 & 0 & \psi_{66} \end{bmatrix} \quad (A-8)$$

It should be noted that the ψ_{12} component effectively constitutes the "Poisson" contribution to the damping; however, for the results presented in this paper, ψ_{12} has been set to zero to simplify the analysis.

The energy dissipation equation for the laminate is the sum of the lamina losses, so

$$\Delta U = \frac{1}{2} \sum_{k=1}^n \int_{h_{k-1}}^{h_k} \{ \epsilon \}_k \{ \psi \}_k \{ Q \}_k \{ \epsilon \}_k dz \quad (A-9)$$

where k = lamina number, n = number of laminae.

One can now transform from the principal material axes (1, 2) to some arbitrary set of structural axes (X, Y) for convenience, thus obtaining,

$$\Delta U = \frac{1}{2} \sum_{k=1}^n \int_{h_{k-1}}^{h_k} \{ \hat{\epsilon} \}_k \{ T' \}_k^T \{ \psi \}_k \{ Q \}_k \{ T' \}_k \{ \hat{\epsilon} \}_k dz \quad (A-10)$$

where

$$\{ \hat{\epsilon} \}_k = \begin{bmatrix} \epsilon_x \\ \epsilon_y \\ \gamma_{xy} \end{bmatrix}_k$$

and

$$\{ T' \}_k = \begin{bmatrix} m^2 & n^2 & mn \\ n^2 & m^2 & -mn \\ -2mn & 2mn & (m^2 - n^2) \end{bmatrix}_k \quad (A-11)$$

where $m = \cos \theta$ and $n = \sin \theta$ with θ equal to the angle of orientation of the lamina with respect to the laminate structural axes.

It should be noted that the strain dependence of the ψ_{ij} generally prohibits the integral from being evaluated explicitly.

The maximum strain energy U in the laminate can be evaluated directly from the laminate constitutive equations,

$$\begin{bmatrix} \epsilon^o \\ K \end{bmatrix} = \begin{bmatrix} A' & B' \\ C' & D' \end{bmatrix} \begin{bmatrix} N \\ M \end{bmatrix}$$

where ϵ^o and K are the mid-plane strains and curvatures and $[N]$ and $[M]$ are the stress and moment resultants given by

$$[N] = \sum_{k=1}^n \int_{h_{k-1}}^{h_k} \{ \sigma \}_k dz, \quad [M] = \sum_{k=1}^n \int_{h_{k-1}}^{h_k} \{ \sigma \}_k z dz \quad (A-12)$$

with

$$\{\epsilon\}_k = \{\epsilon^0\}_k + z(K)_k = \text{total strain in lamina } k$$

Applying these results, the strain energy in terms of laminate axes strains and curvatures is

$$U = \frac{1}{2} [N] \{\hat{\epsilon}^0\} + \frac{1}{2} [M] \{\hat{K}\} \quad (\text{A-13})$$

Therefore the SDC is formulated as

$$\psi = \frac{\sum_{k=1}^n \int_{h_{k-1}}^{h_k} \{\hat{\epsilon}\}_k^T [T']_k^T [\psi] [Q]_k [T']_k \{\hat{\epsilon}\}_k dz}{[N] \{\hat{\epsilon}^0\} + [M] \{\hat{K}\}} \quad (\text{A-14})$$

FREE FLEXURE CASE

The equation above applies to any general strain state in a laminate; however, certain cases are more amenable to analysis because of the attendant simplifications they generate. One of these cases involves the application of a pure bending moment to a beam, thereby creating a state of free flexure. The boundary conditions for free flexure are:

$$\begin{aligned} [N] &= 0 \\ \{\hat{\epsilon}^0\} &= 0 \\ \{\hat{\epsilon}\} &= z\{\hat{K}\} = z[D'] [M] \end{aligned} \quad [M] = \begin{bmatrix} M_x \\ 0 \\ 0 \end{bmatrix}$$

Therefore

$$\{\hat{\epsilon}\} = \begin{bmatrix} D'_{11} \\ D'_{12} \\ D'_{16} \end{bmatrix} z M_x$$

and the expression for ΔU becomes

$$\Delta U = \frac{1}{2} \sum_{k=1}^n \int_{h_{k-1}}^{h_k} M_x^2 z^2 [D'_{11}, D'_{12}, D'_{16}]_k [T']_k^T [\psi] [Q]_k [T']_k \begin{bmatrix} D'_{11} \\ D'_{12} \\ D'_{16} \end{bmatrix} dz \quad (\text{A-15})$$

The corresponding expression for U is

$$U = \frac{1}{2} D'_{11} M_x^2 \quad (\text{A-16})$$

Although others [2, 12] have shown that laminate damping is a function of strain, as a first order approximation, the ψ_{ij} are assumed to be independent of strain. Thus the expression for ΔU can be integrated explicitly to yield

$$\Delta U = \frac{1}{6} \sum_{k=1}^n (h_k^3 - h_{k-1}^3) [D'_{11}, D'_{12}, D'_{16}]_k [T']_k^T [\psi] [Q]_k [T']_k \begin{bmatrix} D'_{11} \\ D'_{12} \\ D'_{16} \end{bmatrix} M_x^2 \quad (\text{A-17})$$

Therefore the free flexure damping is given by,

$$\psi_{FF} = \frac{\sum_{k=1}^n [D'_{11}, D'_{12}, D'_{16}]_k [T']_k^T [\psi] [Q]_k [T']_k \begin{bmatrix} D'_{11} \\ D'_{12} \\ D'_{16} \end{bmatrix}}{3D'_{11}} \quad (\text{A-18})$$

RECORDER'S REPORT

SESSION III - PROPERTIES OF INTEREST

by

Mr A.J. Russell
Defence Research Establishment
Pacific
F.M.O. Victoria
BC VOS 1B0
Canada

Session III covered a wide range of materials and their properties, from the damping behaviour of structural composites in vacuum to the electrical characteristics of solar cells in a simulated deep space environment. The session emphasized the need for careful design and analysis of laboratory tests in order to obtain data relevant to a given space application. In particular the paper by Peacock and Whitaker on long term exposure to a simulated space environment revealed the lack of correlation between short and long term exposure to vacuum. This was further complicated by the effects of subsequent irradiation which, in some instances, led to a recovery in properties while in others, more degradation occurred.

The initial discussion concentrated on problems associated with characterizing the damping properties of composite materials. Professor Santini was concerned with the difficulties in constructing the entire damping matrix, including the coupling terms, from small test coupons. Other aspects of damping which were felt to require further investigation were the standardization of test specimens and methods and the origin of batch-to-batch variations in damping parameters.

The discussion then turned to the relationship between material properties and structural design. Mr Buchs stated that since most space structures were stiffness-critical, one could not afford the luxury of designing material damping into them by means such as the use of $\pm 45^\circ$ plies but rather one designed for stiffness first and if necessary, mechanical damping could be added later. Mr Morison on the other hand, was of the opinion that as space structures became larger and as mechanical fasteners gave way to adhesive bonding, that material damping would become more important and that a design compromise between stiffness, weight, and damping would have to be made from the outset.

TESTING OF FLEXIBLE DEPLOYED SOLAR ARRAY (L-SAT)

by

P.A. McIntyre, Director, Engineering RMSD
 A.S. Jones, Manager, Mechanical Engineering RMSD
 J. Renshall, Group Leader, Mechanism Engineering
 and G.W. Marks, Group Leader, System General
 SPAR Aerospace Ltd.,
 Space & Electronics Group
 1700 Ormont Drive
 Weston, Ontario M9L 2W7
 Canada

Abstract/Summary

The L-SAT Solar Array subsystem is Spar's latest design of light-weight Flexible Deployed Solar Array. It will be flown on a high-powered accurately pointed Communication Satellite namely L-SAT, and will be subjected to qualification testing at both the integrated system, subassembly and component level. In addition, development testing has been carried out on critical items of the design, specifically that associated with blanket behavior during deployment and Apogee Engine and RCS firing, L-SAT being the first flexible array to be operational during Apogee Engine firing.

The test philosophy being adopted is similar to that used on the Communications Technology Satellite (Hermes), however, due to the size of the array and facilities available, array natural frequencies will be predicted by analysis and modal test methods. Electrical component subsystem testing covering solar cell, array blanket pyro-techniques and other electrical items are discussed in this paper and the status of development tests completed to date is reviewed.

Glossary of Terms and Abbreviations

T.V. : Thermal Vacuum
 A.E.F. : Apogee Engine Firing
 RCS : Reaction Control System
 CTS : Communications Technology Satellite (Hermes)
 E.O.L. : End of Life
 B.O.L. : Beginning of Life
 L-SAT Min: 2.5 Kw EOL Array
 L-SAT Max: 6.5 Kw EOL Array
 L-1 : First Satellite in L-SAT Series
 ESA : European Space Agency
 B.Ae. : British Aerospace Corp.
 CRC : Communication Research Centre (Department of Communications Canada)
 T.O. :

FSA : Flexible Solar Array
 M-SAT : Mobil Communications Satellite
 STS : Space Transportation System (Shuttle)
 ACS : Attitude Control System
 SDE : Secondary Deployment Electronics
 SSS : Simulated Spacecraft Sidewall
 DSA : Deployable Solar Array
 ACC : Acceptance Test Level
 S/C : Spacecraft
 SAD : Solar Array Drive

Introduction

The Large Satellite (L-SAT) Solar Array subsystem which is Spar's second generation of light-weight flexible deployed solar arrays for synchronous orbit communication satellites, is designed to cover the range 2.5-6.5 Kw E.O.L. over a mission period of 10 years in orbit with capability of extending to 7.8 Kw. The array is being produced for B.Ae./ESA's L-SAT program (Figure 1) and is a result of continuous development of the CTS (Hermes) array technology, designed and tested under contract for the Department of Communications (Research Centre), Ottawa, Canada, and flown successfully in synchronous orbit from January 1976 - November 1979.

The Large Flexible Solar Array will be partially deployed during transfer orbit, this being the first time for such an array. The Solar Array will be tested as part of the spacecraft system except during Thermal Vacuum testing when it is impractical. A separate qualification, flight acceptance test program will be conducted to ensure satisfactory in-orbit performance when integrated with the spacecraft. This philosophy of testing is similar to that conducted for CTS; however, due to facility limits, partial deployment of the flex array during Thermal Vacuum Tests will be conducted, and array natural frequencies will be calculated using modal analysis techniques. Flight solar arrays subsystems will be vibrated

independently and as part of the spacecraft test in the stowed positions.

Major design features of the Solar Array subsystem are briefly discussed and critical areas requiring development and life testing are addressed.

The vibration, thermal vacuum deployment and partially deployed array thermal vacuum cycling tests to be conducted, plus the overall integrated system test program is also presented.

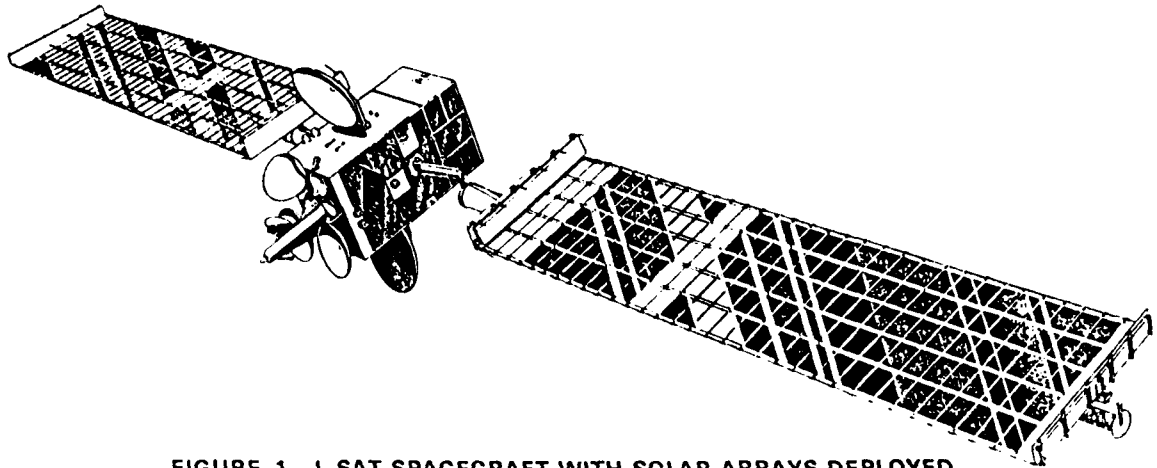


FIGURE 1 L-SAT SPACECRAFT WITH SOLAR ARRAYS DEPLOYED

Design Description

The L-SAT Array is similar in principal to the Hermes (CTS) array in that it is a "concertina" folded arrangement, stowed during launch on the spacecraft north/south body panels of a 3 axis stabilized spacecraft and arranged such that it takes up minimum volume. The array is normally deployed in synchronous orbit using an Astromast deployment system and a more detailed description of L-SAT and Hermes (CTS) array can be found in reference 1 and 2.

The L-SAT array comprises a 2 stage arrangement namely primary and secondary system: both systems are retained using a pyro initiated release arrangement and stowed on the north/south body panels during launch.

The primary system is initiated first and this deploys the astromast deployer and stowed secondary system in a controlled manner using a cable and pulley to co-ordinate motion, and an eddy current damper to control latch up shock loads.

On completion of the primary deployment in transfer orbit, the secondary system is initiated and the array deployed to provide (T.O.) Transfer Orbit power. In this configuration, remaining sections of the solar array panel remain stowed. After injection into synchronous orbit the remaining "stack" is deployed after the Transfer Orbit Tension Mechanism (TOIM) is released, the release system being similar to the secondary release and initiated using pyro-technics commanded from ground.

Figures 2 and 3 show the main features of the L-SAT and Hermes (CTS) array deployment mechanism and overall configuration. These figures illustrate the similarity in overall concept between the two arrays. Figures 4 and 5 illustrates the deployment sequence including primary, partial array and final array deployment in Transfer and Synchronous orbit respectively for the L-SAT array.

To summarize, the main elements of the L-SAT array are:

- : A Primary Deployment System which is restrained during launch via a tie-down system onto the N/S panels. This includes the astromast and stowed array. System is initiated by ground command, firing pyros which release the system and allow primary deployment. Controlled deployment is via cable co-ordinated system and damped by an eddy current damper.
- : A Secondary system, which deploys the stowed array, is initiated by pyros after primary deployment is completed.
- : Solar Array blanket is deployed using the astromast deployer powered from the Secondary Deployment Electronics (SDE), which also provide telemetry and command signals during T.O. Controlled deployment of the array is ensured via parking springs which retain the array during array deployment. Protection interleaves used to protect cells during launch form part of this arrangement.
- : Tip Tension mechanism to control blanket tension and to shut down the system when the correct array tension is achieved. The system can be interrupted, and deployment restarted by ground command.

Testing of the array follows the techniques developed for the Hermes array however, only limited testing is possible due to the size of the array, thus considerable analysis and development testing must be conducted to verify critical areas of the design. These development tests and the planned qualification test program by the two major subcontractors, Fokker of Amsterdam and AEG Telefunken (also the Hermes array blanket supplier) are discussed herein.

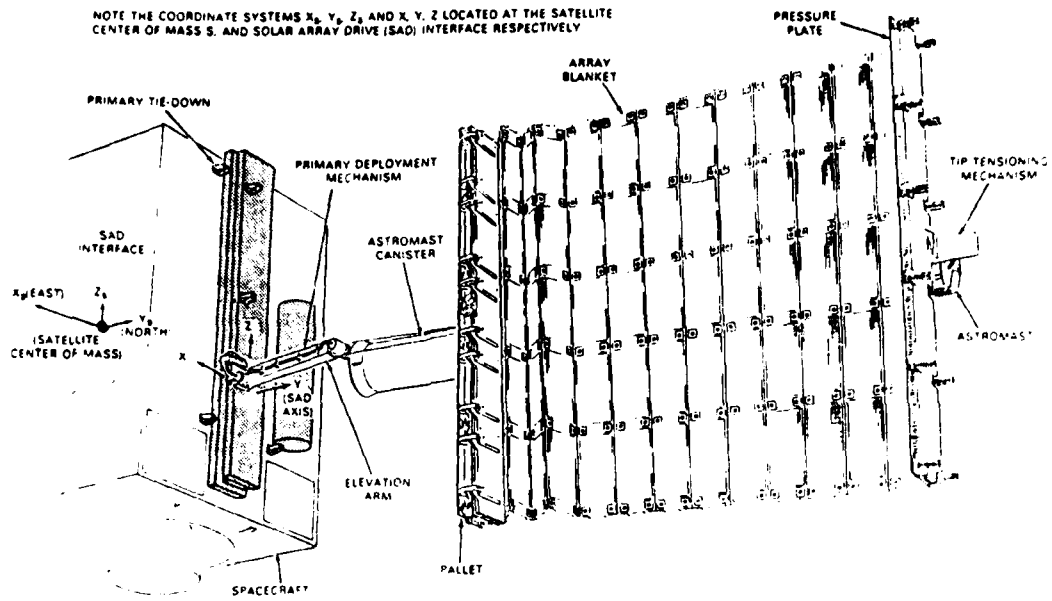
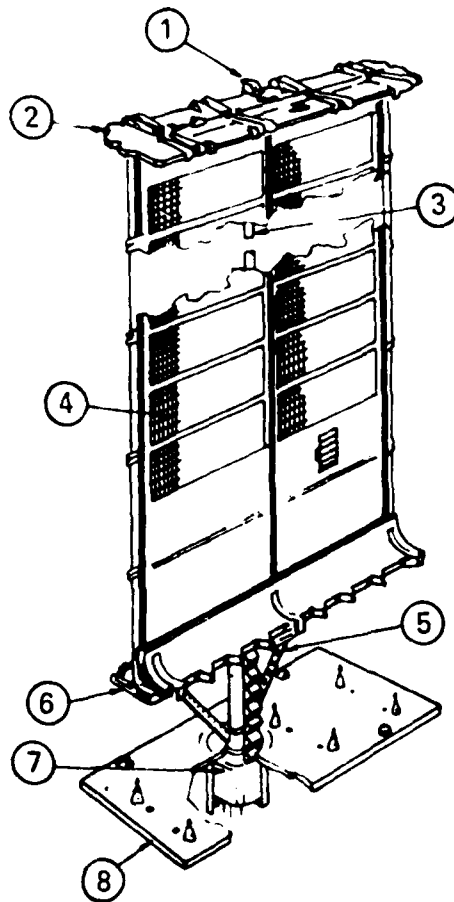


FIGURE 2 L-SAT SOLAR ARRAY DEPLOYED CONFIGURATION



LEGEND

- 1 TIP TENSION DEVICE
- 2 PRESSURE PANEL
- 3 BISTEM BOOM
- 4 BLANKET (NOMINAL SIZE 257" x 51 1/2")
- 5 ELEVATION ARMS
- 6 PALLET
- 7 DEPLOYMENT ACTUATOR
- 8 SPACECRAFT (NORTH OR SOUTH PANEL)

FIGURE 3 TECHNOLOGY SATELLITE (HERMES) SOLAR ARRAY

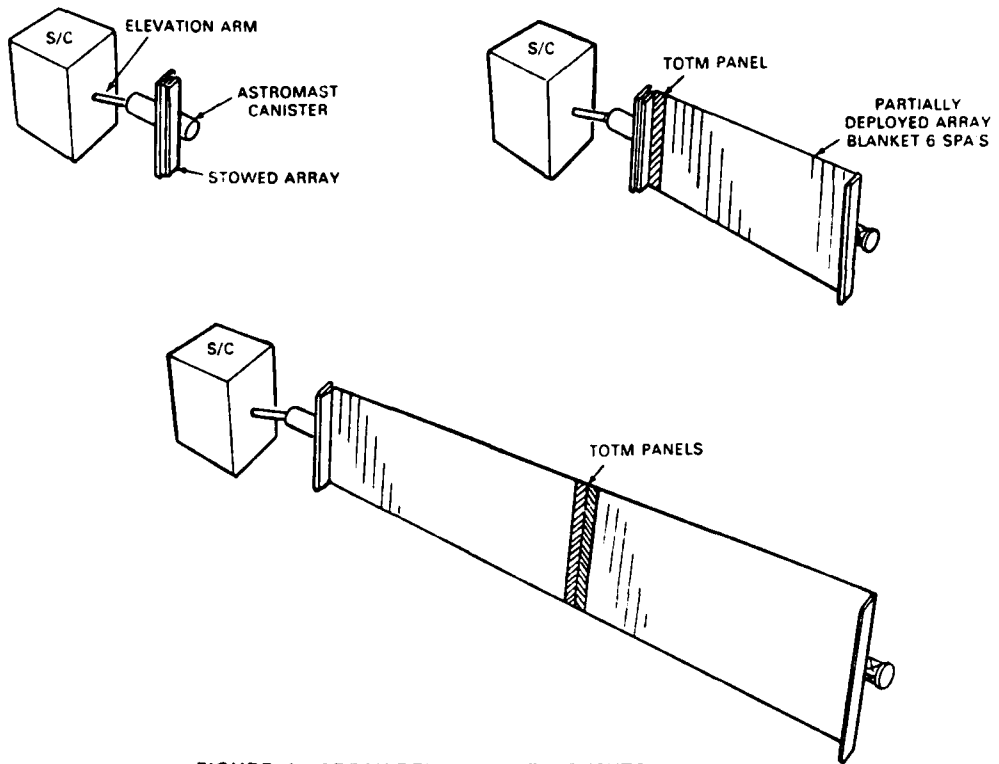


FIGURE 4 ARRAY DEPLOYMENT: EVENTS

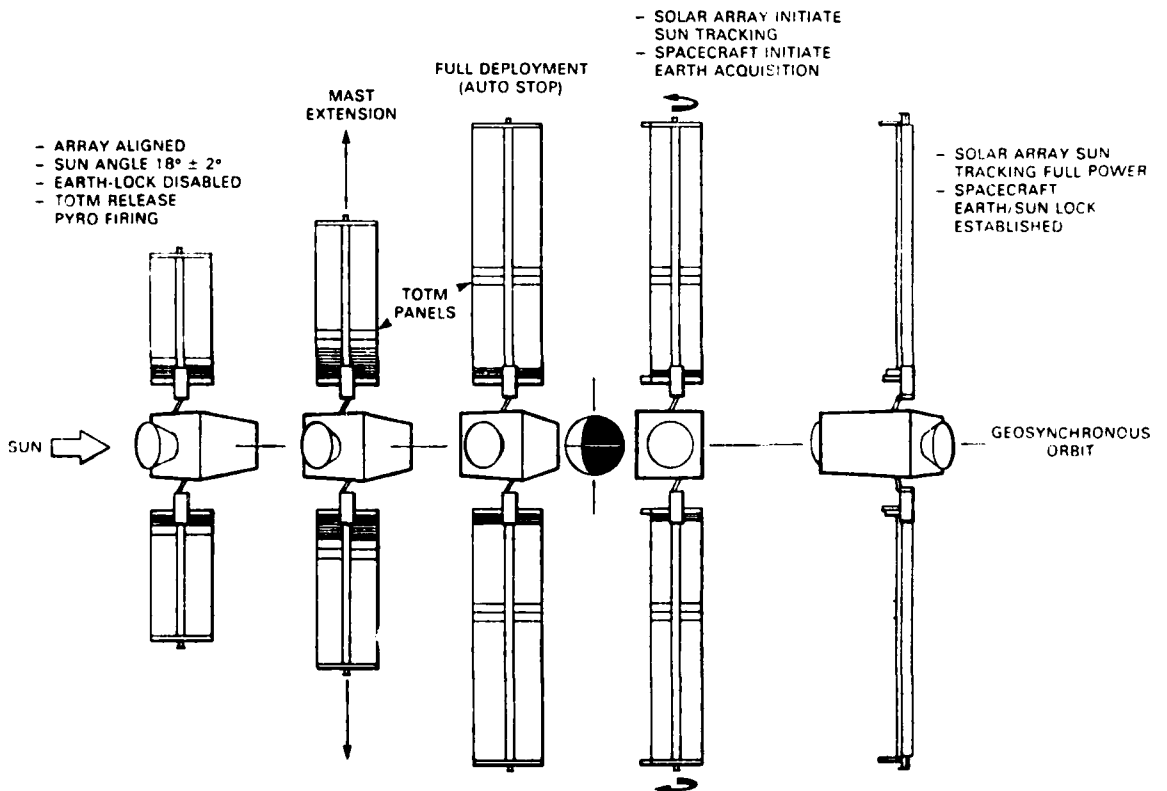


FIGURE 5 ON-ORBIT EVENTS

The array itself is modular in design and capable of providing power from 3.2 Kw Beginning of Life to 7.8 kW End of Life with minimum change. Details of the overall performance capability are given in Table 1 and the main objective of the test program is to demonstrate via ground testing and supporting analysis that these parameters are met.

TABLE 1 MAJOR CHARACTERISTICS OF L-SAT TYPE ARRAYS

PARAMETER	3KW BOL (T.O. ARRAY)	3.2KW EOL DESIGN L-SAT 1	6.5KW EOL DESIGN L-SAT MAX.
DIAMETER OF ASTRO-MAST	254 mm (10 IN.)	254 mm (10 IN.)	254 mm (10 IN.)
SOLAR ARRAY BLANKET TENSION	60 N (14 LB.)	60 N (14 LB.)	80 N (14 LB.)
ESTIMATED LOWEST NATURAL FREQUENCY	0.21 Hz	.177 Hz	.05 Hz
TOTAL MASS PER SPACECRAFT (2 WINGS)	123 Kg (271 LB.)	84 Kg (185 LB.)	123 Kg (271 LB.)
PEAK TRANSFER ORBIT POWER	3 KW	4.2KW	3 KW
BOL SOLSTICE POWER - 2 WINGS	3 KW	4.1KW	8.3KW
EOL SOLSTICE POWER - 2 WINGS	N/A	3.2 KW	6.5 KW
BOL POWER/MASS	N/A	48.8W/Kg	67W/Kg
DIMENSIONS			
BLANKET WIDTH	2852 mm	2852 mm	2852 mm
BLANKET LENGTH	7852 mm	9664 mm	19,952 mm
OVERALL LENGTH	9800 mm	11,664 mm	21,952 mm

Test Philosophy and Test Plan

The L-SAT solar array subsystem is divided into three areas:

- : Flexible Solar Array Blanket (AEG-Telefunken)
- : Solar Array mechanical Assy. including primary and secondary deployment (Fokker)
- : Integrated Solar Array System (Spar Aerospace)

Test plans compatible with these major subcontractors responsibilities were developed.

The test philosophy adopted for this program is to test at the lowest possible level starting with components such as motors and solar cells then stepping up to major components, such as solar panel assemblies (SPA's) and astromast deployer. Testing of major subassemblies such as the primary/secondary deployment and mechanical assemblies follow, and finally testing of the full integrated system takes place.

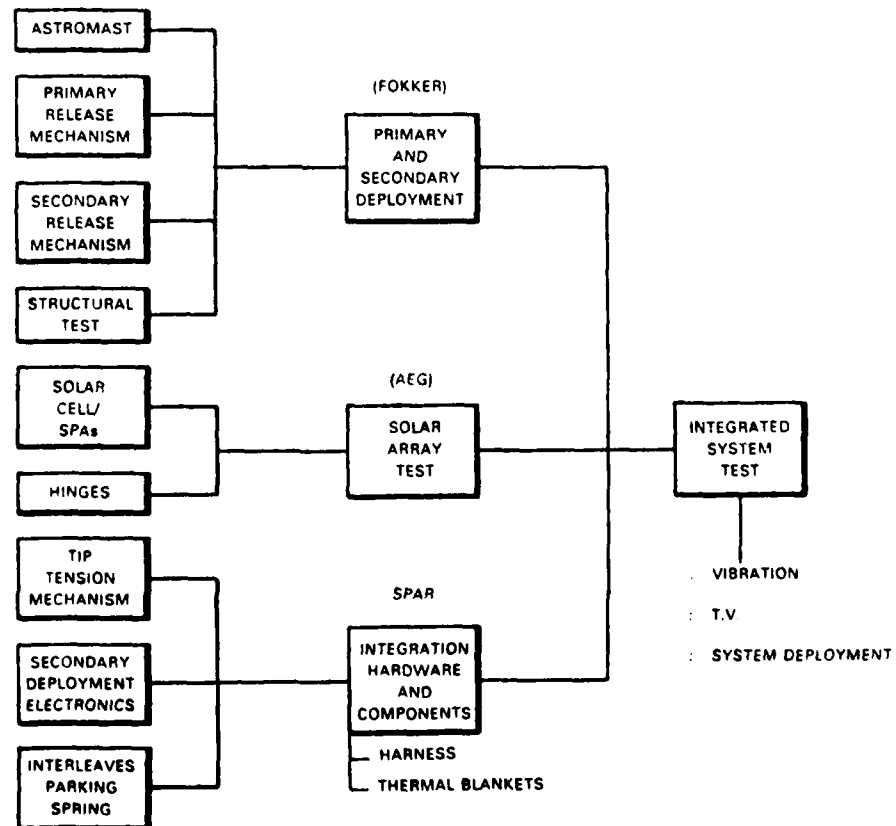


FIGURE 6 INTEGRATED SYSTEM TEST FLOW DIAGRAM

All the above testing will be taken to the qualification level covering EMC, Vibration and Thermal Vacuum environments. In many cases, confidence in new design features is required early in the program, consequently development tests have been conducted to cover both the above and confirm analysis techniques adopted. The latter applying to:

- (a) Natural frequency analysis.
- (b) Blanket behaviour during Apogee motor firing.

The integrated system flow diagram and assembly sequence for the system, subassemblies and components is shown in Figure 6, these include the Mechanical Assembly and component tests to be conducted by Fokker and Solar Array Blanket tests by AEG Telefunken.

In summary, the tests planned for the L-SAT Array are:

- : Development tests to verify critical areas early in the program.
- : Critical components requiring life testing to demonstrate ability to meet mission objectives (10 year) life.
- : Component and subassembly qualification testing.
- : Integrated system Qualification Tests.

These are discussed in detail in the next section.

Development Tests

Development Tests on several hardware items have been carried out to verify their basic design functions and to establish baseline performance and characteristics. The following list identifies development tests completed:

- : Parking spring effectiveness test
- : Foam jump test
- : Behaviour of pressurized foam under vibration
- : Foam material properties test
- : Cable harness stiffness test
- : Stowed solar blanket retention test
- : Array blanket edge crippling test
- : Eddy current damper tests

(a) Parking Spring Effectiveness Tests

A full size representation of the L-SAT solar array was fabricated, and a number of vertical deployment tests were performed to develop the parking spring configuration. This ensured that the blanket deployed correctly and that the interleaves were retained neatly. The test runs were observed and recorded on video tape, and results verified that the parking spring design operates without any hang ups.

(b) Foam Jump Tests

One of the anticipated problems on L-SAT was concerned with the kinetic energy of blanket stowage release. Consequently, tests were performed on pressurized foam stacks in air and vacuum to determine kick-off velocities and kinetic energy levels.

The results were obtained by use of a high speed video camera and recorder. For a representatively pressurized stack, velocities measured were 1 metre/second. The Kinetic energy was then derived for the complete array and used in the design of the Tip Tension Mechanism.

(c) Interleaf Foam Vibration Tests

Tests were performed to determine:

- i) The dynamic stiffness of the foam interleaf material.
- ii) The foam compression required to give adequate stiffness for supporting the solar array blanket when stowed.

A representative sample stack of the stowed solar array blanket, consisting of alternate layers of foam and aluminum plates was used for the tests. The tests were performed using stack configurations representing the L1 and L-MAX array blankets at various values of foam compression.

Principal results were:

- i) The resonant frequency increases with increased foam compression.
- ii) The resonant frequency decreases with increasing input vibration level.
- iii) The "damping" increases with increasing input vibration level.
- iv) Resonant frequencies were higher for the L1 stack than for L-MAX.

A mathematical model for the stiffness of a foam layer was derived from the experimental data and was used to determine the foam compression required for supporting the array blanket.

The required foam compression was determined to be 74% of the free height of the foam, and the tests provided added confidence that the arrangement selected will perform satisfactorily during launch.

(d) Foam Compression and Creep Tests

The interleaf material selected was tested for flammability, vacuum outgassing, compression modulus and long term creep properties. Apart from flammability properties which are under review, acceptable results were achieved.

The compressive modulus is quite non linear on this material, which is commonly observed on foamed materials.

(e) Harness Stiffness

The main cable harness on the L-SAT array wing has to flex during the primary deployment phase, consequently the stiffness of the harness had to be measured in order to provide design information to the designers of the primary deployment system. Restraining torques and bending moments of up to 3 Nm were measured.

Tests were also performed in a thermal chamber at elevated and lowered temperatures to check the variation of cable stiffness over the operational temperature range, and to check whether the cables could provide adequate damping during primary deployment. An "Eddy" current damper is incorporated in the primary deployment system to provide controlled deployment.

(f) Blanket Retention Tests

A feature of the array blanket construction is the use of interlocking rings that mesh together when stowed so as to restrain blanket motions.

The effectiveness of this arrangement will be tested by vibration tests on the engineering/qualification model array. Preliminary testing has indicated that the scheme will work and the array blanket interleaf combination can be stowed and held in position during launch.

(g) Array Blanket Edge Crippling Test

An additional test that was performed was an experiment to study the effects of in-plane loading on a tensioned membrane. (Array Blanket).

The test article was a sample Hermes (CTS) solar array blanket that was covered with dummy solar cells. The blanket was floated on an air bearing table and then "pulled" sideways by inclining the table transversely.

The results obtained indicated that no array edge-on buckling would occur for the anticipated loads, and that a membrane of this type will survive Apogee Engine firing accelerations (low g's).

.022 g is the start up acceleration for L1, and,
.026 g is that specified for other array variations.

(h) Eddy current damper tests have been conducted to establish damper size and characteristics.

Life Testing/Performance

To ensure system reliability and missions life, components which are required to operate over the spacecraft 10 year mission life will be life tested. Items in this category are:

- : The Astromast deployer (electric brush motor) produced by Sperry and the Astromast by Astro.
- : The Tip Tensioning Mechanism (TTM) produced by Spar.

Solar Array blanket performance and cell degradation will be established through type approval testing.

To date Sperry have satisfactorily completed the life testing of the Astromast brush motor; and the Astromast will be life tested during 1983 with a plan to perform 200 partial deployments. A similar test will be conducted on the TTM where 5000 cycles will be performed.

Array Characteristics and Alignment

To ensure correct dynamic characteristics of the array backlash, array alignment and overall system natural frequencies are critical.

With the L-SAT array backlash is non existent since the deployed array is always tensioned, also the primary deployment mechanism backlash is removed during assembly via adjustments and preloaded mechanism design.

Similarly alignment and other mass property requirements will be adjusted during assembly to meet system requirements. The astromast is a major contributor to the in-flight motion of the centre of mass, so special alignment set-up procedures will be prepared to ensure the system meets necessary alignment criteria.

Array natural frequency, modal integrals and modal damping are areas of concern to the spacecraft ACS. The size of the array precludes the ability to conduct deployed frequency tests similar to those conducted in TV Chamber on the Hermes (CTS) array. Instead array frequencies will be confirmed using modal analysis techniques.

Modal Analysis Testing

The L-SAT Flexible Solar Array can be considered to be in the category of low frequency structures whose natural frequency is predicted to be below 0.2 Hz, in fact for L-SAT max. the prediction is .05 Hz (see Figure 7). To demonstrate and confirm damping and frequency characteristics the standard structural test methods conducted on CTS can no longer be applied and Modal Analysis testing techniques must be used.

The objective of modal testing is to obtain and confirm structural natural frequency, mode shapes, damping characteristics, and analysis predictions.

In order to develop test methodology and procedures for the modal test of the L-SAT array a development program study is under way to test a scale model of a flexible Solar Array. A 9" astromast will be used, and membrane tension will be adjusted to represent a low frequency structure. This membrane will be fully represented with mass simulation and tensioned using a CTS tip tension mechanism. Predictions will be made and modal analysis testing will be conducted at the Department of Communications facility at Shirley's Bay, Ottawa.

After testing, predictions versus results will be examined and anomalies noted. Also during testing the effects of air damping and testing in earth's gravitational field will be examined. For example, torsion modes should be less sensitive to gravity than out of plane modes; and in-plane modes should be less sensitive to aerodynamic effects than out of plane modes.

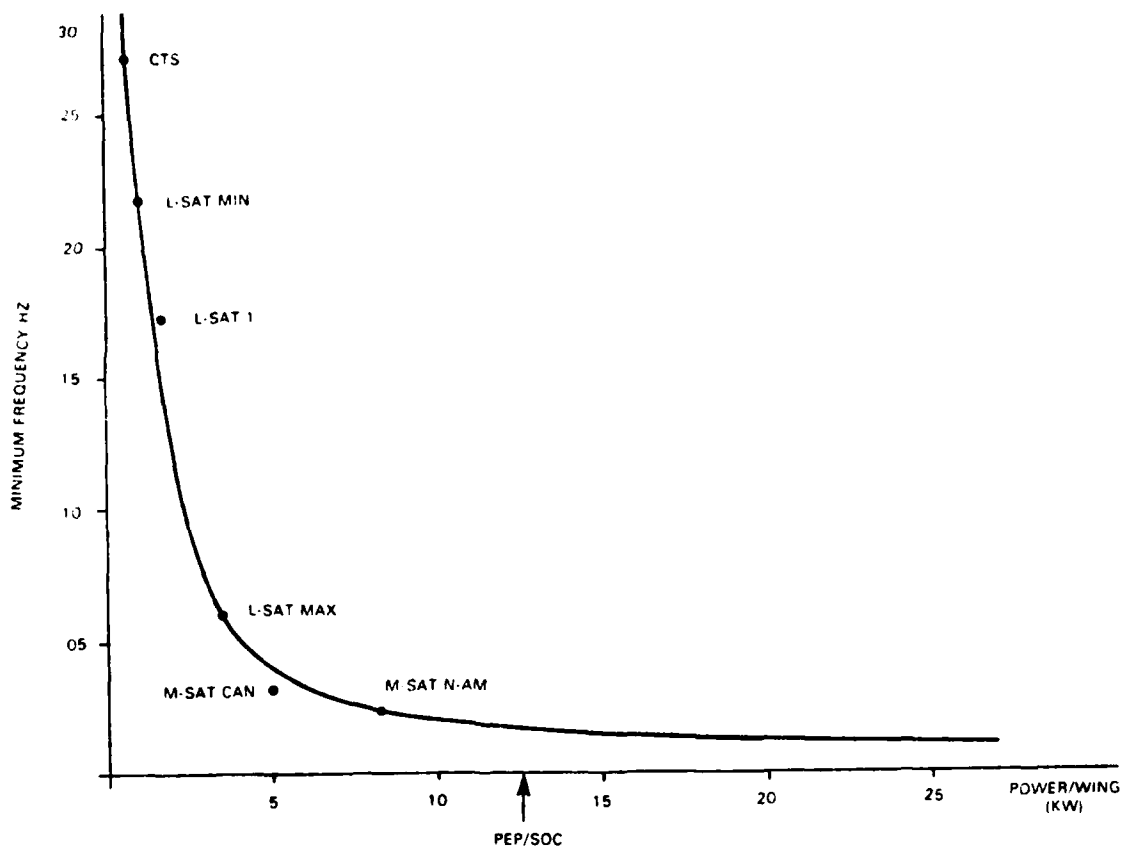


FIGURE 7 TREND OF MINIMUM FREQUENCY VS. ARRAY POWER/WING

To examine the low frequency characteristics of a large flexible array requires special low frequency sensors and the test interval needs to be fairly long, ie. 1/2 hour of continuous test for 0.2 Hz systems. These sensors have been selected from previous development tests used to characterize the astromast.

An advantage to modal analysis testing is that it provides vibration test results in the same format as the solar array analysis. The vibration testing done is to verify the mathematical model and to check for any manufacturing flaws. Manufacturing flaws can be isolated with modal analysis testing since they show up as unexpected large deflections in mode shapes.

If, during test, it becomes apparent that more damping must be incorporated, the modal shapes help to determine where and what kinds of damping will be most effective. Before the hardware is actually implemented, its effects can be modelled in the software and evaluated.

Component/Subassembly Testing

Components or subassemblies of the L-SAT array that fit into this category are the Astromast, TTM, flexible solar array blanket, and Secondary deployment electronics. This will all be qualified to demonstrate that they can survive launch and operate in Transfer and Synchronous orbits.

(a) Astromast

Fully flight representative hardware will be used and tests to be performed include:

- o Vibration Test (Stowed Assy.) to qualification levels.
- o Partial deployment in Thermal vacuum to qualification levels.
- o Deployment Power and stall characteristics of the motor.
- o Deployed stiffness.
- o Extension rate while correctly loaded.
- o Straightness and alignment.
- o Backlash in the system.

(b) Secondary Deployment Electronics (SDE)

The block diagram for this unit showing its functions is given in Figure 8 and testing to be conducted on this unit include:

- : Continuity and performance checks.
- : Vibration, (Sine and Random).
- : Thermal Vacuum.

(c) Tip Tension Mechanism

Will be subjected to normal operating performance tests, (life testing is conducted separately) followed by a sine and random vibration and T.V. testing.

The vibration spectrum for TTM component is shown in Table 2 and these are typical for the SDE and Astromast and represent results from overall system analysis using Ariane and STS launch inputs.

Similarly the Thermal Vacuum duty cycle to which components will be subjected is given in Figure 9.

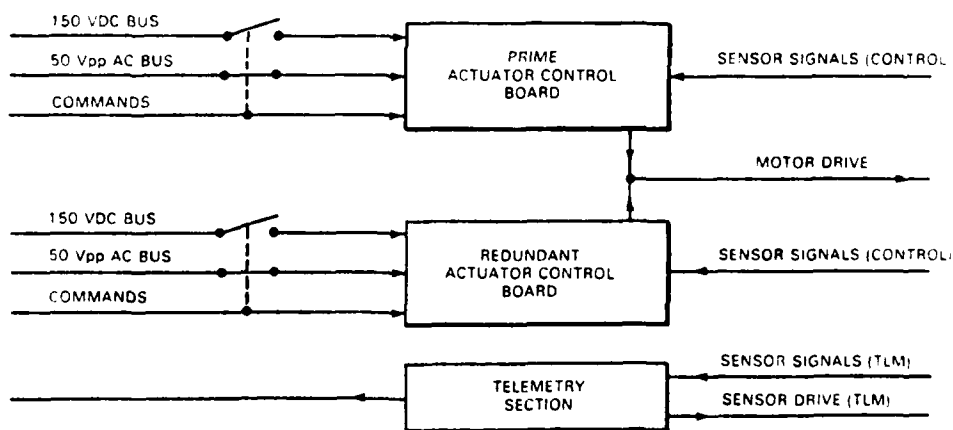


FIGURE 8 SDE GENERAL BLOCK DIAGRAM

RANDOM			
AXIS	FREQUENCY (Hz)	PSD (G ² /Hz)	G RMS
Z	20 - 50	+6 dB/OCT.	14.7
	50 - 1000	0.13	
	1000 - 2000	-3 dB/OCT.	
X,Y	20 - 50	+6 dB/OCT.	19.1
	50 - 90	0.65	
	90 - 120	-12 dB/OCT.	
	120 - 1000	0.20	
	1000 - 2000	-3 dB/OCT.	

TEST DURATION: 2 MINUTES

SINE		
AXIS	FREQUENCY (Hz)	G s (O-PEAK)
Z	5 - 21.3	11 mm (O-PEAK)
	21.3 - 70	20
	70 - 100	10
X	5 - 19.6	11 mm (O-PEAK)
	19.6 - 80	17
	80 - 100	10
Y	5 - 19.6	11 mm (O-PEAK)
	19.6 - 80	17
	80 - 100	8

SWEEP RATE: 2 OCTAVES/MINUTE

TABLE 2 QUALIFICATION VIBRATION LEVELS FOR TTM

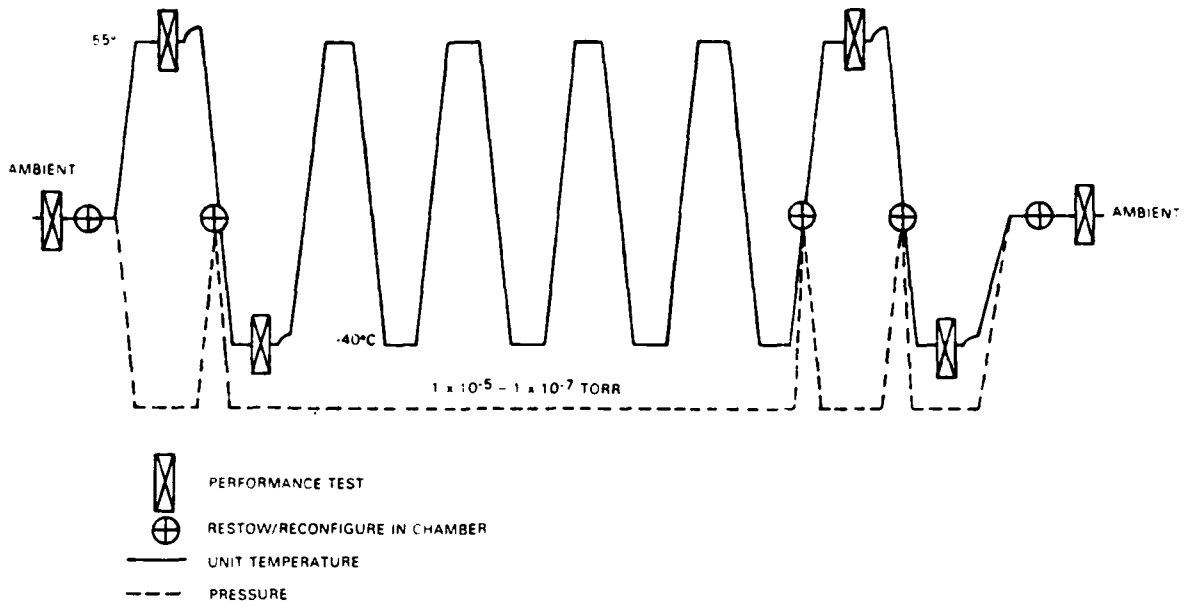


FIGURE 9 QUALIFICATION TTM THERMAL VACUUM SEQUENCE

Flexible Blanket Solar Array

Qualification testing of the Flexible Solar Array (FSA) blanket will be performed by AEG Telefunken up to the Solar Panel Assembly (SPA) level. This does not include vibration and Thermal vacuum of the completed FSA since it is recognized that a meaningful test can only be achieved with the FSA stowed and deployed with the remainder of the system in a representative environment.

The various arrangements of L-SAT FSA are given in Figure 10 and for the qualification program the L-SAT-1 configuration will be tested. The test objectives and performance plan is given below:

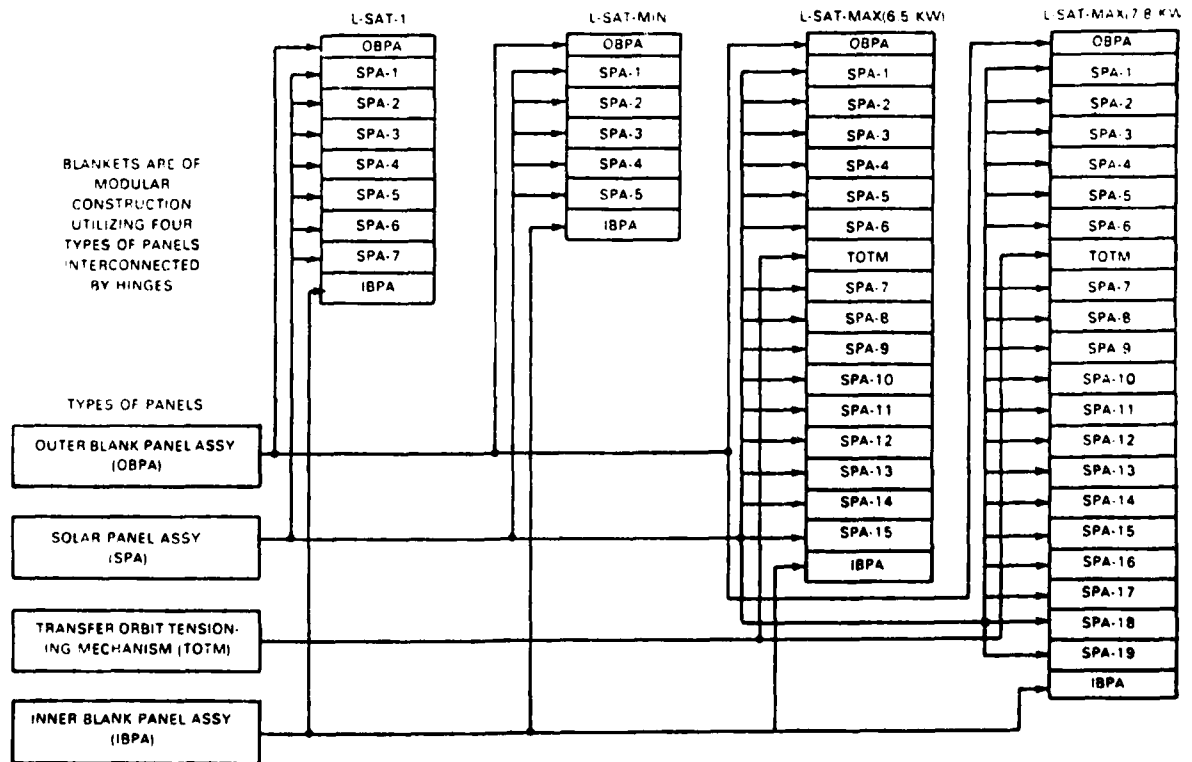


FIGURE 10 L-SAT FLEXIBLE SOLAR ARRAY BLANKET ARRANGEMENTS

Test Purpose : To confirm design suitability for Mission of the following:

- Solar Cell Layout
- Fold Line
- Hinge Line
- Wiring
- Cups
- Anti-charging

Test Hardware : Qual. - Life Samples (Representative blanket areas)
 : Size: 160mm x 280mm
 : Quantity: 5

Test Performance : - Visual Inspection
 - Insulation Check
 - Continuity Check
 - Electrical Performance
 - Folding Test
 - Thermal Vacuum Cycling
 1100 Cycles
 +65/-160°C
 Pressure: Approx. 10^{-6} Torr.
 - Flexing Test Include
 measuring of short circuit

Mechanical Sub-Assemblies

Testing of the mechanical elements at Unit level will be performed by Fokker and includes predevelopment of:

- Primary release and tie-down system
- Primary deployment system
- Secondary release and tie-down system
- Transfer orbit tension mechanism (TOTM)
- Pallet and pressure plate structural/stiffness testing

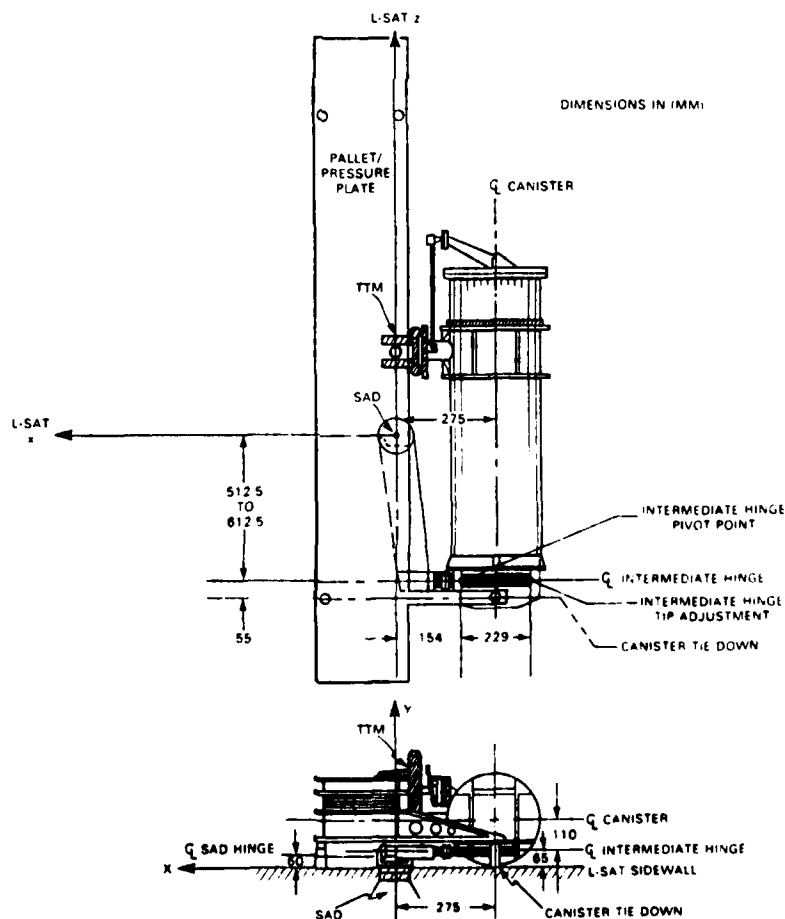


FIGURE 11 STOWED L-SAT ARRAY

Testing at subassembly level will include testing of Primary deployment system; TOTM and solar array stowage system. These tests will verify the following basic requirements:

- : Ability of the release and tie-down system to survive and retain the system during launch, and then actuate, release and deploy the primary system in T.O.
- : Ability of the secondary system to initiate release of the stowed array pack.

The mechanical assembly will be vibration and T.V. tested with the complete system along with the solar array as an integrated system. Figure 11 identifies the mechanical elements mentioned in the stowed configuration.

Integrated System Test Program

In addition to verifying the system parameters mentioned, the test program will also verify:

- : The ability of the stowage system to protect the solar array blanket (solar cells) during launch.
- : The ability of the system to deploy and elevate the primary system, then release and deploy and tension the array in Transfer and Synchronous orbit, and maintain this tension on the array.
- : Ability to meet alignment requirements.
- : Ability of the system thermal design to maintain component within required temperature levels during all mission phases.

To verify the above, an Integrated System Test will be conducted taking the assembly to qualification level tests for both Vibration and T.V. test. For these tests an Engineering/Qualification model FSA comprising a complete system with TOTM and small percentage of live cells will be constructed. To simulate the correct mass for L-SAT-1 weight representative glass chips will be installed. This unit will be subjected to primary release and deployment, followed by secondary release, deployment and tensioning. Repeated deployments will be conducted prior to, and after vibration and TV testing.

Details on the planned Qualification Vibration and T.V. tests follow.

Qualification Vibration Test

Test Objective

The objective of this test is to verify the ability of the qualification model L-SAT Array subsystem to survive qualification level vibration.

Test Configuration

The test article consists of the qualification model mechanical system integrated with the prototype FSA. Testing will be conducted at the CRC David Florida test facility using a vibration fixture designed to represent the spacecraft mechanical interface. The subsystem will be integrated on a simulated spacecraft sidewall. The simulated spacecraft sidewall is attached to the vibration fixture.

Baseline Performance Tests

In order to obtain subsystem performance comparison before and after vibration testing, the following functional tests will be conducted:

- (a) Deployment of primary and secondary systems at ambient room conditions on a specially designed horizontal deployment fixture - see Figure 12.
- (b) Electrical continuity test of the subsystem before and after deployment.
- (c) "Thermovision" testing of the deployed solar array. Forward current is passed through the solar cells so that heat is dissipated in the cells. This is sensed and mapped using an infrared imaging system. Such a test has proven very useful in determining the presence of open circuit or short circuit cells.
- (d) Visual examination, including 100% inspection of cover glass, solar cells and interconnects for evidence of damage.

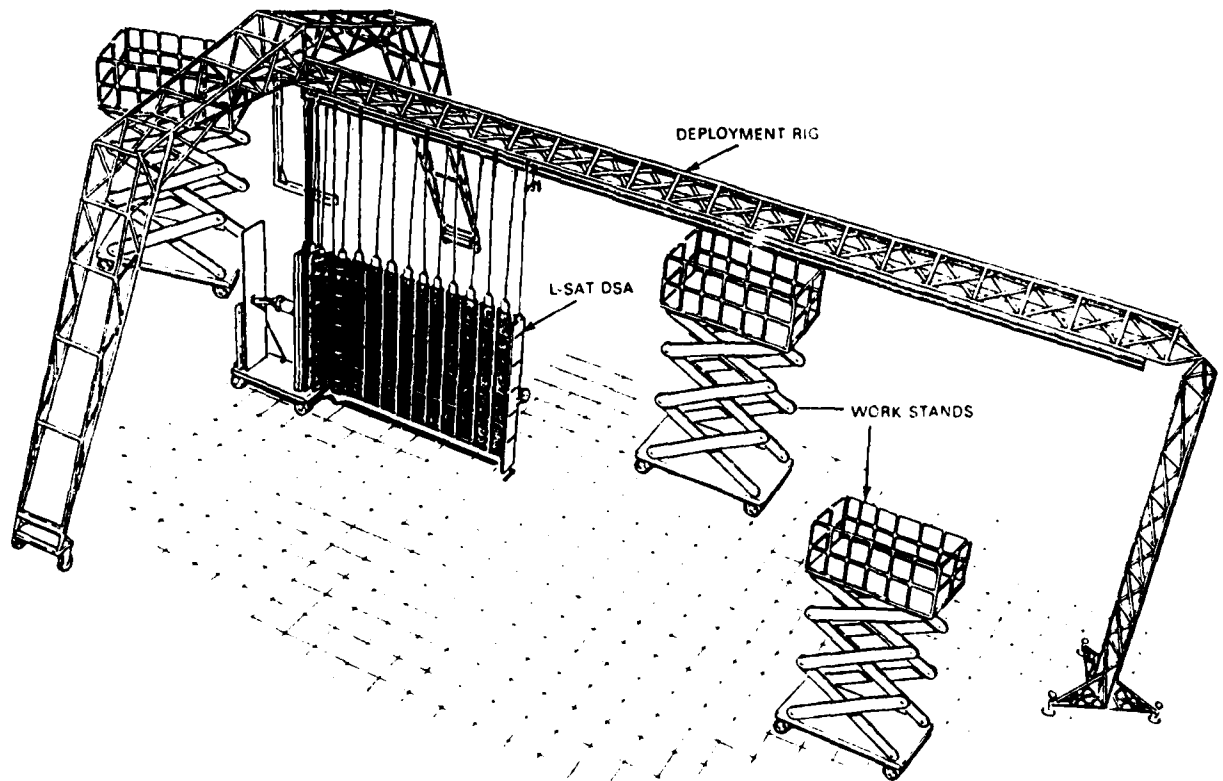


FIGURE 12 DEPLOYMENT TRACK CONCEPT

Test Levels

The vibration control philosophy and the levels to which the subsystem will be subjected are as specified in the subsystem specification. Input to the subsystem will be controlled by a set of three control accelerometers mounted on the test panel for Z axis and on the fixture for X and Y axes at strategic locations. Cross-axis responses will be monitored and limited to be less than input levels by a further set of three accelerometers mounted on the fixture. A total of 30 positions on the specimen and fixture will be instrumented for acceleration data and will be recorded on magnetic tape.

Tables 3 gives the sinusoidal and random vibration levels used for the test. Also identified are the predicted notching responses for the L-SAT Solar Array during vibration testing.

TABLE 3 RANDOM AND SINE QUALIFICATION RESPONSE LEVEL FOR ARRAY SUBSYSTEM

RANDOM			
AXIS	FREQUENCY (Hz)	PSD (G ² /Hz)	G RMS
ALL AXES	20 - 150	+6 dB/OCT.	14.1
	150 - 750	0.13	
	750 - 2000	-3 dB/OCT.	
TEST DURATION:	2 MINUTES		
SINE			
AXIS	FREQUENCY (Hz)	G's (O PEAK)	
Z (ALONG THE APOGEE ENGINE THRUST AXIS)	5 - 15	11 mm (O-PEAK)	
	15 - 30	10	
	30 - 50	15	
	50 - 100	7	
SWEEP RATE: 2 OCTAVES/MINUTE			

PREDICTED NOTCHING RESPONSES FOR THE SOLAR ARRAY SUBSYSTEM

SINUSOIDAL VIBRATION TESTS

AXIS	X AND Y RESPONSES		Z RESPONSES		
	LOCATION	QUALIFICATION LEVEL	ACCEPTANCE LEVEL	QUALIFICATION LEVEL	ACCEPTANCE LEVEL
PRESSURE PLATE		14.7g	10.8g	17.6g	12.9g
PALLET		14.7g	10.8g	17.0g	12.4g
ASTROMAST CANISTER		10.0g	7.4g	16.0g	11.8g

Thermal Vacuum Deployment/Qualification TestObjective

The objective of this test is to demonstrate the ability of the Solar Array subsystem to operate in simulated orbital thermal vacuum conditions by:

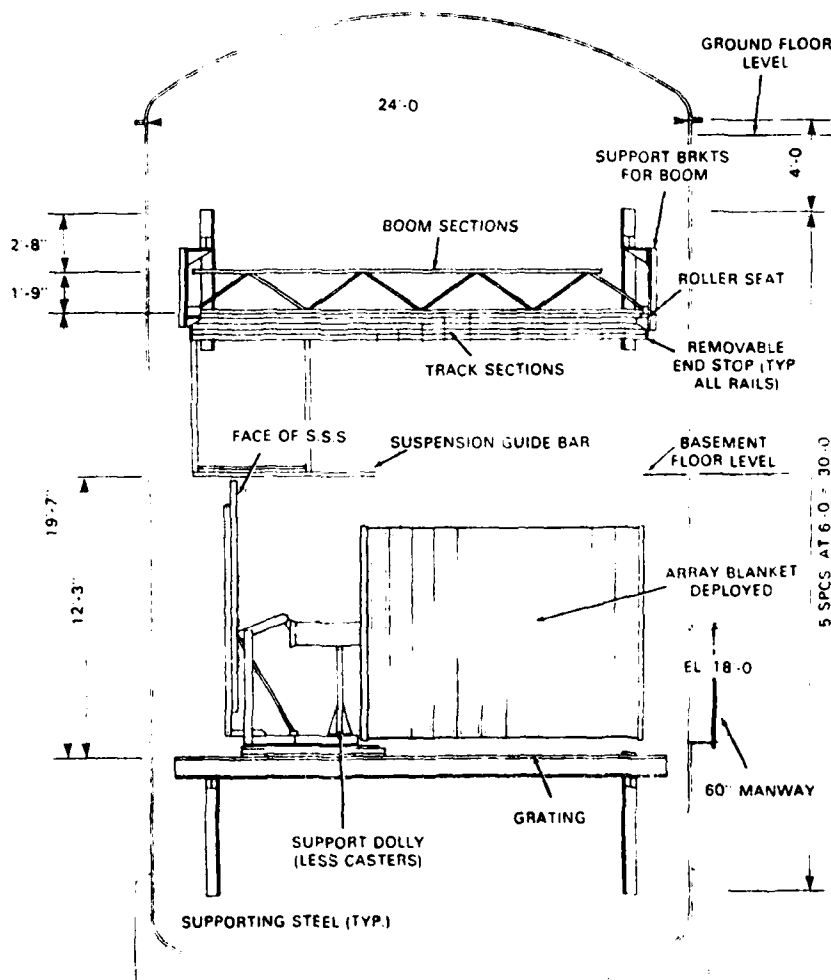


FIGURE 13 THERMAL VACUUM CHAMBER/SOLAR ARRAY DEPLOY TEST

- (a) Imposing thermal vacuum conditions on the stowed Solar Array that would subject the subsystem to the extremes of predicted, thermally induced mechanical strain prior to deployment.
- (b) Performing the complete solar array deployment sequence under simulated orbital conditions commencing with primary deployment and concluding with automatic deployment cut-off after secondary deployment.

(c) Monitoring and recording during deployment:

- i) Pyrotechnic firing current (Primary release)
- ii) Deployment actuator motor current
- iii) Primary deployment and time to deploy
- iv) Secondary system release (pyro firing current)
- v) Astromast length potentiometer
- vi) Primary Deployment Lock Microswitch operation
- vii) TOTM release pyro power operation
- viii) Astromast retract/retract stop

The tests will be conducted at the David Florida Laboratory T.V. Chamber at Shirley's Bay, Ottawa (DOC/CKC facility). Due to facility limits and solar array length for the L-SAT-1 arrangement, partial deployment of the secondary deployment will take place.

The facility and test arrangement is given in Figure 13 and the planned integrated subsystem thermal vacuum duty cycle/sequence is given in Figure 14.

(d) Monitoring and recording during deployment:

- i) Pyrotechnic firing current (Primary release)
- ii) Deployment actuator motor current
- iii) Primary deployment and time to deploy
- iv) Secondary system release
- v) Astromast length potentiometer
- vi) Lock microswitch operation
- vii) Tensioning mechanism potentiometer output
- viii) Deployment stop microswitch operation

Following completion of the thermal vacuum qualification tests and the series of component testing mentioned the L-SAT array will have demonstrated its capability to meet specification and survive mission loads and life time requirements.

Flight systems will be exposed to similar environmental testing at reduced levels both during vibration and Thermal Vacuum testing.

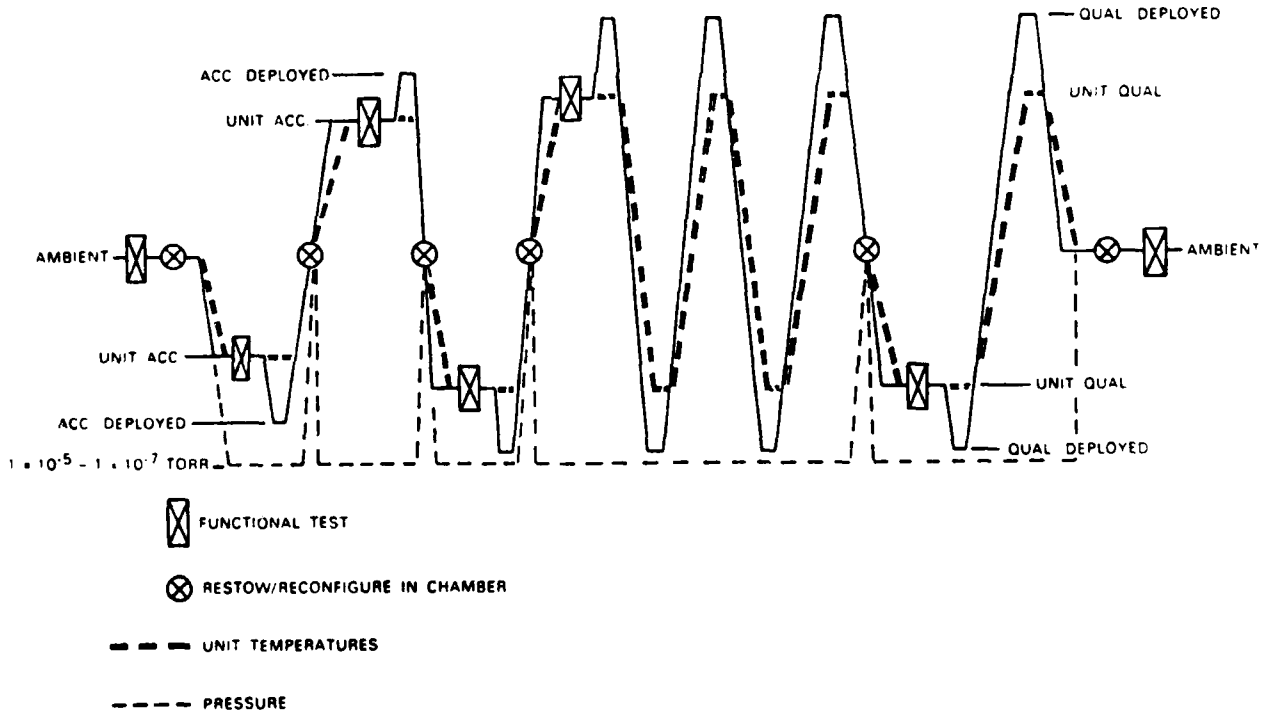


FIGURE 14 DEVELOPMENT QUALIFICATION MODEL SUBSYSTEM THERMAL VACUUM SEQUENCE

Concluding Remarks

This paper has identified the complications of testing large solar arrays of the size to be flown on L-SAT. To prove that the specification requirements have been met, and that all subsystems and components achieve mission goals, there are many stages of testing that must be accomplished. Above all there are limits to the amount of testing one can achieve due to facility and environmental test chambers size. Consequently, for future large flexible solar arrays/structures such as M-SAT solar array (8 Kw/wing) shown in Figure 15 one will have to rely on analysis methods, such as modal analysis, for predicting natural frequencies, and in addition may have to conduct in-flight tests (low orbit using STS). This will be relatively expensive for commercial spacecraft, nevertheless it may be the only way to prove and test out future large systems.

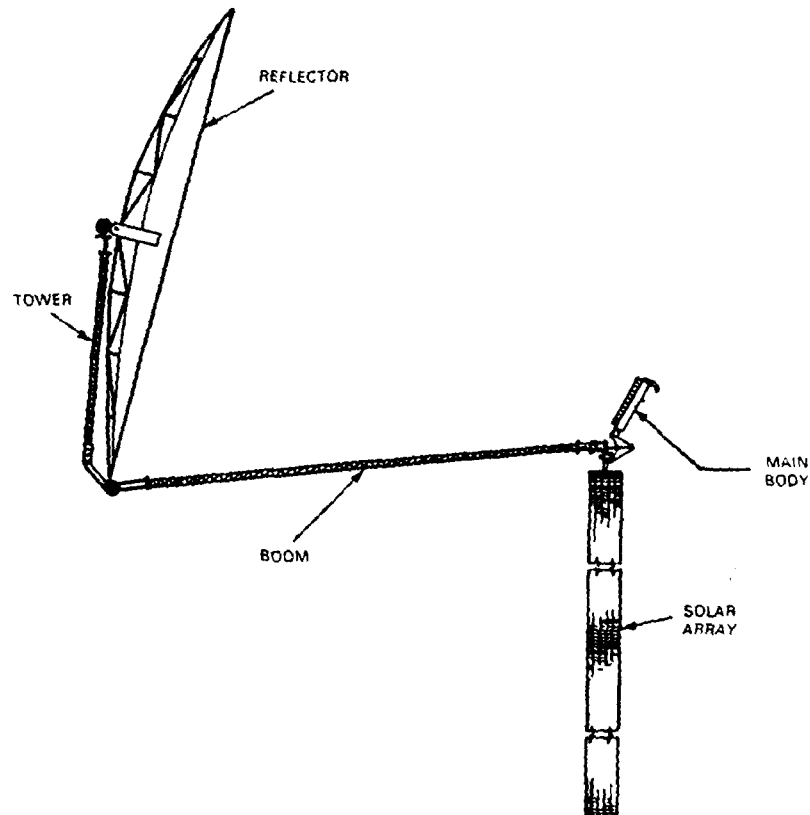


FIGURE 15 M-SAT CONFIGURATION BREAKDOWN

Acknowledgements

The authors would like to thank the many people from the organizations listed below who contributed and provided data to this paper. Also to thank the Department of Communications, Canada, ESA, and B.Ae, Stevenage for permission to publish the paper.

- AEG, Telefunken
- Fokker
- Spar Aerospace

References

1. The design of the L-SAT Array
 Authors: L. Gerlach, AEG Telefunken, wedell
 G. Marks, Spar Aerospace, Toronto
 E. Quittner, Spar Aerospace, Toronto
 J. Renshall, Spar Aerospace, Toronto
 R. Zwanenburg, Fokker BV, Amsterdam
2. Testing of the CTS Deployable Solar Array Subsystem
 Authors: J.S. Smith, Spar Aerospace, Toronto
 S.S. Sachdev, Spar Aerospace, Toronto
 Dr. J.A. Hunter, Department of Communications (CRC), Ottawa

THE MBB COMBINED EFFECTS CHAMBER FOR REAL TIME AND ACCELERATED
TESTS UNDER SIMULATED SPACE ENVIRONMENT

by

Atto F. Husmann
MESSERSCHMITT-BÖLEW-BLOHM MBH
Postfach 80 11 69
8000 München 80, Germany

SUMMARY

The MBB Space Division operates its solar radiation simulation test facility since 1977. This test equipment is fully automated and runs without interruption 24 hours a day, as long as specified, with its radiation sources operating simultaneously or alone. The test chamber provides clean vacuum. The sample temperatures are adjustable between -50°C and $+100^{\circ}\text{C}$. UV - radiation exposure may be accelerated up to 2 solar constants. The electron and the proton current densities can be selected from 10^{10} up to 10^{16} cm^{-2}/s . Their energies may range from a KeV to 20 KeV. Light samples (size 11×11 mm) are exposed simultaneously, on four samples 20×20 mm. The amount of damage inflicted a spectrometer is mated to the vacuum chamber for in situ measurement of sample spectral reflectances from 200 nm to $2,5$ μm . 13.5 μm data in real time are transferred into the sample solar absorption coefficient.

With this test equipment a broad variety of thermo-optical materials has been studied. The test results have been published in technical journals, technical reports, and in conference proceedings (Ref. 1).

1. INTRODUCTION

In space thermal radiation is the only means to dissipative heat, that on the one hand results from solar and planetary radiations, and on the other hand is generated by conversion of electrical power from solar cells. With this technique it is possible to maintain the satellite and satellite component temperatures within specified ranges.

Reliable and efficient temperature control of long life satellites depend on the know how and the technical lay out of the radiation parameter, and in particular on the time dependent stability of the thermo-optical characteristics of the thermal control surfaces. Space radiation inflicted damages predominantly lead to solar absorption coefficient increases of thermal control surfaces. Their thermal emissivity in general is not affected. - It is well known, that in a geostationary orbit not only thermal control surfaces, but also solar cell cover glasses degrade.

Table 1 provides information on the presently known environmental radiation conditions, specified for various missions.

space environment	inner solar system (1 year)	outer solar system (1,5 - 5 years)	spacecraft orbit (10 years)
solar UV	6000 - 60,000 ESH ^{*)}	2500 - 7000 ESH ^{*)}	1000 - 10,000 ESH ^{*)}
solar wind	$4 \cdot 10^{10}$ - $4 \cdot 10^{16}$ p^+/cm^2 ($E \sim 1,5$ KeV)	$2-9 \cdot 10^{15}$ p^+/cm^2 ($E \sim 1,5$ KeV)	--
protons (Van-Allen-belt)	$1,6 - 5,2 \cdot 10^{11}$ p^+/cm^2 ^{**)}	$10^8 - 10^{10}$ p^+/cm^2 ^{**)}	10^{10} p^+/cm^2 (E < 20 KeV)
electrons (Van-Allen-belt)	$1,5 - 7,4 \cdot 10^{11}$ e^-/cm^2 ^{**)}	$10^8 - 10^{10}$ e^-/cm^2 ^{**)}	10^{12} e^-/cm^2 (E < 20 KeV)

*) equivalent sun hours

**) encountered during crossing of the Van-Allen-belt

TABLE 1: Radiation fluxes encountered by long life satellite systems, according to literature (Ref.2)

Solar UV-radiation combined with vacuum represents the near earth environment. In a geostationary orbit charged particles add to the solar UV radiation and the vacuum. The charged particles predominantly are electrons and protons, trapped by the earth magnetic field. Recently, the SCATHA satellite brought information concerning the presence of oxygen ions during solar substorm occurrences.

Operation of satellites in a geostationary orbit may lead to electrical disturbances, caused by differential surface charging through charged particle impact, mainly during solar substorm activities (Ref. 5).

1. THE MBB SPACE RADIATION SIMULATION TEST FACILITY

To avoid application of thermooptical materials with inferior performance, materials for thermal control are laboratory tested under simulated space environmental conditions, according to mission requirements. Such simulation encompasses handling of these thermal control components, their storage and performance during lift-off, and in particular their thermooptical stability under space conditions. The test results are evaluated under consideration of the required life time.

For laboratory studies of the time dependent stability of thermooptical surfaces as well as the differential charging of satellites, MBB has developed and operates a test facility, which in some detail is described below. Simulated are vacuum, sample temperature, UV-, electron- and proton radiations. The major technical data of this test facility are compiled in Table 2. An extra feature of this facility is its capability, to measure static surface charges on dielectric surfaces.

vacuum	$1 \cdot 10^{-7}$ $1 \cdot 10^{-7} \text{ (UV+)}^+$
on-line μ s calculator evaluation	Yes
solar UV - Intensities (mW/cm ²) - wave length range (nm) - 1 μ m to (nm) - μ s measurement, from 140 nm to 2,5 micron.	0 - 1 170 - 400 10 in-situ
proton generator - flux ($\text{p}^+/\text{cm}^2\text{s}$) - energy range (KeV) - measurement	$10^0 - 10^4$ 5 - 10 Faraday-cup scan
electron gun - flux ($\text{e}^-/\text{cm}^2\text{s}$) - energy range (KeV) - measurement	$10^0 - 10^4$ 1 - 10 Faraday-cup scan
differential electrostatic charging - potentials - sensor	up to 20 kVolts capacitive voltage divider
sample holder - temperature range ($^{\circ}\text{C}$) - sample size - number of samples under exposure - total number of samples mounted	-30 to +100 11 x 11 c. 11 x 15 mm 8 32
hours of operation/day	24

TABLE 2: The MBB space simulation chamber - technical data

Fig. 1 presents an overall view of this facility, including the spectrophotometer for in situ spectral reflectance measurements and also some peripheral equipment.

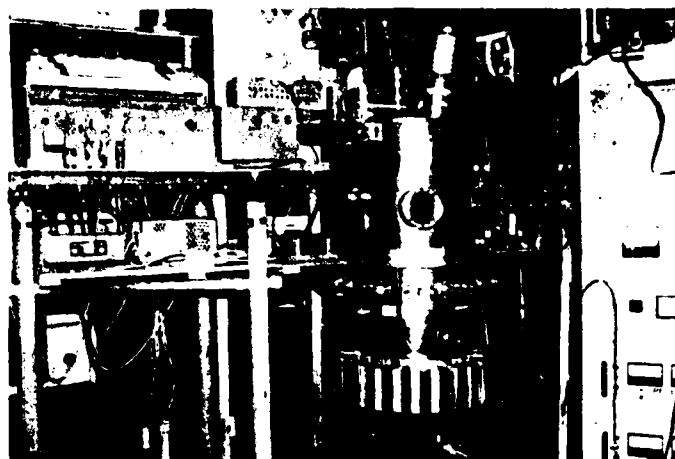


FIG 1: The MBB Combined Effects Chamber

3. THE VACUUM SYSTEM

The central part of the MBB Combined Effects Chamber is a 350 liter cylindrical container with integrated pumping facility. This chamber is divided into an upper and a lower half by a 12" flange. The lower half contains a 350 liter/sec ion pump and a titanium getter pump. The sample holder is supported within this section, extruding somewhat into the upper half. The integration sphere, part of the spectrometer optical system, is mounted above the sample holder. For the experiments, a large number of electrical feed throughs has been provided.

On top of its upper half are installed the UV-lamp, mounted within a heat exchanger, the electron gun, the proton generator, and a residual gas analyser. The three radiation sources as well as the residual gas analyser are focused onto the samples under exposure.

The vacuum chamber is pumped down in four steps: At first, with the help of two sorption pumps, a vacuum of about 30 microns is generated, down from atmospheric pressure. Clean up of the sorption pumps with the help of a mechanical pump is the next step. It is followed by further pump down with the sorption pumps, this time into the 10^{-4} Torr range, where the ion pump takes over. To accelerate this take over, the built in Titanium pump becomes activated. The ion pump suffices in handling the desired pressure, even with the proton generator running. Without operation of the proton generator, the vacuum ranges around 2×10^{-7} Torr, and with the proton generator on it is about 6×10^{-7} Torr. Vacuum in the order of 3×10^{-8} Torr, free of oil vapors and other organic contaminants can be obtained.

The residual gas analyser, a Balzers QMG 101 quadrupole, is mounted between electron gun and proton source. Its ion source faces the area of the samples under radiation exposure. It permits mass scans in the range from 1 to 100 AMU and from 10 to 400 AMU. For high sensitivity this instrument employs a multiplier, whose first dynode is used as a Faraday cup collector, if high sensitivity is not demanded. After sufficient pump down the residual gas atmosphere mainly contains Argon, N_2 , H_2 , and some water vapor. With the proton generator in operation, the H_2 peak dominates.

4. THE UV - LAMP

The electromagnetic radiation of interest is short wave length UV from 170 nm up to 400 nm. OSRAM XBO Xenon high pressure arc discharge lamps with SUPRASIL envelopes permit simulation of this solar spectral range. Here its intensity distribution fairly well corresponds to the solar extraterrestrial intensities according to ASTM E 490 73 a (Ref. 4). SUPRASIL is transparent down to 170 nm. To avoid UV absorption below 186 nm by oxygen and water vapor, the light source is mounted within a heat exchanger, which is filled with dry nitrogen. This technique also eliminates generation of ozone, which would absorb UV radiation between 200 nm and 300 nm. A sapphire window separates the Xenon lamp from the vacuum chamber. This window is transparent for UV down to 150 nm.

AD-A129 847

ENVIRONMENTAL EFFECTS ON MATERIALS FOR SPACE
APPLICATIONS(U) ADVISORY GROUP FOR AEROSPACE RESEARCH
AND DEVELOPMENT NEUILLY-SUR-SEINE (FRANCE) MAR 83

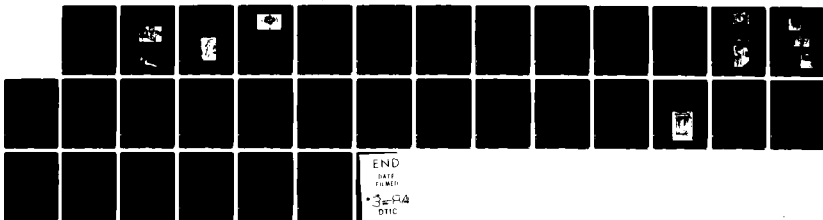
3/3

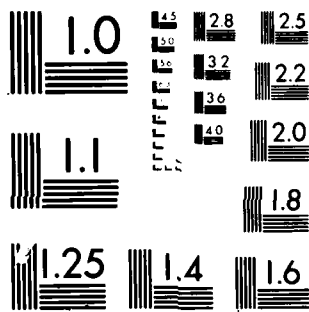
UNCLASSIFIED

AGARD-CP-327

F/G 22/2

NL





MICROCOPY RESOLUTION TEST CHART
NATIONAL BUREAU OF STANDARDS 1963 A

The UV intensities at the sample locations are adjusted from 0.1 to 100 milliwatts. For measurement of these intensities and their distribution across the sample area a Shimadzu Rank IV radiometer is employed. With a bulb in heat in this instrument, the radiometer is calibrated. Measurement of the light intensities at the sample locations is accomplished in a test stand under identical geometrical conditions, as encountered in the photochemical facility. Within the heat exchanger a parallel mirror focuses the light onto the sample. On the test stand this mirror is aligned for optimal light intensity distribution. Under optimal conditions the light intensities tend to drop 10% center sample toward the outer edge by about 53%.

During the course of the long term exposure the Xenon lamp and the parallel mirror, with their aluminum coating, degrade. To assess such degradation within the UV range, the spectral intensity distributions from 200 nm to 470 nm repeatedly are measured prior to, during and after completion of the exposure. For this purpose a quartz vacuum chamber has been placed to the vacuum chamber, in front of a sapphire window (see Fig. 2). A hot radiation lamp, which replaces the Xenon lamp within the heat exchanger, permits accurate calibration of the UV radiation intensities from 200 nm to 470 nm.

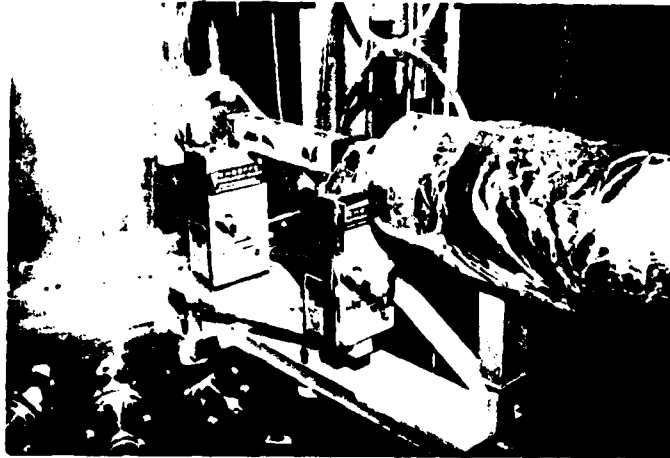


FIG 1: The SCHOEFFEL IM 100-4 double monochromator

2. THE ELECTRON GUN

The electron gun, Fig. 3, is mounted on top of the vacuum chamber. A 100 μ Volt insulator supports its structure. A small insulator, soldered on its top accommodates the electrical feed throughs for the heater of the electron emitter.

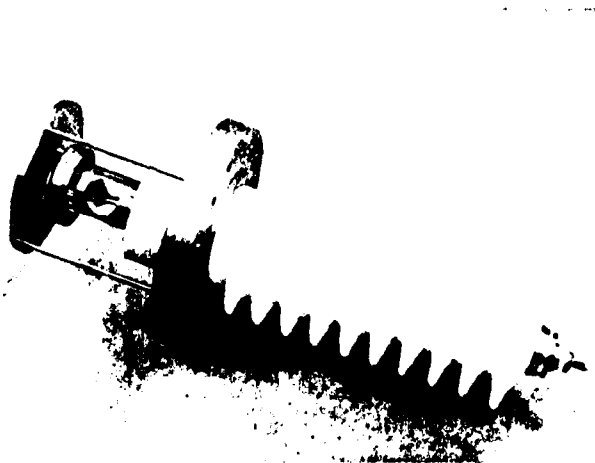


FIG 3: The electron gun

The electron gun is a triode system. To achieve equal current density distribution across the sample area, the electron gun system layout in detail was computed. It is designed around a flat 3 mm \times 1-cathode, surrounded by an electrode, plane with its surface. The Wehnelt electrode is placed opposite to the emitter. These three electron beam confining elements are maintained at the same potential. Together with the acceleration electrode this triode system shapes the electron beam and assures that the electron current density distribution across the sample area is independent of the acceleration potential. This acceleration potential can be selected according to specifications anywhere between 1 k Volts and 60 k Volts.

Below its saturation range the electron current follows the $U^{3/2}$ law. Within the saturation range the electron current density can be adjusted through the heater power input, with current densities ranging from 10^{-10} amps/cm² to 10^{-8} amps/cm². Faraday cups, mounted on a movable support, permit to scan these current densities across the sample area under exposure. For such current density scans a KEITHLEY 602 electrometer instrument is available. Such scans have yielded constant current densities within $\pm 1\%$.

6. THE PROTON GENERATOR

The proton generator is installed close to the electron gun. The RF-proton source is the central part of the proton generator. Here hydrogen by means of a RF field is ionized. Inside the discharge tube the hydrogen pressure is maintained around 50 microns. An automatic pressure control electronic box with valve (operated by the electronic system) keeps the hydrogen pressure constant. The protons, extracted through a 12,5 mm long capillary, consists of about 85% H_1^+ and 15% H_2^+ ions. The proton current densities are adjustable between 10^{-10} amps/cm² and 10^{-8} amps/cm².

To achieve proton current density distributions within $\pm 1\%$ across the sample area, independent of the acceleration potential, an electrostatic multipotential lens has been mounted beneath the capillary exit of the proton source. This multipotential lens serves as proton accelerator and also shapes the proton beam. Through its presence the proton current density distribution over the samples is uniform within $\pm 1\%$, over a wide range independent of the ratio of the acceleration to the extraction potentials. The proton energies can be adjusted according to specifications between 1 keVolts and 10 keVolts (Fig. 4).

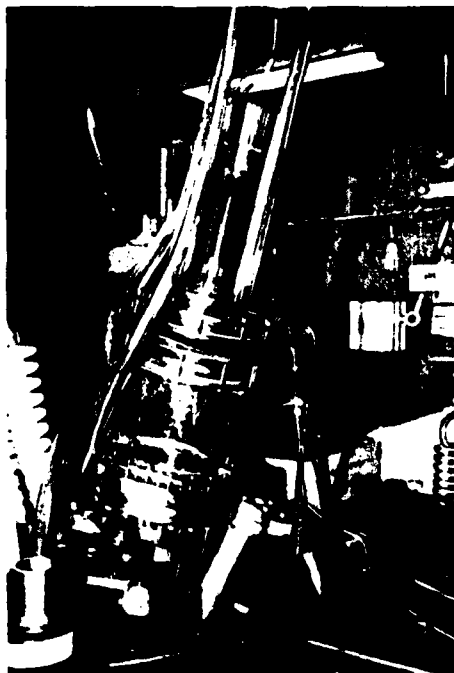


FIG 4: The Proton Generator

7. THE SAMPLE HOLDER

The sample holder, Fig. 5, accepts 32 samples size 11 x 11 mm or 11 x 15 mm. In addition several witness samples and also calibration mirrors may be mounted. Eight samples are exposed simultaneously to the simulated space radiations. Without breaking the vacuum, the sample dish can be rotated to move the samples from the area of exposure sequentially under the integrating sphere for spectral reflectance measurements. During radiation exposure a thermostat keeps the samples at their specified temperature, which may be selected between -30°C and $+100^{\circ}\text{C}$. For each sample two electrical feed throughs are available, e.g.

to measure film surface resistances, to ground contact I/O's, or to monitor sample temperature etc. For measurement of the current density distributions across the lamp area, new Faraday cups are mounted on a rotatable support directly above the irradiated samples. With an additional fixed Faraday cup the electron and the incident current densities are monitored during the exposure.

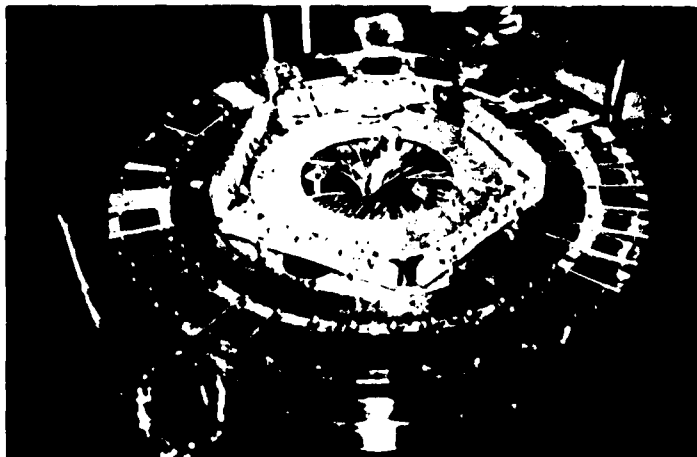
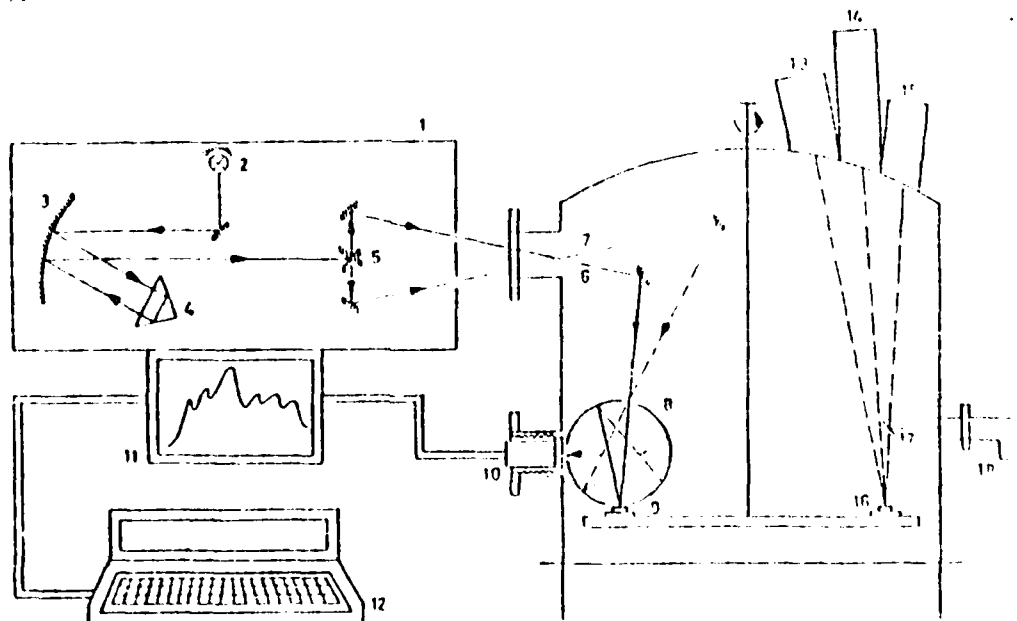


FIG 5: The Sample Holder

7. THE SOLAR ABSORPTION COEFFICIENT

The solar absorption coefficient and its radiation exposure dependent change is measured through the sample spectral reflectances. For measurement of these spectral reflectances a BENTHAM DK - 1A spectrophotometer has been mated to the vacuum chamber. Both, the sample and its reference beams enter the vacuum chamber through apertures. Here these beams are directed onto the sample and onto the inner coating of the integration sphere, for in situ spectral reflectance scans. These reflectances are recorded in the spectral range from 250 nm to 2,5 μ m, without breaking the vacuum (see Fig. 6).



- | | | |
|----------------------|--------------------------|---|
| 1 Spectrophotometer | 7 Reference Beam | 13 e^- Gun |
| 2 Light Source | 8 Integration Sphere | 14 p^+ Generator |
| 3 Parabolic Mirror | 9 Sample | 15 UV Source |
| 4 Prisma | 10 Detector | 16 Sample Exposure Area |
| 5 Oscillating Mirror | 11 Recorder | 17 Deflection Mirror |
| 6 Sample Beam | 12 Programmed Calculator | 18 SCHOFFEL-GM-100-3 Double Monochromator |

FIG 6: The Optical Measurement System

A programmed desk calculator, tied up with the spectrometer, receives a total of 132 reflectance values and calculates in real time the sample solar absorption coefficient under consideration of the corresponding solar spectral intensities according to ASTM E 490 73 a. This measurement proceeds as follows: First the sample is turned under the integration sphere. Within the spectrometer an oscillating mirror generates the monochromatic sample and reference beams. The difference between sample and reference beam then is recorded. From 240 nm to 600 nm a photomultiplier serves light detection. From 600 nm to 2,5 μ m a PbS crystal is used. As calibration standard an aluminium mirror is mounted on the sample dish. The spectrometer is calibrated at about 2,3 μ m wave length. During the spectral scan the wave length dependent reflectances are recorded. 132 such values are digitized and transferred into the programmed calculator for alpha-s determination.

9. STATIC SURFACE CHARGING MEASUREMENTS

Under the influx of charged particles (in a geostationary orbit) dielectric surfaces charge up, governed by their particular secondary electron emission characteristics. Frequently potentials in the K Volt range develop (Ref. 5). To insure long term undisturbed operation of such satellites, without degradation of their thermo-optical surfaces, caused e.g. by electrical discharges, and to avoid break down of semiconductor components, the effects of differential charging are laboratory studied.

The MEB space simulation test facility incorporates the capability of absolute surface potential measurements under electron as well as proton bombardment of dielectric surfaces, independent of the particle energies. Here the sensor is a KEITHLEY capacitive voltage divider, connected to a 602 electrometer instrument. Potentials up to 20 K Volts can be measured.

The sensor is operated under vacuum, during radiation exposure. The distance between sensor and sample is kept constant, independent of angular movements of the sample holder during potential scans. Sample size is 15 x 15 cm. Calibration of the sensor is accomplished through incorporation of one sample with conductive surface, which electrically is connected outside the chamber to a high voltage power supply. The reference sample potential may be adjusted anywhere between 0 and 20 K Volts.

REFERENCES

- Husmann, O.K., "The MEB Space Simulation Test Facility: Performance Data and In Situ Evaluation of the Optical Degradation of SSM under Ultraviolet and Proton Radiation", Conference Proc. "Evaluation De L'Action De L'Environnement Spatial Sur Les Matériaux", Colloque Internat., Toulouse, 17 - 21 juin (1974), p. 17 - 18.

Husmann, O.K. and Kerner, K., "Solar Radiation Resistance Improvement of Second Surface Mirrors and Optical Solar Reflectors by Deposition of Interference Filter", *J. Vac. Sci. Technol.* **14**, 166 - 204 (1977)

Husmann, O.K., "Absolute Calibration of a XBO 900 W/4 Xenon Lamp with Suprasil Built in the Short Wave Length UV, and the Lay Out of the UV Source", Materials Work Shop, Toulouse, July 1977; published by ESA/ESTEC, Noordwijk, (1977)

Husmann O.K. and Ferner, K., "The Alpha-S Stability of Thin FEF SSM Protected by Vapor Deposited Interference Filter under Accelerated Solar Radiation Test Conditions", Materials Work Shop, Toulouse, July 1977; published by ESA/ESTEC, Noordwijk, (1977)

Husmann, O.K., Kerner, K., and Naegle, J., "The Influence of the UV Intensity on the Interference Filter Protected Second Surface Mirror Alpha-S Stabilities, Including Surfaces with Conductive Top Layers", published in Proceedings of the Internat. Spacecraft Contamination Conference, Colorado Springs, (1978), J.M. Semela, Ed., AFML-TR-78-190; NASA CP - 2039

Husmann, O.K., Kerner, K., and Naegle, J., "Improved Alpha-S Stability of Second Surface Mirrors and Optical Solar Reflectors Protected by Thin EnS Coatings or Selected Interference Filter as Top Layer, and the Conductivity of In₂O₃ on SSM", Proc. of the Spacecraft Thermal & Environmental Control Systems Symposium, Munich, October (1978); ESA SP - 139 (1978)

Husmann, O.K., "Accelerated Alpha-S Deterioration in a Geostationary Orbit", Conference Report "Spacecraft Charging Technology", Colorado Springs, 1980, NASA CP 2182, AFGL-TR-81-0270, p. 353 - 364 (1981)
- Feynman, J., Saflekos, N.A., Garrett, H.G., Hardy, D.A., and Mullen, E.G., "Disappearance and Reappearance of Particles of Energies > 50 KEV as seen by P 78-2 (SCATHA) at Near Geosynchronous Orbit", NASA CP 2182, AFGL-TR-81-0270, p. 755 - 767, (1981)

Holman, A.B., "Military Standard for Spacecraft Charging Status Reports", NASA CP 2182, AFGL-TR-81-0270, p. 772 - 788, (1981)

3. Stevens, N. John, "Use of Charging Control Guidelines for Geosynchronous Satellite Design Studies", NASA CP 2182, AFGL-TR-81-0270, p. 789 - 801, (1981)
Bilmain, E.G., and Hirt, W., "Dielectric Surface Discharges: Effects of Combined Low Energy and High Energy Incident Electrons", NASA CP 2182, AFGL-TR-81-0270, p. 119 - 128, (1981)
4. Prakashara, M.P., "The Solar Constant and the Solar Spectrum Measured from a Research Aircraft", GSPC, Greenbelt, Md., 20771, NASA TR R-351
5. Stevens, N.J., Berkopoc, F.D., Staskus, J.V., Blech R.A., and Narciso, St.J., "Testing of Typical Spacecraft Material in a Simulated Substorm Environment" NASA Rep. TMX - 73103, (1976)
Davies, J.K., "The Charging and Discharging of Spacecraft Dielectrics", Spacecraft Materials Conference, ESTEC, Noordwijk, October 2-5, (1979)

THE EFFECT OF COMBINED U.V. RADIATION AND HIGH ENERGY ELECTRONS ON THE
BEHAVIOUR OF POLYMER MATRIX COMPOSITES IN HARD VACUUM

by

R.C. Tennyson, B.A.W. Smith and L.P. Hébert

University of Toronto Institute
for Aerospace Studies
4925 Dufferin Street
Downsview, Ontario
Canada M3H 5T6

SUMMARY

A description of a space simulator capable of thermal-vacuum testing of samples subject to combined UV and high energy electron radiation is presented. Particular attention is given to the use of a natural β emitting Sr^{90} source to simulate space conditions. In-situ thermal and mechanical loading capabilities are also described together with test results obtained on selected polymer matrix composites. Specifically, graphite/epoxy and Kevlar /epoxy laminates have been employed to assess the combined effects of hard vacuum, thermal cycling and radiation on the change in stiffness, creep compliance and coefficient of thermal expansion.

1. INTRODUCTION

One of the main concerns in the use of polymer based materials for space craft applications is the effect of the space environment on the material properties. In addition to vacuum outgassing, degradation due to radiation, atomic oxygen and thermal cycling could occur, for long term exposures.

In the ultraviolet (U.V.) portion of the solar spectrum, photon energies are sufficient to allow them to be absorbed by certain bonds in organic molecules. This can lead to breaking of polymer chains or a splitting off of side groups. This effect may be further compounded by oxidation reactions in low earth orbits. Unlike U.V. radiation, higher energy radiation types such as electrons, protons, gamma and x-rays are non-specific as to chemical structure. In polymers, they can be expected to initially act to ionize radicals. The ion radicals readily react to form excited state molecules. These molecules can then dissociate to form free radicals and the subsequent reaction processes may be similar to those observed for U.V.

In space simulation studies, several aspects should be addressed. These include the necessity of performing in-situ measurements, the significance of synergistic effects (eg: Must irradiation with different radiation types be conducted simultaneously?) and the validity of accelerated testing. This report describes a thermal-vacuum facility that permits in-situ evaluation of material properties such as modulus, creep compliance, coefficient of thermal expansion (CTE) and tensile strength. The combined U.V. and electron radiation capabilities are discussed and some results presented for graphite/epoxy (3M SP 288 T300) and Kevlar / epoxy (3M SP 306) materials.

2. THERMAL-VACUUM RADIATION FACILITY WITH IN-SITU MECHANICAL LOADING

2.1 Facility Description

A thermal-vacuum facility was developed containing both U.V. and electron (β) emitting sources. The working volume within the cylindrical chamber was about 45 cm diameter x 54 cm in height. In addition, the chamber contained a vertical duct, housing the U.V. lamp, running from a port centered in the floor of the chamber out through the chamber lid (Figure 1). One other feature included a carousel arrangement (Figure 2) which supported 30 flat coupons (about 2.54 cm in width), each of which could be rotated into a gimbal mounted load grip having 4500 N capacity. The carousel can be turned externally, thus permitting test data to be obtained for varying radiation exposures on individual specimens. This permitted the determination of modulus, creep compliance and strength. Uniaxial loading was supplied by an external hydraulic piston. The load applied to each sample was measured quite accurately using a calibrated load cell located inside the chamber below the universal joint. The load cell (Figure 3) consisted of a ring fashioned from high strength heat treated SPS steel and load measurements were determined from four bonded strain gauges (Micro Measurements MM EA-06-250BG-120).

Since it was desired to separate U.V. radiation effects from thermal vacuum effects, it was important that control samples were used. Ideally, all samples would be exposed to the same temperature and vacuum histories, the only difference being exposure to the radiation. To attain this goal, a strip of sheet aluminum was attached to the framework on the carousel (Figure 2). This was positioned so as to shield the lower half of each sample from direct U.V. radiation. Since little if any U.V. radiation was reflected, the lower half of each sample acted as a control for the upper half of that same sample. The main drawback of this scheme was that temperatures on the upper and lower parts of each sample would not be exactly the same. This aspect was taken into account by mounting a thermogauge on each section. In addition, the strains in the exposed and shielded portions of each sample were monitored using two longitudinal strain gauges. To prevent possible degradation of the strain gauges due to U.V. radiation, all gauges were placed on the outside of the samples away from the U.V. source. One aluminum specimen was also included to provide a means of calibrating the strain gauges and temperature sensors while the experiment was in progress. It was assumed that the properties of the aluminum would not be affected by the vacuum and U.V. or β radiation.

Control of the thermal environment in the chamber was exercised by the following means. Copper tubing was wrapped around the chamber walls and the exposed ends of the central duct. When desired, water was passed

through these coils to cool the chamber to about 50°F (10 C). Two heating straps attached to the walls allowed the temperature of the chamber to be raised. To obtain a steady state temperature, a Variac was used to control the coil voltage.

The high vacuum environment necessary for space simulation was provided by an oil diffusion pump. A mechanical pump provided both chamber roughing and backing for the diffusion pump. The monitoring and control of the vacuum pumping system and other functions of the facility were carried out from a control panel outside the room in which the chamber was located. (Figure 4). This feature was thought to be a necessary precaution in dealing with the radioactive source described later. The chamber pressure was using a CVC Penthervac G.P.T. 450 system, which used thermistor gauges when the pressure was above 10^{-2} Torr and a Penning gauge when below it. An important feature of the control system was its ability to shut the whole system down if the chamber pressure rose above a prescribed level (eg. in the case of a leak). Temperatures of various parts of the system were also monitored at the control panel.

The high energy electron source consisted of a Strontium-90 (Sr-90) foil contained in a plexiglass holder mounted on the chamber wall (Figure 1). The front panel of this holder can be lowered from outside the chamber to allow samples directly in front of the foil to be irradiated. Different filters can also be placed in front of the holder to vary the intensity of the radiation from the source. One additional factor that must be considered is the conversion of β energy into 'Bremsstrahlung' radiation, with a 'white spectrum' of gamma rays up to the maximum energy of the β rays. Consequently, lead shielding was installed around the complete simulator (Figure 5) to yield a total dose rate exposure at the outer surface of the facility of ~ 0.025 millrems/hr. Safety features included β detectors (Figure 6) mounted in the ozone ventilation line and outside the chamber, both of which could trigger a system shut-down if the radiation levels exceeded a prescribed level.

2.2 Simulation of U.V. Radiation

A Xenon compact arc lamp (Canrad Hanovi. 976C0010) was selected as a U.V. source. Unfiltered, the Xenon lamp's spectrum is quite sun-like in the U.V. region (Figure 7). To allow moderately accelerated testing using direct radiation in the chamber, a one kilowatt bulb and power supply were obtained. The power supply (Figure 6) (Canrad Hanovia 27801.101) can be used with all types of compact arc lamps with powers up to 1000W. This would allow a changeover to the more U.V. rich but less sun-like Mercury-Xenon compact arc lamp if desirable.

By placing the U.V. source at the center of a ring of samples, the use of expensive and inefficient optics was avoided. Because the lamp required an atmosphere for cooling, a pressurized duct had to run through the center of the vacuum chamber to house the bulb. (Figure 1). A clear cylindrical fused silica (Spectrosil) window (Figure 1) placed in the cooling duct was used to transmit the U.V. to the composite samples in vacuum. A structure was constructed over the top of the chamber to allow the upper end of the cooling duct to be rigidly clamped. This, it was hoped, would prevent undue stress being put on the window or the glue joint holding it in place. Once exiting the top of the chamber, the cooling duct was connected to a piping system which led to a fan on the roof of the building. This fan in conjunction with a small one placed at the bottom end of the cooling duct, supplied cooling air to the lamp and drew off ozone produced by the ultraviolet radiation.

While in operation, the U.V. output of the Xenon bulb was measured at regular intervals using two Blak-Ray (J-221, J-225) U.V. detectors. These detectors were solar cells sensitive to different bands in the U.V. region of the spectrum; one around 250 nm (220 nm \sim 280 nm), and 350 nm (300 nm \sim 400 nm). Since these sensors were also sensitive to infrared radiation, readings were taken with and without U.V. absorbing filters installed to obtain the true U.V. irradiance.

2.3 Simulation of Space Electron Environment with a Sr-90/Y-90 β Source

This section describes the use of an electron emitting radioisotope, Strontium - 90 (Sr-90), as an alternative to accelerators for the simulation of the geomagnetically trapped electrons. The main problems associated with accelerators are overheating of the composite samples due to very high acceleration factors and the monoenergetic nature of the particle beams. By contrast, a broad spectrum of electron energies exists in space. However, both of these problems can be overcome with a radioisotope like Sr-90. Because the acceleration factors can be easily controlled by the use of electron absorbing windows and different radioisotope source strengths, overheating of the composite samples can be eliminated. Since one of the characteristics of beta (electron) emitting radioisotopes is a broad continuous spectrum of electron energies, the second problem with accelerator simulation is also eliminated. In this respect, Sr-90 is ideally suited. Sr-90 has a half-life of 28.0 years with a maximum electron energy of 0.544 MeV. Its decay product is Yttrium - 90 (Y-90) which is itself an electron emitter with a half-life of 64.03 hours and a maximum electron energy of 2.25 MeV. The resulting electron spectrum is the sum of the Sr-90 and Y-90 spectra, because, for each Sr-90 electron emitted, a Y-90 electron is also eventually produced. Due to the much shorter half-life of Y-90, a Sr-90 beta source rapidly reaches an equilibrium state where both radioisotopes emit electrons at equal rates. A comparison between the Sr-90/Y-90 β spectrum with the estimated space β spectra at various orbital altitudes is presented in Figure 8 (see Ref. 1 for details). One can readily see that the radioisotope produces fewer electrons of energies less than 0.25 MeV than are found in space but more electrons having energies greater than 0.25 MeV.

Use of β - Absorbing Windows

The β source holder (Figure 1) has provision for β absorbing aluminum (99% purity) windows. A secondary purpose for the windows was also to protect the β source from potential implosion fragments from the U.V. lamp and the quartz glass housing. These two functions were somewhat at odds with each other, since a thick window that protects a source well also absorbs all of the electrons.

Using the analysis of Ref. 1, two aluminum windows of 0.132 cms and 0.274 cms thickness were found capable of absorbing all of the lower energy Sr-90 electrons and providing 90% and 99% absorption of the Y-90 β rays, respectively. The effects of these absorbing windows on the electron energy transmission spectra are

shown in Figure 9. Note that the maximum β energies for the electrons exiting from the 90% and 99% absorption windows are substantially reduced to about 1.56 MeV and 0.81 MeV, respectively, with corresponding average energies of 0.60 MeV and 0.30 MeV. Table 1 provides a comparison of the electron flux one can obtain for two different source strengths (with and without windows) with the space environment at three different orbital altitudes.

Absorbed Radiation Dose in Composite Samples

The equation used to calculate the electron dose rate (EDR in rads / yr) for a given material sample exposed to radioisotope radiation is (1),

$$\text{EDR} = (\text{No. Curries (Ci)}) \times \left(3.7 \times 10^{10} \frac{\text{e}}{\text{sec-Ci}} \right) \times \left(3.1536 \times 10^7 \frac{\text{sec}}{\text{yr}} \right) \times \text{F.F.} \times \text{W.F.} \times \text{A.F.} \\ \times (\% \text{ Absorption of } \beta\text{'s}) \times \bar{E} \times \left(\frac{1}{\text{Sample W.T.}} \right) \times \left(\frac{1}{100} \frac{\text{gr-rads}}{\text{erg}} \right) \quad (1)$$

where 1 rad = 100 ergs/gm of irradiated material

and F.F. = β source form factor, which is the fraction of the source strength (number of Curries) incident on the absorbing windows (=0.2277)

W.F. = window factor

$$= \begin{cases} 1.0, & \text{no window} \\ 0.10, & 90\% \text{ absorption} \\ 0.01, & 99\% \text{ absorption} \end{cases}$$

A.F. = area factor,

$$= \frac{\text{irradiated sample area}}{\text{radiation field area}}$$

The β source used was 9.25 cm wide x 5.97 cm high and each composite sample was 2.54 cm wide and 5.97 cm high. Hence A.F. = 0.2746.

\bar{E} = mean energy of electrons

	W.F.
$\left. \begin{array}{l} 0.19 \text{ MeV, Sr-90 } (3.11 \times 10^{-7} \text{ ergs}) \\ 0.93 \text{ MeV, Y-90 } (1.49 \times 10^{-6} \text{ ergs}) \end{array} \right\} =$	1.0
$\left. \begin{array}{l} 0.60 \text{ MeV, Y-90 } (9.61 \times 10^{-7} \text{ ergs}) \\ 0.30 \text{ MeV, Y-90 } (4.81 \times 10^{-7} \text{ ergs}) \end{array} \right\} =$	0.10
	0.01

The last parameter needed to evaluate Eq. (1) is the % absorption of the β particles, a discussion of which can be found in Ref. 1. Typical values for thin polymer matrix laminates were found to be 97% for Sr-90 and 40% for Y-90.

To demonstrate the application of Eq. (1) to polymer matrix composites, calculations were made of the electron dose rates for various graphite/epoxy laminate thicknesses. These results are summarized in Table 2 for two different source strengths (1 m Ci and 500 m Ci), with and without windows. Again comparisons are given for three altitudes corresponding to a low earth orbit, flight through the radiation belts and near geosynchronous.

From Table 2, it is evident that a 1 m Ci Sr-90/Y-90 electron source can achieve real time (no acceleration) simulation of low earth orbits and that a 500 m Ci source, can, with the use of absorbing windows, achieve acceleration rates of 1 to 200 for low earth orbits and 1 to 100 for high or near synchronous orbits. Without absorbing windows, the 500 m Ci source is within a factor of 10 of achieving real time simulation of intermediate orbits.

3. SAMPLE CONFIGURATIONS AND TEST PROCEDURES

The test samples were made from graphite epoxy (3M-SP288-T300) and Kevlar /epoxy (3M-SP306/Prd-49-III). Only these two material types were used so an adequate number of coupons of each laminate configuration could be included. Graphite and Kevlar /epoxy were particularly interesting for coefficient of thermal expansion (CTE) studies since 4 ply 0 CTE samples could be fabricated from them.

The actual specimens that were used in the experiment consisted of 0°, 90° and 0 CTE (\pm e)s symmetric balance laminates (2). The ply angles used for the 0 CTE samples were determined from previous work. It may be noted that two different thicknesses were used for most of the 0° and 90° laminates to determine the penetration depth effects due to radiation. It was anticipated that only a thin surface layer of the material would be affected by the U.V. radiation. Thinner 90° samples of graphite/epoxy and Kevlar /epoxy were not employed because they were too fragile to handle.

With the samples in the chamber, the baseline data were collected (2). Modulus, CTE and creep data were gathered first in air and later after three thermal cycles in vacuum. These 'thermal cycles' involved turning on the heating elements for a period of time to help drive off moisture and other outgassing products. Following this, the U.V. source was ignited for a comparatively short period of time after which the material properties were again recorded. This procedure was repeated for longer irradiation periods. At a later date, combined U.V. and β radiation experiments were conducted.

Creep Compliance

Assuming that the composite materials being studied could be characterized as linear viscoelastic, a limited number of tests were conducted to investigate how these properties were affected by environmental

conditions. The tests consisted of subjecting a sample to a given load for a certain length of time. Once the load was removed and the sample left unconstrained, the strain was recorded as a function of time. This approach was used instead of the usual creep test because of the difficulty in maintaining a load of constant magnitude in the space simulator. Since the elastic component of the creep compliance was much larger than the time dependent component, the applied load could not be allowed to deviate from its nominal value if one wished to accurately observe the time dependent effects. Thus the method used eliminated this complication because, while strain readings were being recorded, the grips were moved out of contact with the sample. A constant zero load could therefore be assured. The main drawback was that an assumption had to be made about the viscoelastic response in order to obtain compliance curves. The creep tests were performed at ambient conditions and after each of the three U.V. exposure periods. In addition, tests were conducted at two elevated temperatures as well as at room temperature.

4. EXPERIMENTAL RESULTS

Calibrations of environmental effects on the strain gauge response were undertaken using the aluminum sample. Except for a vacuum shift, no U.V. or electron radiation degradation was observed. This can be seen by examining both the tensile modulus and CTE results for the aluminum, as presented in Figure 10. Note that the gauges were shielded from the U.V. radiation.

4.1 Tensile Modulus

Figures 11 and 12 present summary plots of the variation in sample tension modulus with U.V. exposure time for both the graphite/epoxy and Kevlar /epoxy materials. Note that no significant differences between the shielded and unshielded results exist for both materials up to 180 ESD exposure, except for the 4 ply ($\pm 43.5^\circ$)_s Kevlar /epoxy. These latter samples show a significant decrease in modulus with increasing exposure. There appears to be evidence of degradation due to higher specimen temperature on the exposed section (and U.V. damage itself) combining with high internal residual laminate stresses associated with the stacking sequence.

Limited data for a (± 43)_s graphite/epoxy sample were obtained for varying β doses, with and without U.V. radiation present. The results are shown in Figure 13 and it is evident that no significant effect has occurred, at least up to $\sim 6 \times 10^4$ rads, and over 300 equivalent sun days of U.V. exposure.

4.2 Coefficient of Thermal Expansion

Extensive thermal/strain data were obtained for different U.V. exposure periods. Two summary plots are presented in Figures 14 and 15 for graphite/epoxy and Kevlar /epoxy, respectively.

In general, when one compares the unshielded and shielded specimen results, there appears to be no significant U.V. effect for the exposure times investigated.

The effect of electron radiation, with and without U.V. exposure, is shown in Figure 16 for both material systems. For the dosage levels achieved up to present ($\sim 10^5$ rads), no change in CTE is discernible.

4.3 Creep Compliance

Results for several of the creep experiments are given in Figures 17 - 20. Note that the change in compliance (ΔS) was set to zero at 2 seconds because of the comparatively large variations associated with the initial compliance values which tend to mask the time dependent variations.

In examining the data of Figures 17 and 18, it is apparent that the rate of change of the creep compliance becomes smaller with greater exposure to the thermal vacuum environment in the simulation chamber. There is generally no consistent difference between the exposed and shielded sample results. By comparing compliance values recorded for the same stress level at the same time, (Figures 19 and 20) it may be noted that a higher temperature results in a larger compliance value and a greater time dependence.

The observed changes in the creep compliance are what one might expect for a material below its glass transition temperature. The glass transition temperature is actually a surface in a time, temperature and moisture content space. It marks the changeover from low compliance "glassy" behaviour at short times, low temperatures and low moisture levels to larger compliance "rubbery" behaviour. It is also an inflection point where the compliance will exhibit its maximum rate of increase against the log of time. Below the glass transition temperature, the rate of change of compliance, as a function of 'log time', should generally increase with increasing temperature, moisture content and longer times. This is exactly the behaviour observed in the materials investigated.

5. CONCLUSIONS

(a) In the presence of hard vacuum alone the stiffness increases and the CTE changes, depending on the laminate configuration (3). The magnitude of the rate of change of creep compliance (or relaxation modulus) with time is reduced.

(b) Combined U.V. (up to 300 ESD) and β radiation ($\leq 10^5$ rads) were found to produce no significant change in tensile modulus or CTE for the limited material laminates investigated.

ACKNOWLEDGEMENT

The authors wish to gratefully acknowledge the financial support for this research program received from the Natural Sciences and Engineering Research Council of Canada (Grant A-2783) and the United States Air Force Office of Scientific Research (Grant AFOSR - 78 - 3694). We also wish to thank Mr. William Davis of the 3M Co. for donating the composite materials.

REFERENCES

1. Hébert, L. P., "A Simulation of the Space Electron Environment", MA Sc. Thesis, University of Toronto, Institute for Aerospace Studies, 1980.
2. Smith, B. A. W., "Polymer Matrix Composite Materials in a Simulated Space Environment: U.V. and Vacuum Effects", MA Sc. Thesis, University of Toronto, Institute for Aerospace Studies, 1981.
3. Tennyson, R. C., Mabson, G. E. and Ahmed, S., "The effect of Space Environment on the Thermal Distortion of Polymer Matrix Composites", Proc. Specialist Meeting, "Environmental Effects on Materials for Space Applications" AGARD, Toronto, 1982.

TABLE 1 Electron Flux Comparisons Between Sr-90 / Y-90 Sources and Space Environment

Window	Sr-90/y-90 Simulator		Space		Flux (e/cm ² -sec)	
	Max. β -Energy (MeV)	FLUX (e/cm ² -sec) (1m Ci Source)	FLUX (e/cm ² -sec) (500m Ci Source)	Orbit (Km)		Inclination (Degrees)
1.0	2.25	3.051×10^5	1.526×10^6	556	90	7.89×10^5
0.1	1.56	1.526×10^4	7.628×10^6	2315	0	1.13×10^9
0.01	0.81	1.526×10^3	7.628×10^5	33336	0	9.00×10^6

TABLE 1 Composite Electron Dose Rate Comparisons Between Sr-90 / y-90 Sources and Space Environment

Window	Sr-90/y-90 Simulator		Space		Dose Rate (rad/year)	
	Composite Thickness (Plies)*	Dose Rate 1m Ci Source	(rad/year) 500m Ci Source	Orbit (Km)		Inclination (Degrees)
1.0	2	7.2×10^5	3.6×10^8	556 (300 nmi)	90	<u>Surface</u>
	4	5.5×10^5	2.7×10^8			2×10^6
	6	4.6×10^5	2.3×10^8			<u>0.1 cm Depth</u>
	8	3.9×10^5	2.0×10^8			2×10^5
0.1	2	2.7×10^4	1.3×10^7	2315 (1250 nmi)	0	<u>Surface</u>
	4	2.3×10^4	1.2×10^7			4×10^9
	6	2.1×10^4	1.1×10^7			<u>0.1 cm Depth</u>
	8	1.9×10^4	9.6×10^6			3×10^8
0.01	2	1.3×10^3	6.7×10^5	33336 (18000 nmi)	0	<u>Surface</u>
	4	1.2×10^3	5.8×10^5			3×10^7
	6	1.1×10^3	5.4×10^5			<u>0.1 cm Depth</u>
	8	9.7×10^2	4.8×10^5			4×10^6

* Ply thickness = 0.0125 cm, Density = 1.6 gr/cm³

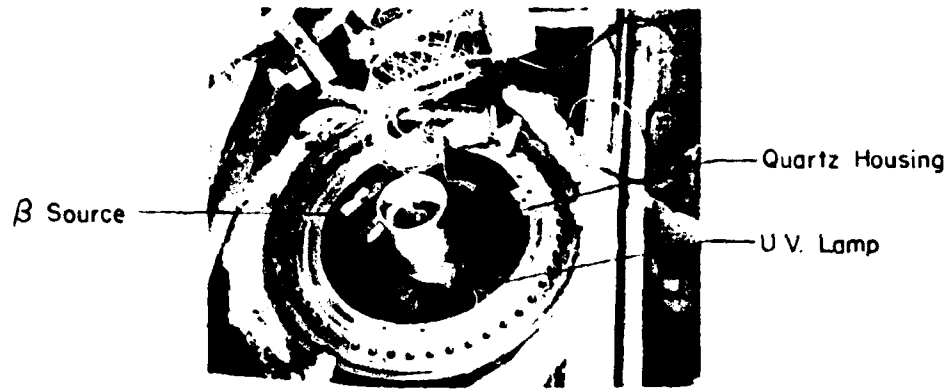


Fig. 1 RADIATION SPACE SIMULATOR

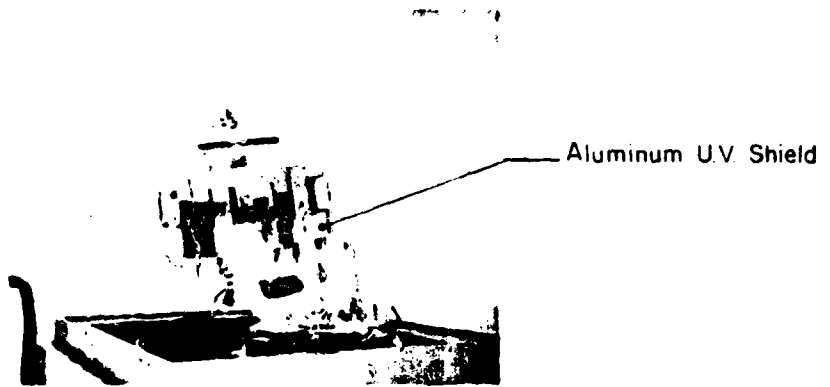


Fig. 2 CAROUSEL OF COMPOSITE SAMPLES

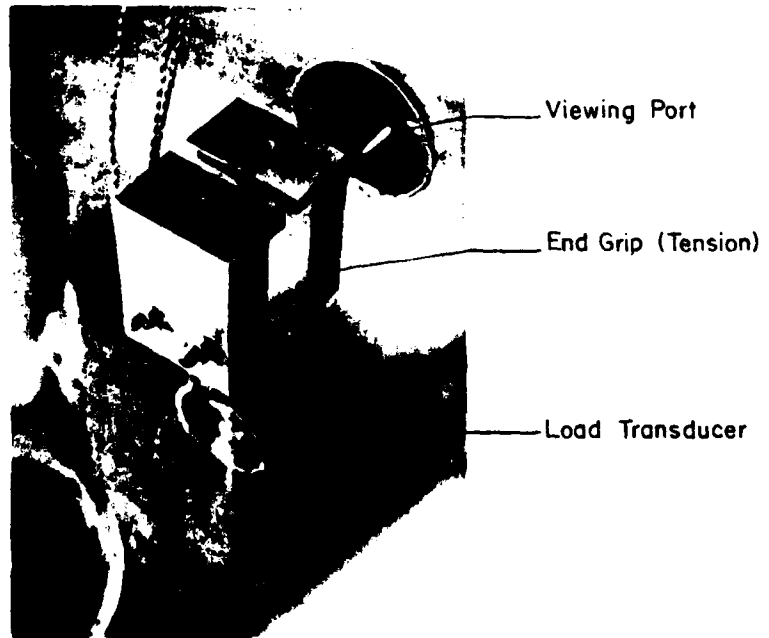
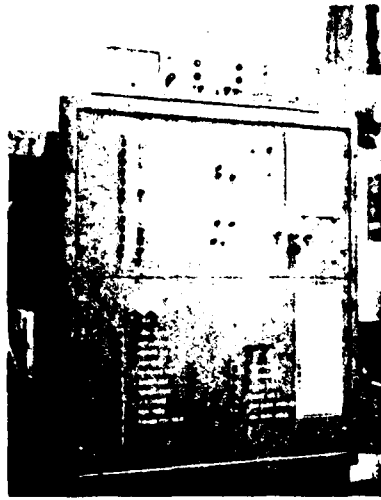


Fig. 3 VIEW OF INTERIOR LOAD GRIP



CONTROL PANELS FOR
RADIATION SPACE SIMULATOR

MONITORS VACUUM, PUMPS,
U.V. SOURCE, β EMISSION

FIG. 4

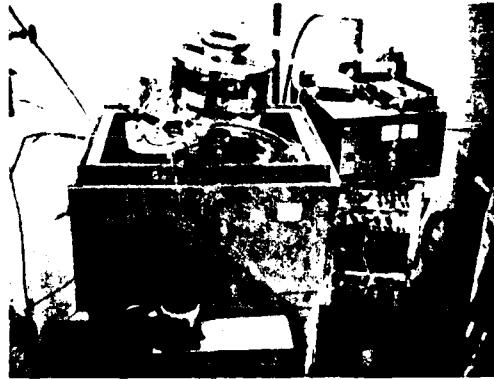


FIG. 5

β EMISSION MONITOR

U.V. POWER SUPPLY

INTERFACE BETWEEN
INSTRUMENTATION AND
DATA LOGGING SYSTEM

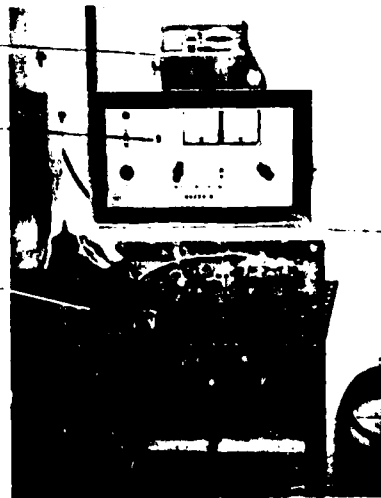
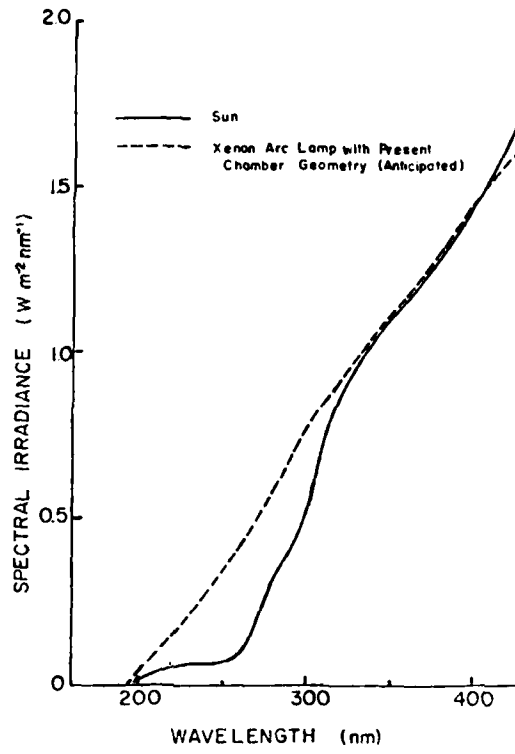


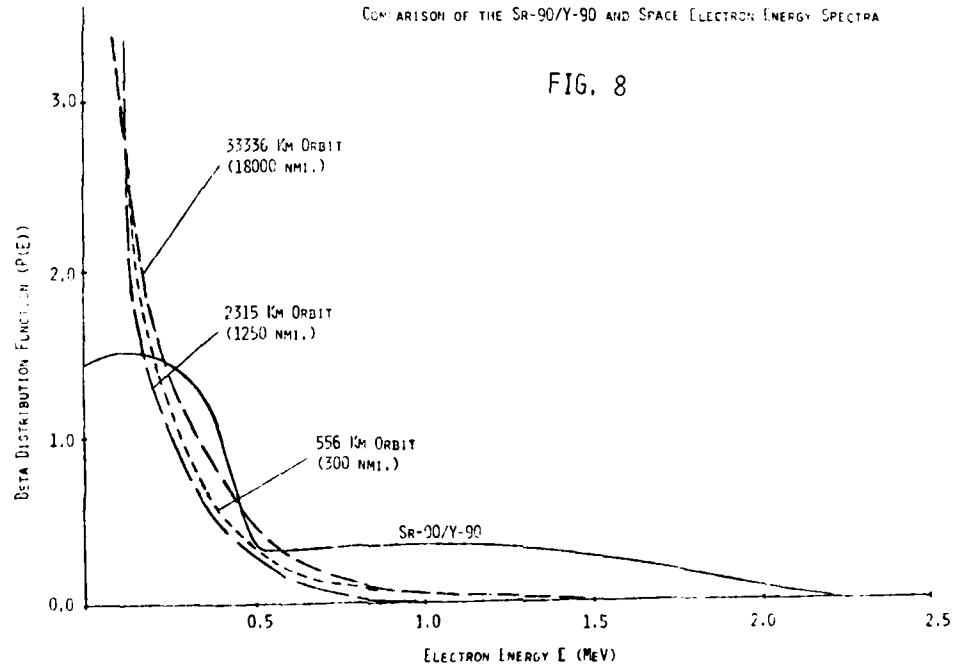
FIG. 6

FIG. 7 COMPARISON OF SOLAR AND XENON ARC LAMP SPECTRA



COMPARISON OF THE SR-90/Y-90 AND SPACE ELECTRON ENERGY SPECTRA

FIG. 8



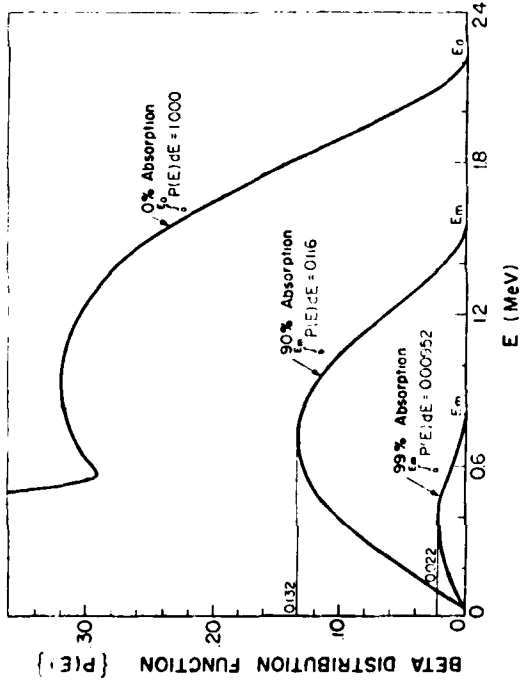


Fig 9 EFFECTS OF ABSORBING WINDOWS ON BETA-RAY ENERGY SPECTRUM
Effect of Electron (β) Radiation on Strain Gauge Response on Aluminum (@ $10^{-6} \sim 10^{-7}$ TORR > 1 YR and 300 ESD of UV.)

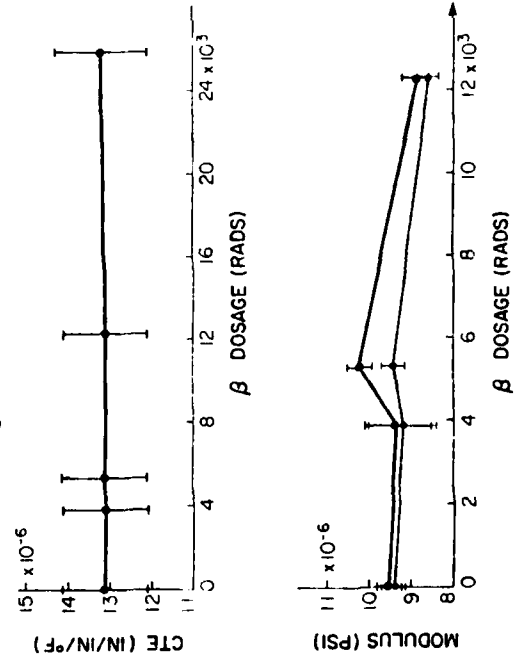


FIG. 10

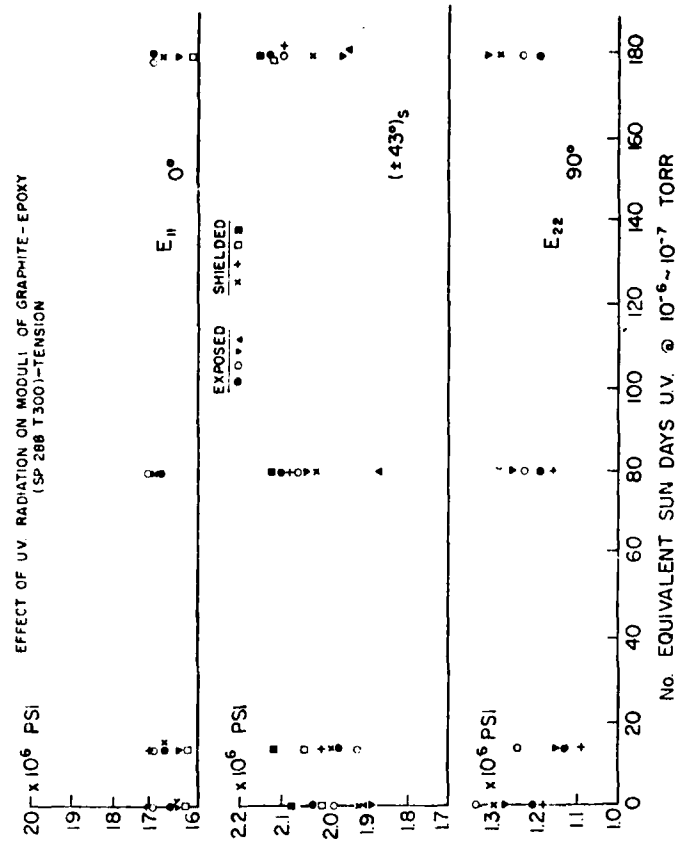


FIG. 11

FIG. 12

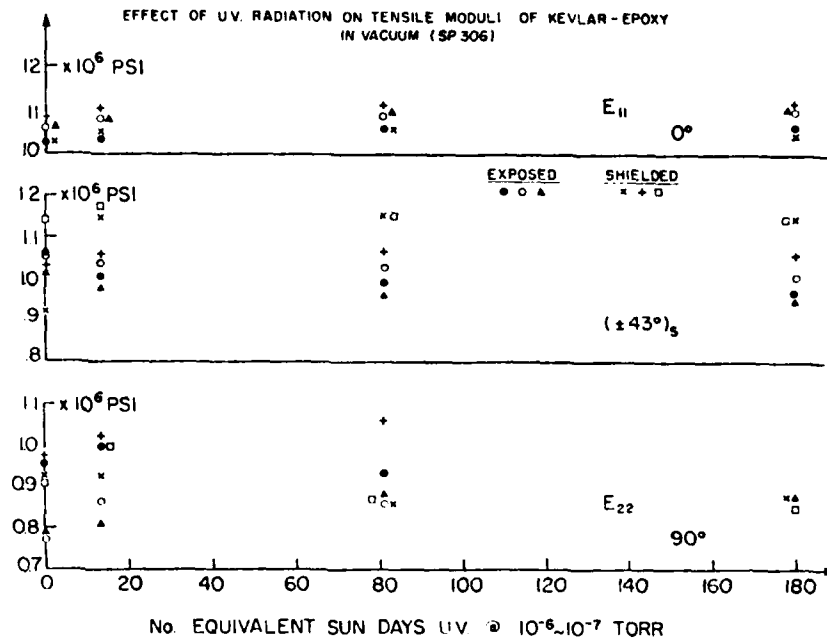


FIG. 13

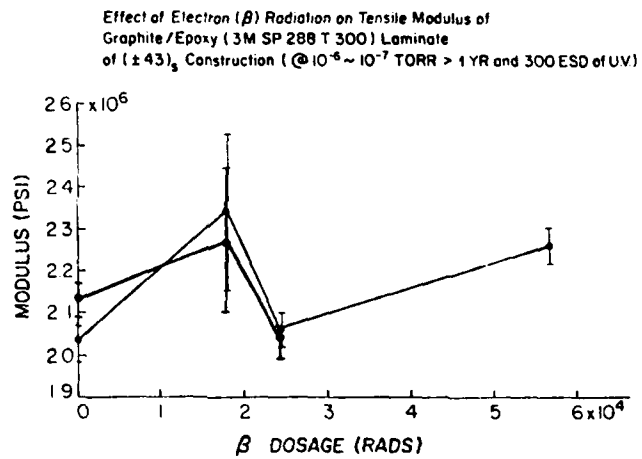
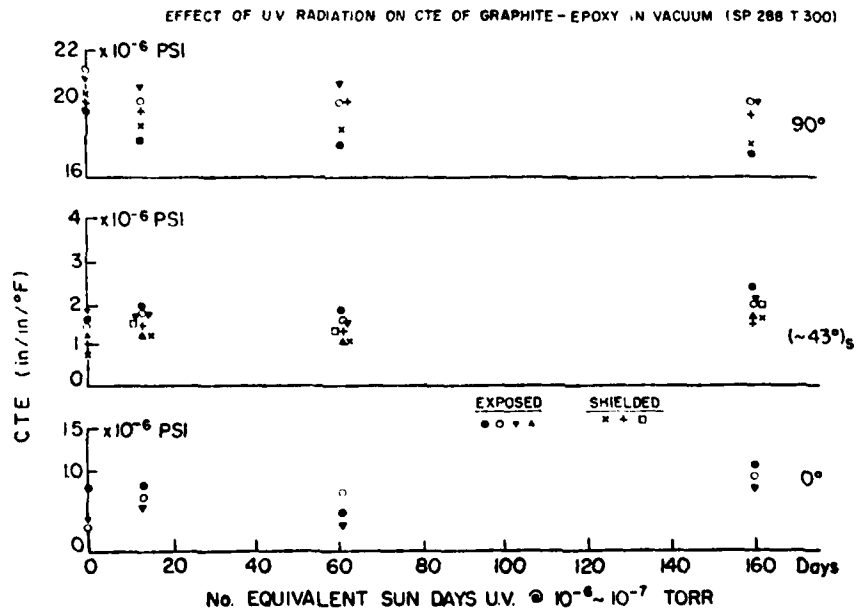


FIG. 14



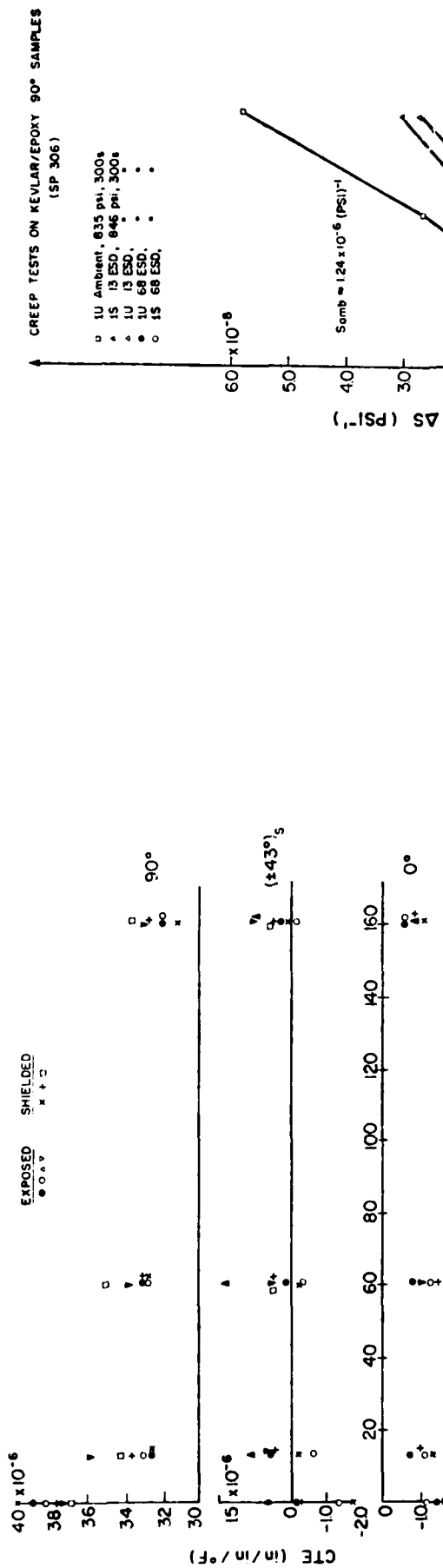


FIG. 17

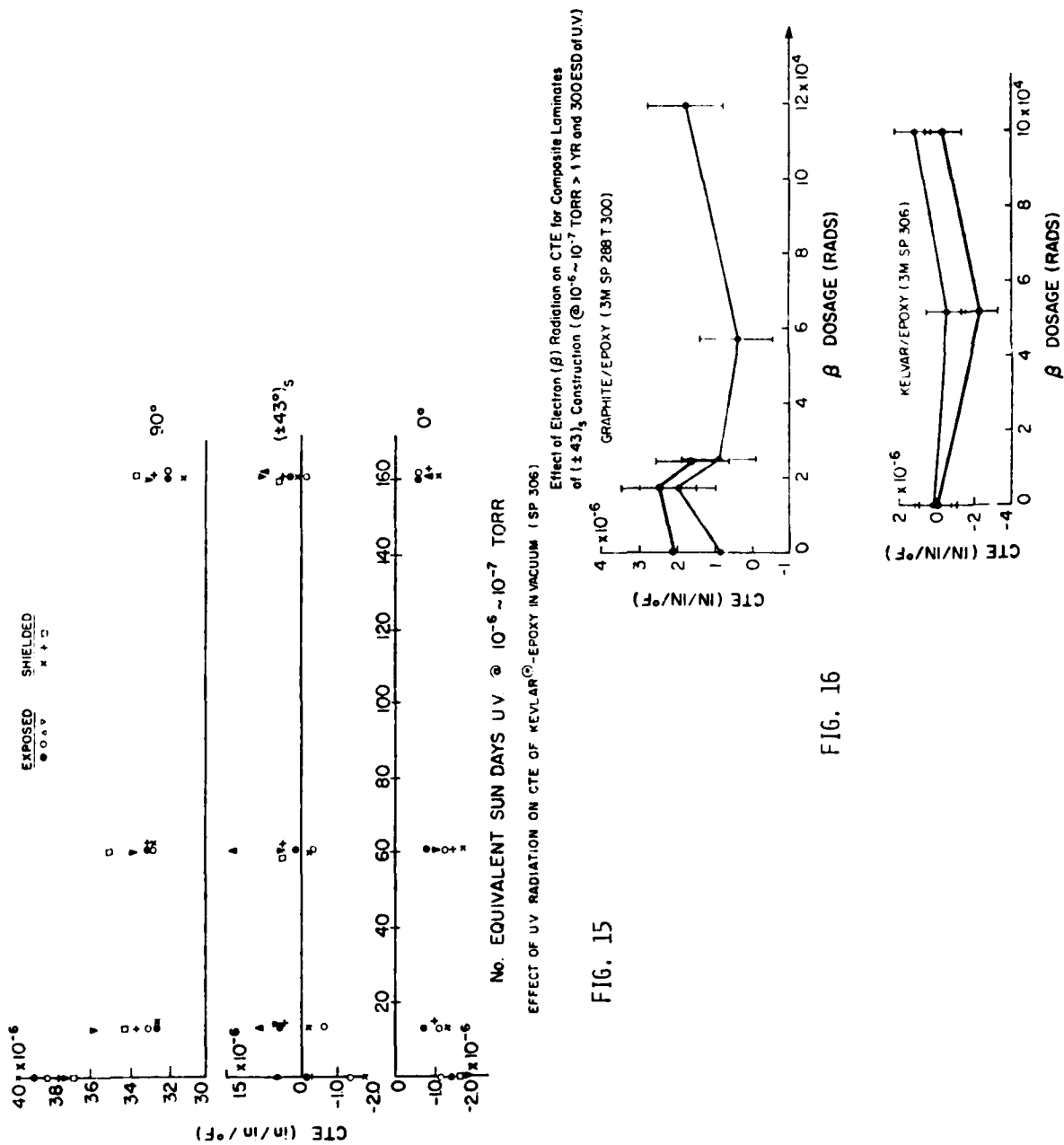
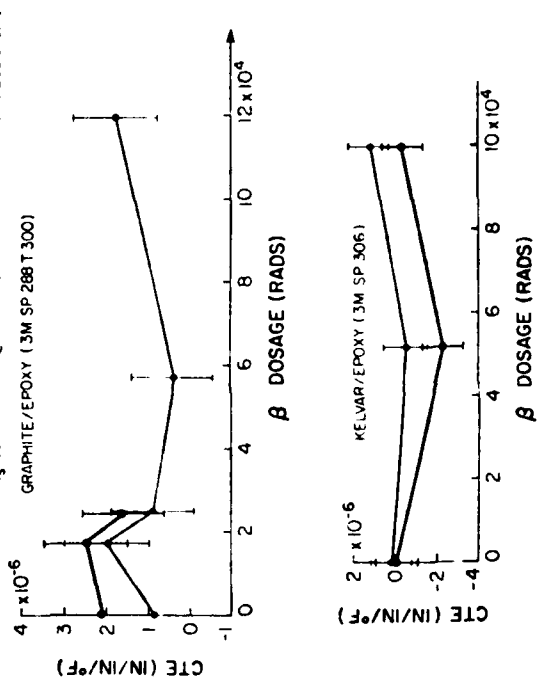


FIG. 16

FIG. 15



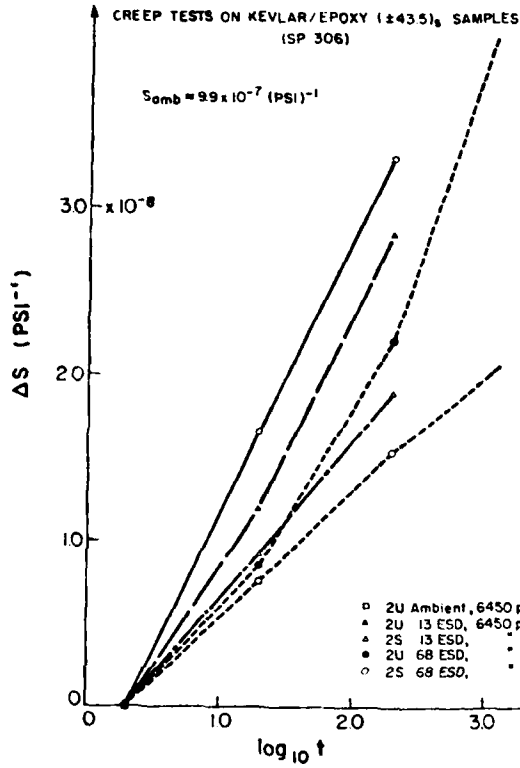


FIG. 18

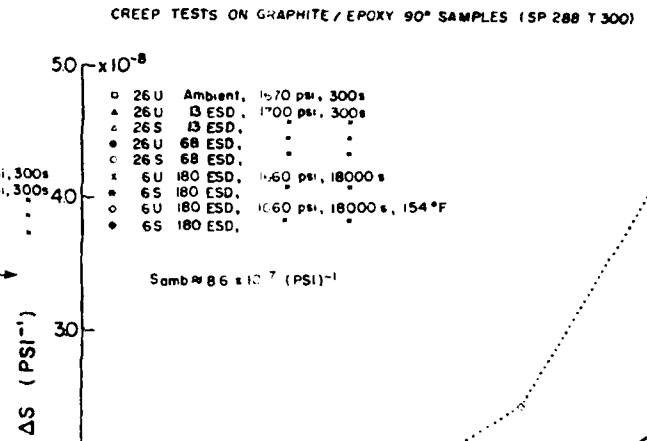


FIG. 19

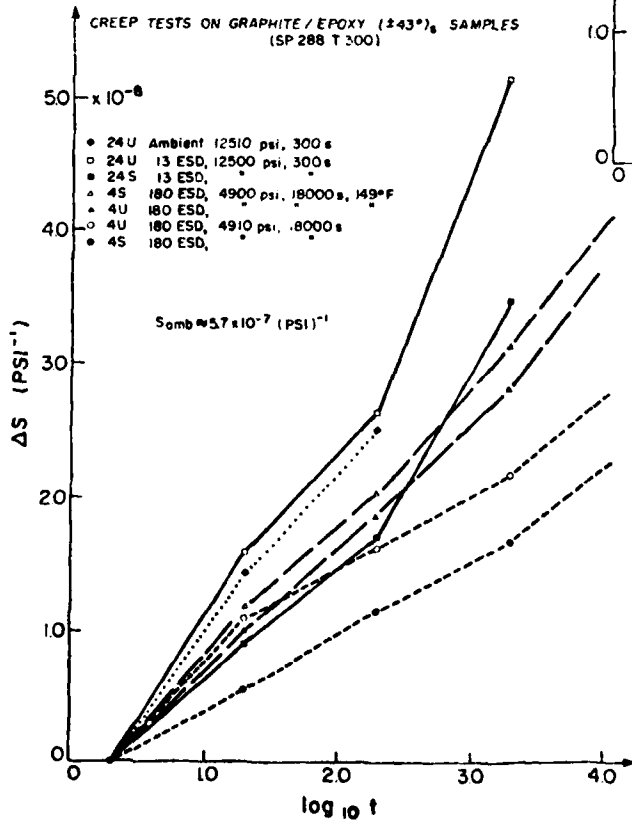


FIG. 20

THERMAL CYCLING TESTS ON MATERIALS AND COMPONENTS FOR SPACE APPLICATIONS

by

H. Hamacher, W. Ley, and K.-V. Rehmann
Deutsche Forschungs- und Versuchsanstalt fuer Luft und Raumfahrt e.V.
Linder Hohe, 5000 Koeln 90, West Germany

Abstract

Thermal cycling tests are performed on materials and components under high vacuum conditions. The purpose of these tests is to investigate changes in properties by thermal fatigue due to microcracking, delamination etc. The test facility used has been developed with respect to the need of true simulation of the strong temperature gradients to be expected in space flight. Tests were performed on CFC materials which are candidates for Large Space Structures use and on solar cell panel samples. The description of the facility, a presentation and discussion of the results is given.

1. Introduction

Thermal degradation of spacecraft materials and its surfaces are mostly studied under stationary test conditions. This is justified for those properties being unaffected by local or time gradients such as the thermo-optical behaviour.

Temperature cycling in the earth orbit, however, has to be considered as a reason for mechanical loading in composite materials and components because of different layer thermal expansions. High total cycle numbers as a consequence of long mission duration results in accelerated fatigue and therefore in shortening of lifetime or changing of physical properties.

The importance of this problem has been identified first in solar cell investigations [4]. The main critical failures are cell to cell interconnect and busbar rupture, cracking of coverslides and solar cells, and delamination of adhesives.

As a material for present and future use in spacecraft technology, carbon fibre composites (CFC) have gained high importance. In comparison to other materials such as metals, CFC offers attractive strength and stiffness to weight relations and high dimensional stability in a wide range of temperature. These properties make them a prime candidate for use in Large Space Structure Technology. However, because of the differences in thermal expansion between the resins and the fibres, intensive cycling tests are necessary for qualification [1,2,3].

In this context, questions are coming up concerning the influence of the other space environmental conditions, such as ultra high vacuum, UV and particle radiation and their combined effects [5,6]. Presently, a full simulation seems to be impossible. Therefore, as a contribution to the first steps in finding properties for materials and components for a long term use, thermal cycling tests are performed under high vacuum conditions. In the following the facility and tests, performed on solar cells and some favourite CFC materials are described.

2. Test Facility

The Thermal Cycling Test Facility has been set up in the Institute of Space Simulation of the Deutsche Forschungs- und Versuchsanstalt fuer Luft- und Raumfahrt e.V. (DFVLR), Koeln. Thermal loads between -180°C and $+100^{\circ}\text{C}$ can be simulated with high temperature gradients in the transition phases under high vacuum conditions. Figure 1 shows the cylindrical vacuum chamber which is used in connection with a vacuum system, data registration and recording equipment. An open cooling cycle supplies the cooling areas with liquid nitrogen. All important components are blocked against unnormal events and change to an uncritical state for the experiment. The duration of the warm and cold phase, can be adjusted and varied with two electrical timers. Figure 2 shows schematically the cross section of the test set-up. The inner cage consists of 4 LN_2 cooled copper sheets, two of which are situated opposite to each other functioning as sample supports. The 4 copper plates of the inner cage are cooled down to the temperature of liquid nitrogen by copper tube lines soldered to the backside. The two infrared heaters consist of copper sheets which are sprayed by black varnish on the plane side. Heating lines are soldered to the polished backside.

The infrared heaters irradiate the front surface of the samples. During the infrared radiation the backsides of the samples face the LN_2 cooled sample support serving as a heat sink. The two cold phase regions (top and bottom) and the two warm phase regions (left and right) are separated by LN_2 cooled copper sheets covered with superinsulation foil in the warm phase regions. An additional flexible packing washer seals the warm phase region hermetically from the cold phase.

The two copper plates, which are not covered by samples, are coated by an insulating foil. The innercage performs reversing rotations of 90° by the pneumatic cycle control system. The total set-up is surrounded by a radiation shield.

Figure 3 shows the opened infrared compartment. The top and bottom cover sheets are mounted to the heater plate perpendicular to the sample plane to ensure that the samples face only infrared heated surfaces.

3. Experimental Results

3.1 Composites

Within DFVLR a technology programm was initiated to investigate the effects of thermal fatigue on CFC material. In table 1 the types of material are listed which were selected with respect to a low thermal expansion coefficient and curing temperature. High modules as well as high tension fibers were considered with curing temperatures between 120°C and 210°C . From each of the materials four samples of 1 mm thickness were fabricated. Three were tested under different cycle numbers, and one was used as the reference. In the test, a 10 year lifetime in the geostationary orbit was simulated. A plot of a single temperature cycle between $+100^{\circ}\text{C}$ and -150°C is shown in figure 4. The chamber pressure was in the range of 10^{-3} Pa.

The effects of thermal cycling on material properties has been investigated by the DFVLR-Institute for Structural Mechanics. The results are described in detail in ref. [3]. The impact on the structural integrity of the samples was studied by

- ultrasonic C-scans
- X-ray photographs
- measurement of natural frequency
- electron beam micrographs

In addition, the residual strength was measured under tensile and compression loading at room temperature and at 100° C. Only these results are reflected in this paper.

In figures 5 and 6 the tensile and compression breaking strengths are plotted vs. cycle number. All values are depicted in ratios to the tensile resp. compression breaking strength of the uncycled samples, tested at 23° C. The test temperatures were 23° C (solid lines) and 100° C (broken lines). A strong change is given for the polyimide based material (T3T F 178) after the first 1170 cycles compared with the other samples. The large size of pores may be the reason for this behaviour. In most cases after 1170 cycles a lower strength was observed than after 2295 or even after 3480 cycles. Post-curing does not seem to be a reasonable explanation, because the upper cycle temperature was too low in comparison to the curing temperature. Surprising was the small reduction of tensile and compression strength of approximately only 3% resp. 10% of the laminates No. 164 and 175 both cured at 180° C compared with at least 20% reduction of the 120° C cured laminate No. 169 and the laminate No. 170A with 120° C curing temperature lying between them. This held for 23° C testing temperature as well as for 100° C.

Table 1 Thermal Cycling Tests
Material Review

Laminate No.	Material Designation	Type of Fiber	Type of Resin	Curing Temperature
164	914 C-TS-5	high tension Toray T 300	Ciba 914	180° C
169	HY-E1548A/B	high modulus Celion GY-70	Fiberite 948A1	120° C
170 A	LY556/HY917/ XB2692/T300	high tension Toray T300-6000	Unmodifide Epoxy	120° C
175	HY-E 2034 D	high modulus Thorel Pitch	Fiberite 934	180° C
PI	T3T F178	high tension Union Carbide T 300-3K	Hexcel F 178	210° C

Stacking Sequence of all Laminates | $^+_{-} 45^{\circ}_2$ | s with
a Total of 8 Plies

3.2. Solar Cells

Details on the solar cells tested are shown in tables 2 and 3 [4].

Item		D	K	L	C
Size			125 x 125 mm ²		
Substrate Thickness		50 μm Kapton	40 μm Glass fibre reinforced Kapton	170 μm Carbon fibre reinforced Kapton	170 μm including 12,5 μm Kapton 150 μm Carb. fibre
Solar Cells	Size	2 x 2 cm ²	2 x 4 cm ²	2 x 4 cm ²	2 x 4 cm ²
	Thickness	200 μm	200 μm	200 μm	200 μm
	Resistivity	10 Ωcm	10 Ωcm	10 Ωcm	10 Ωcm
	Contact Material	Ti/Pd/Ag	Ti/Pd/Ag	Ti/Pd/Ag	Ti/Pd/Ag
Mass		32,50 g	26,485 g		

Table 2: Flexible Panel Details

Item		G	H	I
Size			145 x 115 mm ²	
Substrate	Thickness	18,0 mm	18,0 mm	22,0 mm
	Thickness of Face Sheet	250 μm	250 μm	50 μm
	Al-Foil Thickness	0,0007"	0,0007"	0,0007"
	Honeycomb Cells	3/8" perforated	3/8" perforated	3/8" perforated
	Insulation	25 μm Kapton	25 μm Kapton	25 μm Kapton, 5 μm Dupont poi.adh.
Solar Cells	Size	2 x 4 cm ²	2 x 2 cm ²	2 x 4 cm ²
	Thickness	200 μm	200 μm	200 μm
	Resistivity	10 Ωcm	10 Ωcm	10 Ωcm
	Contact Material	Ti/Pd/Ag	Ti/Pd/Ag	Ti/Pd/Ag
	Mass		35,0 g	33,188 g

Table 3: Rigid Panel Details

In order to ascertain the influences of the temperature cyclings the following representative functions have been measured after 100,500,1034,1490,2000,2500,2949,3500 intervals:

- o Current-Voltage-Characteristic
The irradiations (1370 W/m^2) emitted by a solar simulator (test area 300 mm) was adapted to the extraterrestrial solar spectrum.
Relevant Data are: Short-circuit current, open-circuit-voltage, maximum power output.
- o Dark-Current-Characteristic
After every 50 cycles the dark current characteristic of each panel was recorded during the warm phase under vacuum conditions. Dark current I.-V-measurements are used to detect major electrical defects, e.g. damages of cells or inter-connectors.
- o Thermo-graphical Measurement with the Infrared Camera
The temperature distribution chart of the surface of the solar cell panels was produced with the infrared camera as an electro-optical system.
The solar cell panels were heated using two different methods:
 - The modules were heated to a temperature of approximately 40° C by an electrical current in reverse direction
 - Self-heating of the modules to approximately 40° C from the rear side by infrared heaters
 The information on the condition of the thermal contact between cell and substrate did not show an apparent change of the temperature distribution of the panels.
- o Visual Inspection
The visual inspection was carried out before and after each test phase using a stereo microscope.
Additional cover cracks, interconnector ruptures, bubbles and colour changes have been detected.

4. Conclusions

- o The only material in test showing severe damage due to thermal cycling was a polyimide based laminate.
- o All other materials showed much less severe cracking especially the 180° C cured epoxy based laminates.
- o Furthermore no significant effect on structural integrity stemming from the different thermal expansion coefficients of the high tensile and high modulus fibers could be detected.
- o The temperature-time-profile of the solar cell samples was similar to the calculated curves for typical rigid and flexible solar cell panels. The average initial rates of temperature change from the cold to hot phase were $50^\circ \text{ C min}^{-1}$ for the flexible panels and $30^\circ \text{ C min}^{-1}$ for the rigid panels. From the hot to cold phase these rates of change were between $37^\circ \text{ C min}^{-1}$ and $26^\circ \text{ C min}^{-1}$ respectively.
- o The maximum power of the different solar cell panels decreased slightly with test time as shown in figure 7.

5. References

- [1] Baier, H.J.
Schneermann, M.W. Annual Meeting of DGLR, Aachen
"Analysis and Synthesis of High Precision Structures"
(May 1981)
- [2] Gädke, M. DFVLR-Mitteilung 81-25, Braunschweig
"Auswirkung von Umwelteinflüssen auf die mechanischen Eigenschaften von CFK", (1981), p. 85 - 119
- [3] Hartung, W. DFVLR - Contract-number 132274 A 56446, Braunschweig
"Influence of Thermal Cycling on the Behaviour of CFRP"
(June 1981), un-published
- [4] Ley, W. Proc. of the 12th Photovoltaic Specialists Conference,
Baton Rouge, Louisiana
"DFVLR Facility for Thermal Cycling Tests on Solar Cell Panel Samples under Vacuum Conditions" (November 1976)
- [5] Long, R. Jr. NASA TP-1568, Hampton, Virginia
"Electron and Proton Absorption Calculations for a Graphite/
Epoxy Composite Model" (1979)
- [6] Tennyson, R.C. Proc. of the 21st Structures, Structural Dynamics and Material
Conference, Seattle, Washington
"Composite Materials in a Simulated Space Environment"
(May 1980)

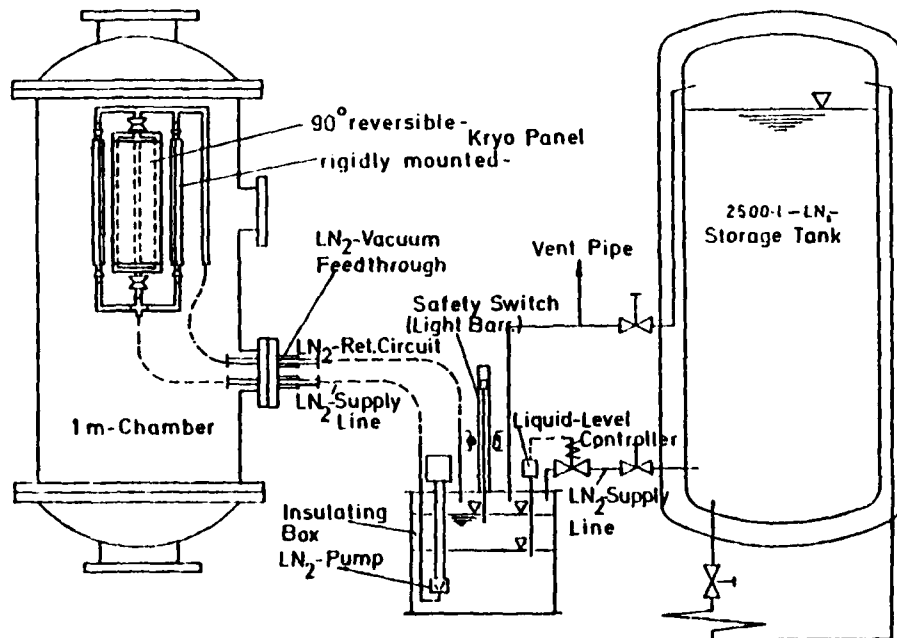


Figure 1

LN₂ - Supply for the Thermal Cycling Test Facility

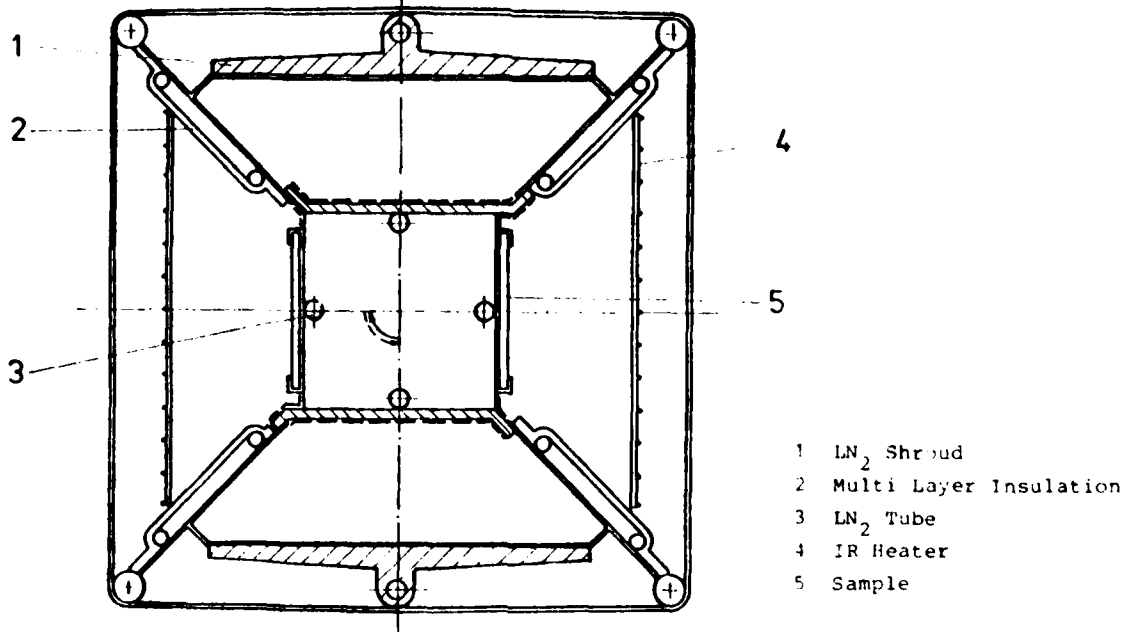


Figure 2 Cross Section of the Thermal Cycling Test Facility



Figure 3 Opened Infrared Compartment and Test Samples

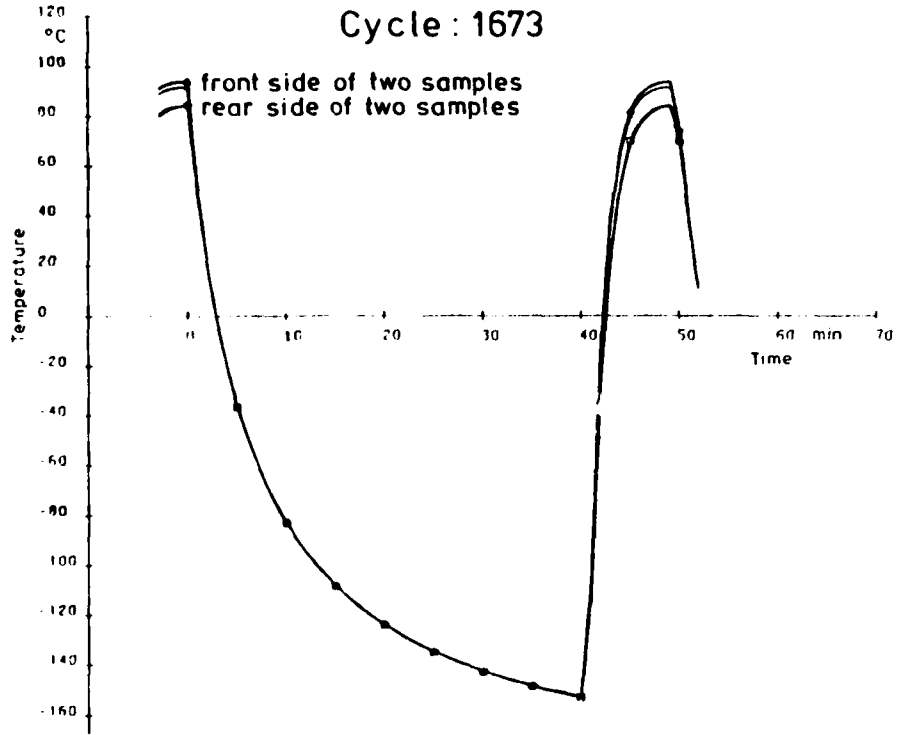


Figure 4 Sample Temperature Profile of a typical Cycle

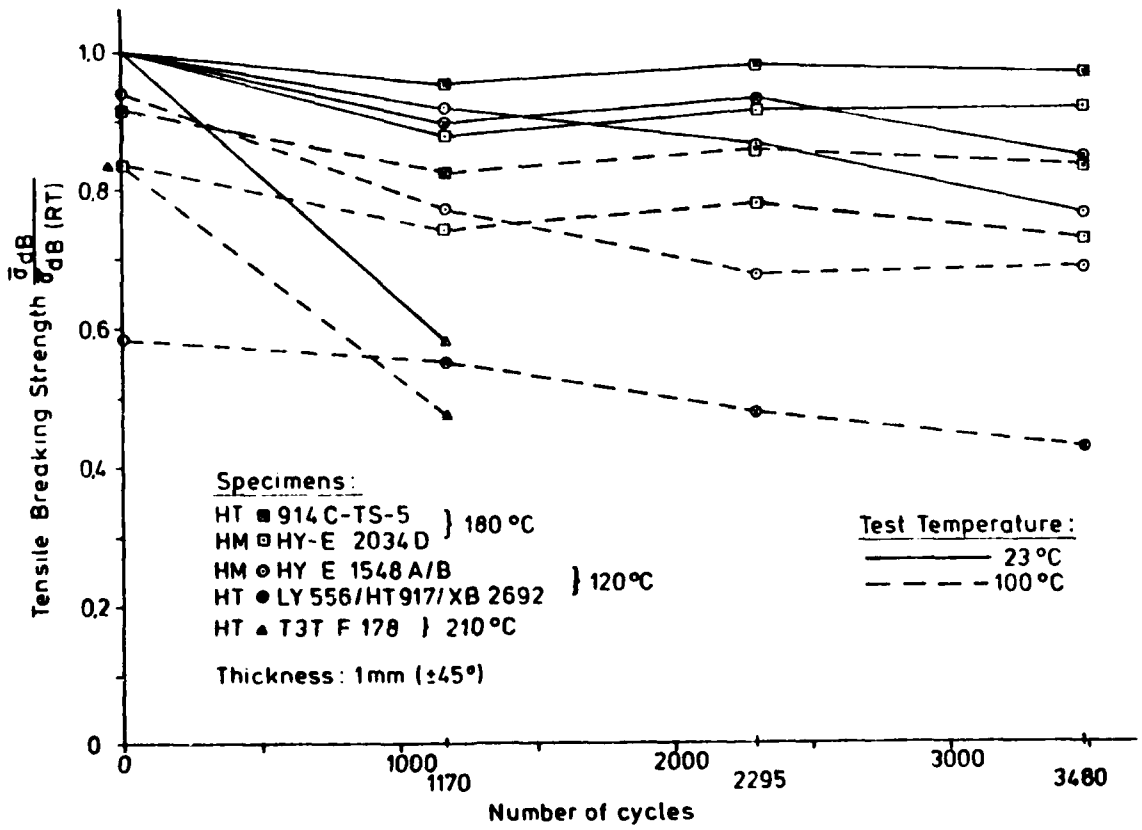


Figure 5 Tensile Breaking Strength vs. Number of Cycles

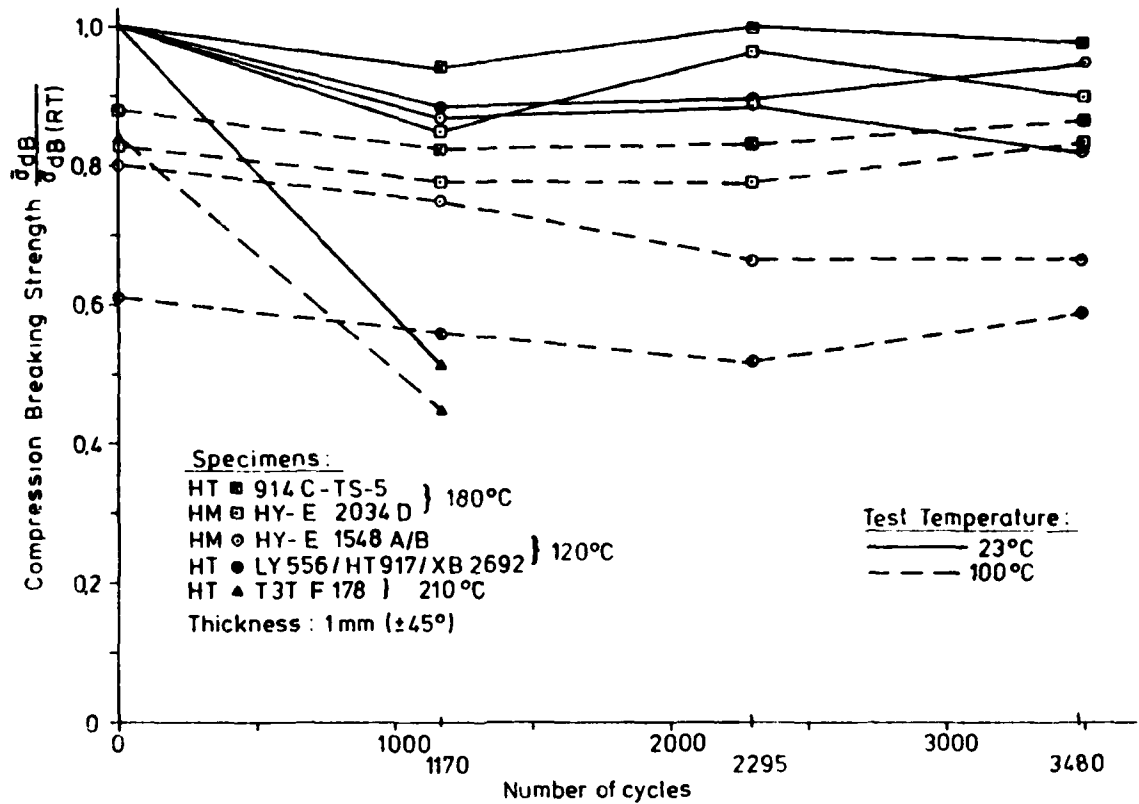


Figure 6 Compression Breaking Strength vs. Number of Cycles

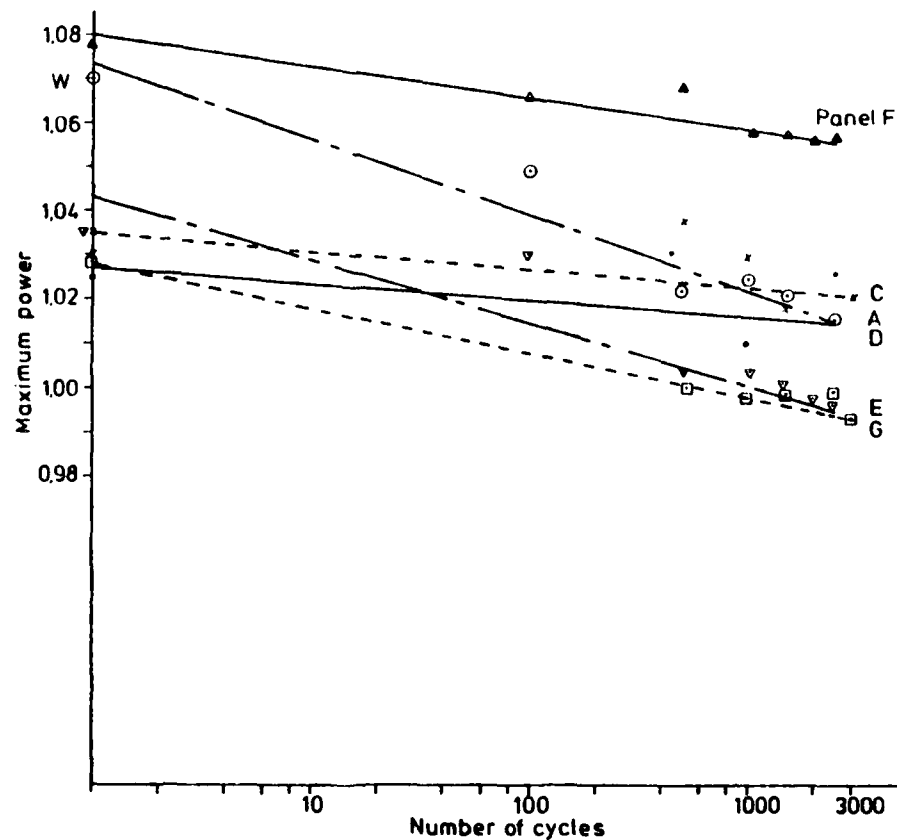


Figure 7 Decrease of maximum Power with Time

RECORDER'S REPORT

SESSION IV - TESTS

by

Dr E.C. van Reuth
 Director, Materials Science
 Advanced Research Projects Agency
 1400 Wilson Boulevard
 Arlington, VA 22209
 USA

Paper 15: "Testing of Large Flexible Substrate Deployable Solar Arrays for Spacecraft", was delivered by Mr Peter McIntyre and Mr Andrew Jones (Ca).

Flexible solar arrays for the Hermes and LSAT satellites were described. The size of these arrays prohibits ground testing so predictive analysis is employed for vibration modes. Mission life is planned for 10 years. The arrays have detectors which tell when they are fully tensioned and sun sensors keep the array locked onto the sun. Solar radiation yields 8.5 KW/Wing.

DISCUSSION

A question was asked concerning what new methods will become available for dynamically qualifying large space structures since shakers are only good for small structures. The authors stated that ground testing today must be limited to low frequencies on low strength members. Therefore, finite-element analyses are used to verify laboratory methods through modal analyses. Some measured results are being used to develop new methods of analysis.

A question was raised as to whether the solar wind could bend this antenna. The authors replied that such instabilities are actually due to thermal gradients and that the conditions which exist in the Alouette system do not exist here. The Alouette system had little torsional stiffness whereas this system has torsional stiffness and end effectors to offset such stresses.

Paper 16: "The MBB Combined Effects Chamber", was delivered by Dr L.Preuss (Ge).

The author pointed out that near-earth orbits subject satellites to electron bombardment. The MBB simulation chamber is capable of a vacuum of 10^{-7} torr, ultraviolet radiation of 2 to 6 solar constants at 170 to 400 nanometers wavelength, electron or proton bombardment of 10^9 to 10^{12} particles/cm²/sec, and potentials of up to 20 kilovolts. The chamber can expose up to 32 samples of material having dimensions of 11 mm x 11 mm.

DISCUSSION

A question was asked as to when the system was operational and why no data were presented here. The reply was that the system was operational in 1972 and that this paper was intended only to make the audience aware that such a capability exists. Another questioner asked what effects were anticipated regarding the bombardment of polymers by protons. The reply was that the effects of electron bombardment would probably have a greater effect.

Paper 17: "The Effect of Combined UV Radiation and High Energy Electrons on the Behavior of Polymer Matrix Composites in Hard Vacuum", was delivered by B.A.Smith (Ca).

A detailed description was presented of the carousel-loaded sample tester. A xenon light source is available for UV radiation; the vacuum is 5×10^{-7} torr; and a foil strip of strontium-90 acts as an electron source. Samples can be rotated into a tensile tester to evaluate degradation in properties. Most samples tested to date have been graphite- or Kevlar-reinforced composites.

A summary of results indicate that there are visible changes in polymers due to UV-radiation.

Initial exposure to vacuum caused an increase in the modulus of elasticity of samples and a decrease in creep resistance. There has been no concrete evidence to suggest changes in modulus or coefficient of thermal expansion with electron bombardment.

DISCUSSION

Two questions were posed during the discussion period. The first questioned whether, in fact, tensile tests had been performed. The answer was "no". The second question asked for the rationale as to why the particular epoxy-resin system was chosen by the University of Toronto. The answer given was that this system was thought to be representative of many systems and it was pointed out that the resultant data followed other trends reported in the literature. A member of the audience then pointed out that there are wide differences in various resin systems and asked whether the authors intended to investigate other systems. The answer was "yes".

Paper 19: "Life Prediction Capability for Space Lubricants", was delivered by Dr B.D. McConnell (US).

It was pointed out that many satellites are intentionally spun for stability. Therefore, their antenna must be despun by an assembly which contains bearings with demanding lifetime requirements. The author has investigated lubrication breakdown, bearing-torque variations and bearing/cage stability.

Because of today's planning for extended-life satellites, full scale testing is no longer possible. Therefore, good life prediction methods are becoming necessary.

The spin-rate of satellites is about 60 rpm and antenna data must be transferred across a gold slip-ring. However, the latest satellites are using coin silver and graphite slip-rings for this purpose. The lubricating fluid has a very low vapor pressure and a loss of 15% is projected over a 10 year lifetime. Fluid degradation is anticipated from volatilization temperature fluctuations, and from contamination (due to excess oxygen before launch and to contaminant pick-up after launch).

Bearing tests have been conducted to 22,000 hours. Twenty parameters were measured throughout the test. The data gathering procedure used microprocessors to record all parameters only when one of them went beyond prescribed limits. For the important measurement of slip-ring noise, brush movement was measured for the first time.

DISCUSSION

Discussion of the paper started with a question of how the apparatus accounted for g-force loading. The answer given was that although g-force cannot be totally circumvented, the bearings in this rig were loaded against each other to minimize such effects. It was also pointed out by the author that there are g-force effects on the apparatus lubrication which are not duplicated in space.

A question was asked whether the experiments would also be useful for solid lubricants. The author answered that another program was making the transition to solid lubricants. Additionally, the author feels that the data acquisition system is so flexible that it could be used with a wide variety of computer programs.

A final question asked whether the bearing-instabilities mentioned earlier could be a problem in the satellites we are now launching and whether we are premature in launching satellites with an expected lifetime of 10 years. The author answered that there has been no such documented lubrication failure and that spin-stabilization is not used on the newer satellites. He doesn't feel that his experiments have unearthed any real problems which should stop satellite launches. He does feel however that a method of better data taking and a method of better design, has been developed.

CHAIRMAN'S FINAL REMARKS

Professor Santini, the Meeting Chairman, expressed his thanks to all of the participants of this first meeting on space under the auspices of the Structures and Materials Panel. He expressed satisfaction with the excellent quality of the papers. He also stated that much more needs to be done to extend life prediction and testing for longer life satellites. Finally, Professor Santini remarked that spacecraft materials and structures are not separate technologies and that we are increasingly realizing that the two technologies interact with one another. Thereafter, we must integrate these technologies into the overall system of the spacecraft.

REPORT DOCUMENTATION PAGE

1. Recipient's Reference	2. Originator's Reference AGARD-CP-327	3. Further Reference ISBN 92-835-0330-9	4. Security Classification of Document UNCLASSIFIED								
5. Originator Advisory Group for Aerospace Research and Development North Atlantic Treaty Organization 7 rue Ancelle, 92200 Neuilly sur Seine, France											
6. Title ENVIRONMENTAL EFFECTS ON MATERIALS FOR SPACE APPLICATIONS											
7. Presented at the 55th Meeting of the AGARD Structures and Materials Panel in Toronto, Canada on 19-24 September 1982.											
8. Author(s)/Editor(s) Various	9. Date March 1983										
10. Author's/Editor's Address Various	11. Pages 230										
12. Distribution Statement This document is distributed in accordance with AGARD policies and regulations, which are outlined on the Outside Back Covers of all AGARD publications.											
13. Key words/Descriptors <table border="0" style="width: 100%;"> <tr> <td style="width: 50%;">Materials</td> <td style="width: 50%;">Aerospace environment</td> </tr> <tr> <td>Spacecraft</td> <td>Environmental tests</td> </tr> <tr> <td>Aerospace engineering</td> <td>Mechanical properties</td> </tr> <tr> <td>Design</td> <td></td> </tr> </table>				Materials	Aerospace environment	Spacecraft	Environmental tests	Aerospace engineering	Mechanical properties	Design	
Materials	Aerospace environment										
Spacecraft	Environmental tests										
Aerospace engineering	Mechanical properties										
Design											
14. Abstract <p>In the Fall of 1982 the AGARD Structures and Materials Panel convened a meeting of specialists entitled "Environmental Effects on Materials for Space Applications". The meeting heard papers on and discussed general requirements and related design philosophies, environment and environmental effects, properties of interest, and tests, with the aim of establishing the current state-of-the-art and encouraging relevant future research.</p> <p>This publication documents the papers presented at that meeting together with summaries of the subsequent discussions.</p>											

<p>AGARD Conference Proceedings No.327 Advisory Group for Aerospace Research and Development, NATO ENVIRONMENTAL EFFECTS ON MATERIALS FOR SPACE APPLICATIONS Published March 1983 230 pages</p> <p>In the Fall of 1982 the AGARD Structures and Materials Panel convened a meeting of specialists entitled "Environmental Effects on Materials for Space Applications". The meeting heard papers on and discussed general requirements and related design philosophies, environment and environmental effects, properties of interest, and tests, with the aim of establishing the current state-of-the-art and encouraging relevant future research.</p> <p>P.T.O.</p>	<p>AGARD-CP-327</p> <p>Materials Spacecraft Aerospace engineering Design Aerospace environment Environmental tests Mechanical properties</p>	<p>AGARD-CP-327</p> <p>Materials Spacecraft Aerospace engineering Design Aerospace environment Environmental tests Mechanical properties</p>	<p>AGARD Conference Proceedings No.327 Advisory Group for Aerospace Research and Development, NATO ENVIRONMENTAL EFFECTS ON MATERIALS FOR SPACE APPLICATIONS Published March 1983 230 pages</p> <p>In the Fall of 1982 the AGARD Structures and Materials Panel convened a meeting of specialists entitled "Environmental Effects on Materials for Space Applications". The meeting heard papers on and discussed general requirements and related design philosophies, environment and environmental effects, properties of interest, and tests, with the aim of establishing the current state-of-the-art and encouraging relevant future research.</p> <p>P.T.O.</p>
<p>AGARD Conference Proceedings No.327 Advisory Group for Aerospace Research and Development, NATO ENVIRONMENTAL EFFECTS ON MATERIALS FOR SPACE APPLICATIONS Published March 1983 230 pages</p> <p>In the Fall of 1982 the AGARD Structures and Materials Panel convened a meeting of specialists entitled "Environmental Effects on Materials for Space Applications". The meeting heard papers on and discussed general requirements and related design philosophies, environment and environmental effects, properties of interest, and tests, with the aim of establishing the current state-of-the-art and encouraging relevant future research.</p> <p>P.T.O.</p>	<p>AGARD-CP-327</p> <p>Materials Spacecraft Aerospace engineering Design Aerospace environment Environmental tests Mechanical properties</p>	<p>AGARD-CP-327</p> <p>Materials Spacecraft Aerospace engineering Design Aerospace environment Environmental tests Mechanical properties</p>	<p>AGARD Conference Proceedings No.327 Advisory Group for Aerospace Research and Development, NATO ENVIRONMENTAL EFFECTS ON MATERIALS FOR SPACE APPLICATIONS Published March 1983 230 pages</p> <p>In the Fall of 1982 the AGARD Structures and Materials Panel convened a meeting of specialists entitled "Environmental Effects on Materials for Space Applications". The meeting heard papers on and discussed general requirements and related design philosophies, environment and environmental effects, properties of interest, and tests, with the aim of establishing the current state-of-the-art and encouraging relevant future research.</p> <p>P.T.O.</p>

<p>This publication documents the papers presented at that meeting together with summaries of the subsequent discussions.</p> <p>Papers presented at the 55th Meeting of the AGARD Structures and Materials Panel in Toronto, Canada on 19 - 24 September 1982.</p> <p>ISBN 92-835-0330-9</p>	<p>This publication documents the papers presented at that meeting together with summaries of the subsequent discussions.</p> <p>Papers presented at the 55th Meeting of the AGARD Structures and Materials Panel in Toronto, Canada on 19 - 24 September 1982.</p> <p>ISBN 92-835-0330-9</p>
<p>This publication documents the papers presented at that meeting together with summaries of the subsequent discussions.</p> <p>Papers presented at the 55th Meeting of the AGARD Structures and Materials Panel in Toronto, Canada on 19 - 24 September 1982.</p> <p>ISBN 92-835-0330-9</p>	<p>This publication documents the papers presented at that meeting together with summaries of the subsequent discussions.</p> <p>Papers presented at the 55th Meeting of the AGARD Structures and Materials Panel in Toronto, Canada on 19 - 24 September 1982.</p> <p>ISBN 92-835-0330-9</p>

B.30

AGARD

NATO  OTAN

7 RUE ANCELLE - 92200 NEUILLY-SUR-SEINE
FRANCE

Telephone 745.08.10 - Telex 610176

**DISTRIBUTION OF UNCLASSIFIED
AGARD PUBLICATIONS**

AGARD does NOT hold stocks of AGARD publications at the above address for general distribution. Initial distribution of AGARD publications is made to AGARD Member Nations through the following National Distribution Centres. Further copies are sometimes available from these Centres, but if not may be purchased in Microfiche or Photocopy form from the Purchase Agencies listed below.

NATIONAL DISTRIBUTION CENTRES

BELGIUM

Coordonnateur AGARD - VSL
Etat-Major de la Force Aérienne
Quartier Reine Elisabeth
Rue d'Evere, 1140 Bruxelles

CANADA

Defence Science Information Services
Department of National Defence
Ottawa, Ontario K1A 0K2

DENMARK

Danish Defence Research Board
Osterbrogades Kaserne
Copenhagen Ø

FRANCE

O.N.F.R.A. (Direction)
29 Avenue de la Division Leclerc
92320 Châtillon sous Bagneux

GERMANY

Fachinformationszentrum Energie,
Physik, Mathematik GmbH
Kernforschungszentrum
D 7514 Eggenstein-Leopoldshafen 2

GREECE

Hellenic Air Force General Staff
Research and Development Directorate
Holargos, Athens

ICELAND

Director of Aviation
c/o Flugrad
Reykjavik

UNITED STATES

National Aeronautics and Space Administration (NASA)
Langley Field, Virginia 23365
Attn: Report Distribution and Storage Unit

THE UNITED STATES NATIONAL DISTRIBUTION CENTRE (NASA) DOES NOT HOLD STOCKS OF AGARD PUBLICATIONS, AND APPLICATIONS FOR COPIES SHOULD BE MADE DIRECT TO THE NATIONAL TECHNICAL INFORMATION SERVICE (NTIS) AT THE ADDRESSES BELOW.

PURCHASE AGENCIES

Microfiche or Photocopy

National Technical
Information Service (NTIS)
5285 Port Royal Road
Springfield
Virginia 22161, USA

Microfiche

Space Documentation Service
European Space Agency
10, rue Mario Nikis
75015 Paris, France

Microfiche or Photocopy

British Library Lending
Division
Boston Spa, Wetherby
West Yorkshire LS23 7BQ
England

Requests for microfiche or photocopies of AGARD documents should include the AGARD serial number, title, author or editor, and publication date. Requests to NTIS should include the NASA accession report number. Full bibliographical references and abstracts of AGARD publications are given in the following journals.

Scientific and Technical Aerospace Reports (STAR)

published by NASA Scientific and Technical
Information Facility
Post Office Box 8757
Baltimore-Washington International Airport
Maryland 21240, USA

Government Reports Announcements (GRA)

published by the National Technical
Information Services, Springfield
Virginia 22161, USA



Printed by *Specialised Printing Services Limited*
40 Chigwell Lane, Loughton, Essex IG10 3TZ

ISBN 92-835-0330-9

D
FI